Tropical-Extratropical Interactions and Extreme Precipitation Events in the Middle East

Dissertation
submitted for the award of the title
"Doctor of Natural Sciences"

to the Faculty of Physics, Mathematics, and Computer Science
of Johannes Gutenberg University Mainz
in Mainz

Andries-Jan de Vries

Born in Leidschendam, The Netherlands

Mainz, November 2017

date of oral examination: 9 March 2018

Abstract

Extreme precipitation events in the arid Middle East can cause flooding with dramatic socioeconomic impacts. At the same time, these events can replenish fresh water resources that are of crucial importance for agriculture and ecosystems. Apart from Israel, such events in the region are largely unexplored in the literature. In this thesis, we present (1) a qualitative concept of an important weather phenomenon that is associated with the most severe flash floods in the Levant, (2) a multiple-perspective analysis and quantification of the larger-scale dynamics of three extreme precipitation cases in Saudi Arabia in different seasons, and (3) an identification method for extreme precipitation events in the Middle East based on synoptic-scale meteorological features. Our main finding is that extreme precipitation events in the Middle East, as in other dry subtropical regions, often result from tropical-extratropical interaction.

The Active Red Sea Trough (ARST) phenomenon is explained as a type of tropical-extratropical interaction whereby a transient midlatitude upper-level trough interacts with the semi permanent surface trough over the Red Sea. Enhanced moisture transport occurs predominantly over the Arabian and Red Seas through an intensified Arabian anticyclone, resulting in an intrusion of tropical moist air masses into the Levant. The devastating flooding of Jeddah, Saudi Arabia, in November 2009 showed the same dynamical characteristics as those of twelve ARST events that affected the Levant, implying that the phenomenon can affect a much larger part of the Middle East than previously assumed.

Three cases of extreme precipitation in Saudi Arabia in autumn (the Jeddah flooding of November 2009), winter, and spring, developed in a tropospheric environment controlled by the larger-scale circulation. Anticyclonic Rossby wave breaking resulted in an intrusion of a midlatitude upper-level trough into low latitudes that interacted with the tropical circulation. Eulerian and Lagrangian analyses revealed moisture transport from nearby and remote tropical regions, leading to above-normal tropospheric moisture content over Saudi Arabia. Upward motion was associated with orographic lifting of moist air masses (all cases), low-level moisture convergence and reduced static stability (autumn case), dynamical lifting and diabatic heating (winter case), and strong surface sensible heating (spring case), favoring the build-up and release of potential instability. The three cases exhibited unusual to extreme (>2 to >4 standard deviations) synoptic characteristics within the varying background large-scale circulation of the different seasons.

Building on these case studies, we developed an identification method for extreme precipitation events in the Middle East that combines stratospheric potential vorticity (PV) intrusions and structures of high poleward vertically integrated water vapor transport (IVT). These meteorological features represent tropical-extratropical interaction, and have previously been postulated as large-scale precursors of extreme precipitation, but had thus far never been combined in an algorithm for its detection. Combined PV and IVT features are intimately connected to the extreme precipitation intensity and seasonality of the region. The farther south a stratospheric PV intrusion reaches, the larger the IVT magnitude, and the longer their combined duration, the more extreme the precipitation. Importantly, IVT is a potentially more pertinent predictor of extreme precipitation than PV. Tropical-extratropical interactions contribute to a large fraction of the annual rainfall amounts (40-70%) and extreme precipitation days (50-90%) at many sites in the arid parts of the Levant and the Arabian Peninsula. This thesis contributes to a better understanding of the larger-scale atmospheric processes that drive extreme precipitation events in the Middle East and provides a tool for their identification that can support weather prediction and early warning systems as well as future studies on their mesoscale and climatological aspects.

Zusammenfassung

Das Auftreten von Extremniederschlägen im ariden Nahen Osten kann Überflutungen mit dramatischen sozioökonomischen Folgen auslösen. Gleichzeitig können diese Ereignisse Süßwasservorräte auffüllen, die äußerst wichtig für Landwirtschaft und Ökosystem sind. Außer in Israel sind solche Ereignisse in der Literatur weitgehend unerforscht. In dieser Dissertation präsentieren wir (1) ein qualitatives Konzept eines wichtigen Wetterphänomens, das mit den schwersten Sturzfluten in der Levante zusammenhängt, (2) eine Analyse und Quantifizierung der großskaligen Dynamik dreier Extremniederschlagsereignisse in Saudi Arabien zu verschiedenen Jahreszeiten und aus unterschiedlichen Perspektiven und (3) eine Identifizierungsmethode für Extremniederschlagsereignisse im Nahen Osten, basierend auf Eigenschaften der synoptischen Meteorologie. Unser Hauptresultat ist, dass Extremniederschläge im Nahen Osten, wie auch in anderen subtropischen Regionen, oft aus der tropisch-außertropischen Wechselwirkung resultieren.

Das Phänomen des aktiven Trogs über dem Roten Meer (Active Red Sea Trough, ARST) wird als ein Typ tropisch-außertropischer Wechselwirkung beschrieben, bei dem ein vorübergehender Höhentrog mittlerer Breite mit dem semi-permanenten Bodentrog über dem Roten Meer interagiert. Durch einen intensivierten arabischen Antizyklon tritt ein verstärkter Feuchtigkeitstransport, vorwiegend über Arabischem und Rotem Meer, auf, wodurch feuchte tropische Luftmassen in die Levante eindringen. Die verheerenden Fluten in Dschidda, Saudi Arabien, im November 2009 zeigten die selben dynamischen Eigenschaften wie zwölf die Levante betreffende ARST-Ereignisse, demzufolge kann dieses Phänomen viel größere Teile des Nahen Ostens betreffen als bisher angenommen.

Drei Fälle von Extremniederschlägen in Saudi Arabien in Herbst (die Dschidda Überflutung im November 2009), Winter und Frühling entwickelten sich in troposphärischen Bedingungen die durch die großskalige Zirkulation beeinflusst waren. Das antizyklonische Brechen von Rossby-Wellen resultierte in dem Eindringen eines Höhentrogs aus mittleren in niedere Breiten, wo es mit der tropischen Zirkulation wechselwirkte. Eulersche und lagrangesche Analysen offenbarten Feuchtigkeitstransport aus nahen und fernen tropischen Regionen, der zu erhöhter troposphärischer Luftfeuchtigkeit über Saudi Arabien führte. Aufwärtsbewegung ging einher mit dem Stau feuchter Luftmassen (in allen Fällen), Feuchtigkeitskonvergenz in niedrigen Höhen und reduzierter statische Stabilität (im Herbst), dynamischer Hebung und diabatischer Erwärmung (im Winter) und starker fühlbarer Erwärmung an der Oberfläche (im Frühling), die Aufbau und Entladung von potentieller Instabilität begünstigten. Die drei Fälle zeigten ungewöhnliche bis extreme (>2 bis >4 Standardabweichungen) synoptische Charakteristika innerhalb der variierenden großräumigen Hintergrundzirkulation der unterschiedlichen Jahreszeiten.

Auf diesen drei Fallstudien aufbauend haben wir eine Methode zur Identifizierung von Extremniederschlagsereignissen im Nahen Osten entwickelt, die das Eindringen stratosphärischer potentieller Vortizität (PV) und Strukturen von hohem, polwärts gerichtetem vertikal integriertem Wasserdampftransport (IVT) berücksichtigt. Diese meteorologischen Eigenschaften repräsentieren tropisch-außertropische Wechselwirkungen und wurden bereits als großskaliger Vorläufer von Extremniederschlag postuliert, wurden bisher allerdings nicht zu einem Algorithmus für dessen Detektierung kombiniert. Kombinierte PV- und IVT-Eigenschaften sind eng mit der Intensität und Saisonalität der Extremniederschläge in der Region verknüpft. Je weiter südlich ein stratosphärisches PV-Eindringen reicht, je grösser das Ausmaß des IVT und je länger ihre kombinierte Lebensdauer, desto

extremer der Niederschlag. Insbesondere scheint der IVT ein potentiell geeigneterer Prädiktor für Extremniederschläge zu sein als die PV. Tropisch-extratropische Wechselwirkungen tragen einen großen Anteil der jährlichen Niederschläge (40-70%) und der Tage mit extremen Niederschlag (50-90%) an vielen Standorten im ariden Teil der Levante und der arabischen Halbinsel bei. Die vorliegende Arbeit trägt zu einem besserem Verständnis de großskaligen atmosphärischen Prozesse, die Extremniederschläge im Nahen Osten antreiben, bei und stellt ein Werkzeug zu deren Identifikation bereit, das Wettervorhersagen und Frühwarnsysteme ebenso unterstützen kann wie künftige Studien ihrer mesoskaligen und klimatologischen Aspekte.

Table of Contents

1 Introduction

1.1 Climate of the Middle East

1.1.1 Flooding in the Desert

The Middle East is a subtropical region with a diverse topography, distinct land-sea contrasts, and steep gradients in annual rainfall and climate regimes. The region borders to the subtropical and tropical waters of the Mediterranean, Arabian and Red Seas, and the Persian Gulf (Figure 1a). Along the eastern Red Sea coast arise the Hijaz and Asir Mountains, while farther to the northeast of the Arabian Peninsula the Zagros Mountains reach altitudes in excess of 4 km above sea level. The larger part of the Middle East region has a hot arid desert climate (*Kottek et al.*, 2006; *Peel et al.*, 2007) with very low annual rainfall amounts that fall below 20-80 mm $year^{-1}$ over eastern Egypt, the Negev desert, northwest Saudi Arabia and the Rub' al Khali desert in the southeastern part of the Arabian Peninsula (*Almazroui et al.*, 2012a; *Tanarhte et al.*, 2012).

Despite these usually dry conditions, recurrent extreme precipitation events can cause flooding with dramatic socioeconomic impacts. For example, in November 2009, flash floods inundated Jeddah, and resulted in 161 deaths, about 10,000 people affected and an estimated damage of about 900 million US dollar (Emergency Events Database, unpublished data, provided on 19 April 2017 by the Centre for Research on the Epidemiology of Disasters; CRED, hereafter, EM-DAT). Over the period of 1900-2016, 39 flood events occurred in Egypt, Israel, Jordan, and Saudi Arabia and caused 1,508 fatalities, affected 291,387 people, and resulted in damages exceeding 1.8 billion US dollars (Appendix A). Most likely, these numbers are an underestimation since not all flood incidences and societal impacts may have been reported, in particular during the early 20^{th} century.

At the same time, these rainfall events can recharge scarce water resources that are important for agriculture and ecosystems (*Sirdas and Sen*, 2007; *Amin et al.*, 2016; *Schulz et al.*, 2016). The Middle East faces a rapid population growth and economic development, leading to an increased fresh water demand, while climate projections for the future anticipate a decrease in annual precipitation over a large part of the region, enhanced heat extremes and an extended dry season (*Evans*, 2009; *Chenoweth et al.*, 2011; *Lelieveld et al.*, 2012, 2016; *Almazroui et al.*, 2013; *Peleg et al.*, 2015; *Amin et al.*, 2016). As a result, a high interest is arising in the harvesting of flood and rainwater that can both alleviate flood hazards and replenish groundwater aquifers and fresh water resources in urban areas (*Sen et al.*, 2013; *Amin et al.*, 2013; *Mahmoud and Alazba*, 2015, 2016; *Guizani*, 2016). These destructive flood impacts and potential fresh water supplies give rise to a dichotomy of important societal implications, which highlight the need for a better understanding of the atmospheric processes that drive extreme precipitation events in the Middle East.

1.1.2 Tropospheric Circulation

The Middle East is situated at the crossroads of the European, African, and Asian continents. Likewise, the weather conditions over the Middle East are subject to the tropospheric circulation regimes that dominate these continents, that is, the extratropics where baroclinic systems and the westerlies prevail, the tropical circulation over Equatorial Africa, and the South Asian monsoon. Their respective influence

alternates with the seasons and gives rise to an intriguing variation of different synoptic-scale circulation patterns over the Middle East. In general, we can distinguish a dry season and a wet season that lasts from June until September and from October until May, respectively (*Almazroui*, 2011; *Almazroui et al.*, 2012b; *Kenawy and McCabe*, 2016).

During boreal summer, the circulation over the Middle East is controlled by the South Asian monsoon (Figure 1b). Vast amounts of water vapor are transported by the Somali jet toward the South Asian continent, where they precipitate and generate strong diabatic heating. This warm structure expands northwestward through Rossby wave propagation (*Rodwell and Hoskins*, 1996; *Tyrlis et al.*, 2013). The combination of this warm structure and the much cooler extratropical air over Europe leads to steep sloping isentropes along which the midlatitude westerly flow descends, imposing large-scale subsidence over the eastern Mediterranean, northeast Africa and the Middle East. This subsidence is further strengthened by the regional heat-driven circulation over the Zagros Mountains (*Zaitchik et al.*, 2007) and is sometimes also associated with the African summer monsoon and the downward branch of the Hadley Cell (*Ziv et al.*, 2004). Near the surface, a massive thermal low expands from South Asia westward across the Arabian Peninsula, which is known as the Persian Trough (*Bitan and Saaroni*, 1992; *Alpert et al.*, 2004a, 2004b; *Saaroni et al.*, 2010b). In addition, a ridge of subtropical anticyclones prevails at mid-tropospheric levels with three centers over the Atlas and Zagros Mountains and the Arabian Peninsula (*Zarrin et al.*, 2010). The subtropical jet stream, that in other seasons is positioned over northeast Africa and the Middle East, is displaced to the north of the Middle East during summer (Figure 1b,c). In short, between June and September, the circulation over the Middle East is characterized by the Persian Trough near the surface, mid-tropospheric subtropical anticyclones, and subsidence at middle- and upper-tropospheric levels (Figure 1b). The large-scale subsidence suppresses convection and precipitation, leading to very dry conditions throughout the Middle East (Figure 1b), except for the southwestern part of the Arabian Peninsula, where local convection over the elevated topography can generate rainfall as a part of the eastern fringes of the African summer monsoon (*Almazroui et al.*, 2012b; *Enzel et al.*, 2015).

After summer, the South Asian monsoon circulation reverses and tropical moist easterlies dominate the Arabian Sea, Indian Ocean and Equatorial Africa (Figure 1c). Near the surface, the Persian Trough retreats and a low pressure system expands northward from the tropical low-pressure belt over Equatorial Africa across the Red Sea region toward the eastern Mediterranean. This inverted V-shaped surface trough is usually referred to as the Red Sea Trough or Sudan monsoon low (*El-Fandy*, 1948; *Alpert et al.*, 2004a, 2004b; *Tsvieli and Zangvil*, 2005). Its formation is attributed to local topographic and thermal forcing factors (*Krichak et al.*, 1997a, 1997b). The Red Sea Trough reaches most frequently over the Levant in late autumn, while being less prominent during winter and spring (*Alpert et al.*, 2004b; *Tsvieli and Zangvil*, 2005). At both flanks of the Red Sea Trough, subtropical anticyclones dominate in the lower and middle troposphere. The subtropical anticyclone at the eastern flank of the Red Sea Trough is located over the Arabian Peninsula and Arabian Sea, and is termed as the Arabian anticyclone, after *Raziei et al.* (2012). Accordingly, during late autumn, winter and early spring, the synoptic circulation over the Middle East is characterized by the semi permanent Red Sea Trough and Arabian anticyclone (Figure 1c). Usually, the associated weather conditions over the arid parts of the Levant and Arabian Peninsula are dry and warm. However, occasionally, midlatitude cyclones intrude into the Middle East following a southerly displaced storm track over the region. The combination of warm and moist air masses from the southerly tropical waters and cold upper-tropospheric air from the extratropics can lead to a destabilized

troposphere and rainfall over the Middle East (*Barth and Steinkohl*, 2004; *Chakraborty et al.*, 2006; *Evans et al.*, 2004; *Evans and Smith*, 2006; *Kumar et al.*, 2015; *Almazroui et al.*, 2016).

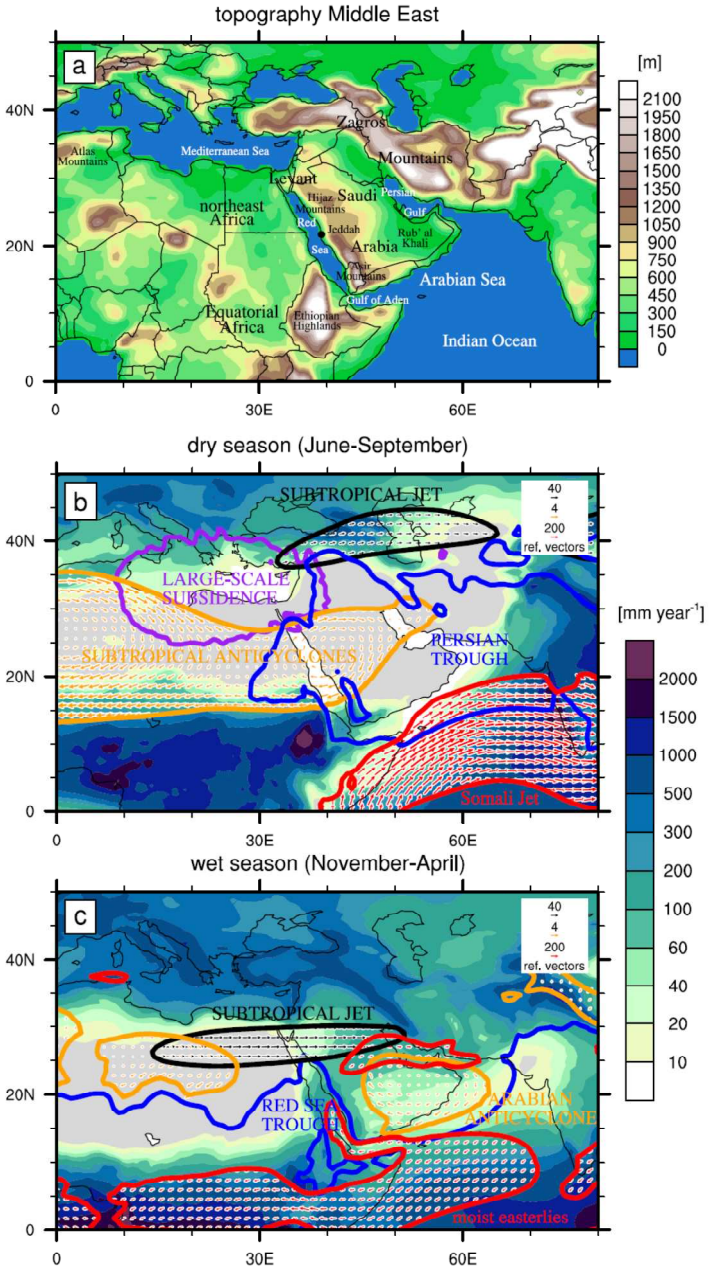

Figure 1. The Middle East region with the ERA-Interim (a) topography and mean circulation (1979-2015) features during the (b) dry season from June to September, and (c) wet season from November to April. Panel (b) shows the monthly mean of the 0.025 Pa s^{-1} omega contour at 200 hPa (purple), the 28 m s^{-1} wind magnitude contour and vectors at 200 hPa (black), the 5880 m geopotential height contour and wind vectors at 500 hPa (orange), the 1007 hPa sea-level pressure contour (blue), and the 250 kg m^{-1} s^{-1} vertically integrated water vapor transport (IVT) contour and vectors (red). Panel (c) shows the monthly mean of the 46 m s^{-1} wind magnitude contour and vectors at 200 hPa (black), the 1522 m geopotential height contour and wind vectors at 850 hPa (orange), the 1013.5 hPa sea-level pressure contour (blue) and the 100 kg m^{-1} s^{-1} IVT contour and vectors (red).

1.2 Extreme Precipitation in the Middle East

1.2.1 From Hourly to Paleoclimatological Time-Scales

The Levant region can receive rainfall from extratropical cyclones and tropical intrusions (*Dayan and Morin*, 2006; *Dayan et al.*, 2015). On hourly time-scales, these weather systems exhibit different convective rain cell characteristics (*Peleg and Morin*, 2012; *Marra and Morin*, 2015) and lightning distribution patterns (*Shalev et al.*, 2011; *Ben Ami et al.*, 2015). Paleoclimatological evidence suggests that frequent extratropical cyclones control the climate and physiography of the relatively wet eastern Mediterranean coastal zone (*Enzel et al.*, 2008), whereas sporadic tropical intrusions may have brought wet episodes during dry interglacials (*Waldmann et al.*, 2010) and extreme floods (*Greenbaum et al.*, 2010) in the hyper-arid deserts to the south and east. Accordingly, the influence of extratropical cyclones diminishes rapidly beyond the eastern Mediterranean coast, whereas a reversed geographical dependency is observed for tropical intrusions (*Enzel et al.*, 2008, 2015). Steep rainfall gradients in the region are regulated by the orientation of the topography that the moist air flows of these weather systems encounter. In this thesis, we are primarily concerned with the synoptic scales of these rain-bearing weather systems.

1.2.2 Synoptic Systems in the Levant

Extratropical cyclones form frequently in the cyclogenetic region over the eastern Mediterranean basin (*Alpert et al.*, 1990; *Trigo et al.*, 1999). They are often referred to as Mediterranean cyclones, or sometimes, as Cyprus Lows or Syrian Lows, depending on the location of the surface cyclone (*Kahana et al.*, 2002; *Alpert et al.*, 2004a; *Romem et al.*, 2007; *Raveh-Rubin and Wernli*, 2015). These baroclinic systems occur throughout the wet season with the highest frequency in winter (*Alpert et al.*, 2004b). They contribute to the majority of annual rainfall along the relatively wet eastern Mediterranean coast (*Saaroni et al.*, 2010a) and flooding in the northern Negev desert (*Kahana et al.*, 2002; *Shentsis et al.*, 2012). The west-northwesterly flow near the surface advects moisture from the Mediterranean Sea (*Shay-El and Alpert*, 1991) toward the coastline where it precipitates under influence of orographic lifting (*Kahana et al.*, 2002; *Tsvieli and Zangvil*, 2005).

Tropical intrusions are mostly associated with the Red Sea Trough and tropical plumes. The Red Sea Trough related weather conditions over the Levant are usually dry and hot. However, when accompanied by an approaching midlatitude upper-level trough, tropical moist air masses can intrude into the Levant and lead to a destabilized troposphere and development of convective storms. This activation of the Red Sea Trough is often termed as the Active Red Sea Trough (*Kahana et al.*, 2002; *Ziv et al.*, 2005; *Krichak et al.*, 2012). Section 1.2.3 elaborates on this phenomenon. Tropical plumes refer to cloud bands that reach from Equatorial or West Africa in a northeastward direction across the Saharan desert toward the Levant. These cloud bands have been observed in satellite imagery and are from a dynamical perspective associated with an intensified subtropical jet stream with anticyclonic curvature, a midlatitude trough, and moisture transport from the tropics over the dry Saharan boundary layer (*Dayan and Abramski*, 1983; *Ziv*, 2001; *Rubin et al.*, 2007; *Tubi and Dayan*, 2014). Tropical plumes are relatively rare, primarily confined to the winter season (December - March), and can produce light to heavy widespread rainfall across the arid desert region (*Rubin et al.*, 2007).

During spring, smaller-scale cyclonic disturbances can form at the lee side of the Atlas mountains over northwest Africa under influence of strong baroclinicity, resulting from intense surface heating over the Sahara and colder extratropical air intrusions over the Mediterranean (*Alpert and Ziv*, 1989; *Egger et al.*, 1995; *Alpert et al.*, 2004b). These cyclonic disturbances, also named as Sharav cyclones, can travel rapidly eastward across North Africa and affect the Levant with severe dust storms (*Salam and Sowelin*, 1967; *Alpert and Ganor*, 2001; *Tsidulko et al.*, 2002; *Karam et al.*, 2010). At times, they may also precipitate when merging with Mediterranean cyclones. Thus, extreme precipitation over the Levant results predominantly from Mediterranean cyclones, ARSTs, tropical plumes and their combinations.

1.2.3 The Active Red Sea Trough

The Active Red Sea Trough (ARST) is of particular interest as this phenomenon is responsible for recurrent dramatic societal impacts and a significant part of the most severe flash floods in the Negev desert (*Kahana et al.*, 2002; *Shentsis et al.*, 2012). Already in the early 20th century, *Ashbel* (1938) and *El-Fandy* (1948) documented several cases of violent thunderstorms and floods in Egypt, Palestine and Syria under influence of the Red Sea Trough. For example, their studies reported a flooding in October 1937 that destroyed near 100 villages and killed 1,000 people in the vicinity of Damascus. More recently, in November 1994, extreme precipitation and flooding occurred in eastern Egypt as a result of an ARST event (*Krichak and Alpert*, 1998; *Krichak et al.*, 2000), which left 600 fatalities and 110,660 people affected (Appendix A). These ARSTs occur predominantly in autumn and to a lesser incidence in winter and spring (*Kahana et al.*, 2002; *Krichak et al.*, 2012; *Shentsis et al.*, 2012). This seasonality was previously also recognized by *El-Fandy* (1952), who stated that "for the last 30 years, not a single autumn passed without the occurrence of a noticeable thunderstorm of this type". *Dayan et al.* (2001) explained the preference of the ARST for autumn by coinciding favorable latitudinal positions of the African monsoon and subtropical jet. However, more profound insight in the ARST seasonality is still lacking.

Several case studies and climatological investigations addressed the involved synoptic-scale dynamics of the ARST. By definition, ARSTs are characterized by the Red Sea Trough near the surface over the Red Sea region and an upper-level trough over Egypt (Figure 2). The Red Sea Trough transports hot air masses at its eastern flank across the western margins of the Arabian Peninsula toward the Levant, while a midlatitude trough brings cold upper-tropospheric air toward the region (*El-Fandy*, 1950; *Krichak et al.*, 2000; *Dayan et al.*, 2001; *Kahana et al.* 2002; *Ziv et al.*, 2005; *Dayan and Morin*, 2006; *Tsvieli and Zangvil*, 2005, 2007; *Krichak et al.*, 2012). In combination with increased moisture, the troposphere becomes highly unstable. Subsequent mesoscale processes and the influence of the local topography organize the formation of the convective storms (*Dayan et al.*, 2001; *Kahana et al.* 2004). In addition, large-scale ascent may favor their development through upper-tropospheric positive vorticity advection and low-tropospheric warm air advection, implying quasi-geostrophic ascent, and by upper-level divergence near the left exit of the subtropical jet or right entrance of the polar jet, being linked to mid-tropospheric ascent (*Dayan et al.*, 2001; *Ziv et al.*, 2005).

The moisture pathways and origin of ARSTs are highly debated. Several ARST case studies indicated various moisture sources, including the Arabian Sea (*Krichak and Alpert*, 1998), western Equatorial Africa (*Dayan et al.*, 2001), and tropical Africa as the primary and the Red Sea as the secondary moisture source (*Ziv et al.*, 2005). *Tsvieli and Zangvil* (2005, 2007) suggested moisture transport from Equatorial Africa and/or the Indian Ocean through southwesterly mid-tropospheric flow and the eastern

Mediterranean by west-northwesterly flow near the surface for 'wet' Red Sea Trough days. *Krichak et al.* (2012) speculated that large amounts of moisture are transported from tropical Africa in the form of an atmospheric river. It is noteworthy that most of these aforementioned studies made inferences to moisture pathways and origin based upon analyses of humidity, wind and moisture flux fields at particular pressure levels, total column water, backward air parcel trajectories from singular grid points, and satellite water vapor imagery.

Apart from the presence of the Red Sea Trough and midlatitude upper-level trough, *Ziv et al.* (2005) found an intensified Arabian anticyclone during an ARST event in December 1993 that transported moisture from tropical origin over the Red Sea basin. Importantly, southerly winds in the mid-troposphere over the Levant served as a successful indicator for ARST flooding in the Negev desert (*Kahana et al.*, 2004) and may reflect southerly tropical moisture transport that is driven by the Arabian anticyclone. Since the Arabian anticyclone is only visible in the lower troposphere, this feature may have been easily overlooked in other studies that focused solely at surface and mid-tropospheric levels. Accordingly, it is not clear whether the Arabian anticyclone was only important for the ARST event in December 1993 or for the ARST in general. In short, several studies addressed the ARST dynamical characteristics. However, the inconsistencies and sometimes controversies that are documented, highlight the need for an integral concept of the common ARST dynamics (*Alpert et al.*, 2006).

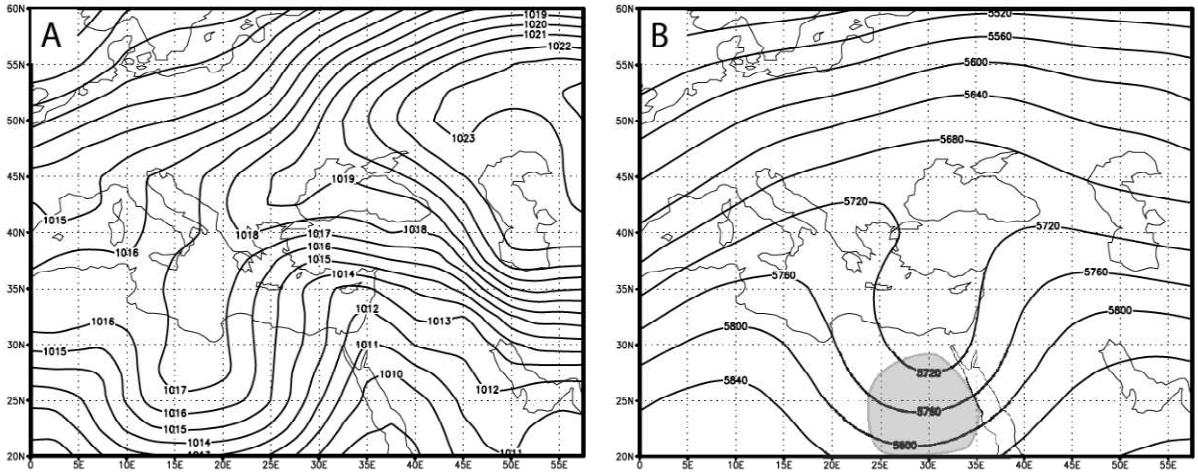

Figure 2. Composites of (a) sea level pressure with 1 hPa intervals, and (b) 500 hPa geopotential height with 40 m intervals for 18 major ARST floods in the Negev desert. Areas in which the normalized anomalies exceed 1.5 STDs are shaded (from *Kahana et al.*, 2004).

1.2.3 Saudi Arabia

Most research on extreme precipitation in the Middle East addressed the Levant region. For example, previous ARST studies focused primarily on Israel. Therefore, it is not yet known to what extent other countries in the region can be affected by the ARST. In Saudi Arabia, Jeddah (for the location, see Figure 1) has repeatedly undergone extreme precipitation and flooding with devastating consequences. Recently, several studies addressed such extreme precipitation cases through modeling approaches (*Haggag and El-Badry*, 2013; *Deng et al.*, 2015; *Yesubabu et al.*, 2016) and diagnostic analyses (*Al-Khalaf and Basset*, 2013). These studies described synoptic and mesoscale characteristics that show substantial similarities to

the ARST; a cold midlatitude upper-level trough that merges with the Red Sea Trough and a stationary Arabian anticyclone that favored moisture transport over the Arabian and Seas. Locally, low-level convergence and upslope winds along the Red Sea coastal mountains supported deep moist convection and development of mesoscale convective systems (*Haggag and El-Badry*, 2013; *Deng et al.*, 2015). In the central part of the Arabian Peninsula, heavy rainfall has been associated with upper- and lower-tropospheric cyclonic circulations and enhanced tropospheric moisture content (*Kumar et al.*, 2015). Apart from these studies, extreme precipitation events in Saudi Arabia have not been investigated and thus remain largely unexplored.

1.3 Extreme Precipitation in Arid Subtropical Regions

1.3.1 Tropical-Extratropical Interactions

Apart from the Middle East, several other dry subtropical regions are affected by extreme precipitation and flooding. These regions include northwestern Africa, southwestern North America, southern Africa, South America, the Himalaya's, and Australia (e.g. *Wright*, 1997; *Knippertz et al*., 2003; *Knippertz and Martin*, 2005, 2007a; *Seluchi and Marengo*, 2000; *Hart et al*., 2010; *Hong et al.*, 2011; *Favors and Abatzoglou*, 2013; *Martius et al.*, 2013; *Vellore et al.*, 2016). These extreme precipitation events have all in common to result from the interaction between the extratropical and tropical circulations, hence, referred to as tropical-extratropical interactions. Several of the aforementioned studies conducted thorough investigations on the dynamical and thermodynamical processes of these events. Perhaps, the most prominent study on this subject is presented by *Knippertz* (2007) who proposed a framework of tropical-extratropical interactions in which the intrusion of upper-level troughs into low latitudes and the formation of tropical plumes take a central place. This section summarizes the atmospheric features and larger-scale and smaller-scale processes that are typically associated with these tropical-extratropical interactions and extreme precipitation events in dry subtropical regions.

1.3.2 Atmospheric Features

Several atmospheric features have a direct relevance to tropical-extratropical interactions and extreme precipitation events such as tropical plumes, tropical moisture exports, monsoon bursts/monsoon surges, and atmospheric rivers. Tropical plumes (Figure 3a) are elongated cloud bands in the middle and upper troposphere that reach from the tropics in pole- and eastward directions toward midlatitudes (*McGuirk et al*., 1988; *Ziv*, 2001; *Knippertz and Martin*, 2005; *Knippertz*, 2005, 2007; *Rubin et al*., 2007; *Tubi and Dayan*, 2014). These appear most frequent during the boreal cool seasons in regions with mean low-latitude westerlies, that is, the central and eastern Pacific and Atlantic Oceans (*Knippertz*, 2007). Tropical moisture exports refer to moist air parcels that originate from the tropics and reach the extratropics (*Knippertz and Wernli*, 2010; *Knippertz et al.*, 2013). Monsoon bursts/monsoon surges are intrusions of tropical monsoonal moisture into higher latitudes, where they can induce wet episodes and flooding (*Hong et al.*, 2011; *Cavazos et al.*, 2002; *Martius et al.*, 2013; *Pascale and Bordoni*, 2016). These atmospheric features have been objectively identified using satellite imagery, air parcel trajectories, and statistically-based thresholds on moisture flux and wind fields, and were found to contribute substantially to annual rainfall amounts and extreme precipitation events in arid subtropical regions (*Knippertz*, 2003; *Hart et al.*, 2012, 2013; *Favors and Abatzoglou*, 2013; *Froelich et al.*, 2013).

Over the last decade, atmospheric rivers have received increased attention as they are a key feature in heavy rainfall and flooding across North America and Europe (*Ralph et al.*, 2006; *Lavers and Villarini*, 2013a, 2013b; *Waliser and Guan*, 2017). Atmospheric rivers are characterized by narrow and elongated plume-like structures of large moisture amounts or strong moisture transports (Figure 3b). These features are usually embedded within multiple developing and decaying extratropical cyclones. Although atmospheric rivers form to a large extent through local low-level moisture convergence (*Bao et al.*, 2006; *Knippertz and Martin*, 2007a; *Dacre et al.*, 2015), and are particularly notorious for impacting midlatitude regions, they have also relevance in the context of this thesis. Their moisture pathways are often rooted in the tropics and their formation can be accompanied by upper-level troughs, implying tropical-extratropical interaction (*Ralph et al.*, 2011; *Moore et al.*, 2012) and, they can also affect dry subtropical regions (*Guan and Waliser*, 2015; *Ramos et al.*, 2015; *Waliser and Guan*, 2017). Atmospheric rivers contribute significantly to extreme precipitation and annual rainfall amounts across coastal regions as well as the interior of continents (*Rutz and Steenburg*, 2012; *Lavers and Villarini*, 2013a, 2013b; *Guan and Waliser*, 2015).

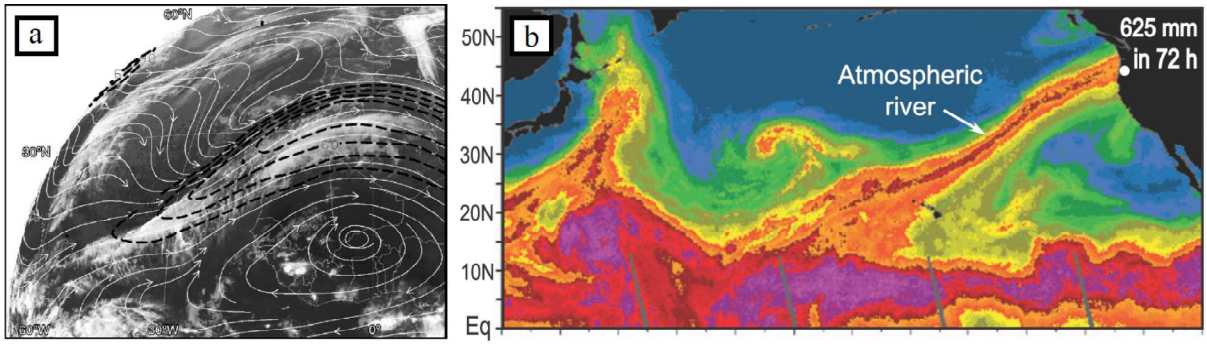

Figure 3. An example of (a) a tropical plume over northwest Africa; meteosat infrared image at 00 UTC 31 March 2002 and overlaid streamlines and isotachs (dashed contours at 40, 50, 60, and 70 m s-1) from the ECMWF TOGA analysis on the 345-K isentropic level (from *Knippertz*, 2007) and (b) an atmospheric river over the Pacific; SSM/I satellite image of Integrated Water Vapor (IWV) in cm on 7 November 2006 (from *Ralph et al.*, 2011).

1.3.3 Larger-Scale and Smaller-Scale Processes

Tropical-extratropical interactions are often preceded by wave trains that propagate from the extratropics toward the tropics (*Knippertz*, 2007; *Luo et al.*, 2015). Sources for this wave energy include upstream diabatic heating and strong baroclinic developments. From a potential vorticity (PV) perspective, the combination of PV reduction through latent-heat release and negative PV advection can lead to rapid ridge amplification (*Knippertz and Martin*, 2005, 2007b; *Martius et al.*, 2008; *Hart et al.*, 2010). As a result, anticyclonic wave breaking occurs (conform the LC1 baroclinic life cycle of *Thorncroft et al.* (1993)) along with the intrusion of an upper-level trough far into low latitudes. The midlatitude upper-level trough interacts with the tropical circulation in the form of a tropical easterly wave (*Knippertz et al.*, 2003; *Favors and Abatzoglou*, 2013), surge in trade winds (*Knippertz and Martin*, 2005), monsoonal depression (*Hong et al.*, 2011; *Martius et al.*, 2013; *Vellore et al.*, 2016) or semi permanent heat low (*Hart et al.*, 2010). In other words, the midlatitude and tropical circulations couple, which provides a corridor for a poleward excursion of tropical moisture. Subtropical anticyclones or ridges were present over the Tibetan Plateau and eastern United States during extreme precipitation events in the Himalaya's

and southern North America, respectively, that may have further strengthened the moisture transports at their eastern flanks (*Galarneau et al.*, 2012; *Moore et al.*, 2012; *Favors and Abatzoglou*, 2013; *Vellore et al.*, 2016).

Moisture transport pathways have been studied in Eulerian and Lagrangian frameworks through calculation of moisture fluxes and air parcel trajectories, respectively (e.g. *Knippertz et al*., 2003; *Bao et al.*, 2006; *Knippertz and Martin*, 2007a; *Moore et al.*, 2012). Enhanced moisture transports can occur predominantly in the lower troposphere at the flanks of advancing monsoonal depressions or subtropical anticyclones (*Galarneau et al.*, 2012; *Moore et al.*, 2012; *Favors and Abatzoglou*, 2013), or in the middle troposphere underneath an intensified subtropical jet and above the planetary boundary layer (*Ziv*, 2001; *Knippertz and Martin*, 2005, 2007a; *Rubin et al.*, 2007). In the former case, moisture often rises gradually toward the middle troposphere while approaching the subtropics, whereas in the latter case convection over the tropics provides moisture to the middle troposphere, which then follows the pole and eastward outflow toward the extratropics. Although Eulerian and Lagrangian analyses can elucidate the pathways of the moist air masses, their sources and quantification often remain an open question due to complex processes of precipitation and evaporation (moisture recycling) and mixing of air masses along their paths.

The forcing for ascent and development of convective storms is governed by complex interactions between larger-scale and mesoscale processes. The larger-scale circulation generates a thermodynamical environment that is conducive to the formation of convective storms, whereas subsynoptic processes initiate convection (*Doswell*, 1987). Dynamical lifting through quasi-geostrophic forcing is too weak to generate the strong updrafts that typically occur within convective storms; however, it can reduce the static stability and perhaps trigger convection processes (*Knippertz and Martin*, 2005; *Hart et al.*, 2010). Strong convective overturning can be explained by potential instability (also termed as convective instability or thermal instability) upon lifting and saturation of air parcels within unstable vertical profiles of equivalent potential temperature. Other processes that may support deep moist convection and precipitation generation are orographic lifting of moist air masses and surface heating over elevated terrain (*Knippertz et al*., 2003; *Hart et al*., 2010; *Martius et al.*, 2013). In relation to extreme precipitation events in northwestern Africa and southwestern North America, *Knippertz and Martin* (2005, 2007a) found negative absolute vorticity along the anticyclonic shear side of a strong subtropical jet, which is indicative of inertial instability. Weak cyclogenesis and frontogenesis was observed at later stages during the development of these events. *Knippertz* (2007) presented a model for tropical plumes over West Africa whereby the precipitation zones are associated with dynamical lifting on the eastern flank of the upper-level trough, potential instability underneath the cold upper-tropospheric air, and inertial instability along the anticyclonic shear side of the jet. In summary, the development of convective storms results from a combination of complex processes across different spacio-temporal scales.

1.4 Larger-Scale Precursors of Extreme Precipitation

1.4.1 Potential Vorticity

Over the last decades, potential vorticity (PV) has proven to be of invaluable meaning for dynamical meteorology. In their landmark review article, *Hoskins et al.* (1985) conveyed the importance and benefits to approach atmospheric dynamical processes from a PV perspective, so called "PV thinking". PV

thinking is based upon two key principles: (1) the material conservation of PV under frictionless and adiabatic conditions, and (2) "PV invertibility", meaning that PV contains all the dynamical information of a balanced flow. The former refers to the approximate conservation of PV following the flow when advective processes dominate frictional and diabatic terms, and the latter tells that through PV inversion all dynamical flow characteristics, such as velocity fields, temperatures, geopotential heights and static stability, can be derived diagnostically when the potential vorticity distribution and the potential temperature at the boundaries are known for an arbitrary field. An important prognostic implication of these two principles is that the evolution of a balanced flow can be predicted based on solely the PV information. These properties render PV particularly useful to identify and trace meteorological disturbances (*Holton*, 2004).

Furthermore, important atmospheric processes such as baroclinic instability can be understood from a PV perspective. PV anomalies in a zonal shear flow can interact and strengthen one another through feeding on each other's induced velocity fields *(Hoskins et al.,* 1985). This mechanism is involved in baroclinic wave growth and cyclogenetic processes when an upper-tropospheric PV anomaly arrives over a low-tropospheric baroclinic region (figure 4), and when two counter-propagating Rossby waves undergo phase-locking and mutually amplify each other (e.g. *Heifetz et al.,* 2004). Finally, *Hoskins et al.* (1985) envisaged the importance of PV for the understanding of two-way interaction between the tropical and extratropical circulations that occurs through Rossby wave breaking and the injection of high (low) PV air into lower (higher) latitudes. Indeed, during the years to follow, these tropical-extratropical interactions have been successfully approached from a PV perspective (e.g. *Knippertz*, 2007 and references therein; *Kunz et al.*, 2015; *MacRitchie and Roundy*, 2016).

Apart from the importance for balanced flow dynamics, PV has also a direct relevance to precipitation generation. Positive upper-tropospheric PV anomalies can drive convection and extreme precipitation through (i) reducing the static stability in the lower troposphere and the buildup of convective potential available energy (CAPE), (ii) inducing dynamical lifting ahead of the PV anomaly, (iii) transporting moisture on its downstream flank, and (iv) orographic lifting through orienting the low-level winds toward a topographic barrier (*Funatsu and Waugh,* 2008; *Schlemmer et al.*, 2010; *Martius et al.*, 2013). Processes (i)-(iii) and baroclinic wave growth are schematically depicted in Figure 4.

Not surprisingly, several case studies of extreme precipitation in the Alpine region, northwestern Africa and southern Africa observed elongated and positively tilted structures of high PV air in the upper troposphere, also termed as stratospheric PV streamers (*Massacand et al.*, 1998; *Knippertz and Martin*, 2005, 2007b; *Hart et al*., 2010). *Martius et al.* (2006) presented climatological evidence for a relation between objectively identified stratospheric PV streamers and extreme precipitation in the southern Alps in Switzerland. Also in the Middle East region, heavy rainfall is associated with positive upper-tropospheric PV anomalies (*Evans and Smith*, 2006; *Kumar et al.* 2015). However, the dynamical importance of objectively identified stratospheric PV intrusions for extreme precipitation events in this region has thus far not yet been evaluated.

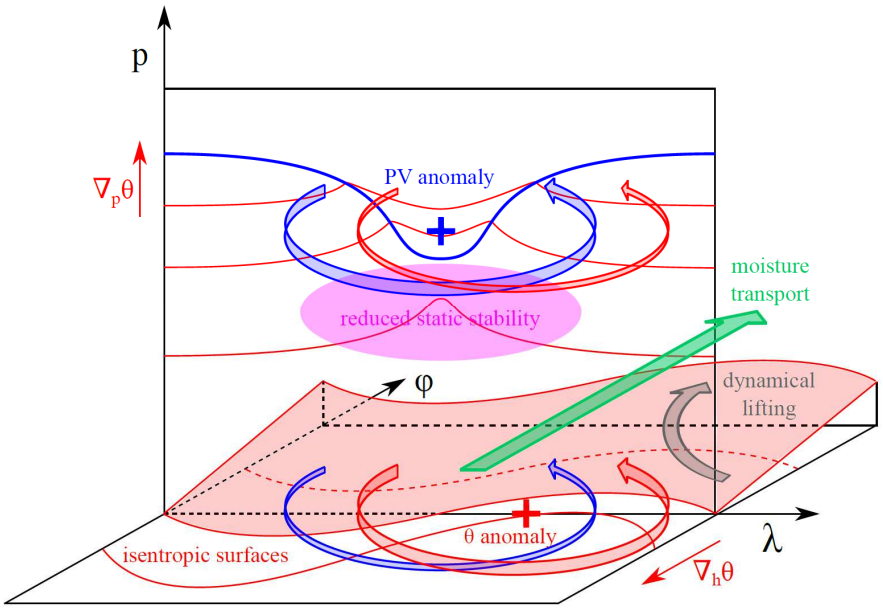

Figure 4. Schematic representation of baroclinic wave growth initiated by an upper-level PV anomaly that arrives over a low-level baroclinic region. The blue (red) contour lines illustrate the dynamical tropopause (isentropic surfaces). The anomalies in the upper and lower troposphere (blue and red + signs) induce cyclonic wind fields (big blue and red arrows) that also affect the lower and upper level circulations (small blue and red arrows), respectively, leading to mutual strengthening of the anomalies and associated wind fields. Furthermore, the upper-level PV anomaly is linked to (i) the uplift of isentropic surfaces beneath the anomaly, leading to a reduced static stability (purple shading), (ii) dynamical lifting of the flow on the sloping isentropic surface ahead of the PV anomaly (grey arrow), and (iii) moisture transport on its downstream flank (green arrow). The schematic is based on a combination of Figures 15 and 21 of *Hoskins et al.* (1985) and Figure 1 of *Funatsu and Waugh* (2008).

1.4.2 Moisture Transport

Numerous studies employed vertically integrated horizontal water vapor transport (IVT) for the identification of atmospheric rivers through applying geometrical criteria on structures of large IVT (e.g. *Rutz et al.*, 2014; *Guan and Waliser*, 2015; *Mahoney et al.*, 2016; *Mundhenk et al.*, 2016a). Besides the importance for detection of atmospheric rivers, IVT has been recognized as a successful medium-range predictor (*Lavers et al.*, 2014), large-scale precursor (*Froidevaux and Martius*, 2016), and environmental characteristic (*Moore et al.*, 2015) of extreme precipitation occurrence. Furthermore, several case and climatological studies adopted IVT to identify moisture transport pathways of extreme precipitation events (e.g. *Knippertz et al.*, 2003; *Lau and Kim*, 2012; *Moore et al.*, 2012; *Swales et al.*, 2016).

Accordingly, stratospheric PV intrusions and large IVT are both widely recognized as important for extreme precipitation. However, they have thus far never been combined for the objective identification of extreme precipitation events. Such an approach can potentially benefit weather prediction and climate studies of extreme precipitation events. Precipitation is often poorly represented in relatively coarse resolution model simulations, whereas the synoptic-scale circulation is much better represented. Thus, an identification method for extreme precipitation events based on synoptic-scale meteorological features may provide information of extreme precipitation without the constraint to depend on precipitation data.

1.5 Aim of the Thesis

From the overview of the existing literature, it is clear that extreme precipitation events in the Middle East and their underlying dynamics have received little scientific attention. Discrepancies between previous ARST studies revealed the need for consensus and a better understanding of this phenomenon. Moreover, heavy rainfall events beyond the Levant region remain largely unexplored. Extreme precipitation events in other arid subtropical regions are much better understood and are often addressed in context of tropical-extratropical interaction. Although few studies of extreme precipitation in the Middle East made brief inferences to tropical-extratropical interaction (*Dayan et al*., 2001; *Ziv et al*., 2005; *Rubin et al*., 2007; *Tubi and Dayan*, 2014), such events have not been thoroughly investigated in this framework. This thesis seeks to fill these gaps in the literature. Based on several case studies, the synoptic-scale dynamics of such events are identified. Building on this knowledge, an algorithm is developed for detection of extreme precipitation in the Middle East that can advance our understanding of these events. More specifically, the goals of this thesis are threefold: (1) to provide a qualitative understanding of the ARST dynamics and its geographical extent and seasonality, (2) to identify and quantify the larger-scale circulation processes of three extreme precipitation cases in Saudi Arabia in different seasons, and (3) to present an identification method for extreme precipitation events in the Middle East based on synoptic-scale meteorological features.

1.5.1 The Active Red Sea Trough

First, this thesis investigates ARST associated dynamics based on a review of the previous literature and analysis of twelve ARST events that affected the Levant region. The selection of these twelve events is based on (i) cases reported in the literature, (ii) the detection method of *Krichak et al.* (2012), and (iii) information from a local scientist (personal communication D. Edry). We identify important synoptic-scale circulation features through analyzing the pressure and geopotential height distributions and wind fields, moisture transport pathways based on IVT, and the tropospheric conditions that favor the forcing of ascent. Furthermore, we study the Jeddah flooding of November 2009 in context of the geographical extent of the ARST. Although Jeddah is located at a distance of almost 1,000 km from the Levant, extreme precipitation events in this region (*Al-Khalaf and Basset*, 2013; *Haggag and El-Badry*, 2013; *Deng et al.*, 2015) show considerable similarities to ARSTs. The torrential rainfall that inundated the city in November 2009 was by far the most devastating flash flood in the region in decades (Appendix A), which motivates us to study the Jeddah flooding of November 2009 in this context. Finally, we seek to explain the ARST seasonality through analyzing the seasonal cycle of the large-scale circulation.

1.5.2 Three Extreme Precipitation Cases in Saudi Arabia

Next, the thesis presents a multiple-perspective analysis of three extreme precipitation cases in Saudi Arabia. The focus is on the larger-scale circulations that governed these heavy rainfall events. This approach follows the widely accepted perspective that the larger-scale processes generate a tropospheric environment that is conducive for development of convective storms (*Doswell*, 1987; *Dayan et al.*, 2015). Mesoscale processes are for this reason, along with the lack of available data at these scales, only briefly discussed. This study examines the precipitation characteristics, the synoptic-scale circulations, moisture transport pathways, and forcing of upward motion of the three cases. We select the extreme precipitation events in the Jeddah region on 25 November 2009, northwestern Saudi Arabia on 22 January 2005, and

the larger part of Saudi Arabia during end April and early May 2013 with the focus on southwestern Saudi Arabia on 1 May 2013, hereafter, the autumn, winter and spring cases, respectively. The choice for these events is motivated by their dramatic societal impacts (Appendix A) and their occurrence in different seasons. This work complements the previous study of the Jeddah flooding in November 2009 by using a combination of diagnostic techniques to elucidate the dynamical processes of this specific case. We quantify circulation anomalies and dynamical lifting, discuss synoptic-scale dynamics from a PV perspective, calculate backward air parcel trajectories to study moisture pathways, and adopt sounding data to gain insight in the local tropospheric stratification and moisture profiles. The same framework is used to examine the two additional cases that have not been previously investigated. The three cases are discussed from a seasonal perspective that will link their different characteristics to the seasonal variability of the large-scale circulation over the region.

1.5.3 Identification of Extreme Precipitation Events in the Middle East

The last part of the thesis develops an object-based identification method for extreme precipitation events in the Middle East. The previous case studies have shown that these events result from tropical-extratropical interaction, whereby a midlatitude upper-level trough and poleward transport of tropical moisture are key synoptic-scale features. This identification method combines stratospheric PV intrusions (after *Wernli and Sprenger*, 2007) and structures of large poleward IVT. The motivations for this approach are threefold: stratospheric PV intrusions and IVT structures (1) represent midlatitude forcing and tropical moisture, respectively, of tropical-extratropical interaction, (2) are both larger-scale precursors of extreme precipitation, and (3) are here for the first time combined in an algorithm for detection of extreme precipitation. The aim of the approach is to identify extreme precipitation events without using precipitation data itself, which is often subject to limitations of relatively coarse resolution model simulations or the observational data products (e.g. *Zhang et al.*, 2011; *Donat et al.*, 2014). In contrast, the synoptic-scale circulation in meteorological data sets is much better represented, which introduces the perspective to apply the algorithm on long term reanalysis data and climate model output. Here, we examine (i) the importance of stratospheric PV intrusions and IVT structures for extreme precipitation, (ii) the relation between the PV and IVT characteristics and the severity of the precipitation, and (iii) the contribution of tropical-extratropical interactions to annual rainfall amounts and extreme precipitation days in the Middle East.

2 Methods and Data

2.1 Data

This thesis uses a combination of reanalysis data, precipitation observations, sounding data and satellite imagery. The ERA-Interim data set of the European Centre for Medium-range Weather Forecasts (ECMWF) contains a global state of the atmosphere and is produced by the Integrated Forecast System at the spectral resolution of T255L60, spanning the years from 1979 until near-real-time (*Dee et al.*, 2011). This thesis utilizes 6-hourly and monthly analysis and forecasts fields on surface, pressure, isentropic and model levels on a N128 Gaussian grid (~0.7ºx0.7º). The ERA-Interim data is employed (1) to produce synoptic charts, (2) to calculate normalized anomalies, backward air parcel trajectories, and dynamical lifting, and (3) to identify PV intrusions and IVT structures.

Also, this thesis employs a variety of precipitation data from reanalysis, gridded, satellite-based and individual station data. The precipitation data provides insight in the rainfall characteristics of the twelve ARST events and three extreme precipitation cases in Saudi Arabia, and facilitates an evaluation of the annual rainfall amounts and extreme precipitation days that can be attributed to tropical-extratropical interaction. Daily precipitation from ERA-Interim is constructed from 12-hourly accumulated forecasts from 00 and 12 UTC. Aphrodite (V1101) contains gridded daily precipitation data, based on stations, with a spatial resolution of 0.25ºx0.25º, spanning the years 1951-2007 (*Yatagai et al.*, 2012). The 3B42 version 7 product of the Tropical Rainfall Measuring Mission Multisatellite Precipitation Analysis (hereafter TRMM) comprises 3 hourly and daily rainfall data with a 0.25ºx0.25º spatial resolution from 1998 to the present (*Huffman et al.*, 2007). TRMM is based on calibrated and combined multiple independent microwave and infrared sensor data, and is adjusted to monthly rain-gauge measurements.

For the study of the twelve ARST events, several rainfall records of stations in Israel are obtained from the Israel Meteorological Service (IMS) archive. Regarding the three extreme precipitation cases, rainfall observations from 37 stations in Saudi Arabia are adopted from the National Climatic Data Center (NCDC) Global Summary of the Day (GSOD) data set version 7. The last part of the thesis benefits from highly valuable rainfall records of numerous stations in Saudi Arabia and Israel that were obtained through collaborations with local scientists in the region. For Saudi Arabia, the data set presented by *El Kenawy and McCabe* (2016) comprises 240 individual rainfall records for the period of 1979 to 2012, from which we use 192 time series with less than 50% missing values. The Israeli Atmospheric and Climatic Data Centre (IACDC) provided 158 rainfall records that cover at least 20 years of the 37-year period of 1979-2015.

Furthermore, for the three extreme precipitation cases in Saudi Arabia, the cloud characteristics and the local vertical structure of the troposphere are explored using Meteosat geostationary satellite images from the Dundee Satellite Receiving Station and sounding data from the University of Wyoming, respectively.

2.2 Methods

2.2.1 Diagnostics

This thesis employs a number of diagnostic techniques to identify and quantify the larger-scale processes that contributed to the formation of the convective storms and extreme precipitation events in the Middle

East. More specifically, we quantify the anomalies in the synoptic-scale circulation, elucidate moisture transport pathways through calculation of moisture fluxes and moist air parcel trajectories, and adopt several diagnostics to examine the forcing mechanisms of upward motion.

Normalized anomalies provide a quantification of how unusual the tropospheric environment was in a climatological context and help to identify the relevant processes in the synoptic-scale circulation. The normalized anomalies are calculated using the long-term 21-day running mean and standard deviation (STD) values of daily means:

$$N = \frac{(X - \mu)}{\sigma} \qquad (1)$$

where X is the daily mean value of the variable, μ the climatological mean value, and σ the STD of the daily mean:

$$\sigma = \sqrt{\frac{\sum_{i=1}^{n}(X_i - \mu)^2}{n-1}} \qquad (2)$$

where n is the number of sample members. Moisture transport pathways are studied in Eulerian and Lagrangian frameworks. Using ERA-Interim data, we compute IVT over different ranges of pressure levels:

$$\mathbf{IVT} = \frac{1}{g}\int_{P_{bottom}}^{P_{top}} q\mathbf{v}\, dp \qquad (3)$$

where g is the gravitational acceleration, q the specific humidity, and $\mathbf{v}$ the horizontal wind. Backward trajectories are calculated based on ERA-Interim data on a regular grid (1ºx1º) and model levels between the surface and 200 hPa, using the Lagrangian analysis tool LAGRANTO (*Wernli and Davies*, 1997; *Sprenger and Wernli*, 2015). We select trajectories that are relevant for moisture transport pathways using relative humidity (>80%) and moisture flux (>100 g kg^{-1} m s^{-1}) thresholds, applied on air parcels over the regions of extreme precipitation at the initial time of the trajectory calculations. Meteorological variables are traced along the trajectories to provide insight into the atmospheric processes and the moisture budget along their pathways. The validity of the air parcel trajectory calculations is subject to limitations that are inherent to the relatively coarse resolution data and the mixing of air masses along their pathways.

Previous studies used the quasi-geostrophic omega equation to estimate the contribution of the balanced dynamics to upward motion in the region of precipitation (*Knippertz and Martin*, 2005, 2007a; *Hart et al.*, 2010; *Martius et al.*, 2013). In this thesis, the omega equation is employed under alternative balance (*Davies-Jones*, 1991), which diagnoses the vertical motion from the non-divergent wind instead of the geostrophic wind. This approach can be considered more accurate, in particular in the vicinity of upper-level troughs where the Rossby number is relatively large. The alternative balance omega equation reads (*Riemer et al.*, 2014):

$$\nabla_p \cdot \left(\sigma \nabla_p \omega\right) + f_0^2 \left[\frac{\partial^2 \omega}{\partial p^2} - \frac{1}{p}\frac{c_v}{c_p}\left(\frac{\partial \omega}{\partial p} + \frac{\omega}{p}\right)\right] = -2\nabla_p \cdot \mathbf{Q}_{\mathrm{AB}}, \qquad (4)$$

with

$$\mathbf{Q}_{\mathrm{AB}} = -\nabla_p \mathbf{v}_\psi \cdot \nabla_p \alpha, \quad (5)$$

where ∇_p is the horizontal gradient on pressure levels, ω the vertical velocity (balanced omega), $\mathbf{v}_\psi$ the non-divergent wind, f_0 the constant Coriolis parameter, and c_v and c_p the specific heats of dry air at constant volume and pressure, respectively. Furthermore, $\sigma = -\alpha_0\theta_0^{-1}\,\partial\theta_0/\partial p$ and $\alpha = \theta\, Rp^{-1}(p/p_0)^{\kappa}$ where R is the gas constant of dry air, $\kappa = R/c_p$, and α_0 and θ_0 denote the reference vertical profiles of specific volume and potential temperature, respectively.

The susceptibility of the tropospheric environment to deep moist convection is examined using sounding data. We examine vertical profiles of the tropospheric state on potential instability, which is defined as:

$$\frac{\partial \theta_e}{\partial p} > 0 \qquad (6)$$

where θ_e is the equivalent potential temperature. An often used index to assess thermodynamic favorable conditions for the occurrence of deep moist convection is convective available potential energy (CAPE), which measures the maximum possible kinetic energy that an air parcel can acquire when lifted to its level of free convection, neglecting mixing of the air parcel with the local environment (*Holton*, 2004):

$$CAPE = \int_{z_{lfc}}^{z_{lnb}} g\left(\frac{T_{parcel} - T_{env}}{T_{env}}\right) dz \qquad (7)$$

where T_{parcel} and T_{env} designate the temperature of the air parcel and the environment, respectively. Furthermore, Z_{lfc} and Z_{lnb} indicate the levels of free convection and neutral buoyancy near the tropopause, respectively.

2.2.2 Definition of Extreme Precipitation Days

We provide a benchmark for the identification method of extreme precipitation events in the Middle East through defining extreme precipitation days (EPD) over the region of interest. The region of interest encompasses eastern Egypt, southern Israel, Jordan and the northern and western parts of Saudi Arabia (Figure 5b), where flash floods with devastating consequences have been recurrent. EPDs are defined by the 99th and 97.5th percentile of daily precipitation in ERA-Interim over this region. These EPDs can include localized heavy rainfall and less intense, widespread rainfall which are both of interest here as precipitation in the dry desert has by nature an extreme character.

The use of ERA-Interim precipitation data for EPDs introduces the potential constraint in that it is the same data as for which we apply the algorithm, but has the advantage of suitable spatial and temporal coverage. Available observational data sets do not cover the extended period of 1979-2015 under consideration (Aphrodite and TRMM) and/or suffer from a relatively poor-density station network (Aphrodite and stations) and limited availability (stations). To evaluate the fidelity of using ERA-Interim data for defining EPDs, we compare these to EPDs derived from Aphrodite and TRMM data for the time period that is covered by all three data sets (1998-2007). Of the 99th (97.5th) percentile EPDs in ERA-

Interim, 79% (71%) matches with EPDs in Aphrodite or TRMM data, indicating a reasonable representativeness of the EPDs using ERA-Interim data.

2.2.3 Algorithm for PV Intrusions and IVT Structures

PV intrusions are identified following *Wernli and Sprenger* (2007). This approach has been adopted by several studies addressing the climatological characteristics of PV intrusions and their relation to extreme weather events (e.g. *Martius et al.*, 2006, 2008; *Sprenger et al.*, 2013). PV was computed from ERA-Interim data on model levels (*Rash and Boville*, 1993):

$$P = -g\left((\nabla \times \mathbf{u} + f)\cdot\frac{\partial\theta}{\partial p} - \left(\frac{\partial\theta}{\partial x}\frac{\partial v}{\partial p} - \frac{\partial\theta}{\partial y}\frac{\partial u}{\partial p}\right)\right) \qquad (8)$$

and then interpolated onto isentropic surfaces between 310-340 K with 5 K intervals. In (8) $f = 2\Omega sin(\phi)$ with Ω the earth angular rotation, and ϕ the latitude. Furthermore, **u** is the horizontal wind, θ the potential temperature, and *u* and *v* the zonal and meridional wind components, respectively. Following *Wernli and Sprenger* (2007), the 2 potential vorticity unit (PVU; 1 PVU = 10^{-6} K kg^{-1} m^2 s^{-1}) surface is considered as the dynamical tropopause, separating the stratospheric (PV>2 PVU) and tropospheric (PV<2 PVU) air masses. The 2 PVU contour on isentropic surfaces can form narrow and elongated filament (PV streamers) and can split off from the main stratospheric or tropospheric reservoirs (PV cutoffs).

The algorithm consists of four steps. First, the 2 PVU contours and contour point coordinates are retrieved for each 6-hourly time interval and each isentropic surface. Second, the stratospheric body is determined, which corresponds to the extensive reservoir of stratospheric air mass that covers higher latitudes. All remaining 2 PVU contours are considered as PV cutoffs. Third, for identification of PV streamers, we evaluate for each pair of contour points of the stratospheric body the geometrical criteria of a potential streamer; the (1) width, (2) length, and (3) ratio of length over width (Figure 5a). Our streamer length definition deviates from *Wernli and Sprenger* (2007), who used the contour length between the start and end points of the streamers. In this study, we define the length of the PV streamer as the distance perpendicular to the great circle of the start and end points of the streamer to avoid features with twisted contour lines. Fourth, all grid points within the polygons of the PV streamers and cutoffs are classified as being stratospheric (PV>2 PVU) or tropospheric (PV<2 PVU) intrusions.

IVT structures are defined as all grid points with a positive meridional IVT > 200 kg m^{-1} s^{-1}. Since the poleward moisture transport is of interest here, the meridional component of IVT is used instead of the full IVT field. Most studies on the identification of atmospheric rivers adopted IVT thresholds that typically range between 250 and 500 kg m^{-1} s^{-1} (*Rutz et al.*, 2014; *Mahoney et al.*, 2016; *Mundhenk et al.*, 2016a). Here, we apply a somewhat lower threshold of 200 kg m^{-1} s^{-1} to adjust to the lower background moisture transport in the Middle East region.

In a final stage, the algorithm retrieves unique characteristics of all individual PV and IVT features. These include the southward extent of stratospheric PV intrusions and the magnitude of IVT structures, defined by the minimum latitude of the stratospheric PV intrusions and the maximum IVT value within the IVT structures, respectively. Furthermore, the algorithm rejects (1) PV intrusions and IVT structures with a relatively small surface area of less than 100.000 km^2, (2) all PV streamers if >50% of the stratospheric

body consists of stratospheric PV streamers (i.e. if the 2-pvu contour of the stratospheric body is very distorted), and (3) cutoffs if any grid point within the structure is below the surface topography.

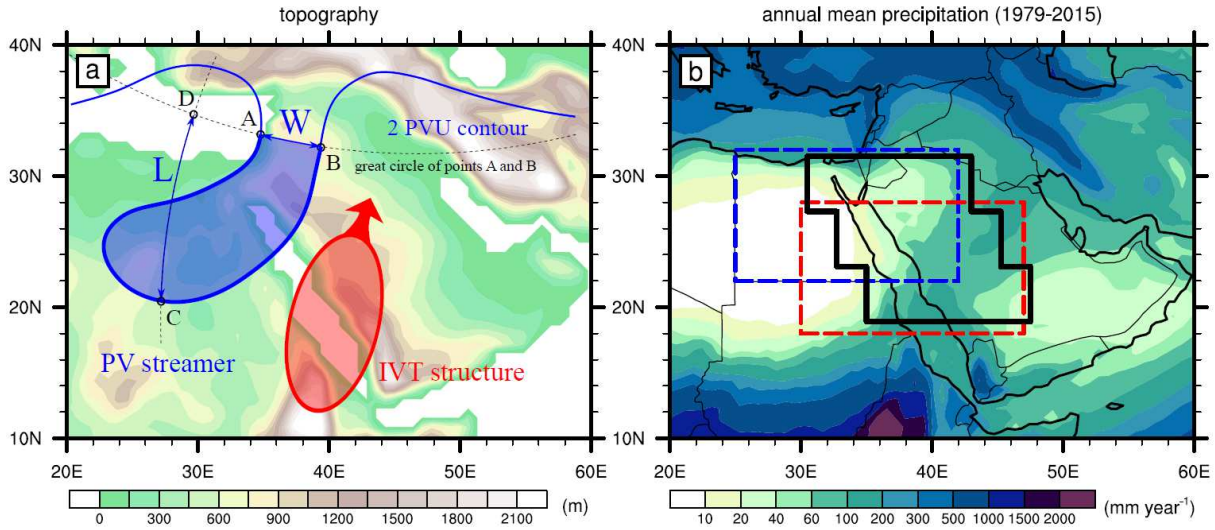

Figure 5. The Middle East region with (a) the topography from ERA-Interim data and a schematic representation of tropical-extratropical interactions, involving a stratospheric potential vorticity intrusion and an incursion of tropical moisture into the region, and (b) the annual mean precipitation (mm year^{-1}) in ERA-Interim data (1979-2015). In (a), the potential vorticity streamer geometrical criteria are depicted, being the width (W) and length (L) for the pair of contour points A and B on a 2 PVU contour at an isentropic surface; see the text in section 2.2.3 for details. In (b) the box for defining the extreme precipitation days is illustrated by black lines encompassing three imaginary boxes from north to south; box 1 (27.3-31.5°N, 30.5-43.0°E), box 2 (23.1-27.3°N, 32.75-45.25°E), and box 3 (18.9-23.1°N and 35.0-47.5°E), see section 2.2.2.

3 Results

3.1 The Active Red Sea Trough

The twelve ARST events were confirmed as ARSTs based on the presence of the Red Sea Trough and a midlatitude upper-level trough as well as substantial rainfall amounts in the Levant region. Most events exhibited a subtropical jet stream or jet streak at the east-equatorward side of the upper-level trough, accompanied by upper-level divergence near its left exit region. Beneath, mid-tropospheric ascent occurred at the eastern flank of the upper-level trough. The combination of advected moisture, low-level warm air and upper-level cold air promoted favorable conditions for development of convective storms, illustrated by moderate or high CAPE values in the region of extreme precipitation. Accordingly, the large-scale forcing and tropospheric instability favored upward motion and the formation of convective storms. These findings corroborate those of previous ARST-related studies. Interestingly, we found that all twelve ARST events were accompanied by an Arabian anticyclone in the lower troposphere over the Arabian Peninsula that forced enhanced moisture transport over the Arabian and Red Seas toward the Levant. We present an ARST concept with six relevant features: (1) the Red Sea Trough, (2) the Arabian anticyclone, (3) a transient midlatitude upper-level trough, (4) a subtropical jet stream or jet streak, (5) enhanced moisture transport over the Arabian and Red Seas, and (6) strong ascent associated with large-scale lifting and tropospheric instability (Figure 6b).

Under normal conditions, the Red Sea Trough manifests as a semi permanent and quasi stationary wave in the tropical easterlies. Tropical moist air masses from the Arabian Sea are diverted northward into the Red Sea basin and are deflected back toward equatorial Africa along the eastern and western flanks of the Red Sea Trough, respectively (Figure 6a). An ARST event occurs when a transient midlatitude upper-level trough, going along with wave breaking, intrudes into the subtropics over northeast Africa and interacts with the climatological Red Sea Trough near the surface. The coupling of the midlatitude and tropical circulations is suggestive of phase locking of a midlatitude Rossby wave and the stationary wave in the lower-tropospheric circulation (i.e. the Red Sea Trough). As a result, tropical moist air masses progress northward over the Red Sea basin and intrude into the Levant region (Figure 6b). Thus, the ARST phenomenon can be interpreted as a type of tropical-extratropical interaction with the signature of the local topography of the region and associated climatological low-level circulation.

Importantly, enhanced moisture transport over the Arabian and Red Seas through an intensified Arabian anticyclone was not only observed for the ARST event in December 1993, but also during the other ARST events. A detailed analysis of IVT showed that the transient upper-level trough and intensified Arabian anticyclone transported large amounts of moisture near the surface over the Arabian and Red Seas, which gradually ascended in the southerly flow while approaching the Levant. Interestingly, the distribution of total column water was suggestive of large moisture amounts reaching from Equatorial Africa across northeast Africa toward the Levant. Thus, our analysis underlines that inferences to moisture transport pathways based on tropospheric moisture amounts, moisture fluxes at particular levels, trajectories from singular grid points or satellite water vapor imagery, as were made in previous studies, can be misleading and are not necessarily representative of moisture transport throughout the troposphere.

The flooding of Jeddah in November 2009 demonstrated all dynamical characteristics of the twelve ARST events over the Levant. This implies that the Jeddah flooding was caused by an ARST. Apparently,

ARSTs can not only can affect the Levant, but also the larger part of the Arabian Peninsula, introducing a substantial geographical extension of the phenomenon.

The seasonality of the ARST can be explained by the seasonal evolution of the large-scale circulation and in particular that of the regional low-level circulation. During summer, the influence of the Asian summer monsoon rules out ARSTs as precipitation is inhibited by large-scale subsidence and through the Persian Trough that absorbs the Red Sea Trough. In winter, ARSTs are less likely since the Red Sea Trough and tropical moisture are farther away from the Middle East than during the transition seasons. During autumn and spring, the semi permanent Red Sea Trough reaches its most northerly position. However, the low-level circulation exhibits an asymmetric seasonal cycle in a manner that the Red Sea Trough and Arabian anticyclone attain their most pronounced state in autumn and early winter as compared to late winter and spring when the Arabian anticyclone remains south over the Arabian Sea and allows frequent Sharav cyclones and Mediterrean cyclones passage over the region. Accordingly, ARSTs over the Levant occur predominantly in late autumn and to a lesser incidence in early winter and spring. Farther south over the Jeddah region, ARST favorable conditions arise later in autumn, end earlier in spring, and can potentially last through the winter. More details on the ARST phenomenon are included in Appendix C1.

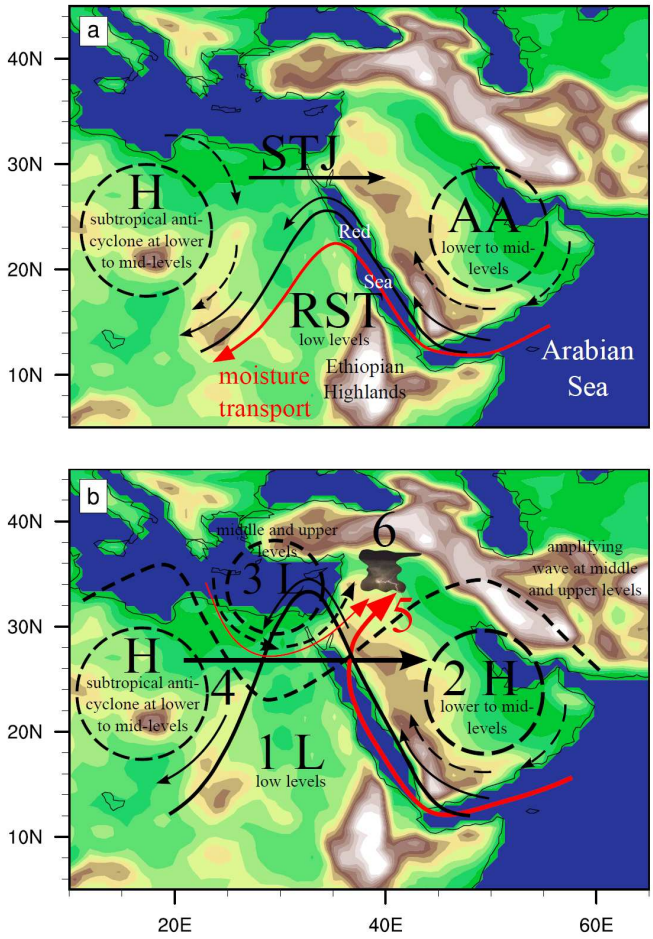

Figure 6. Schematic representation of (a) the low-level circulation climatology in autumn, winter and spring, and (b) the ARST associated features. For numbers mentioned in Figure 6b, see the text in section 3.1.

3.2 Three Extreme Precipitation Cases in Saudi Arabia

All three extreme precipitation cases in Saudi Arabia involved strong tropical-extratropical interactions. The events were preceded by midlatitude wave breaking in the far upstream region over the Atlantic, followed by downstream development toward the Middle East. Subsequent anticyclonic Rossby wave breaking over the region resulted in a midlatitude upper-level trough that intruded into the subtropics (following the LC1 baroclinic life cycle of *Thorncroft et al.* (1993)), and interacted with the tropical lower-level circulation. The accompanying upper-tropospheric PV anomaly and lower-tropospheric potential temperature maximum downstream demonstrate a phase relationship that is consistent with wave amplification through baroclinic growth (*Hoskins et al.*, 1985). The coupling of the midlatitude and tropical circulations facilitated the transport of tropical moisture toward the Arabian Peninsula, leading to above-normal tropospheric moisture content (>2 or >3 STD) over the region of extreme precipitation. The moisture pathways varied between the cases; however, in each case they involved enhanced moisture transport over the Arabian and Red Seas through the intensified Arabian anticyclone (~1 STD above normal in 850 hPa geopotential height). Interestingly, this feature was also found to be important for precipitation over Iran (*Raziei et al.*, 2012) and ARST events that affected the Levant. Detailed Lagrangian trajectory analysis indicates not only an important moisture contribution from the nearby Red Sea, but also from remote tropical regions. The common synoptic-scale key features of the three cases are depicted in Figure 7. Below, the cases are outlined in more detail and their differences are placed in a seasonal context.

The autumn case was characterized by the northward amplification of the Red Sea Trough upon arrival of an eastward moving midlatitude upper-level trough, emphasized by normalized anomalies exceeding 1.5 STD below normal in the mean sea level pressure and 500 hPa geopotential height, respectively. The interaction of the climatological Red Sea Trough and transient midlatitude upper-level trough resulted in enhanced moisture transport toward Jeddah. Air parcels collected most of the moisture over the warm surface of the Red Sea, while some moisture also originated from the Arabian Sea. Importantly, moist air parcel trajectories approached Jeddah from the north and south, implying low-level moisture convergence over the region. Dynamical lifting was relatively weak; however, it may have contributed to a ~20% reduction of static stability over the region. The combination of reduced static stability and high values of precipitable water (~40 kg m^2) and CAPE (>2500 J kg^{-1}), as observed in sounding data, promoted favorable thermodynamic conditions for deep moist convection. Orographic lifting of the westerly moist air flow over the mountainous Red Sea coast may have led to parcel saturation and the release of strong potential instability and high CAPE, as confirmed by sounding data before and after the storm. These processes, in combination with strong vertical wind shear, supported the formation of a large quasi stationary mesoscale convective system (*Haggag and El-Badry*, 2013) that resulted in the local extreme precipitation. A Jeddah station reported 70 mm rainfall on 25 November 2009, which surpassed the annual mean of 52.1 mm (*Almazroui et al.*, 2012a).

On January 2005, widespread and heavy rainfall affected northwestern Saudi Arabia, locally exceeding 120 mm day^{-1} in TRMM data in the Al Madinah region where floods occurred. Satellite imagery demonstrate cloud bands with characteristic of tropical plumes. Also the dynamics show remarkable similarities to those of tropical plumes. A 4-STD midlatitude trough, being part of a Rossby wave train that moved into the tropics, connected with the tropical low-pressure belt over Equatorial Africa. Upper tropospheric charts exhibit poleward outflow from the tropics and a subtropical jet with anticyclonic

curvature, accompanied by a jet streak with velocities reaching over 72 m s^{-1}. Although moist air masses originated predominantly over the Arabian and Red Seas, substantial moisture amounts also stemmed from Equatorial Africa and were transported above the dry planetary boundary layer across northeastern Africa on the eastern flank of the midlatitude trough. In the region of the extreme precipitation, dynamical lifting explains roughly 30-38% of the strong mid-tropospheric ascent. The balanced ascent was further reinforced by diabatic heating and the strong orographic uplifting of the southwesterly flow, bringing the moist air masses to saturation. As for the autumn case, equivalent potential temperature profiles from sounding data revealed the release of potential instability.

In spring 2013, an episode of severe weather affected the larger part of the Arabian Peninsula from 25 April to 7 May with the heaviest precipitation over southwest Saudi Arabia on 1 May. Two stations, Bishah and Wadi al-Dawasir, reported rainfall amounts of 135 and 50 mm day^{-1} that substantially exceeded their annual means of 88.7 and 25.5 mm $year^{-1}$ (*Almazroui et al.*, 2012a), respectively. During this episode, a quasi stationary upper-level through (>3 STD) formed over northern Saudi Arabia, accompanied by a northward expanding Red Sea Trough. The zonal flow exhibited easterly vertical shear and an inflection point in the meridional profile, which suggests that wave amplification over the region developed through a combination of baroclinic and barotropic instability. Moist air masses followed two distinct pathways with roots over the Arabian Sea, driven by the Arabian anticyclone, and along the East African coast through cross-equatorial flow. The former provided most of the moisture that contributed to the extreme precipitation over southwest Saudi Arabia, whereas moisture from the south Indian Ocean may at least have been partly depleted through convective rainfall along their pathways. Satellite imagery reveals a striking diurnal cycle of convective storms that formed in the afternoon over the mountainous Red Sea coast, grew to mature stages during the evening while moving eastward over Saudi Arabia, and decayed at night over its eastern parts. Thus, the multiple convective storms developed in a synoptically destabilized environment under influence of local forcing factors, including strong surface heating, orographic uplift of the moist westerly flow over the mountainous Red Sea coast, and the release of potential instability.

Thus, three cases had in common that their convective storms and local extreme precipitation were governed by the larger-scale circulation. The differences in the synoptic circulation between the three cases are linked to the seasonal variability of the large-scale circulation. The autumn case was characteristic of the ARST phenomenon, which typically occurs in autumn (*Kahana et al.*, 2002; *Krichak et al.*, 2012; *Shentsis et al.*, 2012). The winter case had dynamical and cloud band characteristics of tropical plumes, which are most likely to occur in the winter season (*Dayan and Abramski*, 1983; *Ziv*, 2001; *Rubin et al.*, 2007; *Tubi and Dayan*, 2014) when the baroclinic zone is closest to the Middle East and midlatitude disturbances are most likely to reach deep into the subtropics. The spring case involved persistent northward advection of tropical moist air masses, partly through cross-equatorial flow that is associated with the onset of the Asian summer monsoon in May. In addition, the location of the Arabian anticyclone was farther to the southeast, over the Arabian Sea, as compared to autumn season, and allowed the moist air masses and precipitation to spread across most of Saudi Arabia. Thus, the general circulation patterns of the three cases are consistent with the seasonal variability of the large-scale circulation. The specific events exhibited unusual or extreme synoptic characteristics *within* the varying background large-scale circulation of the different seasons. More details on the three extreme precipitation cases in Saudi Arabia are presented in Appendix C2.

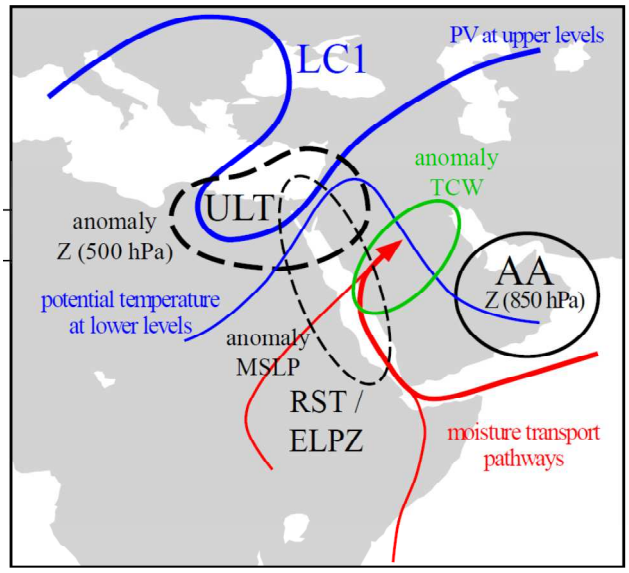

Figure 7. Schematic presentation of the common synoptic-scale key features of the three extreme precipitation cases in Saudi Arabia; anticyclonic Rossby wave breaking (LC1), an upper-level trough (ULT), the Arabian anticyclone (AA), the Red Sea Trough (RST; for the November and April-May cases), equatorial low pressure zone (ELPZ; for the January case), moisture transport pathways and anomalous total column water. "Z" and "MSLP" denote geopotential height and mean sea level pressure, respectively. Note that the thin red lines refer to the moisture transport pathways as only observed during the winter case (equatorial Africa) and the spring case (South Indian Ocean).

3.3 Identification of Extreme Precipitation Events in the Middle East

The functionality of the algorithm is demonstrated by four cases of extreme precipitation and flooding in the Middle East. Each case exhibits a stratospheric PV intrusion over northeast Africa accompanied by an IVT structure on its eastern flank, reflecting Rossby wave breaking along with a midlatitude upper-level trough intrusion into the subtropics that induced southerly moisture fluxes on its downstream flank. In a next step, important regions are identified where stratospheric PV intrusions and IVT structures occur most frequently during the 97.5th percentile EPDs in the period of 1979-2015. These regions serve as target areas for defining days with stratospheric PV intrusions and IVT structures, hereafter, PV and IVT incursions, respectively. Days with *combined* PV and IVT incursion are those when both concur at a particular day.

PV and IVT incursions are intimately linked to extreme precipitation events in the Middle East. Both are highly associated with the precipitation intensity distribution and follow the seasonality of EPDs with dry summer months (June to September) and peaks in late autumn/early winter (November to January) and early spring (March and April). Interestingly, PV incursions are relatively common and occur on 41.4% of all days, whereas IVT incursions occur on only 11.8% of all days. Nevertheless, IVT incursions correspond to higher EPD hits (98% and 92% for the 99th and 97.5th percentile EPDs, respectively) as compared to the EPD hits of PV incursions (92% and 90% for the 99th and 97.5th percentile EPDs, respectively). This finding indicates that IVT is potentially a better predictor of extreme precipitation than PV. We use the combination of PV and IVT incursions instead of only IVT incursions to further reduce

the false alarms and to focus on extreme precipitation that results from tropical-extratropical interaction. Combined PV and IVT incursions occur on 8.5% of all days and detect 90% of the 99th percentile EPDs and 83% of the 97.5th percentile EPDs.

Missed EPDs and false alarms are evaluated on a case-by-case basis and through composites of normalized anomalies of PV and total column water. Missed EPDs that lacked PV incursions had broad PV troughs without an elongated form or stratospheric PV intrusions over the eastern Mediterranean that did not reach far into the subtropics. Likewise, missed EPDs that lacked IVT incursions often exhibited IVT incursions during preceding days, ensuring the prior presence of large tropospheric moisture amounts of the same magnitude as for EPD hits (~1.25 STD). Days with combined PV and IVT incursions without resulting extreme precipitation (<95th precipitation percentile) are considered as false alarms and correspond to a false alarm ratio of 58.3%. These days were in reality not dry, but experienced localized extreme precipitation that is not represented in the ERA-Interim data, or remained dry due to insufficient tropospheric moisture content, indicated by remarkably low above-normal total column water normalized anomalies (~0.5 STD) as compared to EPD hits (~1.25 STD).

The severity of the precipitation depends on the southward extent of the stratospheric PV intrusions, the IVT magnitude, and the persistence of the combined PV and IVT incursions. The ≥99th precipitation percentile is associated with stratospheric PV intrusions reaching an average latitude of about 24°N and an average IVT magnitude of 439 kg m^{-1} s^{-1}. For less severe precipitation categories, stratospheric PV intrusions reach less far south and the IVT magnitudes reduce, following an almost linear relationship. Furthermore, combined PV and IVT incursions lasted 1.36 days, 1.03 days, and 0.93 days prior to the (extreme) precipitation day for the ≥99th, 97.5th-99th, and the 95th-97.5th precipitation percentile categories, respectively. Thus, the farther south a stratospheric PV intrusion reaches, the larger the IVT magnitude, and the longer the duration of combined PV and IVT incursions, the more extreme the precipitation.

Finally, the contribution of tropical-extratropical interactions to annual rainfall amounts and extreme precipitation days are quantified through calculating their fractions that coincide with combined PV and IVT incursions. Combined PV and IVT incursions coincide with more than 50% of the annual rainfall amounts over the larger part of the region of interest in ERA-Interim, Aphrodite and TRMM data, and exceed locally 60% or 70%. Furthermore, a large fraction of the 99.5th percentile precipitation days can be attributed to tropical-extratropical interactions. In the ERA-Interim data, this fraction exceeds 80% in northwestern Saudi Arabia and more than 60% over a region that extends from eastern Egypt across the southern margins of Syria and the larger part of Iraq, as compared to somewhat lower detection rates in Aphrodite and TRMM data. Furthermore, tropical-extratropical interactions contribute to 40-70% of the annual rainfall amounts at many stations in southern Israel and the northern and western parts of Saudi Arabia. Likewise, the algorithm captures a large fraction of the heavy precipitation days exceeding 20 mm day^{-1} (50-80%) and the 10 most severe precipitation days (60-90%) at many sites in the hyper-arid parts of the Arabian Peninsula and Israel (Figure 8). Beyond this region, the detection rates deteriorate quickly as rainfall along the eastern Mediterranean coast stems mostly from Mediterranean cyclones (*Saaroni et al.*, 2010a) and precipitation over the southwestern Arabian Peninsula is associated with the African monsoon in summer (*Almazroui et al.*, 2012b; *Enzel et al.*, 2015). Appendix C3 presents more details on the identification of tropical-extratropical interactions and extreme precipitation events in the Middle East.

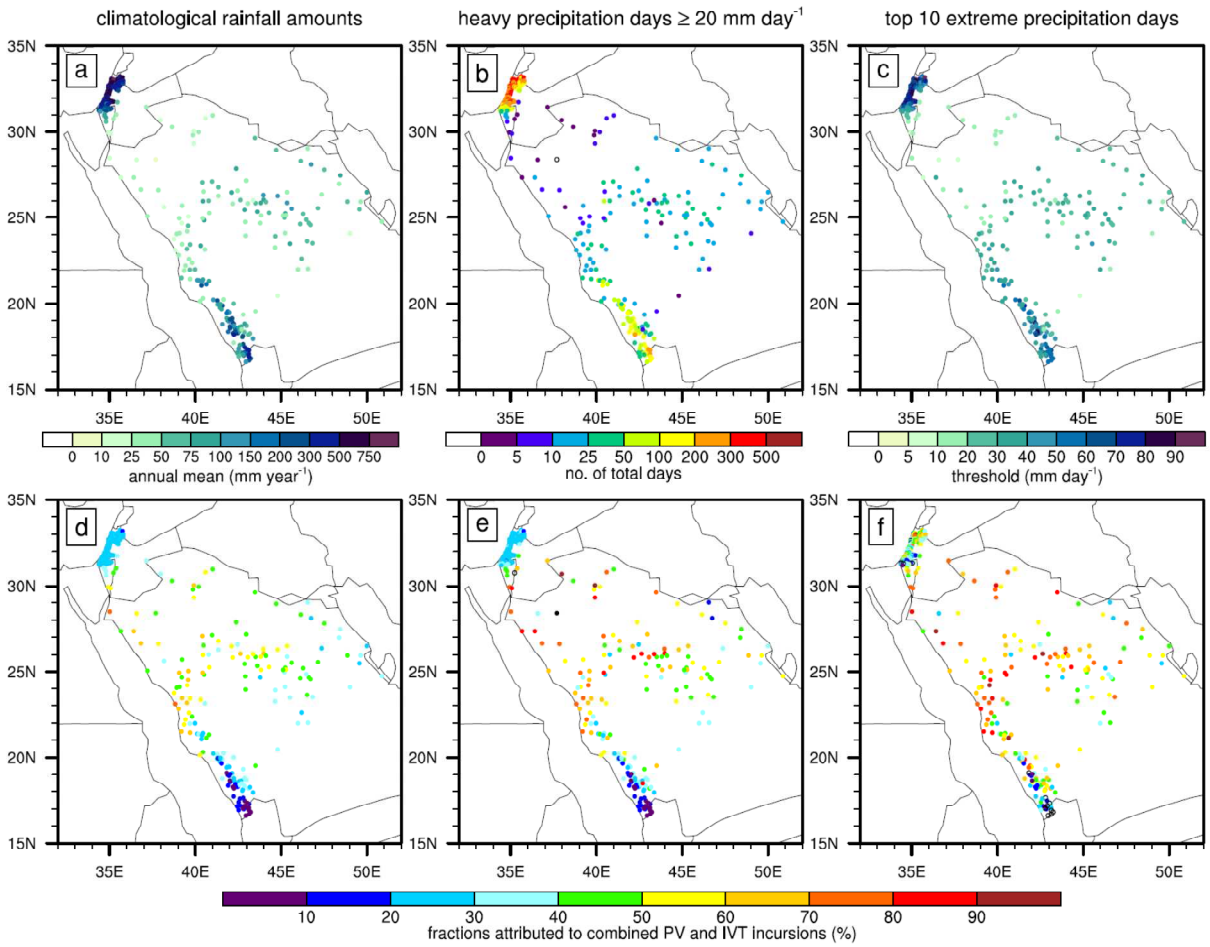

Figure 8. For rainfall observations of stations in Saudi Arabia (1979-2012) and Israel (1979-2015), the (a) annual mean precipitation amounts (mm year^{-1}), (b) total number of heavy precipitation days with ≥20 mm day^{-1}, and (c) the threshold of precipitation (mm day^{-1}) that corresponds to the top 10 extreme precipitation days, and in (d-f) their fractions (%) that coincide with combined PV and IVT incursions. Black open circles in (b,e,f) denote zero values and black filled circles in (e) represent stations without any heavy precipitation day.

4 Conclusions

4.1 Summary

Recurrent extreme precipitation events in the hyper-arid deserts of the Middle East can lead to devastating floods as well as recharge scarce fresh water resources. Such events can go along with rainfall amounts on a single day that substantially exceed those of an average year. These extreme precipitation events often result from tropical-extratropical interactions whereby midlatitude forcing and tropical moisture are of central importance. A midlatitude upper-level trough, going along with wave breaking, intrudes far into low latitudes and interacts with the tropical circulation, leading to an incursion of tropical moisture into the Middle East that fuels the heavy rainfall. These atmospheric processes were observed for twelve ARST events that affected the Levant region as well as three extreme precipitation cases in Saudi Arabia in different seasons.

The ARST is an infrequent weather phenomenon that is associated with the most severe flash floods in the Levant. Based on a literature review and detailed analysis of twelve ARST events, we postulate that the ARST is a type of tropical-extratropical interaction with the signature of the particular topography of region. A transient midlatitude upper-level trough interacts with the climatological Red Sea Trough near the surface, resulting in an intrusion of tropical moist air masses into the Levant. Enhanced moisture transport occurs predominantly over the Arabian and Red Seas through an intensified Arabian anticyclone and is therefore of central importance for the ARST. This feature was previously overlooked in most ARST-related studies, which furthermore made unsubstantiated inferences to moisture pathways and origin. The Jeddah flooding of November 2009 showed the same dynamical characteristics as those of the twelve ARST events in the Levant, implying that the ARST can affect a much larger part of the Middle East than previously thought. The ARST seasonality can be explained by the seasonal cycle of the large-scale circulation and in particular that of the asymmetrical seasonal evolution of the regional low-level circulation.

The Jeddah flooding of November 2009 and two other extreme precipitation cases in winter and spring in Saudi Arabia developed in a tropospheric environment controlled by the large-scale circulation. Anticyclonic Rossby wave breaking resulted in a midlatitude upper-level trough that intruded into the subtropics and interacted with the tropical circulation in a manner that is reminiscent of baroclinic wave growth. The coupling of the tropical and extratropical circulations facilitated the export of tropical moisture, leading to anomalous tropospheric moisture content over Saudi Arabia (>2 or >3 STD). Eulerian and Lagrangian analysis revealed that moisture transport originated from nearby and remote tropical regions. Upward motion was in all three cases associated with orographic lifting of moist air masses over the mountainous Red Sea coast and the release of potential instability. Furthermore, the winter case was accompanied by strong dynamical lifting and diabatic heating, resulting in widespread heavy rainfall. During the autumn and spring cases, concentrated extreme precipitation occurred under the influence of local forcing factors such as low-level moisture convergence and reduced static stability (autumn case), and surface sensible heating (spring case). The differences of the circulation patterns between the three cases were linked to the seasonal variability of the larger-scale circulation.

Building on these case studies, we developed an identification method for extreme precipitation events in the Middle East that combines stratospheric PV intrusions and poleward IVT structures. Both PV and

IVT incursions are intimately linked to the extreme precipitation intensity distribution and seasonality of the region. Importantly, IVT alone performs nearly as good as the combination of PV and IVT for detection of extreme precipitation, indicating that IVT is a potentially more pertinent predictor of extreme precipitation events than PV. The characteristics and duration of PV and IVT incursions influence the severity of the precipitation; the farther south a stratospheric PV intrusion reaches, the larger the IVT magnitude, and the longer the duration of combined PV and IVT incursions, the more extreme the precipitation. Limitations of the algorithm are exemplified through missed EPDs and false alarms. Tropospheric moisture content can explain missed EPDs that lacked IVT incursions (high above-normal total column water) and false alarm days (low above-normal total column water), and should therefore, together with stratospheric PV intrusions and IVT structures, be considered as an important large-scale ingredient and precursor for extreme precipitation occurrence. The strength of the algorithm is the identification of local-scale extreme precipitation solely based on larger-scale meteorological features, without depending on precipitation data and their inherent limitations.

Tropical-extratropical interactions, represented by combined PV and IVT incursions, contribute to a substantial fraction of the annual rainfall amounts (40-70%) and to a large number of extreme precipitation days (50-90%) in the arid parts of the Levant and Arabian Peninsula. Accordingly, tropical-extratropical interactions are not only important for extreme precipitation events that give rise to flood hazards, but also for rainfall events which replenish highly-needed fresh water resources. Whereas tropical-extratropical interactions and extreme precipitation in other dry subtropical regions have been well documented, those for the Middle East remained largely unexplored. This thesis fills this gap in the literature and places the Middle East on the world map as a region where tropical-extratropical interactions and extreme precipitation events have a high societal relevance. Importantly, this thesis contributes to the understanding of the atmospheric processes that drive extreme precipitation events and provides a tool for their identification that may benefit medium-range weather prediction and future studies on their mesoscale and climatological aspects.

4.2 Outlook

Building on the results presented in this thesis, a number of avenues for future research can be followed. As a direct extension, the identification method can facilitate future studies on extreme precipitation events in the Middle East and their (i) teleconnection patterns and large-scale processes, (ii) interannual variability and trends, and (iii) future changes due to global warming. Previous studies of extreme precipitation events in the Alpine region, northwest Africa and southern Africa were associated with upstream wave amplification initiated by diabatic PV reduction and negative PV advection (*Knippertz and Martin*, 2005, 2007b; *Martius et al.*, 2008; *Hart et al.*, 2010). Such large-scale processes are likely involved in extreme precipitation events in the Middle East, and may in turn be subject to atmospheric and oceanic climate variability modes. *Feldstein and Dayan* (2008) found circum-global wave-packets to be associated with winter precipitation over Israel. Other previous studies have shown that tropical oscillation patterns of El-Nino Southern Oscillation, the Indian Ocean Dipole, and the Madden-Julian Oscillation modulate precipitation and extreme precipitation in the Middle East (*Price et al.*, 1998; *Chakraborty et al.*, 2006; *Nazemosadat and Ghaedamini*, 2010; *Tippett et al.*, 2015; *Barlow et al.*, 2016; *Kumar et al.*, 2016). Extratropical atmospheric circulation patterns such as the North Atlantic Oscillation and the East Atlantic West Russia have been suggested to influence precipitation over the region; however, their relevance is debated (*Krichak et al.*, 2002; *Krichak and Alpert*, 2005; *Ziv et al.*, 2006). Our

algorithm may help to disentangle the influences of these teleconnection patterns and can elucidate their underlying physical mechanisms. Furthermore, application of the algorithm on long-term 20th century reanalysis data and climate model simulations for the past and projected future may provide further insight in the trends, interannual variability and expected future changes of extreme precipitation events in the Middle East. Some preliminary results (Figure 9) demonstrate a striking coincidence between El-Nino (La-Nina) years and peaks (dips) in the annual frequency of PV incursions, and a remarkable increase of PV incursions and a reduction of the IVT magnitudes over the last decades, which urges for further investigation.

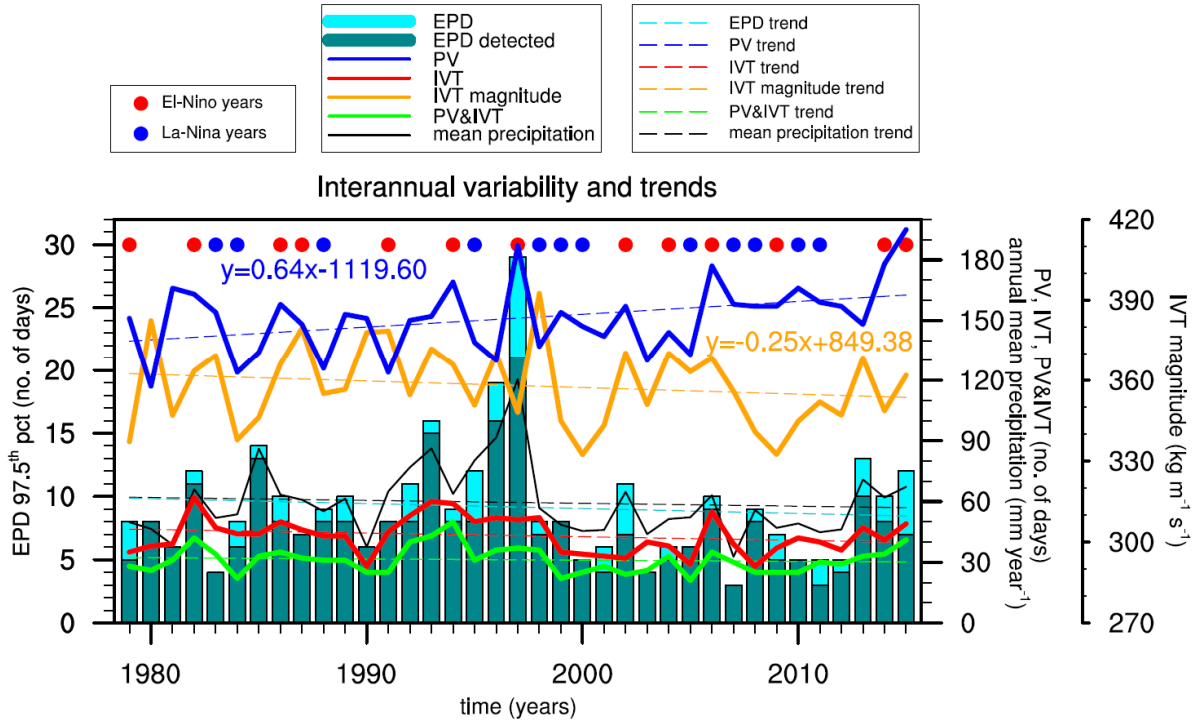

Figure 9. The annual frequencies and trends of all EPDs (light blue color bars), the EPDs detected by the combined PV & IVT incursions (green color bars), PV incursions (blue lines), IVT incursions (red lines), IVT magnitudes (orange lines), combined PV and IVT incursions (green lines), and the mean precipitation amounts (black thin lines). The trends are calculated through linear regression. The El-Nino (red dots) and La-Nina (blue dots) years correspond to moderate, strong and very strong El-Nino/La-Nina years based on the Oceanic Nino Index (ONI) and the Nino 3.4 region (source NOAA).

Other relevant applications of the algorithm can support an evaluation of (1) the contribution of stratospheric PV intrusions and IVT structures to precipitation and extreme precipitation on a global scale, (2) the role of PV intrusions in driving moist air incursions into the Arctic (*Liu and Barnes*, 2015; *Baggett et al.*, 2016), (3) the role of PV intrusions in the formation and landfall of atmospheric rivers (*Payne and Magnusdottir*, 2014; *Mundhenk et al.*, 2016b), and (4) a potentially improved medium-range predictability of extreme precipitation events (*Lavers et al.*, 2014).

Furthermore, this thesis may inspire several lines of future research on extreme precipitation events and/or the atmospheric circulation over the Middle East:

- Although extreme precipitation events over the Levant have received relatively much attention, their understanding can be advanced through adopting the same framework in which we studied the three extreme precipitation cases in Saudi Arabia. In particular, the origin of moist air parcel trajectories may be a means to distinguish between the different phenomena that affect the region with heavy rainfall, being Mediterranean cyclones, ARSTs, tropical plumes, and their combinations.
- As an extension to the elucidated moisture transport pathways, the contributions of various moisture sources to extreme precipitation in the Middle East can be quantified through algorithms (*Sodemann et al.*, 2008) or moisture tagging in high-resolution model simulations.
- The presented case studies may provide context for future studies on modeling studies and mesoscale processes of convective storms in the Middle East.
- Dynamical analysis from a PV perspective suggested wave amplification through baroclinic growth. The impact of upper-tropospheric PV anomalies on the lower-tropospheric circulation can be quantified through PV inversion techniques (*Funatsu and Waugh*, 2008; *Schlemmer et al.*, 2010; *Martius et al.*, 2013).
- Alternative approaches for the classification and identification of extreme weather events based on self-organizing maps (*Johnson et al.*, 2008; *Swales et al.*, 2016) or machine learning.
- Finally, the origin of the Red Sea Trough and Arabian anticyclone can be studied through simplified atmospheric models in a theoretical framework and model simulation experiments that test their sensitivity to the presence of water bodies and orography in the region.

Abbreviations

ARST	Active Red Sea Trough
CAPE	convective available potential energy
ECMWF	European Centre for Medium-range Weather Forecasts
EPD	extreme precipitation days
IACDC	Israeli Atmospheric and Climatic Data Centre
IVT	vertically integrated horizontal water vapor transport
NCDC	National Climatic Data Center
PV	potential vorticity
STD	standard deviation
TRMM	Tropical Rainfall Measuring Mission Multisatellite Precipitation Analysis

References

Almazroui, M. (2011), Sensitivity of a regional climate model on the simulation of high intensity rainfall events over the Arabian Peninsula and around Jeddah (Saudi Arabia), *Theor. Appl. Climatol., 104(1-2)*, 261-276.

Almazroui, M. (2013), Simulation of present and future climate of Saudi Arabia using a regional climate model (PRECIS), *Int. J. Climatol., 33*, 2247–2259.

Almazroui M., M. N. Islam, H. Athar, P. D. Jones, M.A. Rahman (2012), Recent climate change in the Arabian Peninsula: annual rainfall and temperature analysis of Saudi Arabia for 1978-2009, *Int. J. Climatol., 32*, 953-966.

Almazroui, M., M. N. Islam, P. D. Jones, H. Athar, and M. A. Rahman (2012), Recent climate change in the Arabian Peninsula: Seasonal rainfall and temperature climatology of Saudi Arabia for 1979-2009. *Atmos. Res., 111*, 29-45.

Almazroui, M., S. Kamil, K. Ammar, K. Keay, and A. O. Alamoudi (2016), Climatology of the 500-hPa Mediterranean storms associated with Saudi Arabia wet season precipitation, *Clim. Dyn., 48*, 3309-3324.

Amin, M. T., S. H. Mahmoud, and A. A. Alazba (2016), Observations, projections and impacts of climate change on water resources in Arabian Peninsula: current and future scenarios, *Env. Earth Sci., 75*(10).

Al-Khalaf A. K., H.A. Basset (2013), Diagnostic Study of a Severe Thunderstorm over Jeddah, *Atmos. Climate. Sci., 3*, 150-164.

Alpert, P., and E. Ganor (2001), Sahara mineral dust measurements from TOMS – Comparison to surface observations over the Middle East for the extreme dust storm, 14–17 March 1998, *J. Geophys. Res., 106*, 18 275–18 286.

Alpert, P., B. U. Neeman, and Y. Shay-el (1990), Climatological analysis of Mediterranean cyclones using ECMWF data, *Tellus, 42*, 65-77.

Alpert, P., I. Osetinsky, B. Ziv, and H. Shafir (2004a), Semi-objective classification for daily synoptic systems: Application to the Eastern Mediterranean climate change, *Int. J. Climatol., 24*(8), 1001–1011.

Alpert, P., I. Osetinsky, B. Ziv, and H. Shafir (2004b), A new seasons definition based on classified daily synoptic systems: An example for the Eastern Mediterranean, *Int. J. Climatol., 24*(8), 1013–1021.

Alpert, P., M. Baldi, R. Ilani, S. Krichak, C. Price, X. Rodó, H. Saaroni, B. Ziv, P. Kischa, J. Barkan, A. Mariotti, and E. Xoplaki (2006), Relations between climate variability in the Mediterranean region and the Tropics: ENSO, South Asian and African Monsoons, Hurricanes and Saharan Dust, in *Mediterranean Climate Variability*, *Developments in Earth & Environmental Sciences*, vol. 4, edited by P. Lionello, P. Malanotte-Rizzoli and R. Boscolo pp.149-177, Elsevier, Amsterdam, The Netherlands.

Alpert, P ., and B. Ziv (1989), The Sharav cyclone: observatios and some theoretical consideration, *J. Geophys. Res., 94*, 18,495-18,514.

Amin, M. T., A. A. Alazba, and M. N. ElNesr (2013), Adaptation of climate variability/extreme in arid environment of the Arabian peninsula by rainwater harvesting and management, *Int. J. Environ. Sci. Technol., 10* (1), 27e36.

Ashbel, D. (1938), Great floods in Sinai Peninsula, Palestine, Syria and the Syrian desert, and the influence of the Red Sea on their formation, *Quart. J. Roy. Meteor. Soc., 64*, 635–639.

Baggett, C., S. Lee, and S. B. Feldstein (2016), An investigation of the presence of atmospheric rivers over the North Pacific during planetary-scale wave life cycles and their role in Arctic warming, *J. Atmos. Sci., 73*, 4329–

4347.

Bao, J.-W., S. A. Michelson, P. J. Neiman, F. M. Ralph, and J. M. Wilczak (2006), Interpretation of enhanced integrated water vapor bands associated with extratropical cyclones: Their formation and connection to tropical moisture, *Mon. Wea. Rev.*, *134*, 1063–1080.

Barlow, M., B. Zaitchik, S. Paz, E. Black, J. Evans, and A. Hoell (2016) A review of drought in the Middle East and southwest Asia, *J. Clim.*, *29*, 8547–8574.

Barth H. J., and F. Steinkohl (2004), Origin of winter precipitation in the central coastal lowlands of Saudi Arabia, *J. Arid Env.*, *57*, 101-115.

Ben Ami, Y., O. Altaratz, Y. Yair, and I. Koren (2015), Lightning characteristics over the eastern coast of the Mediterranean during different synoptic systems, *Nat. Hazards Earth Syst. Sci.*, *15*(11), 2449–2459.

Bitan, A., and H. Saaroni (1992), The horizontal and vertical extension of the Persian Gulf pressure trough, Int. J. Climatol., *12*(7), 733-747.

Bou Karam, D., C. Flamant, J. Cuesta, J. Pelon, and E. Williams (2010), Dust emission and transport associated with a Saharan depression: February 2007 case, *J. Geophys. Res.*, *115*.

Cavazos, T., A. C. Comrie, and D. M. Liverman (2002), Intraseasonal variability associated with wet monsoons in southeast Arizona, *J. Clim.*, *15*, 2477–2490.

Chakraborty, A., S. K. Behera, M. Mujumdar, R. Ohba, and T. Yamagata (2006), Diagnosis of tropospheric moisture over Saudi Arabia and influences of IOD and ENSO, *Mon. Weather Rev.*, *134*, 598-617.

Chenoweth, J., P. Hadjinicolaou, A. Bruggeman, J. Lelieveld, Z. Levin, M.A. Lange, E. Xoplaki, and M. Hadjikakou (2011), The impact of climate change on the water resources of the eastern Mediterranean and Middle East region: modeled changes and socio-economic implications, *Water Resource Res.*, *47*.

Dacre, H. F., P. A. Clark, O. Martinez-Alvarado, and M. A. Stringer (2015), How do atmospheric rivers form?, *Bull. Am. Meteorol. Soc.*, *96*, 1243–1255.

Dayan, U., and R. Abramsky (1983), Heavy rain in the Middle East related to unusual jet stream properties, *Bull. Amer. Meteor. Soc.*,*64*, 1138–1140.

Dayan U., B. Ziv, A. Margalit, E. Morin, and D. Sharon (2001), A severe autumn storm over the Middle-East: synoptic and mesoscale convection analysis, *Theor. Appl. Climatol. 69*(1-2), 103–122.

Dayan U. and E. Morin (2006), Flash flood-producing rainstorms over the Dead Sea, *Geological Society of America, 401*, 53-62.

Dayan U., K. Nissen, U. Ulbrich (2015), Review Article: Atmospheric conditions inducing extreme precipitation over the eastern and western Mediterranean, *Nat. Hazards Earth Syst. Sci.*, *15*, 2525–2544.

Davies-Jones R. (1991), The frontogenetical forcing of secondary circulations. Part I: The duality and generalization of the Q vector, *J. Atmos. Sci.*, *48*, 497–509.

Dee, D. P., et al. (2011), The ERA-Interim reanalysis: Configuration and performance of the data assimilation system, *Q. J. R. Meteorol. Soc.*, *137*(656), 553–597.

Deng, L. P., M. F. McCabe, G. Stenchikov, J. P. Evans, P. A. Kucera (2015), Simulation of flash-flood-producing storm events in Saudi Arabia using the Weather Research and Forecasting Model, *J. Hydrometeor.*, *16*, 615-630.

Donat, M. G., J. Sillmann, S. Wild, L. V. Alexander, T. Lippmann, and F. W. Zwiers (2014), Consistency of

temperature and precipitation extremes across various global gridded in situ and reanalysis datasets, *J. Clim., 27*(13), 5019–5035.

Doswell III C. A. (1987), The distinction between large-scale and mesoscale contribution to severe convection: A case study example, *Wea. Forecasting*, 2, 3–16.

Egger, J., P. Alpert, A. Tafferner, and B. Ziv (1995), Numerical experiments on the genesis of Sharav cyclones - idealized simulations, *Tellus, 47A*, 162-174.

El-Fandy, M. G. (1948), The effect of Sudan monsoon low on the development of thundery conditions in Egypt, Palestine and Syria, *Quart. J. Roy. Meteor. Soc., 74*, 31–38.

El-Fandy, M. G. (1950), Effects of topography and other factors on the movement of lows in the Middle East and Sudan, *Bull. Amer. Meteor. Soc., 31*, 375–381.

El-Fandy, M. G. (1952), Forecasting thunderstorms in the Red Sea, *Bull. Am. Meteorol. Soc., 33*, 332–338.

El Kenawy, A. M., and M. F. McCabe (2016), A multi-decadal assessment of the performance of gauge- and model-based rainfall products over Saudi Arabia: climatology, anomalies and trends, *Int. J. Climatol., 36*, 656-674.

Enzel, Y., R. Amit, U. Dayan, O. Crouvi, R. Kahana, B. Ziv, and D. Sharon (2008), The climatic and physiographic controls of the eastern Mediterranean over the late Pleistocene climates in the southern Levant and its neighboring deserts, *Glob. Planet. Change., 60*, 165-192.

Enzel, Y., Y. Kushnir, and J. Quade (2015), The middle Holocene climatic records from Arabia: reassessing lacustrine environments, shift of ITCZ in Arabian Sea, and impacts of the southwest Indian and African monsoons, *Glob. Planet. Change, 129*, 69e91.

Evans, J.P. (2009), 21st century climate change in the Middle East, *Clim. Change, 92*, 417–432.

Evans, J. P., and R. B. Smith (2006), Water vapor transport and the production of precipitation in the eastern fertile crescent, *J. Hydrometeorol., 7*(6), 1295-1307.

Evans J. P., S. B. Smith, and R. J. Oglesby (2004), Middle East climate simulation and dominant precipitation processes, *Int. J. Climatol., 24*, 1671-1694.

Favors, J. E., and J. T. Abatzoglou (2013), Regional surges of monsoonal moisture into the southwestern United States, *Mon. Weather Rev., 141*(1), 182-191.

Feldstein, S., and U. Dayan (2008), Circumglobal teleconnections and wave packets associated with Eastern Mediterranean precipitation, *Q. J. Roy. Meteor. Soc., 134*, 455–467.

Fröhlich, L., P. Knippertz, A. H. Fink, and E. Hohberger (2013), An objective climatology of tropical plumes, *J. Clim., 26*(14), 5044–5060.

Froidevaux P., and O. Martius (2016), Exceptional integrated vapour transport toward orography: an important precursor to severe floods in Switzerland, *Q. J. Roy. Meteor. Soc., 142*, 1997-2012.

Funatsu, B. M., and D. W. Waugh (2008), Connections between potential vorticity intrusions and convection in the Eastern Tropical Pacific, *J. Atmos. Sci., 65*, 987–1002.

Galarneau T. J. Jr., R. M. Dole, T. M. Hamill, and J. Perlwitz (2012), A multiscale analysis of the extreme weather events over western Russia and northern Pakistan during July 2010, *Mon. Wea. Rev., 140*, 1639–1664.

Greenbaum, N., U. Schwartz, and N. Bergman (2010), Extreme floods and short-term hydroclimatological fluctuations in the hyper-arid Dead Sea region, Israel, *Glob. Planet. Change, 70(1-4)*, 125-137.

Guan, B., and D. E. Waliser (2015), Detection of atmospheric rivers: Evaluation and application of an algorithm for global studies, *J. Geophys. Res. Atmos.*, *120*, 514–12,535.

Guizani, M. (2016), Storm water harvesting in Saudi Arabia: a multipurpose water management alternative, *water res. management*, *30*, 1819-1833.

Haggag, M., and H. El-Badry (2013), Mesoscale Numerical Study of Quasi-Stationary Convective System over Jeddah in November 2009, *Atmos. Clim. Sci.*, *3*(1), 73-86, doi:10.4236/acs.2013.31010.

Hart, N. C. G., C. J. C. Reason, and N. Fauchereau (2010), Tropical-Extratropical Interactions over Southern Africa: Three Cases of Heavy Summer Season Rainfall, *Mon. Weather Rev.*, *138*(7), 2608-2623.

Hart, N. C. G., C. J. C. Reason, and N. Fauchereau (2012), Building a tropical extratropical cloud band metbot, *Mon. Weather Rev.*, *140*, 4005–4016.

Hart, N. C. G., C. J. C. Reason, and N. Fauchereau (2013), Cloud bands over southern Africa: Seasonality, contribution to rainfall variability and modulation by the MJO, *Clim. Dyn.*, *41*(5-6), 1199-1212.

Heifetz, E., C. H. Bishop, B. J. Hoskins, and J. Methven (2004), The counter-propagating Rossby-wave perspective on baroclinic instability. I: Mathematical basis, *Q. J. Roy. Meteor. Soc.*, *130*, 211–231.

Holton, J.R., (2004) *An introduction to dynamic meteorology*, Elsevier Academic Press, California, USA.

Hong, C-C., H-H. Hsu, N-H Lin, and H. Chiu (2011), Roles of European blocking and tropical–extratropical interaction in the 2010 Pakistan flooding, *Geophys. Res. Lett.*, *38*, L13806.

Hoskins, B. J., M. E. McIntyre and A. W. Robertson (1985), On the use and significance of isentropic potential vorticity maps, *Q. J. R. Meteorol. Soc.*, *111*(470), 877-946.

Huffman, G. J., R. F. Adler, D. T. Bolvin, G. Gu, E. J. Nelkin, K. P. Bowman, Y. Hong, E. F. Stocker, and D. B. Wolff (2007), The TRMM multisatellite precipitation analysis (TMPA): Quasi-global, multiyear, combined-sensor precipitation estimates at fine scales, *J. Hydrometeor.*, *8*, 38-55.

Johnson, N. C., S. B. Feldstein, and B. Tremblay (2008), The continuum of Northern Hemisphere teleconnection patterns and a description of the NAO shift with the use of self-organizing maps, *J. Clim.*, 21(23), 6354–6371.

Kahana, R., B. Ziv, Y. Enzel, and U. Dayan (2002), Synoptic climatology of major floods in the Negev desert, Israel, *Int. J. Climatol.*, *22*(7), 867–882.

Kahana, R., B. Ziv, U. Dayan, and Y. Enzel (2004), Atmospheric predictors for major floods in the Negev desert, Israel, *Int. J. Climatol.*, *24*(9), 1137–1147.

Knippertz, P. (2003), Tropical-extratropical interactions causing precipitation in northwest Africa: Statistical analysis and seasonal variations, *Mon. Weather Rev.*, *131*(12), 3069-3076.

Knippertz, P. (2005), Tropical-extratropical interactions associated with an Atlantic tropical plume and subtoprical jet streak, *Mon. Weather Rev.*, *133*(9), 2759-2776.

Knippertz, P. (2007), Tropical-extratropical interactions related to upper-troughs at low latitudes, *Dyn. Atm. Oceans*, *43*(1-2), 36-62.

Knippertz, P., A. H. Fink, A. Reiner and P. Speth (2003), Three late summer/early autumn cases of tropical-extratropical interactions causing precipitation in northwest Africa, *Mon. Weather Rev.*, *131*(1), 116-135.

Knippertz, P., and J. E. Martin (2005), Tropical plumes and extreme precipitation in subtropical and tropical West Africa, *Q. J. R. Meteorol. Soc., 131*(610), 2337-2365.

Knippertz, P., and J. E. Martin (2007a), A Pacific moisture conveyor belt and its relationship to a significant precipitation event in the semiarid southwestern United States, *Weather Forecast., 22*(1), 125-144.

Knippertz P., J. E. Martin (2007b), The role of dynamic and diabatic processes in the generation of cut-off lows over Northwest Africa. *Meteor. Atmos. Phys., 96***,** 3-19.

Knipperz, P., and H. Wernli (2010), A Lagrangian climatology of tropical moisture exports to the Northern Hemisphere extratropics, *J. Clim.,23*, 987–1003.

Knippertz, P., H. Wernli H, and G. Glaser (2013), A Global Climatology of Tropical Moisture Exports, *J. Climate,*17, 1449-1458.

Kottek K., J. Grieser, C. Beck, B. Rudolf, and F. Rubel (2006), World map of the Koppen-Geiger climate classification updated, *Meteorologische Zeitschrift 15*, 259-263.

Krichak, S. O. and P. Alpert (2005), Decadal trends in the east Atlantic–west Russia pattern and Mediterranean precipitation, *Int. J. Climatol., 25*, 183–192.

Krichak, S. O, P. Alpert, and T. N. Krishnamurti (1997a), Interaction of topography and tropospheric flow – a possible generator for the Red Sea Trough?, *Meteorol. Atmos. Phys., 63*(3-4), 149-158.

Krichak, S. O., P. Alpert, and T. N. Krishnamurti (1997b), Red Sea Trough/cyclone development - numerical investigation, *Meteorol. Atmos. Phys., 63*(3-4), 159-169.

Krichak, S. O., and P. Alpert (1998), Role of large scale moist dynamics in November 1-5, 1994, hazardous Mediterranean weather, *J. Geophys. Res., 103*, 453–468.

Krichak, S. O., J. S. Breitgand, and S. B. Feldstein (2012), A conceptual model for the identification of the Active Red Sea Trough Synoptic events over the southeastern Mediterranean, *J. App. Meteorol. Climatol., 51*(5), 962-971.

Krichak, S. O., P. Kishcha, and P. Alpert (2002), Decadal trends of main Eurasian oscillations and the eastern Mediterranean precipitation, *Theor. Appl. Climatol., 72*, 209–220.

Krichak, S. O., M. Tsidulko and P. Alpert (2000), November 2, 1994, severe storms in the southeastern Mediterranean, *Atmos. Res., 53*(1-3), 45-62.

Kumar, K. N., D. Entekhabi, and A. Molini (2015), Hydrological extremes in hyperarid regions: A diagnostic characterization of intense precipitation over the Central Arabian Peninsula, *J. Geophys. Res. Atmos., 120*, 1637–1650.

Kumar K.N., T. B. M. J. Ouarda, S. Sandeep, and R.S. Ajayamohan (2016), Wintertime precipitation variability over the Arabian Peninsula and its relationship with ENSO in the CAM4 simulations, *Clim. Dyn., 47*, 2443-2454.

Kunz, A., M. Sprenger, and H. Wernli (2015), Climatology of potential vorticity streamers and associated isentropic transport pathways across PV gradient barriers, *J. Geophys. Res. Atmos., 120*, 3802–3821.

Lau, W. L. M., and K. M. Kim (2012), The 2010 Pakistan flood and Russian heat wave: Teleconnection of hydrometeorological extremes, *J. Hydrometeorol., 13*, 392–403.

Lavers, A., G. Villarini (2013a), The nexus between atmospheric rivers and extreme precipitation across Europe, *Geophys. Res. Lett., 40*, 3259-3264.

Lavers, D. A., and G. Villarini (2013b), Atmospheric rivers and flooding over the Central United States, *J. Clim.*, *26*(20), 7829–7836.

Lavers, D. A., F. Pappenberger, and E. Zsoter (2014), Extending medium-range predictability of extreme hydrological events in Europe, *Nat. Commun.*, *5*, 5382.

Lelieveld J., P. Hadjinicolaou, E. Kostopoulou E, J. Chenoweth, M. El Maayar, C. Giannakopoulos, C. Hannidis, M. A. Lange, M. Tanarhte, E. Tyrlis, and E. Xoplaki (2012), Climate change and impacts in the Eastern Mediterranean and the Middle East, *Climate Change*, 114, 667-687.

Lelieveld J., Y. Proestos, P. Hadjinicolaou, M. Tanarhte, E. Tyrlis, and G. Zittis (2016), Strongly increasing heat extremes in the Middle East and North Africa (MENA) in the 21st century, *Climate Change*, 137, 245-260.

Liu, C., and E. A. Barnes (2015), Extreme moisture transport into the Arctic linked to Rossby wave breaking, *J. Geophys. Res. Atmos.*, *120*, 3774–3788.

Luo, D., Y. Yao, A. Dai, and S. Feldstein (2015), The positive North Atlantic Oscillation with downstream blocking and the Middle East snowstorm: The large-scale environment, *J. Clim.*, *28*, 6398–6418.

Mahmoud, S. H., and A. A. Alazba (2015), Geomorphological and geophysical information system analysis of major rainwater-harvesting basins in Al-Baha region, Saudi Arabia, *Arab. J. Geosci.*, *8*, 9959-9971.

Mahmoud, S. H., and A. A. Alazba (2016), Towards a sustainable capital city: an approach for flood management and artificial recharge in naturally water-scarce regions, central region of Saudi Arabia, *Arab. J. Geosci.*, *2*.

Mahoney, K., D. L. Jackson, P. Neiman, M. Hughes, L. Darby, G. Wick, A. White, E. Sukovich, and C. Cifelli (2016), Understanding the role of atmospheric rivers in heavy precipitation in the southeast united states, *Mon. Weather Rev.*, *144*(4), 1617-1632.

Marra, F., and E. Morin (2015), Use of radar QPE for the derivation of intensity-duration-frequency curves in a range of climatic regimes, *J. Hydrol.*, *531*, 427-440.

Martius, O., E. Zenklusen, C. Schwierz, and H. C. Davies (2006), Episodes of Apline heavy precipitation with an overlying elongated stratospheric intrusion: A climatology, *Int. J. Climatol.*, *26*, 1149-1164.

Martius, O., C. Schwierz, and H. C. Davies (2008), Far-upstream precursors of heavy precipitation events on the Alpine south-side, *Q. J. Roy. Meteor. Soc.*, *134*, 417-428.

Martius, O., H. Sodemann, H. Joos, S. Pfahl, A. Winschall, M. Croci-Maspoli, M. Graf, E. Madonna, B. Mueller, S. Schemm, J. Sedlacek, M. Sprenger, and H. Wernli (2013), The role of upper-level dynamics and surface processes for the Pakistan flood of July 2010, *Q. J. Roy. Meteor. Soc.*, 139, 1780–1797.

Massacand, A. C., H. Wernli, and H. C. Davies (1998), Heavy precipitation on the Alpine southside: An upper-level precursor, *Geophys. Res. Lett.*, *25*, 1435-1438.

MacRitchie, K., and P. E. Roundy (2016), The two-way relationship between the Madden–Julian oscillation and anticyclonic wave breaking, *Quart. J. Roy. Meteor. Soc.*, *142*, 2159–2167.

McGuirk J.P., A.H. Thompson, and J.R. Schaefer (1988), An eastern Pacific tropical plume, *Mon. Weather Rev.*,*116*(12), 2505-2521.

Moore B. J., B. J. Neiman, F. M. Ralph, and F. E. Barthold (2012), Physical processes associated with heavy flooding rainfall in Nashville, Tennessee, and vicinity during 1-2 May 2010: The role of an atmospheric river and mesoscale convective systems, *Mon. Wea. Rev.*, *140*, 358-378.

Moore, B. J., K. M. Mahoney, E. M. Sukovich, R. Cifelli, and T. M. Hamill (2015), Climatology and environmental

characteristics of extreme precipitation events in the southeastern United States, *Mon. Weather Rev., 143*, 718–741.

Mundhenk, B. D., E. A. Barnes, and E. D. Maloney (2016a), All-season climatology and variability of atmospheric river frequencies over the North Pacific, *J. Clim., 29*, 4885–4903.

Mundhenk, B. D., E. A. Barnes, E. D. Maloney, and K. M. Nardi (2016b), Modulation of atmospheric rivers near Alaska and the US West Coast by northeast Pacific height anomalies, *J. Geophys. Res. Atmos., 121*, 12,751–12,765, doi:10.1002/2016JD025350.

Nazemosadat M. J., and H. Ghaedamini (2010), On the Relationships between the Madden–Julian Oscillation and Precipitation Variability in Southern Iran and the Arabian Peninsula: Atmospheric Circulation Analysis, *J. Climate, 23*, 887-904.

Pascale, S., and S. Bordoni (2016), Tropical and extratropical controls of Gulf of California surges and summertime precipitation over the southwestern United States, *Mon. Weather Rev*., *144*, 2695–2718.

Payne, A. E., and G. Magnusdottir (2014), Dynamics of landfalling atmospheric rivers over the North Pacific in 30 years of MERRA reanalysis, *J. Clim., 27*, 7133–7150.

Peel, M. C., B. L. Finlayson, and T. A. McMahon (2007), Updated world map of the Koppen-Geiger climate classification, *Hydr. Earth Syst. Sci., 11*, 1633-1644.

Peleg, N., M. Bartov, and E. Morin (2015), CMIP5-predicted climate shifts over the eastern mediterranean: implications for the transition region between Mediterranean and semi-arid climates, *Int. J. Climatol., 35*, 2144-2153.

Peleg, N., and E. Morin (2012), Convective rain cells: radar-derived spatiotemporal characteristics and synoptic patterns over the eastern Mediterranean, *J. Geophys. Res*., *117*, D15116.

Price, C., L. Stone, A. Huppert, B. Rajagopalan, and P. Alpert (1998), A possible link between El Nino and precipitation in Israel, *Geophys. Res. Lett.*, 25, 3963–3966.

Ralph, F. M., G. N. Kiladis, K. Weickmann, and D. W. Reynolds (2011), A multiscale observational case study of a Pacific atmospheric river exhibiting tropical/extratropical connections and a mesoscale frontal wave, *Mon. Wea. Rev., 139*, 1169–1189.

Ralph, F. M., P. J. Nieman, G. A. Wick, S. I. Gutman, M. D. Dettinger, D. R. Cayan, and A. B. White (2006), Flooding on California's Russian River: Role of atmospheric rivers, *Geophys. Res. Lett., 33*, L13801.

Ramos, A. M., R. M. Trigo, M. L. R. Liberato, and R. Tomé (2015), Daily precipitation extreme events in the Iberian Peninsula and its association with atmospheric rivers, *J. Hydrometeorol., 16*, 579–597.

Rash P. and B. Boville (1993), CCM Processor Users' Guide (Unicos version), *NCAR Technical Note*, Appendix B.10, Isentropic Potential Vorticity, p. B19-B20.

Raveh-Rubin, S., and H. Wernli (2015), Large-scale wind and precipitation extremes in the Mediterranean: a climatological analysis for 1979-2012, *Q. J. Roy. Meteor. Soc., 141*, 2404-2417.

Raziei, T., A. Mofidi, A.J. Santos, and I. Bordi (2012), Spatial patterns and regimes of daily precipitation in Iran in relation to large-scale atmospheric circulation, *Int. J. Climatol., 32*(8), 1226-1237.

Riemer M., M. Baumgart, and S. Eiermann (2014), Cyclogenesis downstream of extratropical transition analyzed by Q-vector partitioning based on flow geometry, *J. Atmos. Sci., 71*, 4204-4220.

Rodwell, M. J., and B. J. Hoskins (1996), Monsoon and the dynamics of deserts, *Q. J. R. Meteorol. Soc., 122*(534), 1385-1404.

Romem, M, and H. Saaroni (2007), Scenarios in the development of Mediterranean cyclones, *Adv. Geosci., 12*, 59-65.

Rubin, S., B. Ziv, and N. Paldor (2007), Tropical plumes over eastern North Africa as a source of rain in the Middle East, *Mon. Weather Rev.,135*(12), 4135-4148.

Rutz, J. J., and W. J. Steenburg (2012), Quantifying the role of atmospheric rivers in the interior western Unites States, *Atmos. Sci. Let., 13*, 257-261.

Rutz, J. J., W. J. Steenburgh, and F. M. Ralph (2014), Climatological characteristics of atmospheric rivers and their inland penetration over the western United States, *Mon. Weather Rev., 142*, 905–921.

Saaroni, H., N. Halfon, B. Ziv, P. Alpert, and H. Kutiel (2010a), Links between the rainfall regime in Israel and location and intensity of Cyprus Lows, *Int. J. Climatol., 30*, 1014–1025.

Saaroni, H., B. Ziv, I. Osetinsky, and P. Alpert (2010b), Factors governing the interannual variation and the long-term trend of the 850 hPa temperature over Israel, *Q. J. Roy. Meteor. Soc.*, 136, 305–318.

Salam, M. S., and M. A. Sowelin (1967), Dustfall caused by the spring Khamasin storms in Cairo: a preliminary report, *Atm. Env., 1*, 221-226.

Schlemmer, L., O. Martius, M. Sprenger, C. Schwierz, and A. Twitchett (2010), Disentangling the forcing mechanisms of a heavy precipitation event along the alpine south side using potential vorticity inversion, *Mon. Weather Rev., 138*, 2336–2353.

Schulz, S., G. H. de Rooij, N. Michelsen, R. Rausch, C. Siebert, C. Schüth, M. Al- Saud, and R. Merz (2016), Estimating groundwater recharge for an arid karst system using a combined approach of time-lapse camera monitoring and water balance modelling, *Hydrol. Process., 30*, 771–782.

Seluchi, M. E., and J. A. Marengo (2000), Tropical-midlatitude exchange of air masses during summer and winter in South America: Climatic aspects and examples of intense events, *Int. J. Climatol., 20*, 1167–1190.

Sen, Z., A. Al Aksheikh, A. S. Al-Turbak, A. M. Al-Bassam, and A. M. Al-Dkheel (2013), Climate change impact and runoff harvesting in arid regions, *Arab. J. Geosci., 6*, 287-295.

Shalev, S., H. Saaroni, T. Izsak, Y. Yair, and B. Ziv (2011), The spatiotemporal distribution of lightning over Israel and the neighboring area and its relation to regional synoptic systems, *Nat. Hazards Earth Syst. Sci., 11*, 2125–2135.

Shay-El, Y., and P. Alpert (1991), A diagnostic study of winter diabatic heating in the Mediterranean in relation to cyclones, *Q. J. Roy. Meteor. Soc., 117*, 715–747.

Shentsis, I., J. B. Laronne, and P. Alpert (2012), Red Sea Trough floods in the Negev, Israel (1964-2007), *Hydrol. Sci. J., 57*(1), 42-51.

Sirdas, S., and Z. Sen (2007), Determination of flash floods in Western Arabian Peninsula, *J. of Hydrol. Eng., 12*, 676-681.

Sodemann H., C, Schwierz, and H. Wernli (2008), Interannual variability of Greenland winter precipitation sources: Lagrangian moisture diagnostic and North Atlantic Oscillation influence, *J. Geophys. Res., 113*.

Sprenger, M., O. Martius, and J. Arnold (2013), Cold surge episodes over southeastern Brazil - a potential vorticity perspective, *Int. J. Climatol., 33*, 2758-2767.

Sprenger M., and H. Wernli (2015), The LAGRANTO Lagrangian analysis tool - version 2.0. *Geosci. Model Dev., 8*, 2569-2586.

Swales, D., M. Alexander, and M. Hughes (2016), Examining moisture pathways and extreme precipitation in the U.S. intermountain west using self-organizing maps, *Geophys. Res. Lett.*, *43*,1727-1735.

Tanarhte, M., P. Hadjinicolaou, and J. Lelieveld (2012), Intercomparison of temperature and precipitation data sets based on observations in the Mediterranean and the Middle East. *J. Geophys. Res. Atm.*, *47*, 2361-2371. 117:D12102.

Thorncroft, C. D., B. J. Hoskins, and M. F. Mcintyre (1993), 2 Paradigms of baroclinic-wave life-cycle behavior, *Q. J. R. Meteorol. Soc.*,*119*(509), 17-55.

Tippett, M. K., M. Almazroui, and I. S. Kang (2015), Extended-range forecasts of areal-averaged Saudi Arabia rainfall, *Weather Forecasting*, *30*, 1090-1105.

Trigo, I. F., T. D. Davies, and G. R. Bigg (1999), Objective climatology of cyclones in the Mediterranean region, *J. Clim.*, *12*, 1685–1696.

Tsidulko, M., S. O. Krichak, P. Alpert, O. Kakaliagou, G. Kallos, and A. Papadopoulos (2002), Numerical study of a very intensive eastern Mediterranean dust storm, 13 – 16 March 1998, *J. Geophys. Res.*, *107*(D21), 4581.

Tsvieli, Y., and A. Zangvil (2005), Synoptic climatological analysis of 'wet' and 'dry' Red Sea troughs over Israel, *Int. J. Climatol.*, *25*(15), 1997–2015.

Tsvieli, Y., and A. Zangvil (2007), Synoptic climatological analysis of Red Sea trough and non-Red Sea trough rain situations over Israel, *Adv. Geosci*., 12, 137-143.

Tyrlis, E., J. Lelieveld, and B. Steil (2013), The summer circulation over the eastern Mediterranean and the Middle East: influence of the South Asian monsoon, *Clim. Dyn*., *40*(5-6), 1103-1123.

Vellore, R., M. Kaplan, R. Krishnan, J. Lewis, S. Sabade, N. Deshpande, B. Singh, R. Madhura, and M. V. S. Rama Rao (2016), Monsoon–extratropical circulation interactions in Himalayan extreme rainfall, *Clim. Dyn.*, 46: 3517–3546.

Waldmann, N., A. Torfstein, and M. Stein (2010), Northward intrusions of low- and mid-latitude storms across the Saharo-Arabian belt during past interglacials, *Geology*, *38*, 567–570.

Waliser, D., and B. Guan (2017), Extreme winds and precipitation during landfall of atmospheric rivers, *Nature*, *10*(3), 179-183.

Wernli H., and D. C. Davies DC (1997), A Lagrangian-based analysis of extratropical cyclones. I: The method and some applications, *Q. J. Roy. Meteor. Soc.*, *123*, 467–489.

Wernli, H., and M. Sprenger (2007), Identification and ERA-15 Climatology of Potential Vorticity Streamers and Cutoffs near the Extratropical Tropopause, *J. Atm. Sci*., *64*, 1569–1586.

Wright, W. J. (1997), Tropical-extratropical cloudbands and Australian rainfall: 1. Climatalogy, *Int. J. Climatol.*, *17*(8), 807-829.

Yatagai, A., K. Kamiguchi, O. Arakawa, A. Hamada, N. Yasutomi, and A. Kitoh (2012), Aphrodite constructing a long-term daily gridded precipitation dataset for Asia based on a dense network of rain gauges, *Bull. Am. Meteorol. Soc.*, *93*(9), 1401-1415.

Yesubabu, V., C. V. Srinivas, S. Langodan, and I. Hoteit (2016), Predicting extreme rainfall events over Jeddah, Saudi Arabia: impact of data assimilation with conventional and satellite observations, *Q. J. Roy. Meteor. Soc.*, *142*, 327-348.

Zaitchik, B. J., J. P. Evans, and R. B. Smith (2007), Regional impact of an elevated heat source: the Zagros plateau of Iran, *J. Clim., 20*(16), 4133-4146.

Zarrin, A., H. Ghaemi, M. Azadi, and M. Farajzadeh (2010), The spatial pattern of summertime subtropical anticyclones over Asia and Africa: A climatological review, *Int. J. Climatol., 30*, 159-173.

Zhang, X., L. Alexander, G. C. Hegerl, P. Jones, A. Klein Tank, T. C. Peterson, B. Trewin, and F. W. Zwiers (2011), Indices for monitoring changes in extremes based on daily temperature and precipitation data, *Clim. Change, 2*, 851-870.

Ziv, B. (2001), A subtropical rainstorm associated with a tropical plume over Africa and the Middle-East, *Theor. Appl. Climatol., 68*(1-2), 91-102.

Ziv, B., U. Dayan, Y. Kushnir, C. Roth,and Y. Enzel (2006), Regional and global atmospheric patterns governing rainfall in the southern Levant, *Int. J. Climatol., 26*(1), 55–73.

Ziv, B., H. Saaroni, and P. Alpert (2004), The factors governing the summer regime of the eastern Mediterranean, *Int. J. Climatol., 24*(14), 1859–1871.

Ziv, B., U. Dayan, and D. Sharon (2005), A mid-winter, tropical extreme flood-producing storm in southern Israel: Synoptic scale analysis, *Meteorol. Atm. Phys., 88*(1-2), 53-63.

List of Publications

De Vries, A. J., E. Tyrlis, D. Edry, S. O. Krichak, B. Steil, and J. Lelieveld (2013), Extreme precipitation events in the Middle East: Dynamics of the Active Red Sea Trough, *J. Geophys. Res.*, *118*, 7087-7108.

De Vries A. J., S. B. Feldstein, M. Riemer, E. Tyrlis, M. Sprenger, M. Baumgart, M. Fnais, and J. Lelieveld (2016), Dynamics of tropical-extratropical interactions and extreme precipitation events in Saudi Arabia in autumn, winter and spring, *Q. J. Roy. Meteor. Soc.*, *142*, 1862-1880.

De Vries A. J., H. G. Ouwersloot, S. B. Feldstein, M. Riemer, A. M. El Kenawy, M. F. McCabe, and J. Lelieveld (2018), Identification of tropical-extratropical interactions and extreme precipitation events in the Middle East based on potential vorticity and moisture transport, *J. Geophys. Res.*, *123*,861-881.

Appendices

Appendix A. Socioeconomic Impacts of Floods in the Middle East

Table 1. Floods and their societal impacts in Egypt, Israel, Jordan and Saudi Arabia during the period of 1900-2016 (EM-DAT).

Nr.	Year	Month	Days	Disaster Type	Location	Deaths	Total Affected People	Estimated Damage US$ (M)
1	1954	Mar		Egypt				
2	1963	Apr		Jordan		25		
3	1964	Apr	4	Saudi Arabia	Nedjaran	20	1000	
4	1965	Jan	13	Jordan	Amman to Ma-An	8	500	1000
5	1966	Mar	11	Jordan	Maian	259	5792	1400
6	1975	Feb	20	Egypt	Nile river Valley	15		
7	*1979*	*Oct*		*Egypt*	*Upper Egypt*	*50*	*66 000*	*14 000*
8	1985	Dec	24	Saudi Arabia	North West	32	5000	450 000
9	*1987*	*Oct*	*16*	*Jordan*	*Zarqa*	*9*	*29*	
10	1991	Mar	23	Egypt	South Sina	1	208	
11	1991	Mar	21	Jordan	Karak, Tafileh, Ma\'an	8	18 000	
12	*1994*	*Nov*	*2-8*	*Egypt*	*Asyut, Sohag, Qena, Luxor governorates*	*600*	*160 660*	*140 000*
13	1995	Mar	20	Egypt	El Minja	7	3000	
14	*1996*	*Nov*	*13-18*	*Egypt*	*Manfalout, Minya, Sohag, Dairout, Mallawi (Aswan, Sohag, Asyut provinces)*	*12*	*260*	
15	*1997*	*Oct*	*17-19*	*Israel*	*Near Beersheba (near Beersheba)*	*15*		*40 000*
16	*1997*	*Oct*	*18-20*	*Egypt*		*4*		*1000*
17	*1997*	*Oct*	*18-20*	*Jordan*		*2*		*1000*
18	1998	Dec	31	Israel	Carmel Region		1000	
19	2002	Mar	3-11	Egypt	Shallatin district (Red Sea province)	4	800	
20	2002	Apr	8-13	Saudi Arabia	Makkah province	19		
21	2002	Dec	20	Egypt	Ayat district (Giza province), Cairo province	14	70	
22	2003	Aug	8-12	Saudi Arabia	Jizan province		13 000	
23	2003	Nov	11	Saudi Arabia	Makkah province	12	50	
24	2004	Apr	14-16	Saudi Arabia	Jizan province	5	430	
25	**2005**	**Jan**	**22-27**	**Saudi Arabia**	**Madinah province**	**29**	**67**	
26	2005	Apr	28	Saudi Arabia	Asir, Makkah provinces	34		
27	**2009**	**Nov**	**24-26**	**Saudi Arabia**	**Jeddah, Mecca cities (Makkah province)**	**161**	**10 000**	**900 000**
28	2011	Jan	25-31	Saudi Arabia	Jeddah city (Makkah province)	11		300 000
29	2010	Jan	18-19	Egypt	El Arish 1 district (North Sinai province), Ras Sidr, Sharm el-Sheikh, Nuweiba, Taba districts (South Sinai province), Hurghada 1, Hurghada 2 districts (Red Sea province), Aswan province	12	3500	
30	2010	Jan	19	Israel	Southern District province	2		
31	2010	Jun	23-25	Saudi Arabia	Taif city (Makkah province), Asir, Jizan, Najran provinces	14		
32	2010	Jun	10-12	Saudi Arabia	Al Lith, Al Qunfudhah cities (Makkah province), Najran, Jizan provinces	10	85	
33	2010	Dec	30	Egypt	Menia province	15		
34	2012	Apr	14-18	Saudi Arabia	Asir, Baha, Hail, Jizan, Madinah, Makkah, Tabuk provinces	19		
35	**2013**	**May**	**2**	**Saudi Arabia**	**Tabala area (Asir province)**	**24**	**900**	
36	2013	Nov	16-19	Saudi Arabia	Riyad, Northern Frontier provinces	15	121	
37	2015	Mar	23-27	Saudi Arabia	Makkah, Asir, Najran, Riyad provinces	11		
38	2015	Nov	17-18	Saudi Arabia	Madinah, Makkah, Hail, Tabuk provinces	12		
39	2016	Apr	8-15	Saudi Arabia	Jizan, Riyadh, Makkah, Madinah, Baha, Asir provinces	18	915	
total						**1508**	**291 387**	**1 848 400**

The events in italic correspond to ARST events that affected the Levant and the events in bold refer to the three extreme precipitation cases in Saudi Arabia.

Appendix B. Contributions of Collaborating Scientists

De Vries, A. J., E. Tyrlis, D. Edry, S. O. Krichak, B. Steil, and J. Lelieveld (2013), Extreme precipitation events in the Middle East: Dynamics of the Active Red Sea Trough, *J. Geophys. Res.*, *118*, 7087-7108.

This paper presents a qualitative concept of the Active Red Sea Trough dynamics. The idea for this paper developed after exploring several ARST cases and the existing literature on the subject as well as discussions with D. Edry and S. O. Krichak during my visit to Tel Aviv in summer 2011. D. Edry provided empirically-based dates of several ARST cases as well as rainfall observations of stations in Israel and S. O. Krichak provided dates of ARST cases based on a developed algorithm (*Krichak et al*., 2012). E. Tyrlis contributed to the study through sharing his expertise in dynamical meteorology, and helped with the interpretation of the results and the writing of the paper. B. Steil provided the ERA-Interim reanalysis data that was used for the larger part of the analysis. J. Lelieveld helped shaping the plans for this study from the start and suggested to involve the Jeddah flooding of November 2009 in context of the geographical extent of the ARST phenomenon. I performed the analysis as presented in the paper, prepared all figures, and wrote the whole manuscript.

De Vries A. J., S. B. Feldstein, M. Riemer, E. Tyrlis, M. Sprenger, M. Baumgart, M. Fnais, and J. Lelieveld (2016), Dynamics of tropical-extratropical interactions and extreme precipitation events in Saudi Arabia in autumn, winter and spring, *Q. J. Roy. Meteor. Soc.*, *142*, 1862-1880.

This manuscript investigates and quantifies the larger-scale dynamical processes of three extreme precipitation events in Saudi Arabia. The initial idea for this study came from J. Lelieveld and had the intention of performing a mesoscale modeling study on an extreme precipitation event in Saudi Arabia in collaboration with scientists from the country. Eventually, we investigated the larger-scale dynamics of three extreme precipitation events in different seasons. S. B. Feldstein and E. Tyrlis contributed to the work through sharing their expertise in dynamical meteorology and helped with the interpretation the results. M. Sprenger provided the LAGRANTO model, and helped with the installation and preparation of the input data. M. Riemer and M. Baumgart provided the code for the calculation of the balanced vertical motion, and helped with adjusting the code for ERA-Interim data and application in a subtropical region. Furthermore, M. Riemer contributed substantially to the dynamical interpretation of the results and the formulation of the paper. J. Lelieveld helped with the writing of the paper and guided the overall process that led to the manuscript. I performed the dynamical analysis, calculated normalized anomalies, backward trajectories and balanced ascent, prepared all figures, and wrote the entire paper.

De Vries A. J., H. G. Ouwersloot, S. B. Feldstein, M. Riemer, A. M. El Kenawy, M. F. McCabe, and J. Lelieveld (2018), Identification of tropical-extratropical interactions and extreme precipitation events in the Middle East based on potential vorticity and moisture transport, *J. Geophys. Res.*, *123*,861-881.

This study combines object-based features of PV and IVT for the identification of tropical-extratropical interactions and extreme precipitation events in the Middle East. The idea arose from the two previous studies in combination with an extensive literature review on cutting edge research methods. S. B. Feldstein was involved from the early stages and encouraged the use of PV. H. G. Ouwersloot contributed substantially to the development of the algorithm with many clever solutions for problems that we encountered during the writing of the code. M. Riemer suggested ideas for the analysis of the results. A. M. El Kenawy and M. F. McCabe provided highly-valuable rainfall observations of stations in Saudi Arabia. Furthermore, M. F. McCabe helped improving the precipitation-related content of manuscript. J. Lelieveld supervised the overall process of the work and advised on the choice for an appropriate journal for publication. I wrote the entire algorithm for the identification of PV intrusions and IVT structures, performed all analyses as presented in the paper, prepared all figures, and wrote the whole manuscript.

Appendix C1. *De Vries et al.* (2013)

Published in the Journal of Geophysical Research - Atmospheres in 2013

Extreme Precipitation Events in the Middle East: Dynamics of the Active Red Sea Trough

Authors: A. J. De Vries[1], E. Tyrlis[1], D. Edry[2], S. O. Krichak[2], B. Steil[3], and J. Lelieveld[1,3]

[1]) Energy, Environment and Water Research Center, The Cyprus Institute, Nicosia, Cyprus
[2]) Department of Geophysical, Atmospheric and Planetary Sciences, Tel Aviv University, Tel Aviv, Israel
[3]) Atmospheric Chemistry Department, Max Planck Institute for Chemistry, Mainz, Germany

JOURNAL OF GEOPHYSICAL RESEARCH: ATMOSPHERES, VOL. 118, 7087–7108, doi:10.1002/jgrd.50569, 2013

Extreme precipitation events in the Middle East: Dynamics of the Active Red Sea Trough

A. J. de Vries,[1] E. Tyrlis,[1] D. Edry,[2] S. O. Krichak,[2] B. Steil,[3] and J. Lelieveld[1,3]

Received 20 February 2013; revised 3 June 2013; accepted 7 June 2013; published 11 July 2013.

[1] The Active Red Sea Trough (ARST) is an infrequent weather phenomenon that is associated with extreme precipitation, flash floods, and severe societal impacts in the Middle East (ME). Using reanalysis (ERA-Interim) and observational precipitation (Aphrodite and stations) data, we investigate its underlying dynamics, geographical extent, and seasonality. Twelve ARST events affecting the Levant have the same dynamical characteristics as those associated with a major flood in Jeddah (Saudi Arabia) on 25 November 2009. Hence, the Jeddah flooding was caused by an ARST, which implies that ARSTs can affect a much larger part of the ME than previously assumed. We present an ARST concept involving six dynamical factors: (1) a low-level trough; the Red Sea Trough (RST), (2) an anticyclone over the Arabian Peninsula; the Arabian Anticyclone (AA), (3) a transient midlatitude upper trough, (4) an intensified subtropical jet stream, (5) moisture transport pathways, and (6) strong ascent resulting from tropospheric instability and the synoptic-scale dynamical forcing. We explain the ARST as the interaction of a persistent stationary wave in the tropical easterlies (i.e., the RST) with a superimposed amplifying Rossby wave, resulting in northward propagating moist air masses over the Red Sea. Our findings emphasize the relevance of the AA, causing moisture transport from the Arabian and Red Seas. The particular topography in the Red Sea region and associated low-level circulation makes the ARST unique among tropical-extratropical interactions. The ARST seasonality is explained by the large-scale circulation and in particular the seasonal cycle of the semipermanent quasi-stationary RST and AA.

Citation: de Vries, A. J., E. Tyrlis, D. Edry, S. O. Krichak, B. Steil, and J. Lelieveld (2013), Extreme precipitation events in the Middle East: Dynamics of the Active Red Sea Trough, *J. Geophys. Res. Atmos.*, *118*, 7087–7108, doi:10.1002/jgrd.50569.

1. Introduction

[2] Subtropical regions are usually characterized by a semiarid to arid climate with very limited annual precipitation. However, occasionally, extreme precipitation events affect these dry regions, causing flash floods that can have dramatic societal impacts, including major economic damage and loss of lives [e.g., *Llasat et al*., 2010]. Extreme precipitation events in the subtropics are often caused by tropical-extratropical interactions. They affect the southwestern part of North America [e.g., *Knippertz and Martin*, 2006; *Favors and Abatzoglou*, 2013], northwest Africa [*Fink and Knippertz*, 2003; *Knippertz et al*., 2003; *Knippertz*, 2003; *Knippertz and Martin*, 2005], Australia [e.g., *Wright*, 1997], South Africa [e.g., *Hart et al*., 2010], and the Middle East (ME). These tropical-extratropical interactions are associated with phenomena such as tropical plumes [*McGuirk et al*., 1988; *Knippertz*, 2007] and atmospheric rivers [e.g., *Neiman et al*., 2008].

[3] In the ME (Figure 1), the Levant (eastern Egypt, Sinai Peninsula, Israel, Jordan, Lebanon, and Syria) is frequently under the influence of a synoptic system known as the Red Sea Trough (RST). The RST refers to a low-level pressure trough that extends from the African Monsoon over equatorial Africa, northward over the Red Sea region toward the eastern Mediterranean (EM) [e.g., *Alpert et al*., 2004a; *Tsvieli and Zangvil*, 2005]. The RST is attributed to the local topography and thermal forcing factors [*Krichak et al*., 1997a, 1997b], and is most frequent in autumn while being less prominent in winter and spring [*Alpert et al*., 2004b; *Tsvieli and Zangvil*, 2005; *Krichak et al*., 2012]. The associated weather conditions in the Levant are usually dry and hot. However, when accompanied by a midlatitude upper trough, unstable conditions can develop that trigger convective storms, referred to as the Active Red Sea Trough (ARST) [*Kahana et al*., 2002; *Ziv et al*., 2005; *Krichak et al*., 2012]. Accordingly, the ME can be affected by extreme precipitation resulting from tropical-extratropical interactions, including tropical plumes [*Ziv*, 2001; *Rubin et al*., 2007] and ARSTs.

Additional supporting information may be found in the online version of this article.

[1]Energy, Environment, and Water Research, Cyprus Institute, Nicosia, Cyprus.
[2]Department of Geophysical, Atmospheric, and Planetary Sciences, Tel Aviv University, Tel Aviv, Israel.
[3]Atmospheric Chemistry Department, Max Planck Institute for Chemistry, Mainz, Germany.

Corresponding author: A. J. de Vries, Energy, Environment, and Water Research, Cyprus Institute, 20 Konstantinou Kavafi St., 2121 Aglantzia, Nicosia, Cyprus. (a.devries@cyi.ac.cy)

2169-897X/13/10.1002/jgrd.50569

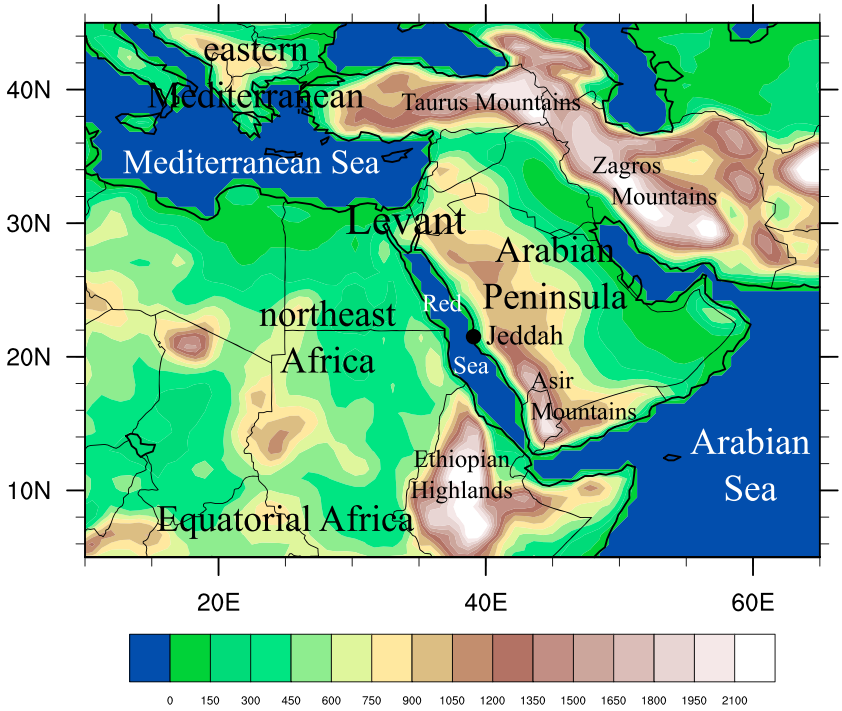

Figure 1. ME region with topography from ERA-Interim data (m).

[4] Climatological studies show that the ARST is a rare weather phenomenon that can occur in late autumn and to a lesser incidence in early winter and spring [*Kahana et al*., 2002; *Krichak et al*., 2012; *Shentsis et al*., 2012]. *Dayan et al*. [2001] explain the ARST preference for autumn by coinciding favorable latitudinal positions of the African Monsoon and the subtropical jet (STJ) stream. Previous ARST case studies relate several dynamical aspects to the phenomenon [e.g., *Krichak and Alpert*, 1998; *Dayan et al*., 2001; *Ziv et al*., 2005], elaborated in section 2. However, an integral concept fully comprising the involved atmospheric dynamics has not yet been defined [*Alpert et al*., 2006, chapter 2], which highlights the need for a better and comprehensive understanding of the ARST dynamics at synoptic scales as well as a seasonal perspective.

[5] The ARST is known to affect Egypt, Israel, Jordan, Lebanon, and Syria [*Dayan et al*., 2001; *Kahana et al*., 2002]. For example, a significant part of the severest floods that occurred in the Negev desert (Israel) resulted from ARSTs [*Kahana et al*., 2002; *Shentsis et al*., 2012]. Also, the catastrophic flash floods in Egypt in November 1994, leaving 600 casualties and additionally affecting 110,660 people (Emergency Events Database, unpublished data, 2012, available from Centre for Research on the Epidemiology of Disasters; http://www.emdat.be/database, hereafter EM-DAT), were caused by an ARST. Previous ARST studies, however, focused primarily on Israel. Therefore, it is yet unknown to what extent other countries in the ME region are also affected by the ARST.

[6] On 25 November 2009, Jeddah (Saudi Arabia) was dramatically hit by heavy precipitation and consequent flash floods (hereafter Jeddah 2009 event). The number of reported fatalities ranges from 122 [*Haggag and El-Badry*, 2013] to 161 (EM-DAT). The EM-DAT database lists the event as the natural disaster with the largest number of casualties in Saudi Arabia in the period 1900–2011 and furthermore mentions that 10,000 people were directly affected, while the estimated financial damage was about US$ 900 million. *Haggag and El-Badry* [2013] investigated the Jeddah 2009 event based on model simulations and describe synoptic and mesoscale aspects that show substantial similarities with the ARST, which has motivated us to study the Jeddah flooding in this context.

[7] This study aims to improve the understanding of the ARST dynamics, its geographical extent, and seasonality. We review previous literature addressing ARST associated dynamics (section 2). Section 3 describes the atmospheric reanalysis and observational precipitation data that were used. We analyze the ARST associated precipitation (section 4), and the synoptic dynamics of 12 ARST events (section 5) and the Jeddah 2009 event (section 6). Section 7 addresses the ARST seasonality in view of the large-scale circulation. Section 8 presents a unified concept of ARST dynamics and places the phenomenon in the context of tropical-extratropical interactions. The paper ends with conclusions and suggestions for further research (section 9).

2. ARST Dynamics in Previous Studies

[8] Several dynamical aspects contribute to the formation of ARSTs. The flow near the surface at the eastern flank of the RST transports warm air masses over the Arabian Peninsula (AP) toward the Levant, while at upper levels, a midlatitude trough and associated cold air approaches the region [e.g., *Krichak et al*., 2000; *Dayan et al*., 2001; *Kahana et al*. 2002; *Ziv et al*., 2005; *Dayan and Morin*, 2006; *Tsvieli and Zangvil*, 2005, 2007; *Krichak et al*., 2012]. In combination with increased moisture, the troposphere can become highly unstable, triggering strong convection. Upper level positive vorticity advection in combination with

Table 1. Selected ARST Events in the Levant

Nr.	Years and Months	Days	Sources of Motivation[a]	Societal Impact	Case Studies
1	Oct 1979	20–23	1,2	50 casualties, 66,000 people affected, and US$ 14 M damage in Egypt (flood)[b]	
2	May 1982	13			
3	Oct 1987	16–18	1,2	30 casualties in Egypt (storm on 17 Oct) and nine casualties in Jordan (flood on 16 Oct)[b]	
4	Oct 1988	16–19	1		
5	Oct 1991	12–14	1,2,3		*Greenbaum et al*. [1998]
6	Dec 1993	20–23	3	two casualties and estimated damage US$ 10 M in Israel[c]	*Ziv et al*. [2005]
7	Oct 1994	10	1,2		
8	Nov 1994	2–4	1,2,3	600 casualties,160,660 people affected, and US$ 140 M damage in Egypt (flood, 2–8 Nov)[b]	*Krichak and Alpert* [1998], *Krichak et al*. [2000]
9	Nov 1996	16–18		12 casualties and 260 people affected in Egypt (flood, 13–18 Nov)[b]	
10	Oct 1997	17–19	1,2,3	15 casualties and US$ 40 M damage in Israel (flood from 17 to 19 October), four casualties, and US$ 1 M damage in Egypt (flood, 18–20 Oct) and two casualties and US$ 1 M damage in Jordan (flood, 18–20 Oct)[b]; at least six casualties in Egypt, nine in Israel, and two in Jordan[c]	*Dayan et al*. [2001]
11	Nov 2003	23–25			
12	Oct 2004	28–29	3		*Greenbaum et al*. [2010]

[a]See text for explanation.
[b]EM-DAT.
[c]Case studies mentioned in right column.

low-level warm air advection implies quasi-geostrophic forced ascent [*Tsvieli and Zangvil*, 2005; *Ziv et al*., 2005]. In addition, the STJ intensifies over North Africa and the ME [*Krichak et al*., 1997a; *Krichak and Alpert*, 1998], associated with strong upper level divergence that favors midtropospheric ascent [*Dayan et al*., 2001; *Ziv et al*., 2005; *Tsvieli and Zangvil*, 2007].

[9] The origin of the moisture that is involved in ARSTs is debated as previous studies suggest various sources. Case studies indicate the Arabian Sea [*Krichak and Alpert*, 1998], west equatorial Africa [*Dayan et al*., 2001], and tropical Africa as the primary and the Red Sea as the secondary moisture source [*Ziv et al*., 2005]. *Tsvieli and Zangvil* [2005, 2007] suggest two acting moisture sources: equatorial Africa and/or the Indian Ocean through the southwesterly midtropospheric flow, and the EM by the west-northwesterly flow near the surface. *Krichak et al*. [2012] indicate transport of large moisture quantities from tropical Africa in the form of an atmospheric river.

[10] Southerly winds in the midtroposphere over the Levant are considered to be a key feature of the ARST since they are associated with an upper trough that reaches sufficiently far southward to initiate moisture transport of tropical origin [*Kahana et al*., 2004]. In addition, *Ziv et al*. [2005] found an intensified high at lower to middle levels over the AP for an ARST event in December 1993, causing persistent southerly winds and tropical moisture transport over the Red Sea. The present study will show that the role of the anticyclone over the AP, hereafter called the Arabian Anticyclone (AA) [after *Raziei et al*., 2012], is not restricted to the December 1993 event, but is very important for the ARST in general, as well as for the seasonal pace of the low-level circulation.

[11] In summary, the ARST has been associated with the following dynamical features: the RST, the AA, a transient midlatitude upper level trough, an intensified STJ, enhanced moisture transport, and upward motions resulting from tropospheric instability and the synoptic-scale dynamical forcing.

3. Data and Methods

3.1. Reanalysis and Precipitation Data

[12] The ARST dynamics are studied with the most recent European Centre for Medium-Range Weather Forecasts reanalysis data (ERA-Interim). The data set covers the period from 1979 and continues in near real time, and is produced with the Integrated Forecast System at a spectral resolution T255 and 60 model levels, reaching up to 0.1 hPa [*Dee et al*., 2011]. We utilize the monthly mean and 6 hourly analysis and forecasted variables at pressure and surface levels, as well as vertically integrated quantities derived from pressure levels.

[13] The Aphrodite precipitation data set (version V1101) and station observations are used to provide insight into the evolution and characteristics of the ARST associated rainfall. Aphrodite is a daily gridded data set based on rain gauge observations [*Yatagai et al*., 2012]. Version V1101 spans the period 1951 – 2007 at a resolution of 0.25° × 0.25° and covers the ME including the larger part of the AP. Station data over Israel are obtained from the Israel Meteorological Service archive.

3.2. Levant ARST Events

[14] Twelve ARST events (Table 1) that affected the Levant are analyzed, hereafter referred to as Levant ARST events. Their selection is motivated by one or more of the following reasons: (1) ARST events identified by the algorithm presented by *Krichak et al*. [2012], (2) empirical analysis by D. Edry (personal communication, 2011), and (3) ARST events investigated by previous case studies. Additional ARSTs (May 1982, November 1996 and 2003) are identified via ERA-Interim precipitation, showing events with northward progressing rainfall over the Red Sea region toward the Levant. All Levant ARST events are evaluated on the presence of the RST and upper trough (Figure 2), as well as significant observed precipitation (supporting information Figure S1 and Table 2, see section 4).

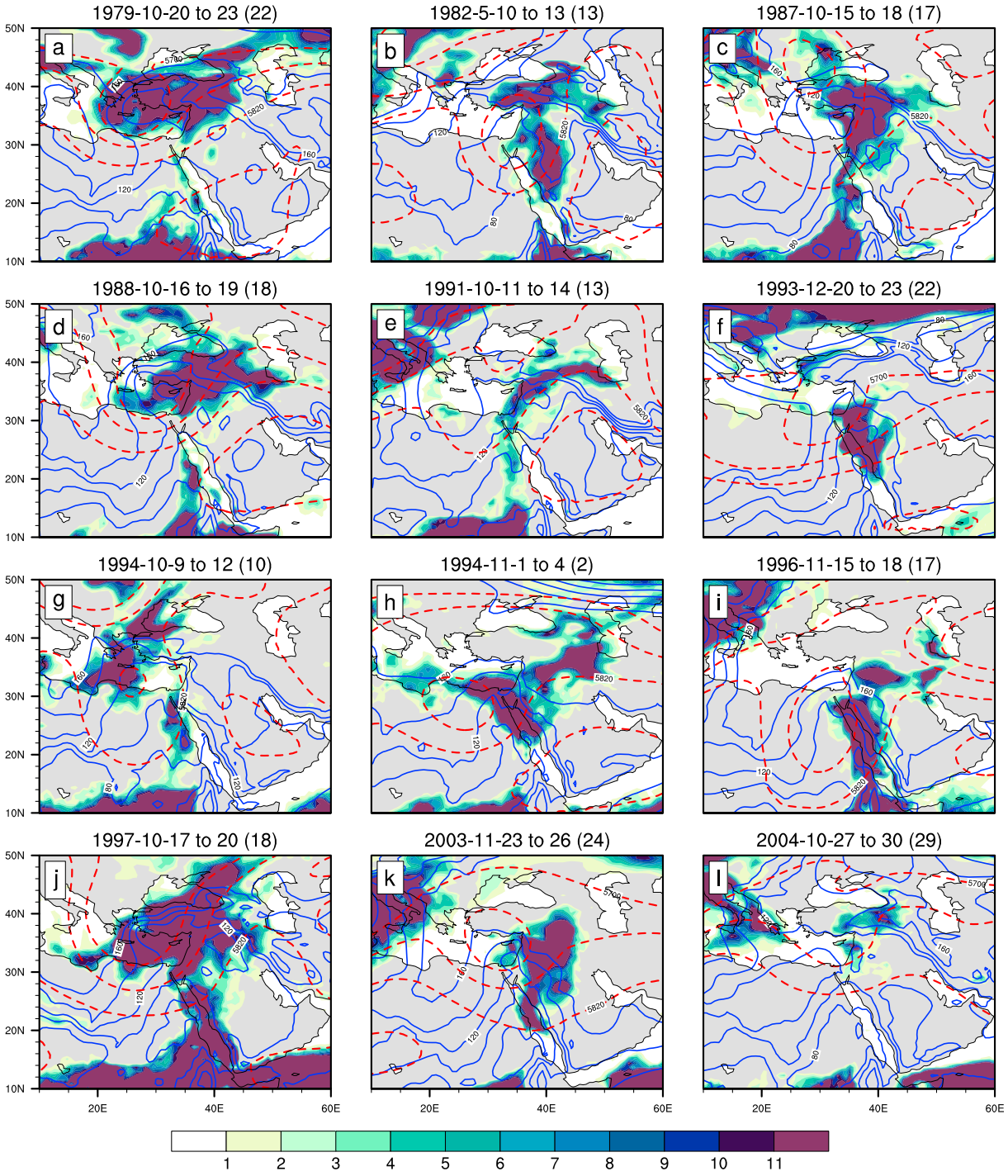

Figure 2. Precipitation (mm) from ERA-Interim, forecasted quantities (accumulated up to +12 h from 00 and 12 UTC), accumulated over the indicated days, for all Levant ARST events. The contour lines illustrate the daily averaged (00, 06, 12, and 18 UTC) geopotential height at 1000 hPa (solid blue lines, 80 to 160, 20 gpm intervals) and at 500 hPa (dashed red lines, 5700 to 5880, 60 gpm intervals) that represent the RST and midlatitude upper level trough, respectively, on the day with maximum rainfall, indicated between parentheses.

[15] For the October 1988, November 1996 and 2003 events, negligible rainfall amounts are observed over Israel (Table 2); however, the Aphrodite (and ERA-Interim) data show precipitation over the surrounding region, illustrating that these events should be considered as ARSTs. Moreover, flash floods occurred in Egypt during the October 1988 [*Cools et al.*, 2012] and November 1996 [*Moawad*, 2012] events, while an extraordinarily long rain spell (13–20 November 1996) affected the west coast of the AP with the most intense rainfall occurring from 16 to 18 November [*Almazroui*, 2012].

[16] The October 1979, 1988, and 1997 events deviate slightly from typical ARSTs. Whereas several ARST events

Table 2. Precipitation Observations[a]

					Accumulated Precipitation (mm) for Selected Levant ARST Events[b]											
Location	Lat	Lon	Elevation	Annual Mean[c] (mm)	Oct 1979	May 1982	Oct 1987	Oct 1988	Oct 1991	Dec 1993	Oct 1994	Nov 1994	Nov 1996	Oct 1997	Nov 2003	Oct 2004
	(°N)	(°E)	(m) ASL													
Beer-sheba	31:15	34:48	280	195	30	45	15	0	13	25	1	16	1	31	0	22
Beit Qama	31:26:44	34:45:37	250	302	9	0	2	0	0	4	0	27	1	14	0	0
Eilat	29:33:30	34:57:32	12	22	1	1	32	0	0	31	0	9	1	32	0	1
Hebron	31:32:00	35:05:42	1005	601	11	12	39	0	9	28	4	9	0	5	-	-
Jerusalem	31:46	35:13	810	537	19	0	23	2	3	13	11	10	5	16	1	5
Jericho	31:51	35:27	−260	150	14	0	61	1	1	0	17	8	5	31	1	-
Ma'ale-Efrayim	32:04:13	35:24:13	220	-	-	0	10	2	7	1	13	7	5	19	-	-
Mitzpe Ramon	30:37	34:47	837	69	70	17	7	0	12	17	22	19	4	6	0	6
Ovda	29:56:25	34:56:09	432	25	-	0	0	0	2	38	12	9	1	8	0	4
Sde Boker	30:52:08	34:47:33	475	93	2	0	0	0	15	14	10	13	2	4	0	4
Sedom	31:01	35:23	−390	41	3	0	2	0	1	37	0	9	2	2	0	8
Tirat Zvi	32:25:18	35:31:28	−220	270	9	18	0	1	4	0	4	21	6	8	0	0
Yotvata	29:53:44	35:03:36	75	28	0	0	36	0	1	7	7	6	1	3	0	3

[a]A dash means that no observational data are available.
[b]Station data are measured from 8 am to 8 am the next day, and are accumulated over the days as indicated in Table 1.
[c]Annual mean values are calculated over the period 1981–2010.

are associated with weak cyclogenesis to the east of the Levant, these events show closed isobars at surface levels over the EM Sea (supporting information Figures S11d, S21d, S51d, and S51g), indicating cyclogenesis to the northwest of the Levant, and therefore suggest resemblance of another phenomenon, the Cyprus Low (a midlatitude cyclone over the EM Sea) [*Alpert et al*., 2004a]. Accordingly, *Dayan et al*. [2001] describe the October 1997 event as the transformation from a convective storm into a midlatitude baroclinic system. Nevertheless, we include the three events to maintain consistency with previous literature, and because the three events exhibit all ARST dynamical characteristics and had major societal impacts (the October 1979 and 1997 events).

[17] The selection of Levant ARST events is assumed to be representative for identifying the key ARST dynamics. Note that we did not include all occurred ARSTs affecting the Levant during the period under consideration. Such an effort will be part of a quantitative climatological analysis in a subsequent study.

4. Precipitation

[18] Table 2 shows the observed precipitation at stations in Israel for all Levant ARST events. Rainfall affects the Levant for a time period from one to four consecutive days and maxima reach about 10 to 60 mm per day, with the exception of the October 1988, November 1996 and 2003 events (discussed earlier). ERA-Interim and Aphrodite data show that the precipitation during Levant ARST events evolves and progresses northward over the Red Sea, intensifies over the Levant, and eventually decays while moving in a northeasterly direction (Figure 3). In some cases, the precipitation intensifies at a later stage over the Taurus and Zagros mountains due to orographic effects. The intensity and spatial extent of the rainfall differs significantly between the events under consideration. Whereas several events (e.g., October 1979, 1987, 1997, November 1994, 1996, and December 1993) show widespread heavy rainfall over the Levant region for several days, other events (e.g., October 1994 and 2004) affect the region more locally and for shorter periods. However, this does not imply that local amounts are less intense. For example, *Shentsis et al*. [2012] mentions for the October 2004 event a historical maximum in peak discharge at a station in the Negev desert with a 100 year return period.

[19] For the Jeddah 2009 event, extremely high precipitation quantities are reported. Whereas annual averages are roughly 50 mm per year, 140 and 180 mm (accumulated over 24 to 26 November) were observed at two stations in Jeddah, while mesoscale model simulations show accumulated maxima exceeding 400 mm for the most severely affected parts in Jeddah [*Haggag and El-Badry*, 2013]. Rainfall during the Jeddah 2009 event is only shown for the ERA-Interim data (Figure 4) as the Aphrodite data set spans until 2007. The daily precipitation exhibits a maximum over the Red Sea coast near Jeddah on 25 November 2009 (up to ~25 mm day^{-1}) and, although strongly underestimating the amounts, clearly indicates the location and timing of heavy rainfall affecting Jeddah. Similar to the Levant ARST events, rainfall advances northeastward during the following days and decays afterward.

[20] The daily precipitation during the Levant ARST events shows a roughly similar temporal and spatial evolution in the Aphrodite and ERA-Interim data; see for example Figure 3. However, significant differences in spatial distribution and amounts are apparent between the data sets. For example, ERA-Interim shows for several events (e.g., October 1987, 1988, 1991, November 1994, 2003, and December 1993) more intense and widespread rainfall over the Levant region than Aphrodite. It is not clear if either ERA-Interim or Aphrodite is closer to reality. One should bear in mind that ERA-Interim precipitation is a forecasted quantity, limited by the model resolution and parameterizations, and therefore should be considered with caution. On the other hand, Aphrodite suffers from a relatively low station density over the region, in particular over Egypt, Jordan, and Syria (supporting information Figure S2). Moreover, extreme precipitation quantities are smoothed as a consequence of the interpolation from station to gridded data. A detailed discussion of the strengths and limitations of the precipitation data is beyond the scope of this study.

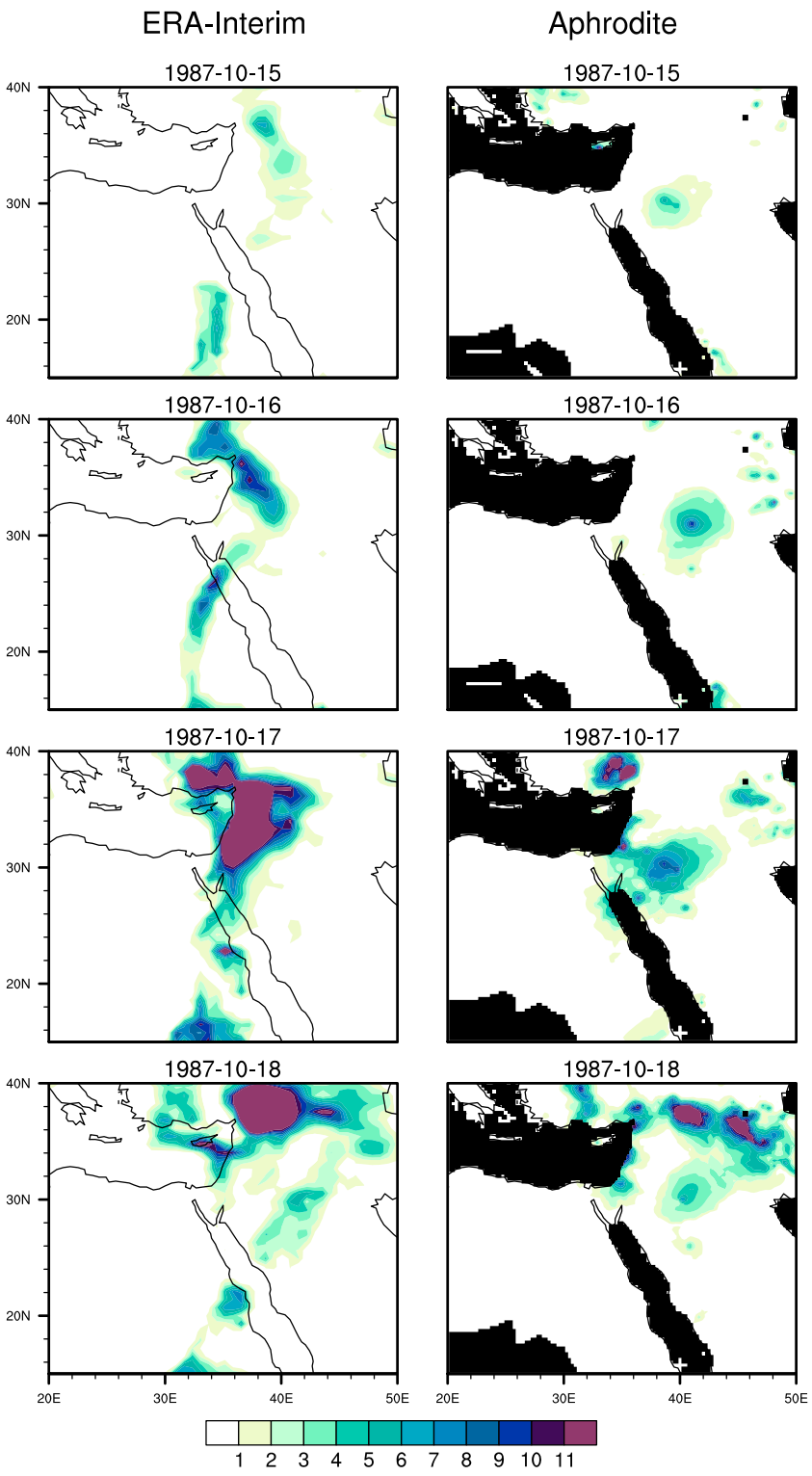

Figure 3. Daily precipitation (mm day^{-1}) from 15 to 18 October 1987 of (left) ERA-Interim, forecasted quantities (accumulated up to +12 h from 00 and 12 UTC), and (right) Aphrodite. Black colors indicate missing values in Aphrodite.

5. Dynamics of the Levant ARST Events

[21] The results described in section 5 are based on all 12 Levant ARST events. Minor differences in dynamics among the events are explicitly mentioned in the text. The ARST dynamics are illustrated by one typical event (October 1987) that has, despite its severe societal impacts (Table 1), not been the subject of previous work addressing

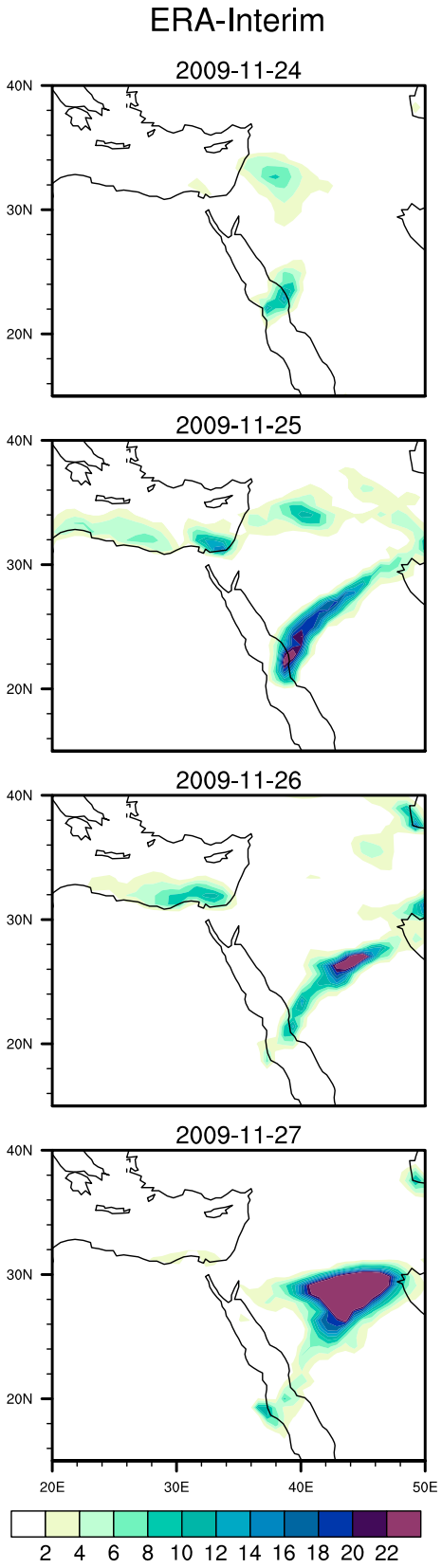

Figure 4. Daily precipitation (mm day^{-1}) from 24 to 27 November 2009 of ERA-Interim, forecasted quantities (accumulated up to +12 h from 00 and 12 UTC). Note the different color scales as compared to Figures 2 and 3.

the synoptic dynamics. Similar figures for all other Levant ARST events are included in the electronic supplement (supporting information Figures S10–S64).

5.1. Tropical and Subtropical Influences

[22] All Levant ARST events are associated with the presence of the RST at low altitudes and the AA at lower to middle tropospheric levels. The RST is positioned over northeast Africa and the Red Sea region, and is most pronounced at 1000 hPa (Figure 5a) and to a lesser degree at 850 hPa (Figure 5b), illustrating its shallow extent. During ARST occurrence the RST reaches over the Levant up to Turkey and retreats afterward (Figures 5d, 5e, 5g, and 5h). Some events are associated with closed isobars at lower levels to the east of the Levant during or after ARST occurrence, suggesting weak cyclogenesis (e.g., Figure 5g). The RST shows a strong diurnal variation, in agreement with *Tsvieli and Zangvil* [2005]. The 6 hourly data indicate lowest geopotential height values at 12 UTC, increasing at 18 and 00 UTC and reaching highest values at 6 UTC (not shown). The AA is positioned over the AP and demonstrates different structures with altitude. At low levels, a high pressure system stretches from the northeast over the AP (Figures 5b, 5e, and 5h). At higher levels, the AA has a more isolated and pronounced character with a closed circulation (Figures 5c, 5f, and 5i), and reaches up to midlevels as part of a ridge (Figures 6a, 6c, and 6e).

[23] Both the RST and AA have a strong semipermanent and quasi-stationary character. Hence, the question arises how the RST and AA behave during ARST events as compared to their mean state. Anomalies from the daily climatological mean (not shown) indicate that the RST extends northward prior to ARST occurrence [cf. *Dayan et al*., 2001; *Kahana et al*., 2002; *Tsvieli and Zangvil*, 2005; *Ziv et al*., 2005], and that the AA intensifies prior to ARST occurrence and weakens at a later stage during, or after the event. The northward extension of the RST and intensification of the AA result in enhanced pressure gradients, strong south-southeasterly winds, and moisture transport over the Red Sea region at lower levels.

5.2. Midlatitude Forcing

[24] Obviously, all Levant ARST events are accompanied by a midlatitude upper level trough penetrating into the subtropics (Figure 2). The upper level troughs are associated with cold air advection (not shown) and a strong cyclonic, southwesterly flow over the EM and Levant (Figure 6c). The upper troughs show various characteristics for the individual Levant ARSTs. Some events (October 1987, 1988, and 1994) demonstrate a pronounced trough over eastern Europe, extending southward over the EM and northeast Africa (Figure 6). Other events (May 1982, November 1994 and 1996) are characterized by a quasi-stationary cutoff over northeast Africa and the Levant, explaining for example the exceptionally long lasting period of precipitation affecting Jeddah during the November 1996 event [*Almazroui*, 2012]. Most events (October 1979, 1991, 1997, 2004, November 2003, and December 1993) go together with an eastward moving trough and/or cutoff over the EM and ME.

[25] The origin of the upper level troughs results for all ARST events from an amplified Rossby wave that imposes a trough over the EM and Levant with ridges at both flanks,

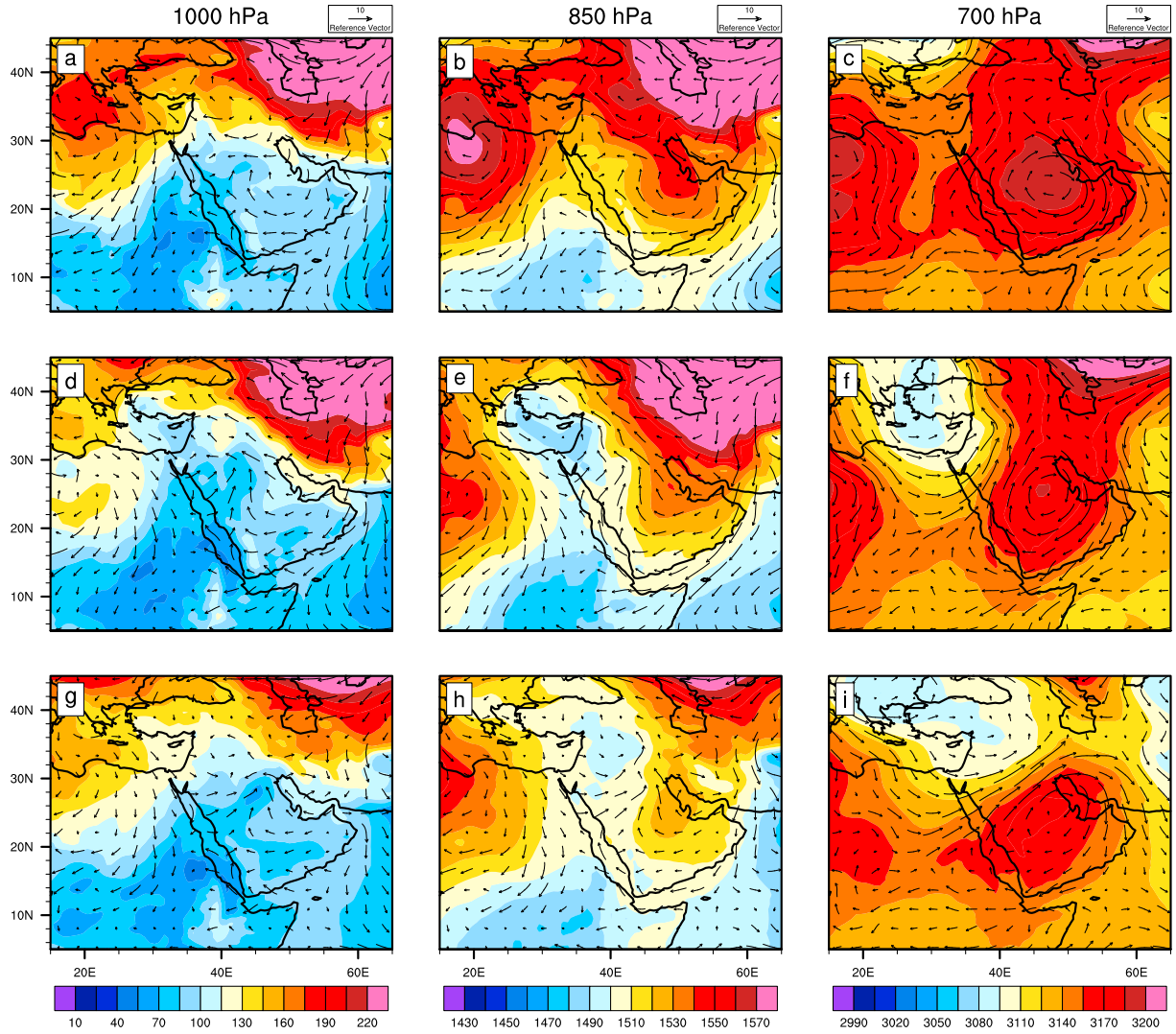

Figure 5. Geopotential height (gpm) and wind vectors (m s^{-1}) at (left) 1000 hPa, (middle) 850 hPa, and (right) 700 hPa at (a)–(c) 12 UTC, 15 October 1987, (d)–(f) 12 UTC, 17 October 1987, and (g)–(h) 12 UTC, 19 October 1987.

positioned over northwest Africa and the AP, respectively (Figures 6a, 6c, and 6e). Most events are associated with an amplification of a stationary wave, while a few events (November 2003 and December 1993) are characterized by an eastward propagating wave, which in both scenarios goes along with wave breaking and cutoff formation. For at least a majority of events (May 1982, October 1979, 1988, 1997, November 1994, 1996, and December 1993) the backward-tilting trough (southwest-northeast orientation) and the anticyclonic shear (increasing wind speed with latitude) indicate anticyclonic wave breaking (supporting information Figures S12, S17, S22, S32, S42, S47, and S52), following the LC1 baroclinic life cycle [*Thorncroft et al.*, 1993] which is characterized by a thinning trough that moves equatorward. Accordingly, wave amplification and breaking causes the intrusion of midlatitude upper level troughs into the subtropics that trigger ARSTs.

[26] For all Levant ARSTs, an intensified STJ is observed over northeast Africa and/or the AP. During several events (e.g., October 1987, 1997, November 1994, and December 1993), the STJ intensifies and approaches from the west over North Africa prior to ARST occurrence (Figure 6b), reaches over northeast Africa and/or the AP during ARST occurrence (Figure 6d), and ceases and/or moves eastward afterward (Figure 6f). For other events (e.g., May 1982, October 1988, 1991, 1994, and November 1996 and 2003), the STJ intensifies rather in situ over the region. During most events, the STJ streak develops to the southeast of the upper trough and follows its evolution in time and space over the region. Maxima in wind speed at 200 hPa range from 45 up to 65 m s^{-1}. ARST events during late autumn/early winter show relatively higher wind speeds compared to events in autumn, which reflects the seasonality of the STJ that pronounces toward winter. The intensification of the STJ was previously suggested to result from enhanced convection over the tropics [*Krichak and Alpert*, 1998], indicating an intensified local Hadley Cell overturning. However, visual inspection of upper levels (200 hPa) reveals only for the October 1979, 1987 and November 1996 events substantial poleward outflow from the tropics. In fact, more events

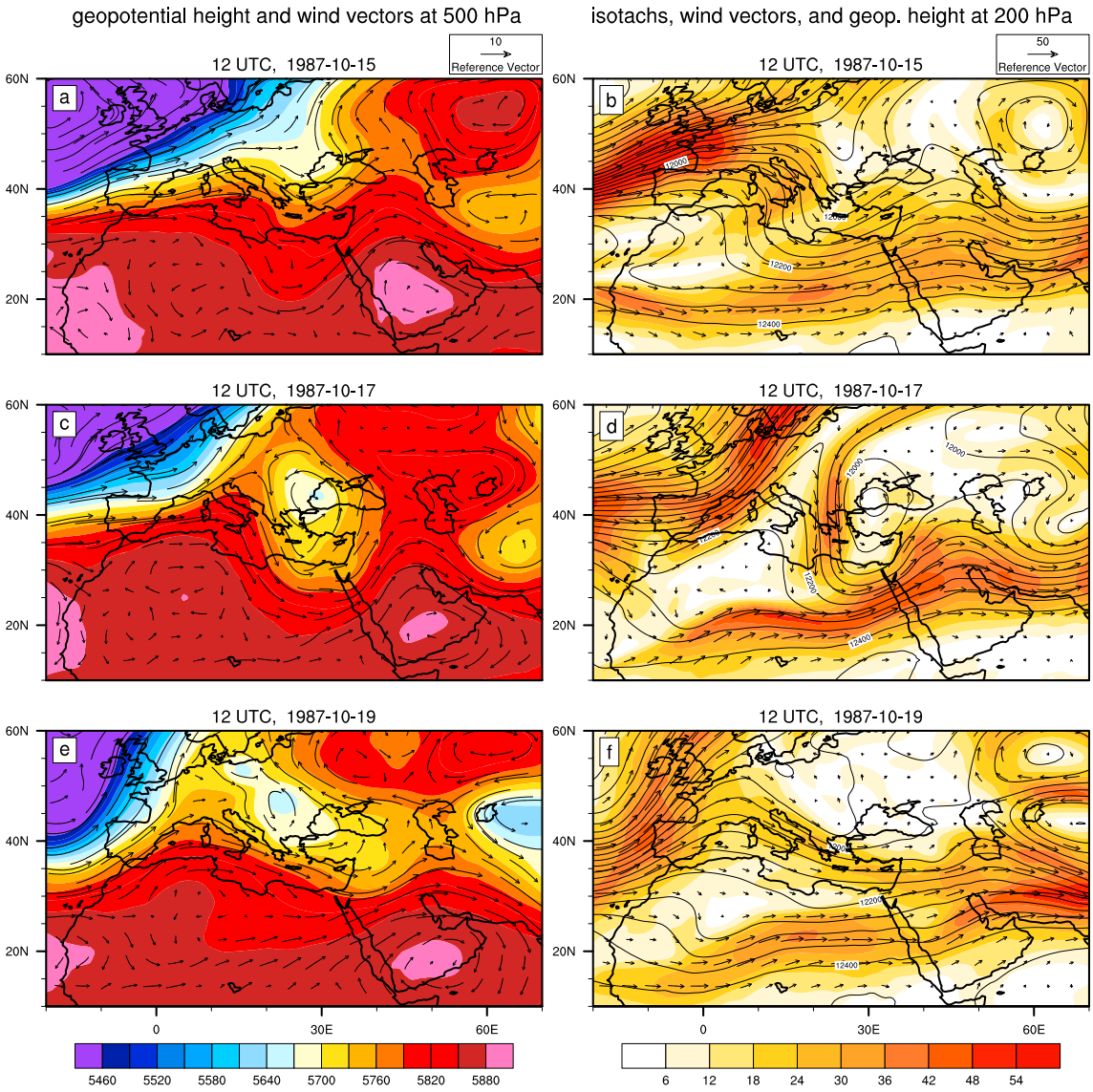

Figure 6. (left) Geopotential height (gpm) and wind vectors ($m\,s^{-1}$) at 500 hPa and (right) wind speed ($m\,s^{-1}$, shaded), wind direction (vectors) and geopotential height contours (50 gpm interval) at 200 hPa at (a, b) 12 UTC, 15 October 1987, (c, d) 12 UTC, 17 October 1987, and (e, f) 12 UTC, 19 October 1987.

(October 1979, 1987, 1994, 1997, November 1994, and December 1993) show a branch of the polar jet, which curves around the western flank of the upper trough and confluences with the STJ (e.g., Figure 6d). Cold upper air advection from the midlatitudes enhances the meridional temperature gradient, implying a thermally driven intensification of the STJ [cf. *Dayan et al*., 2001].

5.3. Moisture Dynamics

[27] To investigate moisture dynamics, we analyze the vertically integrated moisture quantities, i.e., total column water (TCW), and vertically integrated water vapor fluxes (VIWVFs). During ARST events, large amounts of TCW (with maxima of 27 up to 39 $kg\,m^{-2}$) advance northward over northeast Africa and the Red Sea region toward the Levant, perhaps suggesting central equatorial Africa as dominant moisture source (Figure 7a). However, the VIWVFs reveal pronounced moisture transport from the Arabian and Red Seas curving anticyclonically around the AP (Figure 7b). Figure 8 shows that this moisture transport pathway not only characterizes the October 1987 event, but in fact all Levant ARST events. In addition, several events also show weak westerly moisture transport over the EM (Figures 8a, 8c, 8d, 8f, 8j, and 8l).

[28] The moisture transport involves a complex picture due to its variability in the vertical direction and in time. Hence, we analyze in more detail the VIWVFs over three layers (Figures 7c–e) as well as its temporal evolution (Figures 7f–h). At low altitudes (~1000 to ~875 hPa), VIWVFs intensify over the Arabian and Red Seas prior to ARST occurrence (Figures 7c, 7f, and 7g), while for several ARSTs (October 1979, 1987, 1988, 1997, 2004 and December 1993) shortly prior to and during ARST occurrence, also weak west-northwesterly VIWVFs evolve over the Mediterranean Sea (Figures 7c and h). At higher levels (~850 to ~700 hPa), southerly VIWVFs over the Red Sea

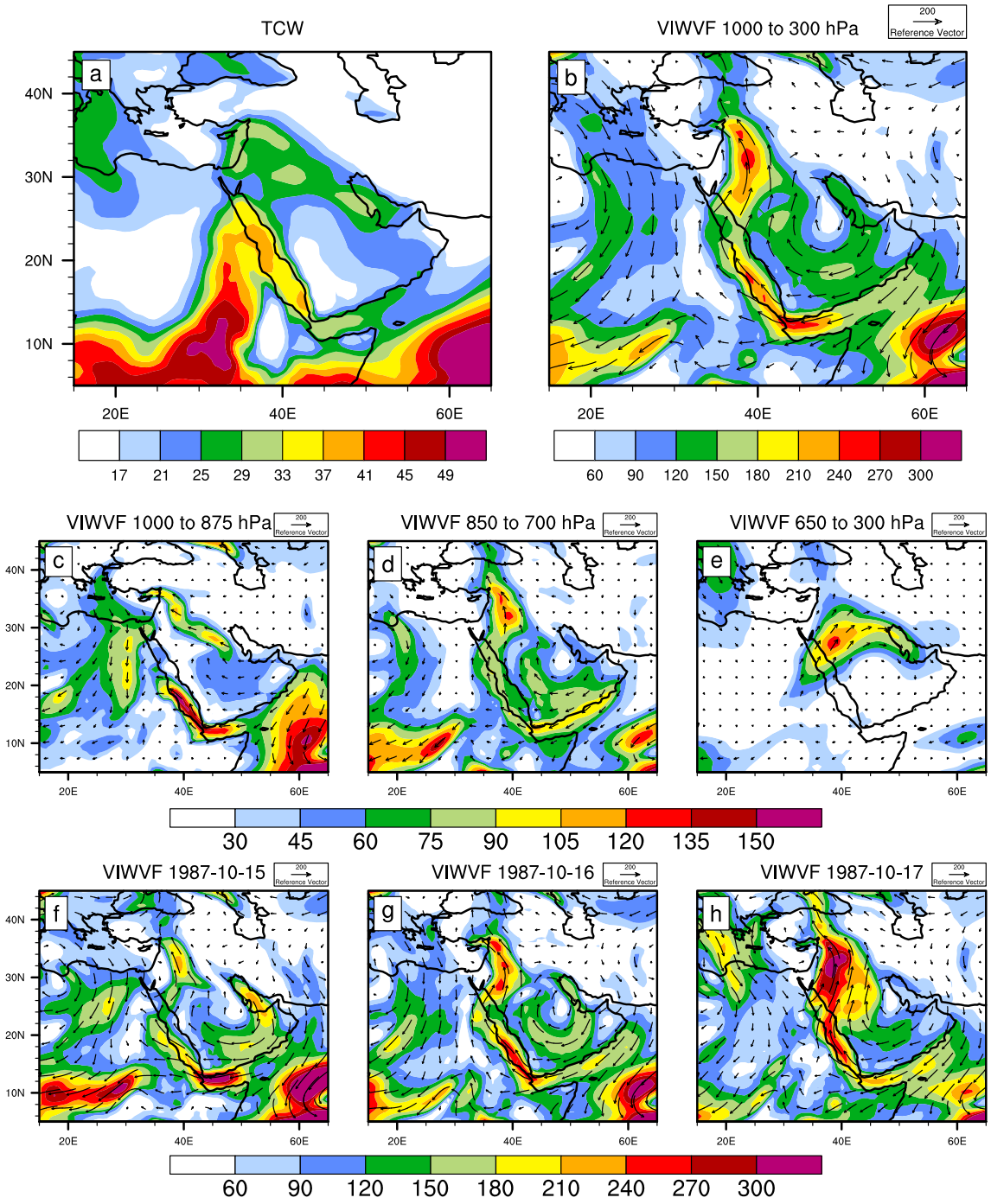

Figure 7. (a) TCW (kg m^{-2}) and the VIWVFs (kg m^{-1} s^{-1}) magnitude (shaded) and direction (vectors) over (b) 1000 to 300 hPa, (c) 1000 to 875 hPa, (d) 850 to 700 hPa, and (e) 650 to 300 hPa, averaged over 15–17 October 1987. The lower panels show the daily averaged VIWVFs (1000 to 300 hPa) over (f) 15, (g) 16, and (h) 17 October 1987. Note the different color scales.

region are present (Figure 7d), while at middle to upper levels (~650 to ~300 hPa), during ARST occurrence, pronounced south-southwesterly VIWVFs are observed over the Levant (Figures 7e and 7h). In addition, several ARST events show minor moisture transport at low levels from central Africa (October 1991), and at middle to upper levels from West Africa (October 1997 and December 1993) and central Africa (October 1979, 1988, 1991 and November 1996).

[29] The evolution of VIWVFs during the Levant ARST events reveals that the moisture originates predominantly from the Arabian and Red Seas. The persistent anticyclonic flow around the AP and the developing cyclonic flow over the EM, associated with the AA and upper trough, respectively, transport the gradually ascending moisture northward to the Levant. This corroborates that the Red Sea serves as a corridor (and supplier) for moisture transport as suggested by *Krichak et al*. [2000] and *Dayan and Morin*

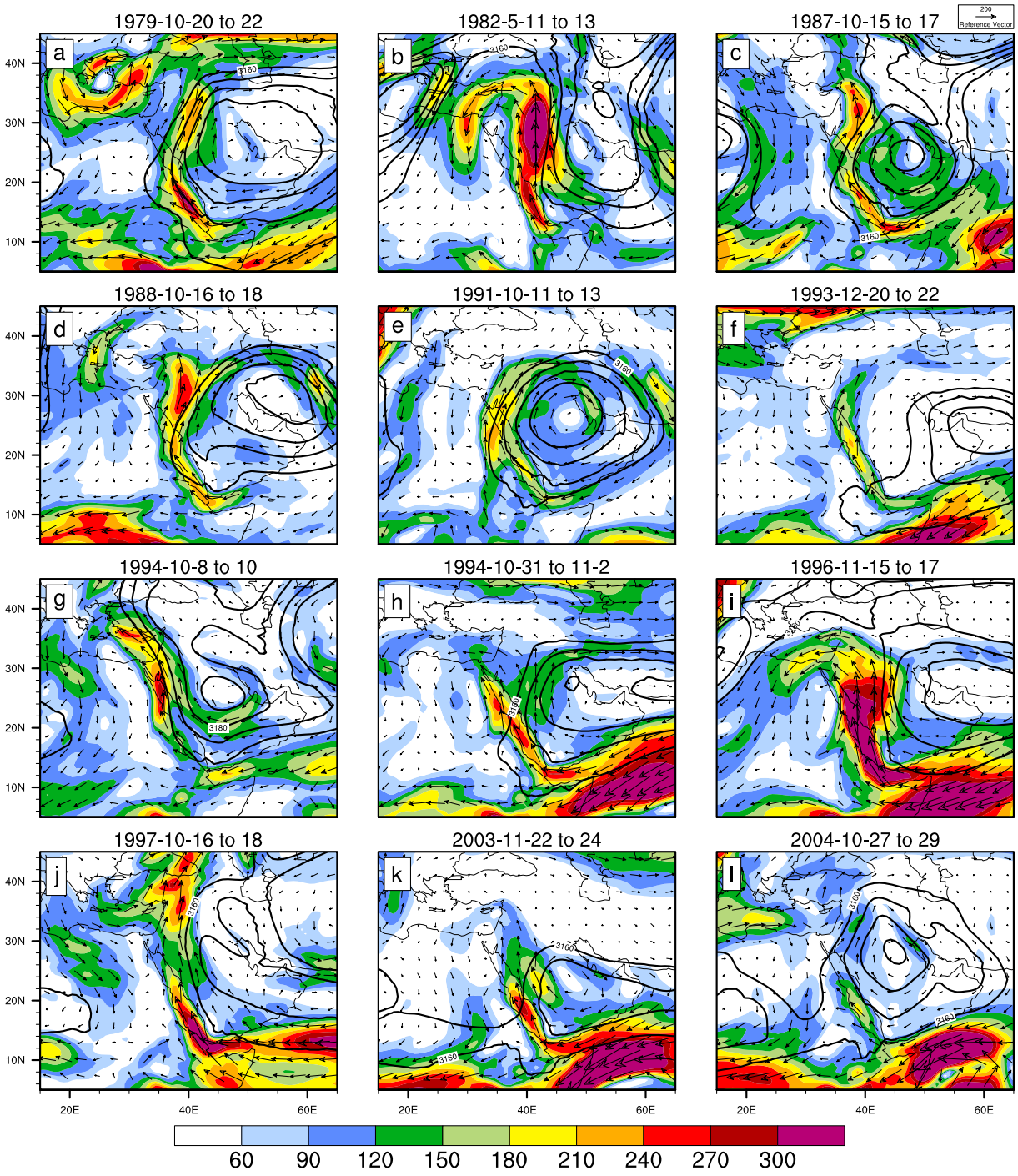

Figure 8. The VIWVFs (kg m^{-1} s^{-1}) magnitude (shaded) and direction (vectors) over 1000 to 300 hPa and superimposed the geopotential height contours at 700 hPa (3160 to 3190, 10 gpm interval) for all Levant ARST events, averaged over the day with maximum rainfall and the two preceding days. See for the geopotential height at 850 hPa overlaid supporting information Figure S3.

[2006]. Also, relatively weak moisture quantities from the Mediterranean Sea are advected in the developing cyclonic flow over the EM during several events. Most remarkably, the contribution of moisture from tropical/equatorial Africa that was observed for some events appears negligible in view of the total VIWVF quantities. Hence, our results contrast considerably with several previous ARST studies that address moisture dynamics. This emphasizes the necessity to include not only moisture quantities, but also moisture fluxes in the analysis to reveal the sources and pathways of moist air masses. Also, it appears important to take into account the vertical moisture distribution, since single levels may not be representative of the total moisture transport throughout the troposphere. Finally, relatively coarse

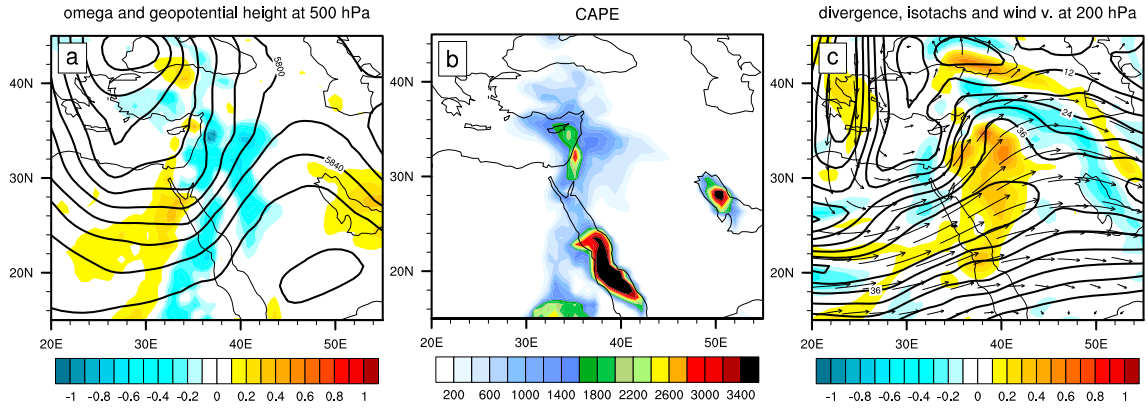

Figure 9. (a) Omega (Pa s^{-1}, blue colors denote ascent) and the geopotential height (20 gpm interval) at 500 hPa at 12 UTC, 17 October 1987, (b) CAPE (J kg^{-1}), +12 h forecast at 00 UTC, 17 October 1987, and (c) the divergence (in 10^{-4} s^{-1}, shaded), wind direction (vectors), and isotachs (contours, 6 m s^{-1} interval) at 12 UTC, 17 October 1987.

data sets may underestimate the moisture contribution from small and poorly resolved water bodies like the Red Sea.

5.4. Upward Motions and Precipitation Generation

[30] All Levant ARST events are associated with strong midtropospheric ascent (Figure 9a), varying from −0.6 up to −2 Pa s^{-1} at 500 hPa. The combination of advected moisture, low-level warm air, and upper level cold air causes tropospheric instability, illustrated by high convective available potential energy (CAPE) values over the Levant (Figure 9b) that vary from about 500 to more than 3400 J kg^{-1}, depending on the event. Not surprisingly, events during midautumn show higher CAPE values compared to events in late autumn and early winter. Note that the high CAPE values over the warm Red Sea waters in Figure 9b are common, whereas occasionally high CAPE values over land indicate severe weather.

[31] Strong upper level divergence is observed, mostly near the left exit region of the STJ streak (Figure 9c), which implies midtropospheric ascent based on continuity principles [*Stull*, 2000, chapter 13]. During ARST occurrence, the upper level divergence center is positioned over the Levant and reaches maxima of about 0.4×10^{-4} up to 1×10^{-4} s^{-1}. Also, the upper level positive vorticity advection and low-level warm air advection (not shown) imply quasi-geostrophic forced ascent [*Holton*, 2004, chapter 6]. Finally, orographic effects play an important role in the precipitation generation [*Dayan et al.*, 2001], though this aspect is not discussed for the Levant ARST events in this study.

6. Jeddah 2009 Event as an ARST

6.1. Dynamics of the Jeddah Event in November 2009

[32] Next we analyze the dynamics during the Jeddah 2009 event and compare them to those of the Levant ARSTs. We find a narrowly shaped and meridionally elongated RST over the Red Sea region near the surface and the AA over the AP at lower to middle levels (Figures 10a, 10b, and 10c). The RST extends northward prior to and during the Jeddah flooding and retreats afterward (Figures 10a, 10d, and 10g), while the AA slightly intensifies prior to the Jeddah flooding and weakens afterward (Figures 10b, 10c, 10e, 10f, 10h, and 10i). Furthermore, at upper levels, wave breaking occurs over northwest Africa on 20 November 2009, resulting in a cutoff low that moves eastward over North Africa during subsequent days (Figure 11a). During the Jeddah flooding (the 25th), the cutoff merges with a trough, positioned over the EM and Levant, with ridges at both flanks (Figure 11c). After the Jeddah flooding (the 26th/27th), another (anticyclonic) wave breaking event occurs over the EM and Levant, leading to a next pronounced cutoff low (Figure 11e). The STJ intensifies over northeast Africa prior to and during the Jeddah flooding (Figures 11b and 11d), and stretches over the AP during the subsequent days, while intensifying further (Figure 11f). The wind speed at 200 hPa reaches maxima of ~55 m s^{-1} on the 25th and ~75 m s^{-1} on the 27th. As for most of the Levant ARST events, a southward branch of the polar jet merges with the STJ and forces advection of upper level cold air (Figure 11d). High TCW quantities from central Africa reach northward over the Red Sea region (Figure 12a), again suggesting central Africa as a moisture source. However, Figure 12b corroborates that, similar to the Levant ARST events, the moisture originates predominantly from the Arabian and Red Seas, and to a lesser extent from the Mediterranean Sea, and is transported by the persistent anticyclonic flow around the AP and the evolving cyclonic flow over the EM. Closer inspection of the VIWVFs over distinct layers and its temporal evolution reveals that the moisture from the adjacent seas gradually ascents and converges over the Jeddah region during the flooding (Figures 12c–h). In addition, at midlevels, moisture is transported from central Africa (Figure 12e) although the amounts are negligible in view of the total vertically integrated quantities.

[33] During the Jeddah 2009 event, the upper trough and STJ are positioned somewhat more southerly compared to the Levant ARST events. In addition, the AA shows a closed structure over the southeastern part of the AP, whereas during the Levant ARST events, the AA (at 850 hPa) stretches northward over the entire AP (cf. Figures 10e and 5e). Thus, the configuration of the AA and upper trough explain why the moist airflow converges over the Jeddah region and intrudes into the AP, whereas during the Levant ARST

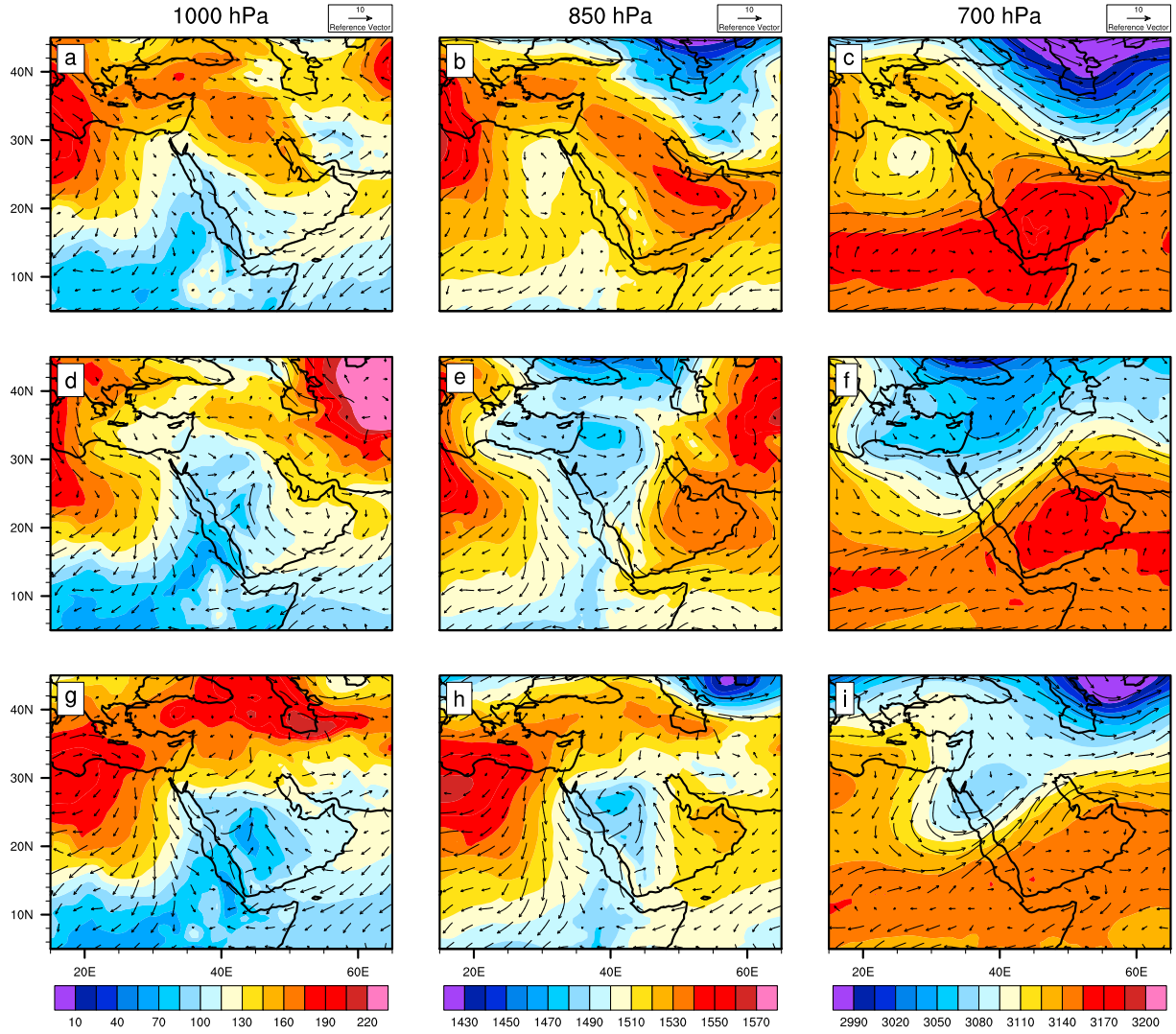

Figure 10. As Figure 5 for the Jeddah event at (a)–(c) 12 UTC, 23 November 2009, (d)–(f) 12 UTC, 25 November 2009, and (g)–(i) 12 UTC, 27 November 2009.

events, the moist air masses propagate farther northward across the Red Sea (cf. Figures 12b, 12h, 7b, and 7h).

[34] During the Jeddah 2009 event, high CAPE values ($>3400\,\mathrm{J\,kg^{-1}}$) are observed over the Red Sea coast nearby Jeddah (Figure 13b). The upper level divergence over the Jeddah region, ahead of the STJ streak, is relatively weak (Figure 13c). Apparently, the upward motions (Figure 13a) and severe weather on the 25th over the Jeddah region result predominantly from the tropospheric instability and to a lesser degree from the synoptic-scale forcing. Accordingly, *Haggag and El-Badry* [2013] refer to a quasi-stationary mesoscale convective system. In this respect, the Jeddah 2009 event is similar to the ARST, considering the suggestion by *Dayan and Morin* [2006] that the convective ascent resulting from tropospheric instability dominates the synoptic-scale forced ascent. During the subsequent days after the Jeddah flooding, the tropospheric instability weakens, while the upper level divergence and related large-scale ascent significantly increase over the central part of the AP (Figures 13d–13f), demonstrating strong cyclogenesis. This evolution of initially strong convective activity (developing into mesoscale convective systems), which at a later stage organizes into large-scale ascent (suggesting cyclogenesis), is mentioned in several ARST case studies [*Krichak et al.*, 2000; *Dayan et al.*, 2001; *Ziv et al.*, 2005]. Accordingly, the December 1993 and November 1994 events show initially high CAPE values, while the upper level divergence at a later stage gradually becomes dominant. Nevertheless, this evolution could not clearly be distinguished during most other Levant ARST events.

6.2. Geographical Extent of the ARST and Jeddah

[35] *Haggag and El-Badry* [2013] report several important synoptic-scale dynamical aspects that caused the Jeddah 2009 event. First, an eastward migrating Mediterranean cyclone joins an extension of the Sudan low-pressure zone (i.e., the RST), second, a stationary anticyclone over the southeastern AP (i.e., the AA) and associated clockwise flow provide moisture from the Arabian and Red Seas, and third, upper level tropospheric instability and associated deep moist convection result in a quasi-stationary mesoscale convective system and heavy rainfall over Jeddah. Our

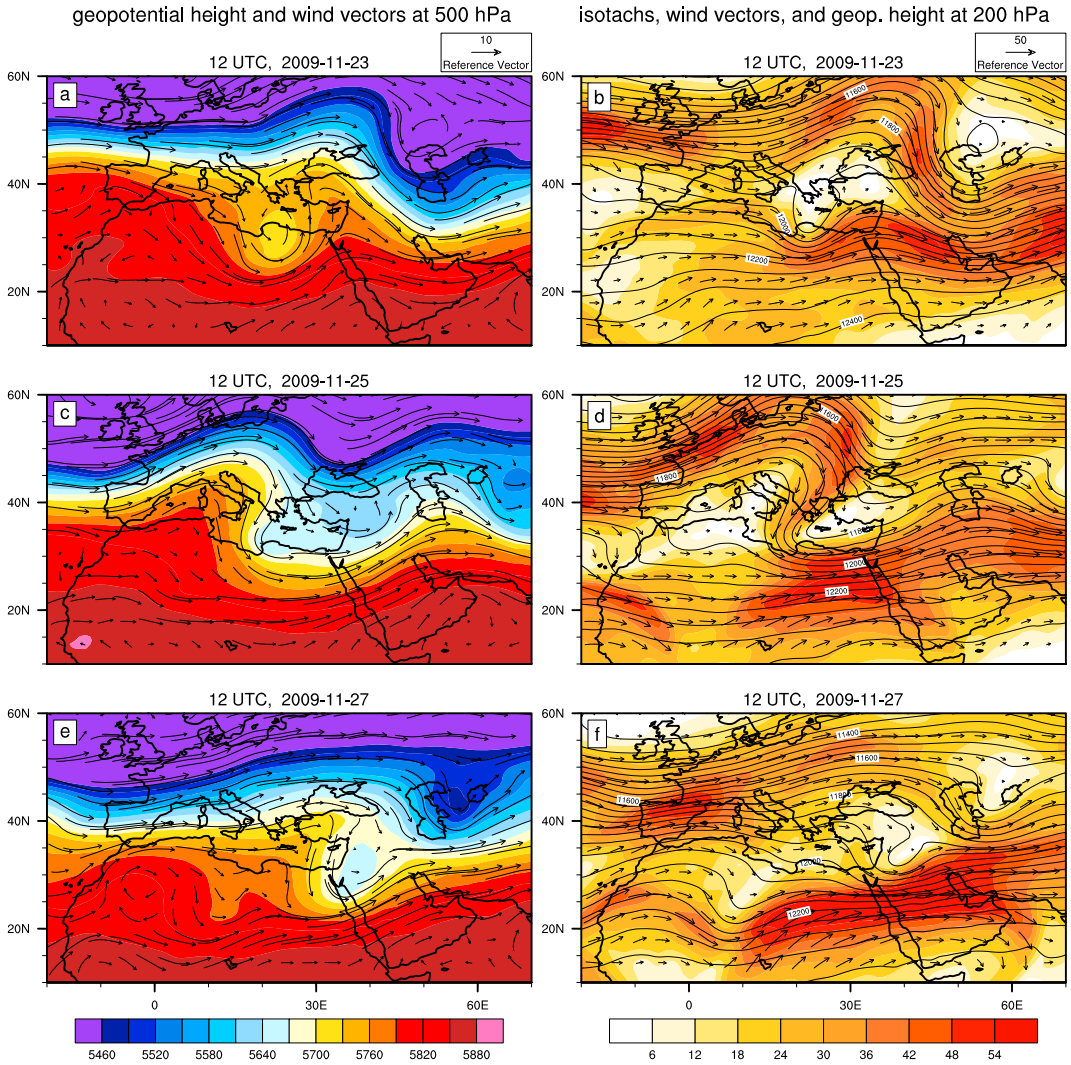

Figure 11. As Figure 6 for the Jeddah event at (a, b) 12 UTC, 23 November 2009, (c, d) 12 UTC, 25 November 2009, and (e, f) 12 UTC, 27 November 2009.

results are fully in agreement and include the role of the STJ and large-scale ascent. Moreover, we explain the Jeddah 2009 event in terms of the ARST phenomenon and conclude that the associated dynamics and evolution are identical to those observed for the Levant ARST events. This reveals that the Jeddah 2009 event was in fact an ARST. Apparently, the ARST affects not only the Levant, but also the larger part of the AP, introducing a significant geographical extension of the phenomenon.

[36] Importantly, the Jeddah flooding on 25 November 2009, being a result of an ARST, is not an isolated case. For example, heavy rainfall affected Jeddah on 8 January 1999 [*Almazroui*, 2011], while more recently flash floods struck Jeddah in December 2010 and caused four casualties [*Haggag and El-Badry*, 2013]. Based on exploration of the synoptic conditions (not shown), we identify these events as ARSTs. Furthermore, the Levant ARST event in November 1996 also affected Jeddah with large precipitation amounts [*Almazroui*, 2012]. This illustrates that the Jeddah region has been affected more often by extreme precipitation and resulting flash floods as a consequence of ARSTs. The orography in the region is characterized by steep slopes along the eastern Red Sea coast. Nearby Jeddah, the mountain range is interrupted by a pass that forms a corridor to Makkah with the Hejaz mountains to the north and the Asir mountains to the south. Hence, the local orography promotes channeling of the moist airflow from the Red Sea over the Jeddah region into the AP and potentially makes this region extraordinarily favorable for extreme precipitation and flash floods.

7. Seasonality of the ARST

7.1. Large-Scale Circulation

[37] *Dayan et al.* [2001] explain the occurrence of ARSTs in autumn by favorable latitudinal positions of the STJ and the African Monsoon, i.e., the local Inter Tropical Convergence Zone (ITCZ). In spring, the STJ and ITCZ reach a similarly favorable setting. In winter, the ITCZ is positioned farther south from the ME, while in summer, the baroclinic zone is positioned farther north from the ME, making intrusions of tropical moist air masses and

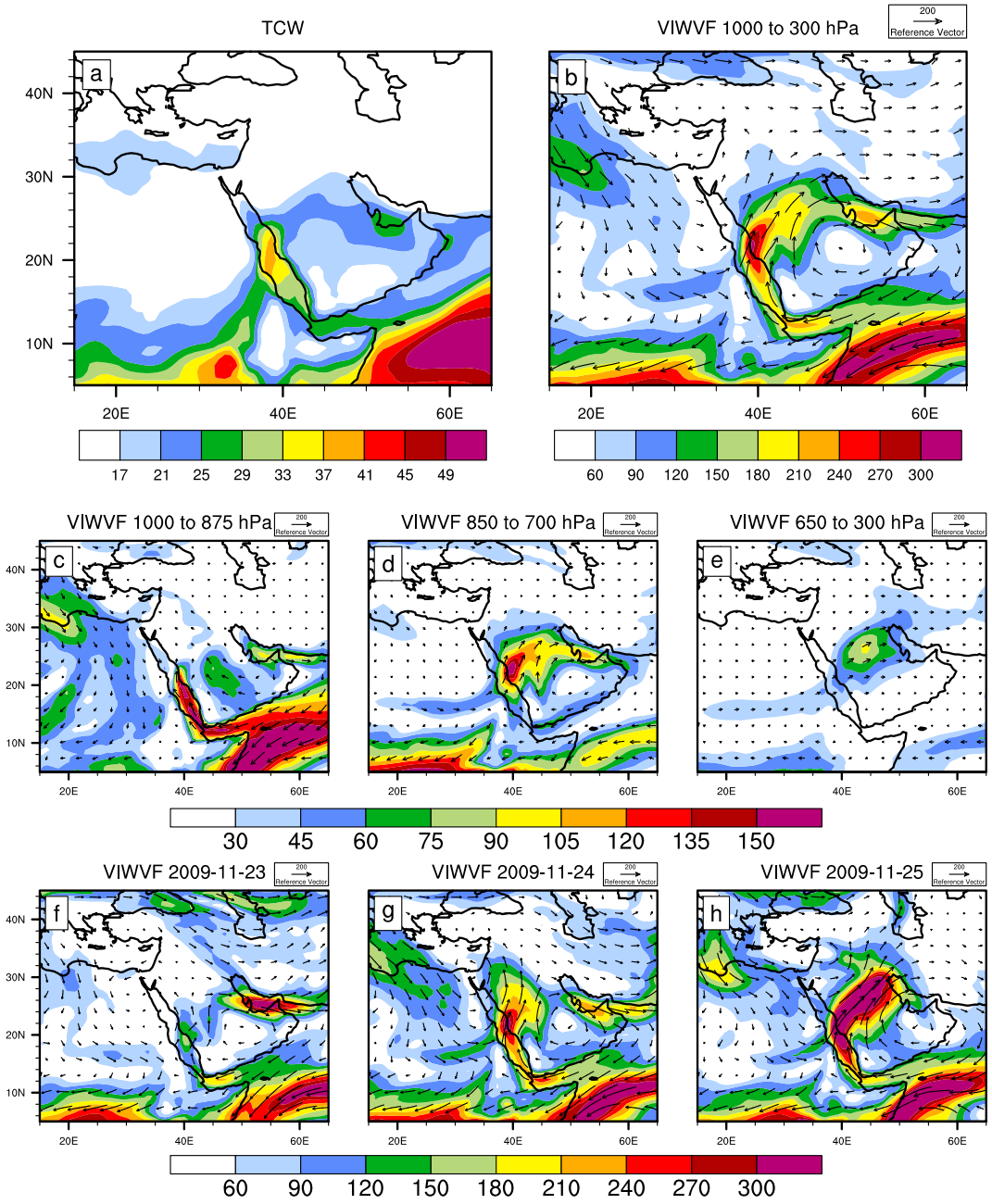

Figure 12. As Figure 7 for the Jeddah event, averaged over (a)–(e) 23–25, (f) 23, (g) 24, and (h) 25 November 2009.

midlatitude upper level troughs in the ME, respectively, less likely. Moreover, in summer, convective ascent over the ME is inhibited because strong subsidence prevails at middle and upper levels over the ME and EM under the influence of the South Asian monsoon [*Rodwell and Hoskins*, 1996; *Ziv et al.*, 2004; *Tyrlis et al.*, 2013], the local Hadley Cell circulation associated with the African Monsoon [*Ziv et al.*, 2004], and the heat driven circulation over the Zagros mountains [*Zaitchik et al.*, 2007]. Hence, ARSTs are suppressed in summer. Thus, the seasonal variability of the large-scale circulation suggests ARST favorable conditions during autumn and spring, limited potential in winter, whereas ARSTs are unlikely in summer.

7.2. Origin and Seasonality of the RST and AA

[38] In summer, a chain of subtropical anticyclones at midlevels dominates over northwest Africa, the AP, and Iran [*Galarneau et al.*, 2008; *Zarrin et al.*, 2010]. When the Hadley Cell circulation migrates southward in autumn, the associated subtropical anticyclonic ridge divides into two subtropical anticyclones over the AP (i.e., the AA) and northwest Africa, respectively. In between, a surface trough extends from the ITCZ, reaching over northeast Africa and the Red Sea region; that is, the RST. The RST and AA are to a greater or lesser extent always present in the daily synoptics during autumn, winter, and spring. In other words, the RST and AA have a strong semipermanent

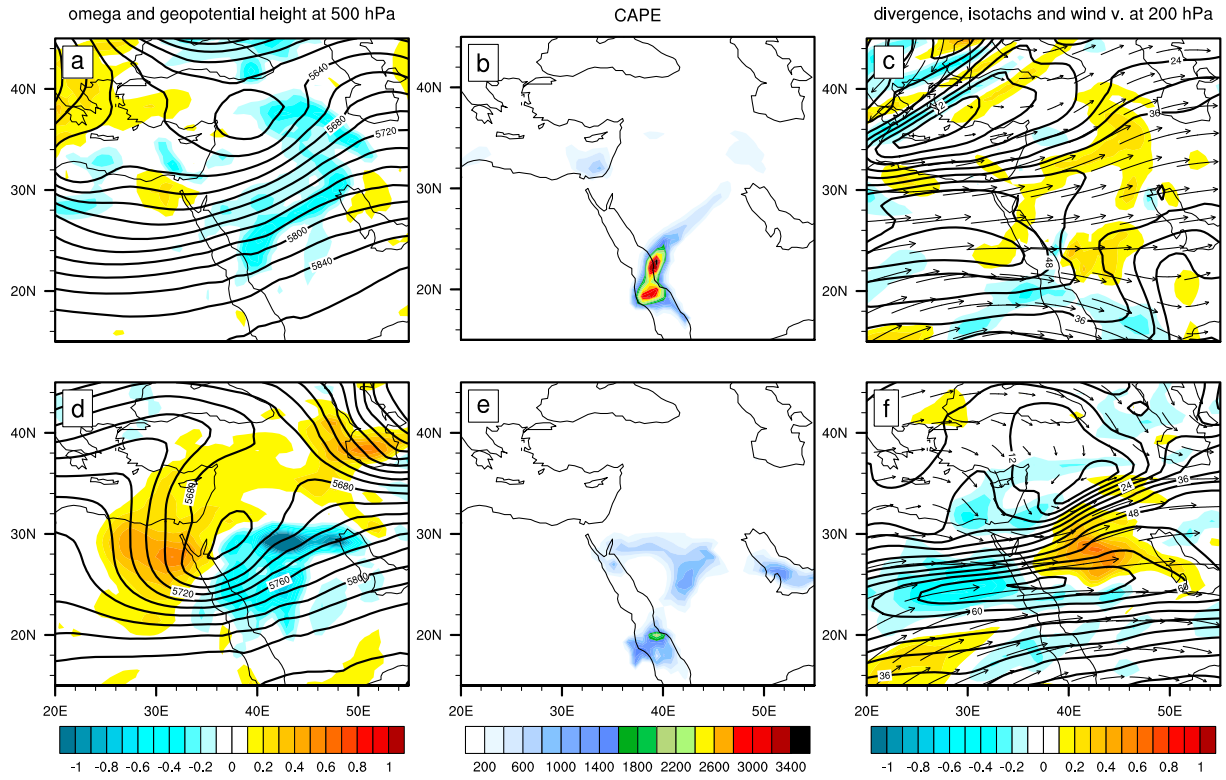

Figure 13. As Figure 9 for the Jeddah event at (a)–(c) 12 UTC, 25 November 2009 and (d)–(f) 12 UTC, 27 November 2009.

quasi-stationary character and leave signatures in the mean low-level circulation during these seasons. Figures 14a–14f and 14j–14l show the climatology of the RST and AA for January, April, and November (see for the monthly means of all months supporting information Figures S4–S7).

[39] The RST and AA reach their northernmost position in late autumn (October and November) and spring (April and May), attain their southernmost position in winter (January and February), and are absent in summer (June until September). In addition, the AA is also visible at midlevels (500 hPa) in October and May (supporting information Figures S7e and S7j), consistent with its transformation from an isolated anticyclone near the surface in winter to a subtropical anticyclonic ridge at midlevels in summer. In essence, the vertical and horizontal extent, as well as the latitudinal position of the AA, follows the solar inclination and, more specifically, the intensity of the surface sensible heating over the AP [after *Wu et al.*, 2011, 2012] and the descending branch of the Hadley Cell. The monthly means suggest that the RST during early winter (December and January) is in fact not less frequent [*Alpert et al.*, 2004b; *Tsvieli and Zangvil*, 2005; *Krichak et al.*, 2012], but is positioned more southerly and therefore affects Israel less frequently. During summer months (June until September), when potentially reaching its northernmost position, the RST is fully absorbed by the Persian Trough, a thermal low-level trough developing from the east under the influence of the South Asian monsoon [e.g., *Bitan and Saaroni*, 1992; *Alpert et al.*, 2004a, 2004b; *Tyrlis et al.*, 2013], see Figures 14g and 14h. Apparently, the influence of the South Asian monsoon does not only inhibit ARSTs in summer via the imposed subsidence at middle and upper levels over the ME, but also by dominating the atmospheric circulation at lower altitudes.

[40] The RST and AA show an asymmetric seasonal evolution. The RST and AA (at ~850 hPa) are most pronounced in late autumn and early winter (October until January) and weaker in late winter and spring (February until April). The AA at higher levels (~700 hPa) is most pronounced in autumn (October and November) and spring (April and May), and weakest in winter (January and February). Furthermore, at lower levels (~850 hPa), the AA remains at its southerly position over the southeastern AP and Arabian Sea in spring (February until April), and disappears afterward (May). It appears that the South Asian winter monsoon northeasterly wind over the Arabian Sea reinforces the anticyclonic flow around the AP from autumn until early spring (e.g., Figures 14b and 14k), while in late spring (May), oppositely directed wind, associated with the onset of the South Asian summer monsoon, counteracts the anticyclonic flow. In combination with increasing surface sensible heating over the AP, this may lead to the disappearance of the AA at lower levels during spring. The less pronounced RST in spring compared to autumn (in terms of pressure gradients) is obvious since spring is rather characterized by the Sharav cyclone [*Alpert et al.*, 2004a, 2004b] and suggests at the same time a relation to the less pronounced AA at low levels.

[41] In summary, the RST and AA (at ~700 hPa) reach their most northerly position in autumn (October and November) and spring (April and May), while the RST and AA (at ~850 hPa) are most pronounced in autumn and early winter (October until January). Thus, the seasonal pace of

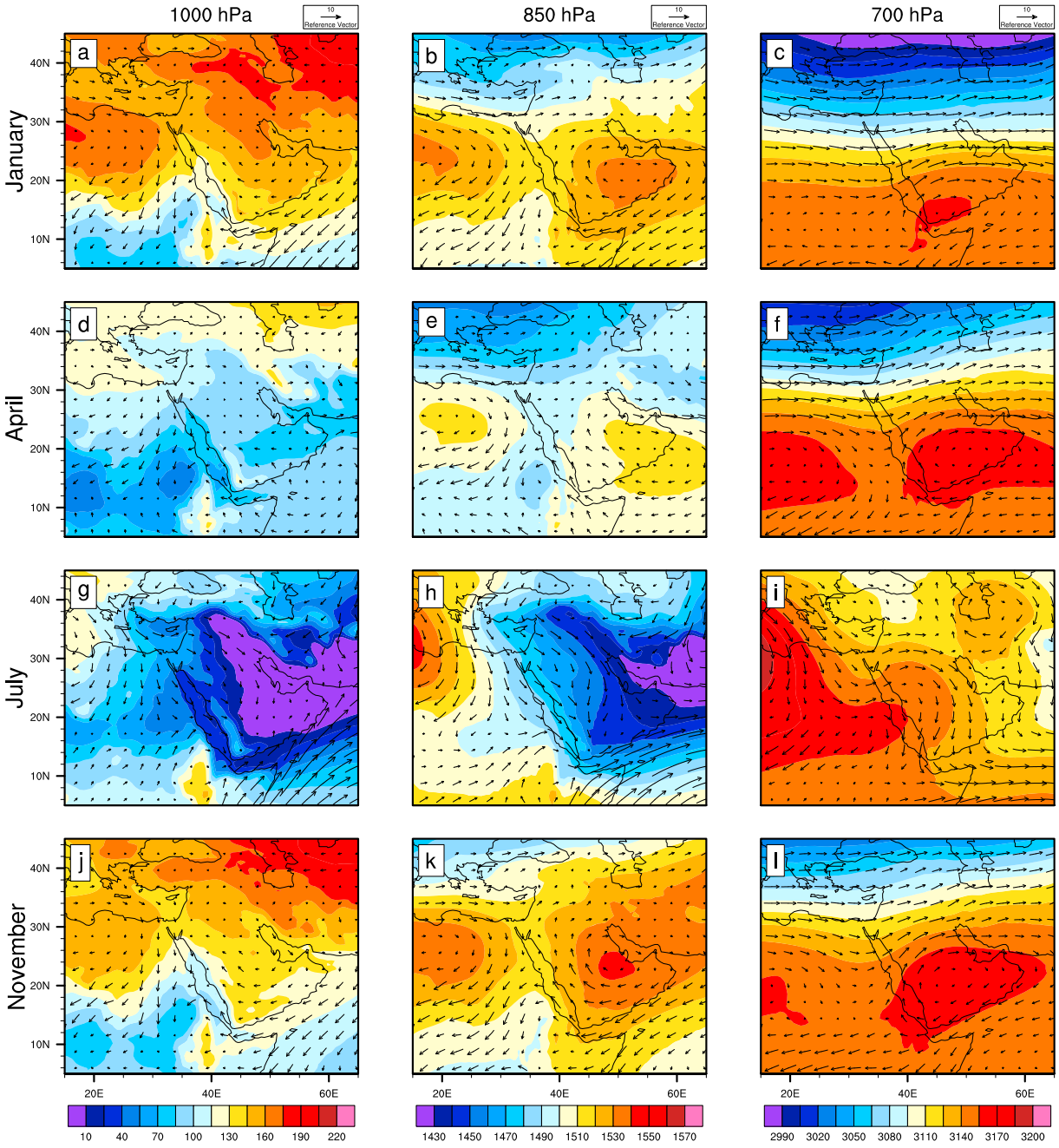

Figure 14. Monthly means of ERA-Interim (1979–2010) geopotential height (gpm) and wind vectors ($m\,s^{-1}$) at 1000, 850, and 700 hPa for January, April, July, and November.

Table 3. Seasonality of the ARST

Large-Scale and Low-Level Circulation	Autumn (Oct, Nov)	Winter (Dec, Jan, Feb)	Spring (Mar, Apr, May)	Summer (Jun until Sep)[a]
ITCZ/African Monsoon and baroclinic zone	Shifts southward	Most southerly	Shifts northward	Most northerly
RST and AA	Shift southward, most pronounced	Most southerly, weaken	Shift northward (RST and AA at 700 hPa), weak (RST and AA at 850 hPa)	Absent
ARST favorable conditions	Optimal	Low	Moderate	Negligible

[a]In addition, the ME is dominated by the influence of the South Asian summer monsoon; see text.

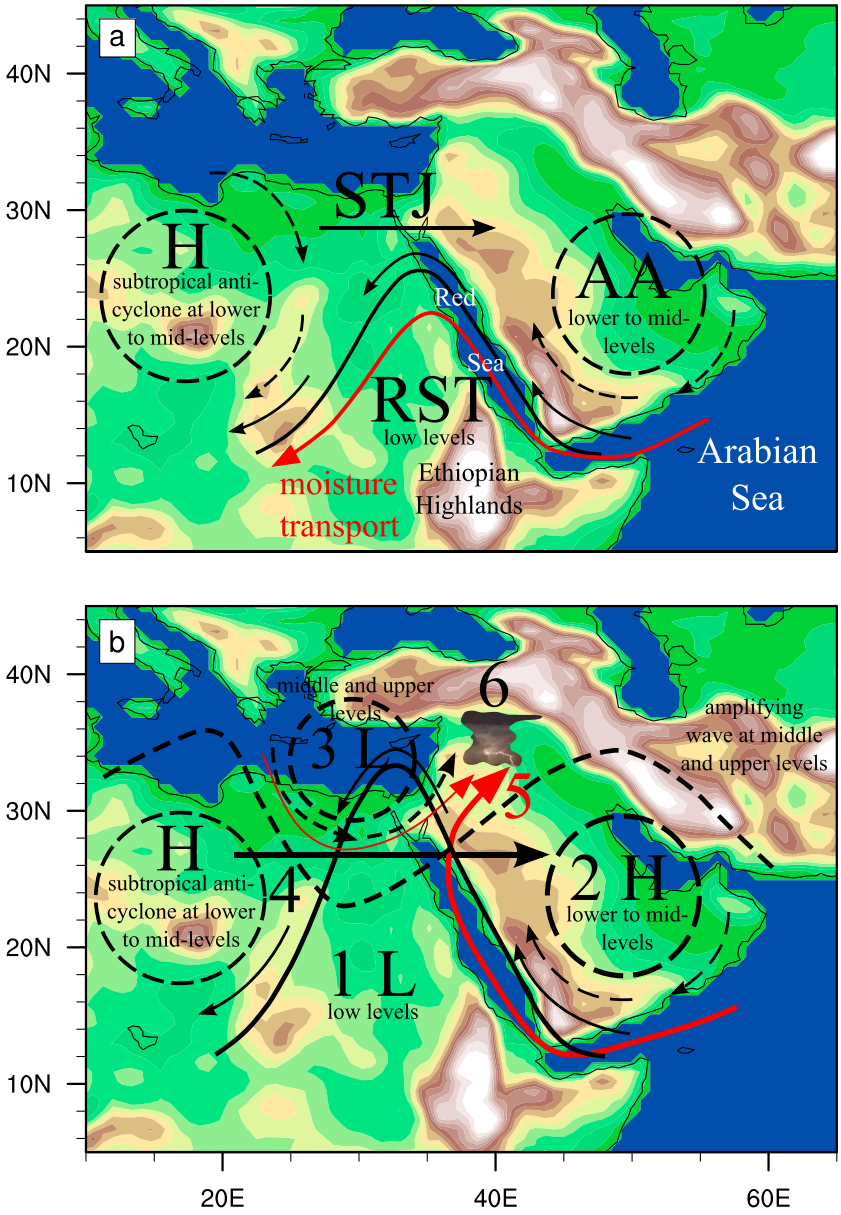

Figure 15. Schematic representation of (a) the low-level circulation climatology in autumn, winter, and spring, and (b) the ARST associated dynamical factors. For numbers mentioned in Figure 15b, see the text.

the RST and AA explains, in addition to the seasonal variability of the large-scale circulation, why ARSTs over the Levant occur predominantly in autumn (October and November) and to a lesser extent in early winter (December and January) and spring (March, April, and May), summarized in Table 3. At more southerly locations (e.g., the Jeddah region), ARST favorable conditions arise later in autumn, end earlier in spring, and can potentially last throughout the winter.

8. Discussion

8.1. Low-Level Circulation Climatology

[42] Figure 15a schematically depicts the seasonally averaged low-level circulation during autumn, winter, and spring. The RST appears in fact as an inverted trough in the low-level circulation that interrupts the trade winds and the subtropical anticyclones. The RST is characterized by pronounced moisture quantities (supporting information Figure S8) that contribute to the decreased barometric pressure. The high humidity makes the air more buoyant and, under the influence of sensible heating over northeast Africa, causes pressure fluctuations that explain the observed diurnal variations of the RST described in section 5.1. The moisture originates from the Arabian and Red Seas, in particular during the period when the RST and AA (at ~850 hPa) are most pronounced (October until January), as illustrated by the monthly means of the VIWVFs (supporting information Figure S9). The topography plays an important role. While the Arabian and Red Seas moisten the air, the Ethiopian Highlands block the AA intensified easterly low-level flow and enhance its northward propagation into the Red Sea region. In other words, we explain the RST as a persistent and stationary

Table 4. Dynamical Factors of the ARST

Dynamical Factors	Origin/Character	Behavior During ARST	Impact	Role in ARST
RST	Surface trough from tropics (upward branch Hadley Cell, African Monsoon/ITCZ)	Extends northward	Southeasterly advection warm moist air	Precondition
AA	Subtropical anticyclone (downward branch Hadley Cell and surface sensible heating)	Intensifies	Southeasterly advection warm moist air	Precondition
Upper trough	Midlatitude forcing, Rossby wave amplification and breaking	Intrudes into the EM	Cyclonic flow and cold air advection	Trigger
STJ	Positioned over North Africa and the ME	Intensifies due to midlatitude forcing	Upper level divergence	(Trigger)
Moisture dynamics	Predominantly Arabian and Red Seas, and to a lesser extent Mediterranean Sea	Transport by AA and upper trough, ascends gradually, converges, and intrudes the ME	Enhances tropospheric instability	Fuels precipitation
Upward motions	Tropospheric instability and synoptic-scale dynamical forcing	Convective and large-scale ascent	Precipitation generation	Determines location and timing (extreme) precipitation

wave in the moist tropical easterlies, induced by the interaction between the low-level circulation, the AA forcing, and the topography in the Red Sea region.

8.2. Unified Concept of the ARST Dynamics

[43] Based on the 12 analyzed Levant ARSTs and the Jeddah 2009 event, and building on previous studies, we present an ARST concept that includes six important dynamical factors (Figure 15b): (1) the northward extension of the semipermanent quasi-stationary RST, (2) the intensification of the semipermanent quasi-stationary AA, (3) the intrusion of a midlatitude upper level trough, (4) the intensification of the STJ, (5) enhanced moisture transport from the adjacent seas, and (6) upward motions resulting from the synoptic-scale dynamical forcing and tropospheric instability.

[44] The RST and AA are always present in ARST favorable seasons and show only a relatively weak anomaly from their mean state during ARSTs [cf. *Kahana et al*., 2002]; hence, they are considered to serve as a precondition. ARSTs are triggered by the upper level trough. Thus, the midlatitude forcing plays a key role and determines the frequency of ARSTs. *Knippertz and Martin* [2005], *Knippertz* [2007], and *Rubin et al*. [2007] found that for heavy precipitation events, associated with tropical plumes, either a quasi-stationary upper level trough or two consecutive upper troughs were essential to initiate sufficient poleward moisture transport from the tropics. Also, *Kahana et al*. [2002, 2004] highlighted, in relation to the evolution of upper troughs during ARSTs, that a "period of incubation" is required for the southerly transport of tropical moisture. Therefore, the persistence and southward extent of the midlatitude upper level trough plays a crucial part in the amounts of (extreme) rainfall. Accordingly, a fast travelling upper trough that does not reach far southward and is not preceded by another upper trough may result in events with the ARST dynamical configuration without associated precipitation. The moisture originates from the adjacent seas in the region and fuels the precipitation process. Therefore, sea surface temperatures and atmospheric moisture quantities potentially influence the amount of precipitation and the intensity of ARSTs, being of interest in the context of global warming. The combination of all synoptic-scale dynamical factors sets the scene for severe weather and favors strong upward motions. Processes at smaller scales determine the exact location and timing of the convective storms and (localized) heavy rainfall. The dynamical factors and their roles in the ARST are summarized in Table 4.

[45] *Krichak and Alpert* [1998] proposed an ARST mechanism in five stages, involving enhanced convection over the tropics, an intensification of the STJ, the development of the RST, and the northward advection of moist air masses into the Red Sea area. Our results are partially in agreement; however, the following observations provide additional insights: (1) The northward extension of the surface pressure trough, the enhanced moisture quantities (TCW), and the intensified northward moisture transport (VIWVFs) over the Red Sea evolve rather synchronously, illustrating the involvement of moisture from the Arabian and Red Seas in the northward extension of the RST. (2) The RST extends northward simultaneously with the intensification of the AA and/or the approach of the midlatitude upper trough. Previously, the RST extension was attributed to the positioning and strength of the STJ [*Krichak et al*., 1997a]. Based on our analysis, we postulate that the northward progression of the RST and associated moisture is forced by the combination of the intensifying anticyclonic flow around the AP and the developing cyclonic flow over the EM and Levant. Thus, the persistent AA and the approaching upper trough undergo phase locking and drive the northward advancement of the RST and tropical moisture. (3) The temporal and spatial evolution of the intensifying STJ progresses simultaneously with the development of the upper level trough, showing that the STJ intensification results predominantly from the midlatitude forcing rather than from intensified convection over the tropics and east-poleward outflow at upper levels, consistent with the results of section 5.2.

[46] Emerging from the above, we propose the following revised ARST mechanism: (1) Rossby wave amplification and breaking results in the formation of a midlatitude upper level trough that intrudes into the EM. As a result, (2) the upper and lower tropospheric circulations couple and interact. The midlatitude upper level trough and preexisting RST merge, and the ridge over the AP (further)

intensifies the persistent anticyclonic flow around the AP at low to midlevels, together forcing pronounced southerly winds over the Red Sea region. Consequently, (3) the RST extends northward, and the associated tropical moist air masses progress over the Red Sea and intrude into the Levant and/or AP regions. (4) The enhanced tropospheric instability and dynamical forcing cause ascending motions, promoting the development of convective storms and heavy precipitation. (5) Subsequently, the midlatitude upper level trough dissipates, the RST retreats, and the AA weakens, and the moisture transport from the Arabian and Red Seas is again directed toward equatorial Africa.

[47] In summary, ARST occurrence is triggered when an amplified Rossby wave superimposes over the preexisting low-level wave (i.e., the RST). The upper trough deepens and merges with the RST, in line with *Tsvieli and Zangvil* [2007], while the ridge over the AP (further) intensifies the AA. The anomalies in the upper and lower troposphere phase lock and amplify each other according to the cyclogenetic process as described by *Hoskins et al*. [1985, Figure 21]. Consequently, the persistent easterly moist airflow toward equatorial Africa is interrupted and progresses northward to the ME, implying that pronounced southerly moisture fluxes over the Red Sea are a key signal of the ARST, which is confirmed by Figure 8.

8.3. AA, Associated Moisture Transport, and Rainfall Over the ME

[48] Our study underscores that the intensified AA and associated moisture transport not only characterize the December 1993 event [*Ziv et al*., 2005] and the Jeddah 2009 event [*Haggag and El-Badry*, 2013], but are relevant for all analyzed Levant ARSTs (Figure 8). Apart from the ARST, the AA and associated moisture transport are also involved in precipitation and floods in Iran [*Farajzadeh et al*., 2007; *Sabziparvar et al*., 2010; *Raziei et al*., 2012]. The latter study found the AA to induce lower tropospheric moisture transport from tropical water bodies (Arabian Sea, Oman Sea, Persian Gulf, Red Sea, and northern Indian Ocean) into cyclonic systems near Iran. In a climatological modeling study, *Evans and Smith* [2006] identified southerly moisture fluxes, characteristic for a minority of rainfall events, to be responsible for a major contribution to the annual precipitation over the Fertile Crescent (southeast Turkey, northeast Syria, north Iraq, and northwest Iran), suggesting the involvement of the AA. We therefore postulate that the AA and associated moisture transport are not only relevant for the ARST, but also for other precipitation generating phenomena over the ME such as tropical plumes and midlatitude cyclones (e.g., Mediterranean cyclones).

8.4. ARST and Other Tropical-Extratropical Interactions

[49] The ARST shows strong similarities to other tropical-extratropical interactions that affect semiarid to arid subtropical regions with extreme precipitation. In general, poleward transport of tropical moisture is initiated by the midlatitude forcing. More specifically, important synoptic dynamics include upper troughs and/or cutoffs resulting from (Rossby) wave breaking, intensification of the STJ, wave disturbances in the low-level tropical easterlies (easterly waves), trade surges (strong trade winds), and precipitation generation resulting from orographic lifting, tropospheric instability, quasi-geostrophic forcing, and STJ associated upper level divergence [e.g., *McGuirk et al*., 1988; *Ziv*, 2001; *Fink and Knippertz*, 2003; *Knippertz et al*., 2003; *Knippertz*, 2005; *Knippertz and Martin*, 2005; *Knippertz and Martin*, 2006; *Knippertz*, 2007; *Rubin et al*., 2007; *Hart et al*., 2010; *Favors and Abatzoglou*, 2013].

[50] However, the ARST dynamics differ in particular aspects. Most of the aforementioned studies indicate that the moisture is lifted within the ITCZ through convection and advected in the midtroposphere over the (dry Saharan) planetary boundary layer toward the subtropics, as illustrated by *Nicholson* [1981, Figure 3] and *Knippertz* [2003, Figure 1]. For the ARST events, we infer gradually ascending moisture in the anticyclonic flow around the AP. Moreover, the driving mechanism, a subtropical anticyclone at lower levels, is not observed for any other type of tropical-extratropical interaction. Therefore, the particular topography in the Red Sea region and the associated low-level circulation (the RST, AA, and associated moisture transport) makes the ARST a unique phenomenon among tropical-extratropical interactions.

9. Summary and Conclusions

[51] We investigated the ARST associated atmospheric dynamics, geographical extent, and seasonality. ERA-Interim data were used to study the underlying synoptic dynamics of 12 ARST events that affected the Levant and the flooding that struck Jeddah on 25 November 2009. Further, the seasonal variability of the large-scale and local low-level circulation was analyzed to explain the ARST seasonality. In addition, we considered observational precipitation data to gain insight into the ARST-associated rainfall evolution and characteristics.

[52] Rainfall during ARSTs evolves over the Red Sea region and progresses in a northeasterly direction. The Levant can be affected for a time period from one to four days with rainfall maxima typically ranging from 10 up to 60 mm per day. Precipitation in ERA-Interim and Aphrodite data show a similar spatial and temporal evolution, however, can locally differ significantly in the timing and amounts of rain. Based on the analyzed events, including the Jeddah 2009 event, and building on previous studies, we present an ARST concept involving six dynamical factors (Figure 15b). This concept comprises (sub)tropical influences (the RST and AA), midlatitude forcing (the upper level trough and intensified STJ), moisture transport pathways, and the resulting upward motion. The AA and associated moisture transport from the Arabian and Red Seas are of central importance for the ARST, and are probably also involved in other precipitation generating phenomena over the ME. The dynamics associated with the Jeddah 2009 event are identical to those associated with the Levant ARST events. Hence, the Jeddah flooding was caused by an ARST. This implies that, in addition to the Levant, also the AP is affected by the ARST, introducing a significant geographical extension of the phenomenon.

[53] Further, we explain the ARST seasonality by the seasonal pace of the large-scale circulation and in particular that of the low-level circulation. More specifically, the latitudinal positions of the midlatitude baroclinic zone and

the African Monsoon (i.e., the local ITCZ) induces ARST favorable conditions during autumn and spring, and limited potential in winter, whereas the South Asian monsoon influence rules out ARSTs during summer. The semipermanent quasi-stationary RST and AA show their most northerly position in autumn and spring, and most pronounced state in autumn and early winter, revealing why ARSTs in the Levant occur predominantly during autumn (October and November) and have a reduced incidence during early winter (December and January) and spring (March to May). ARST favorable conditions in more southerly locations (e.g., the Jeddah region) arise later in autumn and earlier in spring, and possibly last throughout the winter.

[54] The mean low-level circulation in the Red Sea region is strongly influenced by the local topography. In fact, we explain the RST as a persistent and stationary wave disturbance in the tropical easterlies, induced by the AA forcing, the flow blocking by the Ethiopian Highlands, and the moistening of air masses by the Arabian and Red Seas (Figure 15a). An ARST event is triggered when a midlatitude upper level trough intrudes the EM, going along with a Rossby wave that amplifies and superimposes over the preexisting low-level wave (Figure 15b). Their interaction causes pronounced southerly moisture transport over the Red Sea toward the ME (Figure 8). Hence, the ARST is a tropical-extratropical interaction resulting in a tropical moist air intrusion. The ARST dynamics show substantial similarities with other type of tropical-extratropical interactions affecting semiarid to arid subtropical regions elsewhere, however, differ in particular aspects due to the particular topography in the Red Sea region and the associated low-level circulation, justifying the term "ARST."

[55] In ME countries, floods are a main cause of natural disasters and have severe societal impacts. For example, seven of the top ten disasters in Saudi Arabia in the period 1900–2011, ranked by number of casualties as well as numbers of people affected, resulted from floods (EM-DAT). Therefore, the causes (e.g., atmospheric dynamics), potential impacts, and preemptive measures need increased attention. Our study provides a better understanding of the ARST dynamics and should benefit weather forecasting and early warning systems. Further work may quantify the contribution of the identified moisture sources in ARSTs using back trajectory methods. Modeling sensitivity studies could explore the impact of the mountains and land-water surface differences in the Red Sea region on the low-level circulation, and in particular the RST and AA. It will also be important to investigate the role of climate change, for example in view of increasing sea surface temperatures and associated moisture fluxes. The new insights in the ARST dynamics and the expanded geographical extent of the phenomenon, as presented in this work, introduce interesting possibilities to study the ARST in a climatological context. In a subsequent study, we will investigate the ARST climatology, the influence of large-scale circulation patterns on ARST occurrence, and the ARST contribution to total rainfall amounts in the ME.

[56] **Acknowledgments.** The research leading to these results has received funding from the European Research Council under the European Union's Seventh Framework Programme (FP7/2007-2013)/ ERC grant agreement 226144. S.O. Krichak and D. Edry acknowledge financial support by the United States-Israel Binational Science Foundation (BSF) under research grant 2008436. The research was partly supported by The Cyprus Institute and Tel Aviv University through their cooperative agreement. The authors wish to thank Aphrodite, CRED, ECMWF, and IMS for providing their data. The data are visualized with the National Center for Atmospheric Research (NCAR) Command Language (NCL) package (version 6.0.0). We are grateful for helpful discussions with M. Tanarhte from the Max Planck Institute for Chemistry. We greatly appreciate the comments of three anonymous reviewers that improved the manuscript.

References

Almazroui, M. (2011), Sensitivity of a regional climate model on the simulation of high intensity rainfall events over the Arabian Peninsula and around Jeddah (Saudi Arabia), *Theor. Appl. Climatol.*, *104*(1-2), 261–276, doi:10.1007/s00704-010-0387-3.

Almazroui, M. (2012), The life cycle of extreme rainfall events over western Saudi Arabia simulated by a regional climate model: Case study of November 1996, *Atmosfera*, *25*(1), 23–41.

Alpert, P., I. Osetinsky, B. Ziv, and H. Shafir (2004a), Semi-objective classification for daily synoptic systems: Application to the Eastern Mediterranean climate change, *Int. J. Climatol. 24*(8), 1001–1011, doi:10.1002/joc.1036.

Alpert, P., I. Osetinsky, B. Ziv, and H. Shafir (2004b), A new seasons definition based on classified daily synoptic systems: An example for the Eastern Mediterranean, *Int. J. Climatol. 24*(8), 1013–1021, doi:10.1002/joc.1037.

Alpert, P., et al. (2006), Relations between climate variability in the Mediterranean region and the Tropics: ENSO, South Asian and African monsoons, hurricanes and Saharan dust, in *Mediterranean Climate Variability*, *Dev. Earth Environ. Sci.*, vol. *4*, edited by P. Lionello, P. Malanotte-Rizzoli and R. Boscolo, pp. 149–177, Elsevier, Amsterdam.

Bitan, A., and H. Saaroni (1992), The horizontal and vertical extension of the Persian Gulf pressure trough, *Int. J. Climatol.*, *12*(7), 733–747, doi:10.1002/joc.3370120706.

Cools, J., P. Vanderkrimpen, G. El Afandi, A. Abdelkhalek, S. Fockedey, M. El Sammany, G. Abdallah, M. El Bihery, W. Bauwens, and M. Huygens (2012), An early warning system for flash floods in hyper-arid Egypt, *Nat. Hazards Earth Syst. Sci.*, *12*(2), 443–457, doi:10.5194/ nhess-12-443-2012.

Dayan, U., and E. Morin (2006) Flash flood-producing rainstorms over the Dead Sea, *Geol. Soc. Am.*, *401*, 53–62, doi:10.1130/2006.2401(04).

Dayan, U., B. Ziv, A. Margalit, E. Morin, and D. Sharon (2001), A severe autumn storm over the Middle-East: Synoptic and mesoscale convection analysis, *Theor. Appl. Climatol.*, *69*(1-2), 103–122, doi:10.1007/s007040170038.

Dee, D. P., et al. (2011), The ERA-Interim reanalysis: Configuration and performance of the data assimilation system, *Q. J. R. Meteorol. Soc.*, *137*(656), 553–597, doi:10.1002/qj.828.

Evans, J. P., and R. B. Smith (2006), Water vapor transport and the production of precipitation in the eastern fertile crescent, *J. Hydrometeorol.*, *7*(6), 1295–1307, doi:10.1175/JHM550.1.

Farajzadeh, M., M. K. Ahmadabad, H. Ghaemi, and M. R. Mobasheri (2007), Studying the moisture flux over west Iran: A case study of January 1 to 7, 1996 rain storm, *J. Appl. Sci.*, *7*(20), 3023–3030.

Favors, J. E., and J. T. Abatzoglou (2013), Regional surges of monsoonal moisture into the southwestern United States, *Mon. Weather Rev.*, *141*(1), 182–191, doi:10.1175/MWR-D-12-00037.1.

Fink, A. H., and P. Knippertz (2003), An extreme precipitation event in southern Morocco in spring 2002 and some hydrological implications, *Weather*, *58*, 377–387.

Galarneau, T. J., L. F. Bosart, and A. R. Aiyyer (2008), Closed anticyclones of the subtropics and midlatitudes: 54-yr climatology (1950-2003) and three case studies, in *Synoptic-Dynamic Meteorology and Weather Analysis and Forecasting*, *Meteorol. Monogr.*, vol. *33*(55), edited by L. F. Bosart, and H. B. Bluestein, pp. 349–392, Springer, New York.

Greenbaum, N., A. Margalit, A. P. Schick, D. Sharon, and V. R. Baker (1998), A high magnitude storm and flood in a hyperarid catchment, Nahal Zin, Negev Desert, Israel, *Hydrol. Processes*, *12*, 1–23.

Greenbaum, N., U. Schwartz, and N. Bergman (2010), Extreme floods and short-term hydroclimatological fluctuations in the hyper-arid Dead Sea region, Israel, *Global Planet. Change*, *70*(1-4), 125–137, doi:10.1016/j. gloplacha.2009.11.013.

Haggag, M., and H. El-Badry (2013), Mesoscale numerical study of quasi-stationary convective system over Jeddah in November 2009, *Atmos. Clim. Sci.*, *3*(1), 73–86, doi:10.4236/acs.2013.31010.

Hart, N. C. G., C. J. C Reason, and N. Fauchereau (2010), Tropical-extratropical interactions over southern Africa: Three cases of heavy summer season rainfall, *Mon. Weather Rev.*, *138*(7), 2608–2623, doi:10.1175/2010MWR3070.1.

Holton, J. R., (2004), *An Introduction to Dynamic Meteorology*, Academic, San Diego, Calif.

Hoskins, B. J., M. E. McIntyre, and A. W. Robertson (1985), On the use and significance of isentropic potential vorticity maps, *Q. J. R. Meteorol. Soc.*, *111*(470), 877–946, doi:10.1256/smsqi.47001.

Kahana, R., B. Ziv, Y. Enzel, and U. Dayan (2002), Synoptic climatology of major floods in the Negev desert, Israel, *Int. J. Climatol.*, *22*(7), 867–882, doi:10.1002/joc.766.

Kahana, R., B. Ziv, U. Dayan, and Y. Enzel (2004), Atmospheric predictors for major floods in the Negev desert, Israel, *Int. J. Climatol.*, *24*(9), 1137–1147, doi:10.1002/joc.1056.

Knippertz, P. (2003), Tropical-extratropical interactions causing precipitation in northwest Africa: Statistical analysis and seasonal variations, *Mon. Weather Rev.*, *131*(12), 3069– 3076, doi:10.1175/1520-0493.

Knippertz, P. (2005), Tropical-extratropical interactions associated with an Atlantic tropical plume and subtoprical jet streak, *Mon. Weather Rev.*, *133*(9), 2759–2776, doi:10.1175/MWR2999.1.

Knippertz, P. (2007), Tropical-extratropical interactions related to upper-troughs at low latitudes, *Dyn. Atmos. Oceans*, *43*(1-2), 36–62, doi:10.1016/j.dynatmoce.2006.06.003.

Knippertz, P., and J. E. Martin (2005), Tropical plumes and extreme precipitation in subtropical and tropical West Africa, *Q. J. R. Meteorol. Soc.*, *131*(610), 2337–2365, doi:10.1256/qj.04.148.

Knippertz, P., and J.E. Martin (2006), A Pacific moisture conveyor belt and its relationship to a significant precipitation event in the semiarid southwestern United States, *Weather Forecast.*, *22*(1), 125–144, doi:10.1175/WAF963.1.

Knippertz, P., A. H. Fink, A. Reiner, and P. Speth (2003), Three late summer/early autumn cases of tropical-extratropical interactions causing precipitation in northwest Africa, *Mon. Weather Rev.*, *131*(1), 116–135, doi:10.1175/1520-0493(2003)131<0116:TLSEAC>2.0.CO;2.

Krichak, S. O., and P. Alpert (1998), Role of large scale moist dynamics in November 1-5, 1994, hazardous Mediterranean weather, *J. Geophys. Res.*, *103*, 453–468, doi:10.1029/98JD01710.

Krichak, S. O., P. Alpert, and T. N. Krishnamurti (1997a) Interaction of topography and tropospheric flow – A possible generator for the Red Sea Trough?, *Meteorol. Atmos. Phys.*, *63*(3-4), 149–158, doi:10.1007/BF01027381.

Krichak, S. O., P. Alpert, and T. N. Krishnamurti (1997b) Red Sea Trough/cyclone development - Numerical investigation, *Meteorol. Atmos. Phys.*, *63*(3-4), 159–169, doi:10.1007/BF01027382.

Krichak, S. O., M. Tsidulko, and P. Alpert (2000), November 2, 1994, severe storms in the southeastern Mediterranean, *Atmos. Res.*, *53*(1-3), 45–62, doi:10.1016/S0169-8095(99)00045-9.

Krichak, S. O., J.S. Breitgand, and S. B. Feldstein (2012), A conceptual model for the identification of the Active Red Sea Trough Synoptic events over the southeastern Mediterranean, *J. App. Meteorol. Climatol.*, *51*(5), 962–971, doi:10.1175/JAMC-D-11-0223.1.

Llasat, M. C., et al. (2010), High-impact floods and flash floods in Mediterranean countries: The FLASH preliminary database, *Adv. Geosci.*, *23*, 47–55, doi:10.5194/adgeo-23-47-2010.

McGuirk J. P., A. H. Thompson, and J. R. Schaefer (1988), An eastern Pacific tropical plume, *Mon. Weather Rev.*, *116*(12), 2505–2521, doi:10.1175/1520-0493(1988)116<2505:AEPTP>2.0.CO;2.

Moawad, M. B. (2012), Predicting and analyzing flash floods of ungauged small-scale drainage basins in the eastern desert of Egypt, *J. Geomatics*, *6*(1), 23–30.

Neiman, P. J., F. M. Ralph, G. A. Wick, J. D. Lundquist, and M. D. Dettinger (2008), Meteorological character and overland precipitation impacts of atmospheric rivers affecting the West Coast of North America based on eight years of SSM/I satellite observations, *J. Hydrometeorol.*, *9*(1), 22–47, doi:10.1175/2007JHM855.1.

Nicholson, S. E. (1981), Rainfall and atmospheric circulation during drought periods and wetter years in West Africa, *Mon. Weather Rev.*, *109*(10), 2191–2208, doi:10.1175/1520- 0493.

Raziei, T., A. Mofidi, A. J. Santos, and I. Bordi (2012), Spatial patterns and regimes of daily precipitation in Iran in relation to large-scale atmospheric circulation, *Int. J. Climatol.*, *32*(8), 1226–1237, doi:10.1002/joc.2347.

Rodwell, M. J., and B. J. Hoskins (1996), Monsoon and the dynamics of deserts, *Q. J. R. Meteorol. Soc.*, *122*(534), 1385–1404, doi:10.1002/qj.49712253408.

Rubin, S., B. Ziv, and N. Paldor (2007), Tropical plumes over eastern North Africa as a source of rain in the Middle East, *Mon. Weather Rev.*, *135*(12), 4135–4148, doi:10.1175/2007MWR1919.1.

Sabziparvar, A. A., A. Parandeh, H. Lashkari, and H. Yazdanpanah (2010), Mid-level synoptic analysis of flood-generating systems in south-west of Iran (case study: Dalaki watershed river basin), *Nat. Hazards Earth Syst. Sci.*, *10*(11), 2269–2279, doi:10.5194/nhess-10-2269-2010.

Shentsis, I., J. B. Laronne, and P. Alpert (2012), Red Sea Trough floods in the Negev, Israel (1964-2007), *Hydrol. Sci. J.*, *57*(1), 42–51, doi:10.1080/02626667.2011.636922.

Stull, R. B. (2000), *Meteorology for Scientists and Engineers*, Brooks/Cole Thomson Learning, Pacific Grove, Calif.

Thorncroft, C. D., B. J. Hoskins, and M. F. Mcintyre (1993), Two paradigms of baroclinic-wave life-cycle behavior, *Q. J. R. Meteorol. Soc.*, *119*(509), 17–55, doi:10.1002/qj.49711950903.

Tsvieli, Y., and A. Zangvil (2005), Synoptic climatological analysis of 'wet' and 'dry' Red Sea troughs over Israel, *Int. J. Climatol.*, *25*(15), 1997–2015, doi:10.1002/joc.123.

Tsvieli, Y., and A. Zangvil (2007), Synoptic climatological analysis of Red Sea trough and non-Red Sea trough rain situations over Israel, *Adv. Geosci.*, *12*, 137–143.

Tyrlis, E., J. Lelieveld, and B. Steil (2013), The summer circulation over the eastern Mediterranean and the Middle East: Influence of the South Asian monsoon, *Clim. Dyn.*, *40*(5-6), 1103–1123, doi:10.1007/s00382-012-1528-4.

Wright, W. J. (1997), Tropical-extratropical cloudbands and Australian rainfall. 1. Climatalogy, *Int. J. Climatol.*, *17*(8), 807–829, doi:10.1002/(SICI)1097-0088(19970630)17:8<807::AID-JOC162>3.0.CO;2-J.

Wu, G., Y. Guan, T. Wang, Y. Liu, J. Yan, and J. Mao (2011), Vortex genesis over the Bay of Bengal in spring and its role in the onset of the Asian summer monsoon, *Sci. China Earth Sci.*, *54*(1), 1–9, doi:10.1007/s11430-010-4125-6.

Wu, G., Y. Guan, T. Wang, Y. Liu, J. Yan, and J. Mao (2012), Air-sea interaction and formation of the Asian summer monsoon onset vortex over the Bay of Bengal, *Clim. Dyn.*, *38*(1-2), 261–279, doi:10.1007/s00382-010-0978-9.

Yatagai, A., K. Kamiguchi, O. Arakawa, A. Hamada, N. Yasutomi, and A. Kitoh (2012), Aphrodite constructing a long-term daily gridded precipitation dataset for Asia based on a dense network of rain gauges, *Bull. Am. Meteorol. Soc.*, *93*(9), 1401–1415, doi:10.1175/BAMS-D-11-00122.1.

Zaitchik, B. J., J. P. Evans, and R. B. Smith (2007), Regional impact of an elevated heat source: The Zagros plateau of Iran, *J. Clim.*, *20*(16), 4133–4146, doi:10.1175/JCLI4248.1.

Zarrin, A., H. Ghaemi, M. Azadi, and M. Farajzadeh (2010), The spatial pattern of summertime subtropical anticyclones over Asia and Africa: A climatological review, *Int. J. Climatol.*, *30*, 159–173, doi:10.1002/joc.1879.

Ziv, B. (2001), A subtropical rainstorm associated with a tropical plume over Africa and the Middle-East, *Theor. Appl. Climatol.*, *68*(1-2), 91–102, doi:10.1007/s007040170037.

Ziv, B., H. Saaroni, and P. Alpert (2004), The factors governing the summer regime of the eastern Mediterranean, *Int. J. Climatol.*, *24*(14), 1859–1871, doi:10.1002/joc.1113.

Ziv, B., U. Dayan, and D. Sharon (2005), A mid-winter, tropical extreme flood-producing storm in southern Israel: Synoptic scale analysis, *Meteorol. Atmos. Phys.*, *88*(1-2), 53–63, doi:10.1007/s00703-003-0054-7.

Appendix C2. *De Vries et al.* (2016)

Published in the Quarterly Journal of the Royal Meteorological Society in 2016

Dynamics of Tropical-Extratropical Interactions and Extreme Precipitation Events in Saudi Arabia in Autumn, Winter and Spring

Authors: A. J. De Vries[1,2], S. B. Feldstein[3], M. Riemer[4], E. Tyrlis[2], M. Sprenger[5], M. Baumgart[4], M. Fnais[6], and J. Lelieveld[1,2]

[1]) Atmospheric Chemistry Department, Max Planck Institute for Chemistry, Mainz, Germany
[2]) Energy, Environment and Water Research Center, The Cyprus Institute, Nicosia, Cyprus
[3]) Department of Meteorology, The Pennsylvania State University, University Park, USA
[4]) Institut für Physik der Atmosphäre, University of Mainz, Germany
[5]) Institute for Atmospheric and Climate Science, ETH, Zurich, Switzerland
[6]) Department Geology and Geophysics, King Saud University, Riyadh, Saudi Arabia

RMetS
Royal Meteorological Society

Dynamics of tropical–extratropical interactions and extreme precipitation events in Saudi Arabia in autumn, winter and spring

A. J. de Vries,[a,b]* S. B. Feldstein,[c] M. Riemer,[d] E. Tyrlis,[b] M. Sprenger,[e] M. Baumgart,[d] M. Fnais[f] and J. Lelieveld[a,b]

[a]*Atmospheric Chemistry Department, Max Planck Institute for Chemistry, Mainz, Germany*
[b]*Energy, Environment and Water Research Center, The Cyprus Institute, Nicosia, Cyprus*
[c]*Department of Meteorology, The Pennsylvania State University, University Park, USA*
[d]*Institut für Physik der Atmosphäre, University of Mainz, Germany*
[e]*Institute for Atmospheric and Climate Science, ETH Zürich, Switzerland*
[f]*Department Geology and Geophysics, King Saud University, Riyadh, Saudi Arabia*

*Correspondence to: A. J. de Vries, Atmospheric Chemistry, Max Planck Institute for Chemistry, Hahn-Meitner-Weg 1, DE-55128, Mainz, Germany. E-mail: a.devries@mpic.de

Extreme precipitation in the arid Middle East can cause flash floods with dramatic societal impacts. This study investigates the synoptic-scale dynamics of three extreme precipitation events that occurred in Saudi Arabia in autumn, winter and spring. Using ERA-Interim reanalysis, soundings and observational precipitation data, we study precipitation characteristics, the synoptic circulations, moisture transport pathways and forcing mechanisms for upward motion. All three cases involved strong tropical–extratropical interactions whereby midlatitude forcing instigated an incursion of tropical moisture over the Arabian Peninsula that fuelled the heavy rainfall. In each case, a midlatitude upper-level trough, associated with anticyclonic Rossby wave breaking, intruded into the subtropics. The phase relationship between this trough and the tropical low-level circulation was consistent with wave amplification through baroclinic growth. Eulerian and Lagrangian analyses reveal moisture transport from nearby and remote tropical regions, leading to above-normal tropospheric moisture content over Saudi Arabia. The autumn case (November 2009) showed a transient midlatitude upper-level trough that interacted with the climatological Red Sea Trough near the surface, being an 'Active Red Sea Trough' event. The winter case (January 2005) resembled tropical plume-like characteristics and demonstrated the coupling of a midlatitude cyclone and the equatorial low-pressure zone over Africa, an intensified subtropical jet stream, and pronounced moisture fluxes at middle and upper levels. The spring case (April–May 2013) involved a quasi-stationary cut-off low and persistent advection of low-level moist air masses, partly from the south Indian Ocean through cross-equatorial flow. The forcing of ascent was associated with low-level moisture convergence and decreased static stability (autumn case), dynamical lifting (winter case), strong surface sensible heating (spring case), and orographic lifting (all cases), favouring the build-up and release of potential instability. We discuss the three cases from a seasonal perspective and present a synthesis of their common key synoptic features.

Key Words: extreme precipitation; flash floods; Lagrangian analysis; Middle East; moisture transport pathways; Rossby wave breaking; synoptic-scale dynamics; tropical–extratropical interactions

Received 10 November 2015; Revised 3 February 2016; Accepted 29 February 2016; Published online in Wiley Online Library 2 May 2016

1. Introduction

The Middle East is characterised by a hot and arid desert climate (Kottek *et al.*, 2006), making its population vulnerable to climate change and severe weather events (Lelieveld *et al.*, 2012, 2013). In Saudi Arabia, extreme precipitation has frequently led to flooding with loss of human life, injuries, evacuations and extensive damage to infrastructure and property (Table 1). For instance, in November 2009, flash floods inundated Jeddah, resulting in 161 deaths, about 10 000 people affected and an estimated damage of about US$ 900 million. These dramatic societal impacts of flooding motivate our study of the atmospheric

Table 1. Floods and their societal impacts in Saudi Arabia (Emergency Events Database, 2013; unpublished data, provided by Centre for Research on the Epidemiology of Disasters).

Number	Year	Month	Days	Disaster type	Disaster subtype	Location	Deaths	Total affected people	Estimated damage US$ (M)
1	1964	Apr	4	Flood	Flash flood	Najran	20	1000	0
2	1985	Dec	24	Flood	–	North West	32	5000	450
3	2002	Apr	8–13	Flood	General flood	Makkah region	19	0	0
4	2003	Aug	8–12	Flood	General flood	Jizan province	0	13 000	0
5	2003	Nov	11	Flood	General flood	Makkah	12	50	0
6	2004	Apr	14–16	Flood	General flood	Jizan region	5	430	0
7	**2005**	**Jan**	**22–27**	**Flood**	**Flash flood**	**Al Madinah region**	**29**	**67**	**0**
8	2005	Apr	28	Flood	Flash flood	Asir Jeddah regions	34	0	0
9	**2009**	**Nov**	**24–26**	**Flood**	**General flood**	**Jeddah Makkah**	**161**	**10 000**	**900**
10	2010	Jul	10–12	Flood	General flood	Najran Al Lith Al Qunfidhah Jizan	10	85	0
11	2010	Jul	23–25	Flood	General flood	Asir Jizan Najran provinces; Taif	14	0	0
12	2011	Jan	25–31	Flood	General flood	Jeddah	11	0	300
13	2012	Apr	14–18	Flood	General flood	Western regions	19	0	0
14	**2013**	**May**	**2**	**Flood**	**General flood**	**Bishah region**	**20**	**0**	**0**

The events in bold refer to the selected cases analysed in this study, and the locations of the affected regions are indicated in Figure 1.

environment in which these extreme precipitation events occur. Such understanding is of crucial importance for improving weather forecasting and for establishing early warning systems to alleviate the potential impacts of flash floods, and will also benefit research on the climate and rainfall characteristics of the region.

The atmospheric circulation and associated rainfall over the Middle East exhibit strong seasonality. In summer, the large-scale circulation over the entire region is dictated by the South Asian monsoon, imposing middle- and upper-level subsidence over the Middle East and eastern Mediterranean (Rodwell and Hoskins, 1996; Tyrlis *et al.*, 2013). As a consequence, upward motion and precipitation over the Arabian Peninsula are suppressed during summer, except for the southwestern mountainous area where convective activity over the local topography can cause rainfall (Abdullah and Almazroui, 1998).

During boreal autumn, winter and spring, midlatitude cyclonic disturbances can intrude into the Middle East. In combination with the low-level northward advection of warm, moist air from nearby tropical waters, this can lead to a destabilized troposphere and rainfall over the Arabian Peninsula (Barth and Steinkohl, 2004; Evans *et al.*, 2004; Chakraborty *et al.*, 2006; Evans and Smith, 2006; Nazemosadat and Ghaedamini, 2010; Kumar *et al.*, 2015). During these seasons, the climatological synoptic-scale circulation is dominated by an inverted low-level trough with subtropical anticyclones at both flanks (Figure 1). The low-level trough expands northward from the tropical low-pressure zone over equatorial Africa across the Red Sea region and is usually referred to as the Red Sea Trough or Sudan Low (e.g. Alpert *et al.*, 2004a, 2004b; Tsvieli and Zangvil, 2005). Its formation can be attributed to the interaction between the easterly low-level flow and the topography in the Red Sea region (De Vries *et al.*, 2013 and references therein). The subtropical anticyclone at the eastern flank of the Red Sea Trough is located over the Arabian Peninsula and the Arabian Sea at lower- and middle-tropospheric levels and is known as the Arabian anticyclone (Raziei *et al.*, 2012; De Vries *et al.*, 2013).

Extreme precipitation events in semiarid and arid subtropical regions often result from tropical–extratropical interactions. Numerous studies investigated the dynamics of such extreme events in subtropical regions, including southwestern North America, northwestern Africa, South Africa, Pakistan and the Levant (Dayan *et al.*, 2001; Ziv, 2001; Knippertz *et al.*, 2003; Knippertz, 2005; Knippertz and Martin, 2005, 2007a; Ziv *et al.*, 2005; Hart *et al.*, 2010; De Vries *et al.*, 2013; Martius *et al.*, 2013).

Regarding the Arabian Peninsula, torrential rainfall in its central part in the winter season is associated with potential vorticity (PV) intrusions, upper- and lower-level cyclonic circulations and enhanced tropospheric moisture content (Kumar *et al.*, 2015). Recently, extreme precipitation and flooding events in the Jeddah region received increased attention in modelling

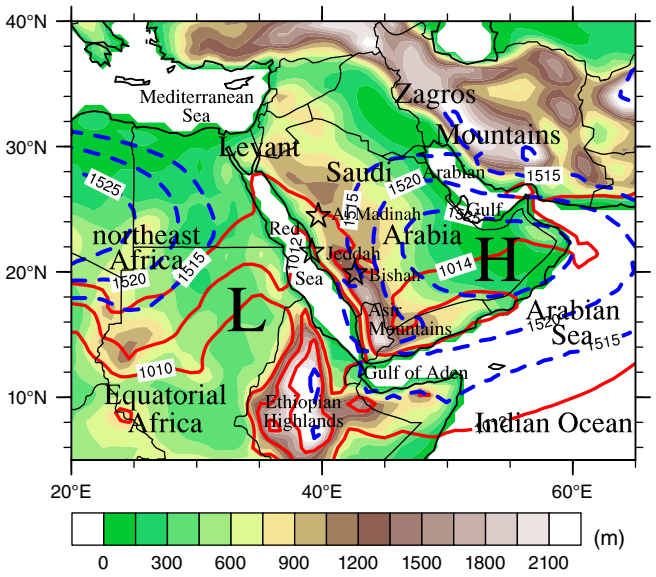

Figure 1. The Middle East region with topography from ERA-Interim data (m). The climatology (October–April; 1979–2012) of the mean-sea-level pressure (solid red contour lines at 1010, 1012 and 1014 hPa) and 850 hPa geopotential height (dashed blue contour lines at 1515, 1520 and 1525 gpm) depict the features of the Red Sea Trough ('L') and Arabian anticyclone ('H'), respectively. The locations of the regions affected during the three cases are indicated by stars.

studies (Haggag and El-Badry, 2013; Deng *et al.*, 2015) and diagnostic analyses (Al-Khalaf and Basset, 2013), while De Vries *et al.* (2013) addressed the Jeddah flooding of November 2009 in the context of the Active Red Sea Trough phenomenon. These studies described synoptic and mesoscale conditions: a cold midlatitude upper-level trough that merged with the Red Sea Trough, a stationary Arabian anticyclone which favoured moisture transport over the Arabian and Red Seas towards Jeddah, low-level convergence, upslope winds over the coastal zone and deep moist convection.

Apart from these studies, extreme precipitation events in Saudi Arabia and their underlying dynamics have not been investigated and are thus largely unexplored. This article presents a multiple-perspective analysis of three extreme precipitation cases in Saudi Arabia. The focus of this work is on the larger-scale circulations that govern the three extreme precipitation events. This approach follows the widely accepted perspective that large-scale processes generate the tropospheric environment that is conducive for development of convective storms (Doswell, 1987; Dayan *et al.*, 2015). Mesoscale processes are for this reason, along with the lack of available data at these scales, only briefly discussed in this article.

This study complements previous work on the Jeddah flooding of November 2009 by using a combination of diagnostic techniques to elucidate the dynamical processes of this specific case. We quantify circulation anomalies and dynamical lifting, discuss synoptic-scale dynamics from a PV perspective, calculate backward trajectories to study moisture pathways, and adopt sounding data to gain insight into the local tropospheric stratification and moisture profiles. Furthermore, the same framework is used to examine two additional cases that have not been previously investigated. The choice for these three events is motivated by their severe societal impacts, as emphasised in Table 1, and their occurrence in different seasons, that is, autumn, winter and spring. Although extreme precipitation and floods have also occurred during summer (Table 1), we do not include a summer case since such events are typically associated with tropical dynamics and the intertropical convergence zone (ITCZ). Finally, the three cases are discussed from a seasonal perspective that will link their different characteristics to the seasonal variability of the large-scale circulation over the region.

The organisation of the article is as follows. Section 2 describes the datasets and diagnostics used to study the precipitation characteristics, the synoptic circulation, moisture transport pathways and forcing mechanisms of upward motion of the three cases. We investigate the extreme precipitation events over the Jeddah region on 25 November 2009 (section 3), northwestern Saudi Arabia on 22 January 2005 (section 4), and the larger part of Saudi Arabia during late April and early May 2013 with the focus on southwestern Saudi Arabia on 1 May 2013 (section 5), hereafter referred to as the November, January and April–May cases, respectively. Section 6 discusses the three cases in a seasonal context. Finally, in section 7, we present the conclusions and synthesise the three cases by identifying their common key synoptic-scale features.

2. Data and methods

2.1. Employed datasets

We used ERA-Interim reanalysis data, precipitation observations, satellite imagery and sounding data. The ERA-Interim dataset of the European Centre for Medium-range Weather Forecasts (ECMWF) is produced by the Integrated Forecast System at the spectral resolution of T255L60 and spanning the years from 1979 until near-real-time (Dee *et al.*, 2011). We utilized 6-hourly analysis and forecast fields on surface, pressure, and isentropic levels to produce synoptic charts and to calculate time series based on arithmetic means over grid points in defined domains. Furthermore, the ERA-Interim data were employed for the calculation of normalized anomalies, backward air parcel trajectories and dynamical lifting (sections 2.2–2.4).

Precipitation observational data from stations and satellites provide insight into the temporal and spatial distribution of the rainfall, and their amounts highlight the extreme nature of the events. We employed 3-hourly and daily gridded rainfall estimates from the Tropical Rainfall Measuring Mission Multisatellite Precipitation Analysis (TMPA) 3B42 product, research version 7, at a high spatial resolution ($0.25^\circ \times 0.25^\circ$) with a quasi-global coverage (50°N–50°S), starting in 1998 (Huffman *et al.*, 2007). The TMPA 3B42 product (hereafter TRMM) is based on calibrated and combined multiple independent microwave and infrared sensor data, and is adjusted to monthly rain-gauge measurements.

We also included surface precipitation observations from 37 stations in Saudi Arabia from the National Climatic Data Center (NCDC) Global Summary of the Day (GSOD) dataset version 7, derived from sub-daily or hourly station observations*. Unfortunately, the station records have time series with missing data and interruption periods, in particular for the January case, and thus the data should be interpreted with caution. Furthermore, we used Meteosat geostationary satellite images from the Dundee Satellite Receiving Station† to explore cloud characteristics. Sounding data from the University of Wyoming‡ provide insight into the local vertical structure of the troposphere during the extreme rainfall events.

2.2. Synoptic circulation and normalized anomalies

We produced synoptic charts of the upper-level and low-level troposphere to identify the relevant features in the large-scale flow. In addition, normalized anomalies were calculated using the long-term (1979–2013) 21-day running mean and standard deviation (STD) values of daily means, subtracting the seasonal cycle, following Hart and Grumm (2001), Moore *et al.* (2012), and Galarneau *et al.* (2012):

$$N = \frac{(X - \mu)}{\sigma}, \tag{1}$$

where X is the daily mean value of the variable, μ the climatological mean value and σ the STD of the daily mean. The normalized anomalies provide a quantification of how unusual the large-scale flow was in a climatological context and help to identify the relevant processes in the synoptic-scale circulation.

2.3. Moisture pathways and air parcel trajectories

Moisture transport pathways are studied in Eulerian and Lagrangian frameworks. Using ERA-Interim data, we computed vertically integrated horizontal water vapour fluxes (IVFs) over different ranges of pressure levels:

$$\mathrm{IVF} = \frac{1}{g}\int_{P_{\mathrm{bottom}}}^{P_{\mathrm{top}}} q\mathbf{v}\,\mathrm{d}p, \tag{2}$$

where g is the gravitational acceleration, q the specific humidity, and $\mathbf{v}$ the horizontal wind.

Backward trajectories were calculated from defined target areas based on 6-hourly ERA-Interim data on a regular grid ($1^\circ \times 1^\circ$) and model levels between the surface and 200 hPa, using the Lagrangian analysis tool (LAGRANTO) model (Wernli and Davies, 1997; Sprenger and Wernli, 2015). We selected trajectories that are relevant for moisture transport pathways using relative humidity (>80%) and moisture flux ($>100\,\mathrm{g\,kg^{-1}\,m\,s^{-1}}$) thresholds, applied to air parcels at the initial time of the trajectory calculations. The first criterion is used to identify air parcels that are likely to contribute to precipitation (Sodemann *et al.*, 2008; Piaget *et al.*, 2015). The second criterion, following studies that addressed tropical moisture export (Knippertz *et al.*, 2013), identifies air parcels that bring significant amounts of moisture into the area of interest, and is applied only for the November and April–May cases since ERA-Interim strongly underestimates precipitation amounts in these cases (sections 3.1 and 5.1). Meteorological variables were traced along subsets of trajectories to provide insight into atmospheric processes and the moisture budget along their pathways. It should be noted that there are potential limitations to the validity of the trajectory calculations which are inherent to the resolution of the ERA-Interim data, in particular for trajectories that pass through regions of strong convection where air masses can undergo deep and rapid mixing. This caveat should be borne in mind when interpreting the results from the Lagrangian analysis.

*Available at http://www.ncdc.noaa.gov/, accessed 11 November 2014.

†Available at http://sat.dundee.ac.uk/, accessed 18 December 2013.

‡Available at http://weather.uwyo.edu/upperair/sounding.html, accessed 15 December 2014.

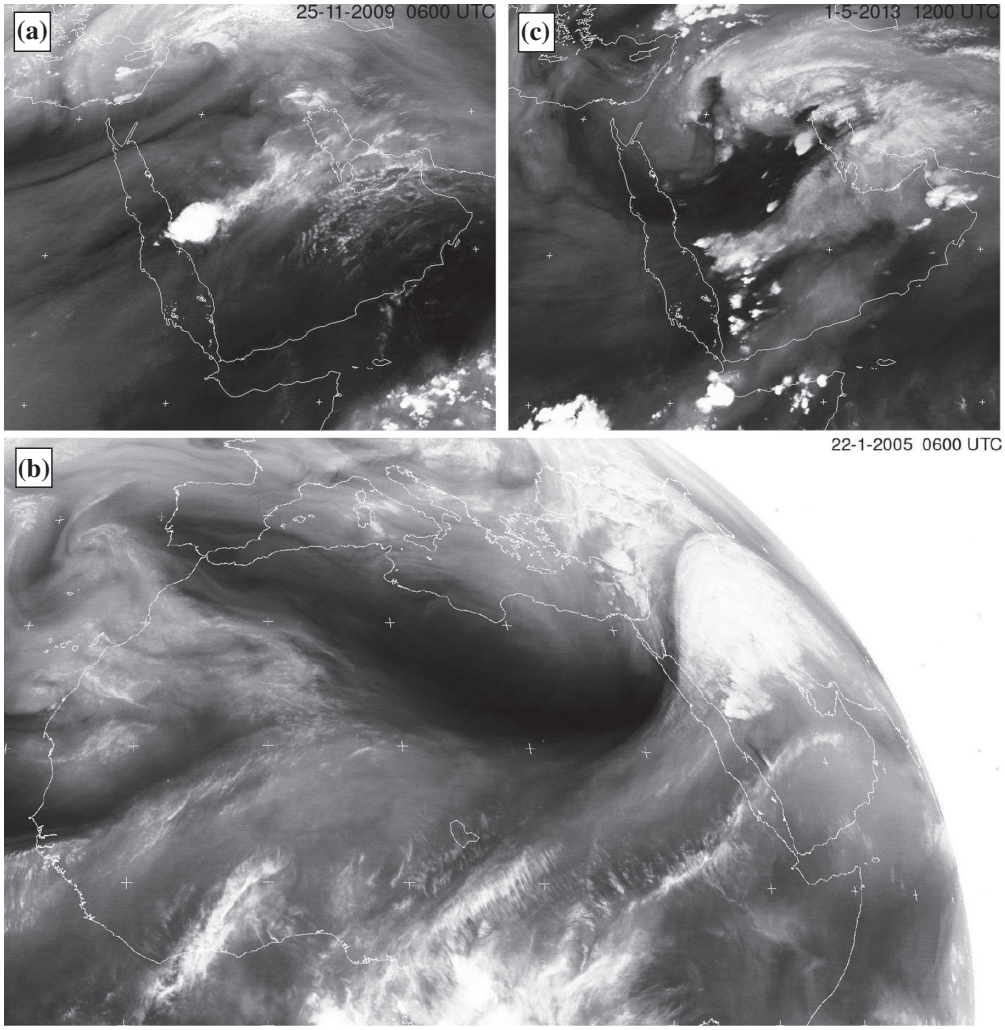

Figure 2. Meteosat Visible and Infrared Spin-Scan Radiometer (VISSR) images, channel 3 (range of 5.7–7.1 μm; mid-IR/water vapour), on (a) 0600 UTC 25 November 2009, (b) 0600 UTC 22 January 2005, and (c) 1200 UTC 1 May 2013.

2.4. Forcing of ascent and dynamical lifting

The quasi-geostrophic omega equation has been used in previous studies of extreme precipitation to estimate the contribution of the balanced dynamics to upward motion in the region of precipitation (Knippertz and Martin, 2005, 2007a; Hart *et al.*, 2010; Martius *et al.*, 2013). In this study, we employed the omega equation under alternative balance (Davies-Jones, 1991). This approach diagnoses vertical motion from the non-divergent wind instead of the geostrophic wind and can thus be considered more accurate, in particular in the vicinity of upper-level troughs where the flow exhibits strong curvature and the Rossby number is relatively large. The alternative-balance omega equation reads (Riemer *et al.*, 2014):

$$\nabla_p \cdot (\sigma \nabla_p \omega) + f_0^2 \left\{ \frac{\partial^2 \omega}{\partial p^2} - \frac{1}{p} \frac{c_v}{c_p} \left(\frac{\partial \omega}{\partial p} + \frac{\omega}{p} \right) \right\} = -2 \nabla_p \cdot \mathbf{Q}_{\mathrm{AB}}, \tag{3}$$

with

$$\mathbf{Q}_{\mathrm{AB}} = -\nabla_p \mathbf{v}_\psi \cdot \nabla_p \alpha, \tag{4}$$

where ∇_p is the horizontal gradient on pressure levels, ω the vertical velocity (balanced omega), $\mathbf{v}_\psi$ the non-divergent wind, f_0 the constant Coriolis parameter, and c_v and c_p the specific heats of dry air at constant volume and pressure, respectively. Furthermore, $\sigma = -\alpha_0 {\theta_0}^{-1} \, \partial\theta_0/\partial p$ and $\alpha = \theta \, R p^{-1} (p/p_0)^\kappa$ where R is the gas constant of dry air, $\kappa = R/c_p$, and α_0 and θ_0 denote the reference vertical profiles of specific volume and potential temperature, respectively. The omega equation was applied on ERA-Interim data for the domain (9.5–40.5°N, 10–70°E) and the isobaric surfaces between 900 and 1 hPa. Hereafter, we refer to balanced upward motion as dynamical lifting.

We also explored the orographic influence and susceptibility of the atmosphere to deep moist convection. Based on sounding data from the Jeddah (November case), Al Madinah (Medina) (January case), and Abha (April–May case) stations and satellite data, some inferences can be made about the potential mesoscale organisation of the precipitating systems. Clearly, however, the ERA-Interim data do not resolve this scale and our analysis is limited in this regard.

3. Flooding of Jeddah in November 2009

3.1. Precipitation characteristics

Satellite images demonstrate a large quasi-stationary mesoscale convective system over the Jeddah region on 25 November 2009 from 0000 to 1200 UTC, depicted at 0600 UTC in Figure 2(a). The storm produced localized extreme precipitation over Jeddah (Figure 3). Rainfall maxima from TRMM exceeded 80 mm day^{-1} (Figure 3(b)) and the Jeddah station in the GSOD data observed 70 mm (Figure 3(c)), surpassing the annual mean of 52.1 mm (Almazroui *et al.*, 2012). Precipitation in ERA-Interim agrees fairly well with TRMM estimates in terms of timing and spatial distribution (Figure 3(a,b,d), see also Figure 7(e)), but underestimates rainfall amounts over the Jeddah region on 25 November by more than a factor 2 (Figure 3(d)).

The extreme character of the Jeddah flooding was also emphasised by Haggag and El-Badry (2013), reporting a station in

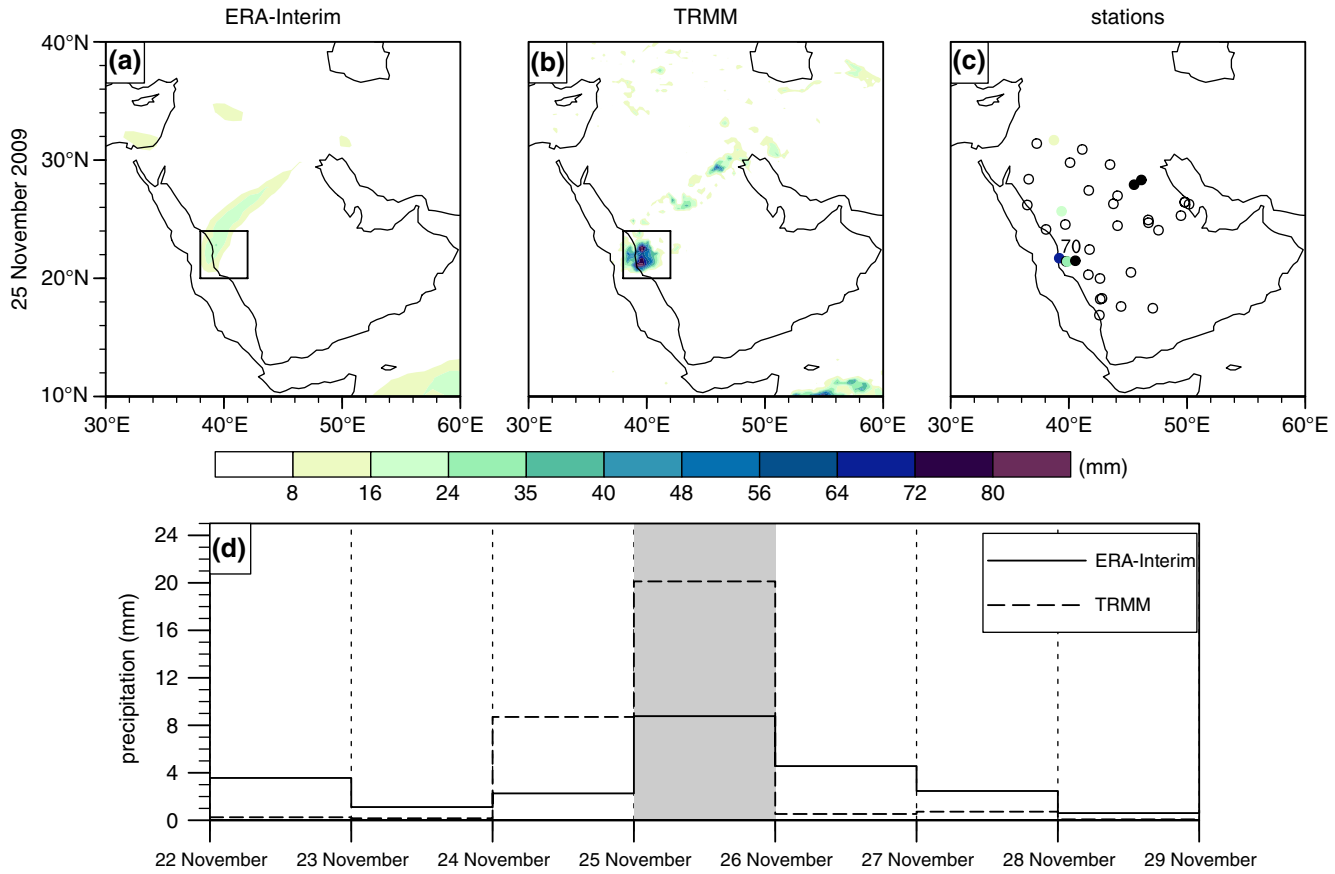

Figure 3. Daily accumulated precipitation (mm) on 25 November 2009 in (a) ERA-Interim, (b) TRMM, (c) GSOD station data, and (d) the time evolution of domain-averaged daily precipitation in ERA-Interim and TRMM over the grid points in the box (38–42°E, 20–24°N) depicted in (a) and (b). Missing values in GSOD data in (c) are indicated by black circles. The Jeddah station (410240), indicated in (c), measured 70 mm rainfall. The grey shading in (d) emphasises the day of interest.

Jeddah that measured 180 mm rainfall from 24 to 26 November 2009, being more than threefold the local annual mean, while their mesoscale model simulated rainfall in excess of 400 mm over the same time span over the most strongly affected parts of Jeddah.

3.2. *Synoptic circulation*

Preceding the Jeddah flooding, amplification of the midlatitude Rossby wave pattern occurred in the far upstream region over the North Atlantic, resulting in anticyclonic Rossby wave breaking[§] (Thorncroft *et al.*, 1993) and cut-off low formation along the northwestern coast of Africa (not shown). Subsequently, the cut-off low travelled eastward over North Africa (Figure 4(a,j)). The cut-off low was entrained within the large-scale trough over the eastern Mediterranean on 24 November, followed by another anticyclonic Rossby wave breaking event over the Middle East on 25 November (Figure 4(b,c,k,l)). The associated midlatitude upper-level trough intruded far into low-latitudes over northeastern Africa (Figure 4(c)). Farther downstream and near the surface, the Red Sea Trough amplified northward and the Arabian anticyclone intensified on 24 and 25 November (Figure 4(d–i)), which will be shown to be important for moisture transport.

Normalized anomalies in the mean-sea-level pressure exceeded 1.5 STD below normal over the Red Sea region on 24 and 25 November, and emphasize the northward amplification of the Red Sea Trough (Figure 4(d–f)). In the 500 hPa geopotential height, normalized anomalies exceeded 1.5 STD below normal over northeastern Africa on 25 November, and highlight the equatorward intrusion of the midlatitude trough (Figure 4(a–c)). The synoptic circulation was thus characterized by an unusual, but not extreme, deviation from climatology. Nevertheless, these normalized anomalies reveal that the Red Sea Trough amplification occurred upon arrival of the midlatitude trough over northeastern Africa, indicating an important interaction between the upper-level and lower-level circulations.

This interaction can be understood from a PV perspective whereby an upper-tropospheric PV maximum is located upstream of a lower-tropospheric potential temperature maximum (Hoskins *et al.*, 1985). Figure 4(j–l) clearly reveals this phase-relationship between the upper-level PV maximum over northeastern Africa and the lower-level potential temperature maximum downstream over the Red Sea region, which suggests that the anomalies in Figure 4(a–f) developed through baroclinic growth. Thus, the transient midlatitude upper-level trough that arose from anticyclonic Rossby wave breaking interacted with the climatological Red Sea Trough near the surface, and was instrumental for guiding the moist air masses towards Jeddah, as will be discussed in section 3.3.

3.3. *Moisture transport pathways*

In autumn, moist tropical air masses usually travel westward over the Arabian Sea, curve northward across the Red Sea region, and then return towards the Tropics over equatorial Africa, following the climatological easterly low-level circulation (De Vries *et al.*, 2013). During the November case, however, the particular configuration of the synoptic circulation deflected the moist air flow towards the Arabian Peninsula. The average IVFs between 1000 and 300 hPa during 23–25 November 2009 demonstrate enhanced moisture transport over the Arabian and Red Seas towards Jeddah, leading to anomalous total column water (TCW) amounts over the Jeddah region (>2 STD) and

[§]Anticyclonic wave breaking, also referred to as LC1 wave breaking, is characterized by warm air located poleward of cold air together with northeast–southwest tilt of the trough–ridge pair.

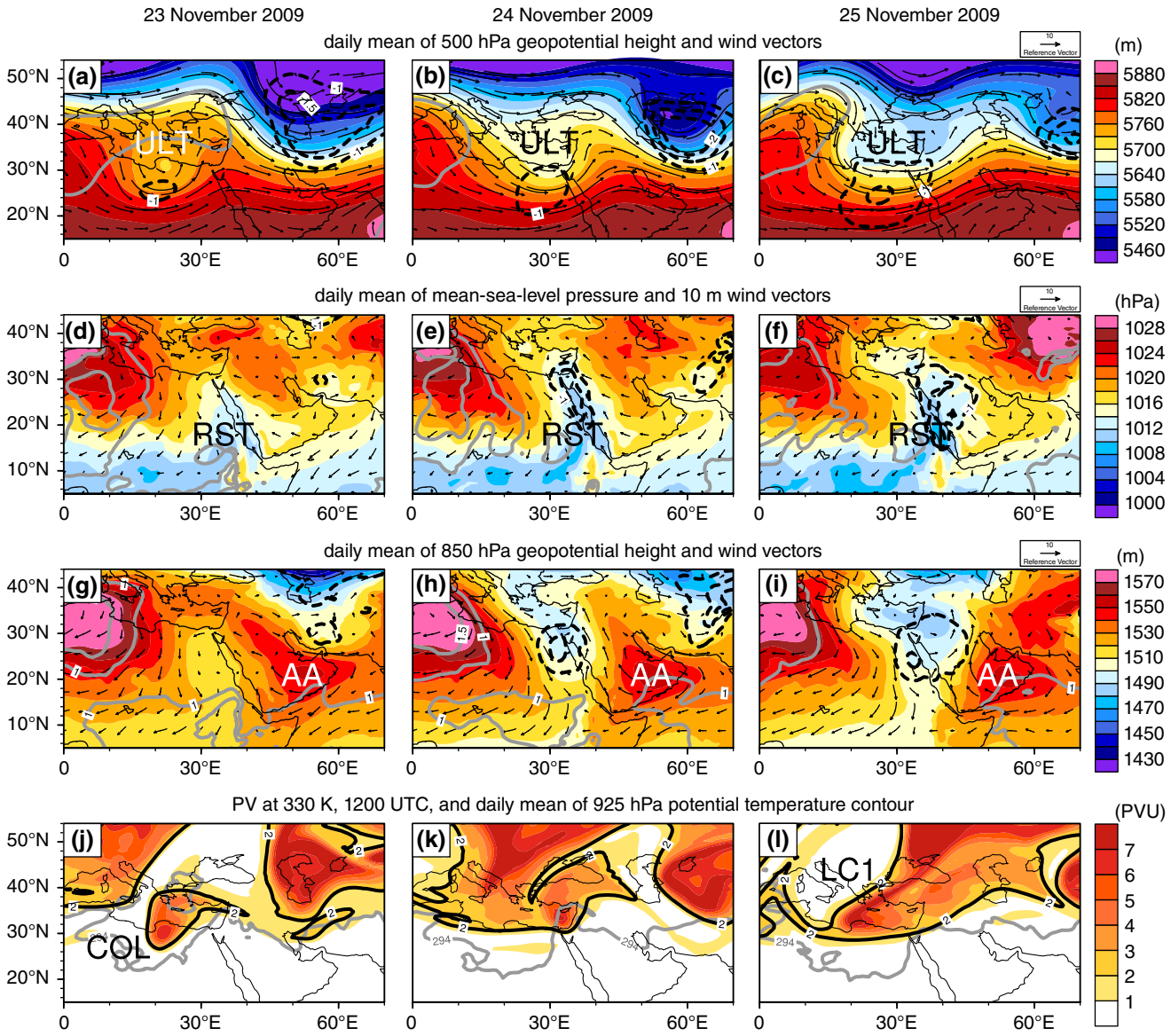

Figure 4. (a)–(c) Geopotential height (shaded, gpm) and wind vectors ($m\,s^{-1}$) at 500 hPa, (d)–(f) mean-sea-level pressure (shaded, hPa) and 10 m wind vectors ($m\,s^{-1}$), (g)–(i) geopotential height (shaded, gpm) and wind vectors ($m\,s^{-1}$) at 850 hPa, and (j)–(l) PV (shaded, PVU) with the 2 PVU contour (thick black line) at 330 K and the 294 K potential temperature contour (thick grey line) at 925 hPa. The panels show 6-hourly data (1200 UTC) for PV and daily means for all other variables at (left) 23, (middle) 24, and (right) 25 November 2009. Normalized anomalies of mean-sea-level pressure in (d)–(f) and geopotential height in (a)–(c) and (g)–(i) are displayed in thick contours at 1, 1.5, 2, 3 and 4 STD in grey solid lines (positive values) and black dashed lines (negative values); see the text for details. The positions of the upper-level trough (ULT), Red Sea Trough (RST), Arabian anticyclone (AA) and anticyclonic Rossby wave breaking (LC1) are indicated.

the interior of the Arabian Peninsula (>3 STD) on 25 November (Figure 5). Previous studies demonstrated that the moisture transport was predominantly confined to lower-tropospheric levels over the warm sea waters (De Vries *et al.*, 2013; Haggag and El-Badry, 2013), favoured by the intensified Arabian anticyclone (>1 STD) on 24 and 25 November 2009 (Figure 4(h,i)).

We calculated backward trajectories, started at 1200 UTC 25 November 2009, from all grid points in the box (38–42°E, 20–24°N) as depicted in Figure 3(a,b). Air parcels with a relative humidity >80% or moisture flux >100 $g\,kg^{-1}\,m\,s^{-1}$ at the initial time are retained to select the trajectories that contributed to precipitation or brought substantial moisture amounts into the region of interest. These air parcels were predominantly advected over the Arabian and Red Seas where their moisture content increased significantly (Figure 6(a)). The trajectories were calculated for a relatively long period (168 h) back in time as the wind velocities were relatively weak and loss of moisture was little since only minimal precipitation occurred along their pathways (not shown).

The backward trajectories were subjectively subdivided into three different branches with distinct origins and pathways. One bundle of trajectories originated over the northern Arabian Peninsula (Box A in Figure 6(a)), reaching across the northern Red Sea where strong evaporation led to a rapid increase in the mean specific humidity from 7 up to 15 $g\,kg^{-1}$ during the 72 h prior to arrival over the Jeddah region (Figure 6(b)). A second cluster of initially dry air parcels passed over the Arabian Peninsula at middle levels (Box B in Figure 6(a)), progressed in a descending anticyclonic motion over the Gulf of Aden into the southern Red Sea basin, and gained humidity at lower-tropospheric levels over the sea surface during the 72 h before reaching Jeddah (Figure 6(c)). Apart from the nearby Red Sea, moisture from the remote Arabian Sea also reached the target area. Air parcels that resided at lower-tropospheric levels over the Arabian Sea (Box C in Figure 6(a)) already contained large mean absolute moisture amounts (6.5 $g\,kg^{-1}$) at −168 h that further increased up to 15.5 $g\,kg^{-1}$ along their pathways over the Gulf of Aden and the Red Sea (Figure 6(a,d)). Loss of moisture along these trajectory branches was negligible since minimal precipitation was observed along their pathways (not shown).

Accordingly, the Lagrangian analysis reveals that most of the moisture was collected over the warm surface of the Red Sea, while some moisture also originated from the Arabian Sea. Importantly, the trajectory bundles approached Jeddah from the north and

south (Figure 6(a)), respectively, and imply low-level moisture convergence over the region, in agreement with previous work (Al-Khalaf and Basset, 2013; Haggag and El-Badry, 2013; Deng *et al.*, 2015). The confluence of low-level moist air masses resulted from the coupling of the midlatitude and tropical circulations, and supported the heavy rainfall over Jeddah.

3.4. *Upward motion*

The coexistence of the anticyclonic circulation over the Arabian Peninsula and the cyclonic circulation over the eastern Mediterranean (Figure 4(h,i)) steered a southwesterly low-level flow against the topographic barrier along the Red Sea coast, resulting in orographic lifting of the moist air masses (Figure 7(c)). In agreement with previous work, this suggests that orographic influence was important for the forcing of upward motion (Haggag and El-Badry, 2013).

At 1200 UTC 25 November, an upper-level trough dominated over the region of interest, accompanied by relatively weak upward motion on its eastern flank (Figure 7(a)). Balanced omega at 500 hPa demonstrates a roughly similar spatial structure compared to the 500 hPa total omega in ERA-Interim data; however, its maximum ($-15\,\mathrm{Pa\,s^{-1}}$) is substantially weaker and slightly displaced to the north compared to the maximum in the 500 hPa total omega ($-0.5\,\mathrm{Pa\,s^{-1}}$). Accordingly, dynamical lifting was not the primary contribution to the strong localized upward motion over the Jeddah region; however, it may have indirectly contributed through a reduction of the static stability. The static stability between 850 and 500 hPa, averaged over the region of interest, decreased between 0000 UTC and 1800 UTC

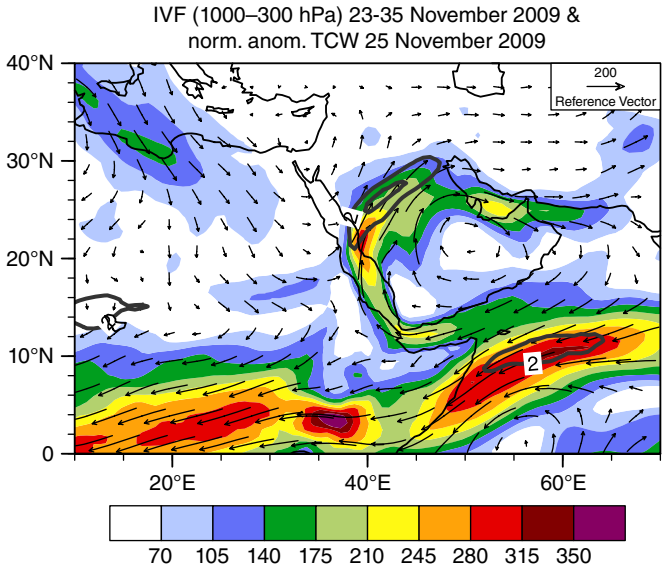

Figure 5. Magnitude (shaded) and direction (vectors) of IVFs ($\mathrm{kg\,m^{-1}\,s^{-1}}$) averaged over 23–25 November 2009 over pressure levels from 1000 to 300 hPa. The thick grey contour lines depict the normalized anomalies of TCW at 2 and 3 STD above normal at 25 November 2009.

24 November from 0.0054 to 0.0043 $\mathrm{K\,m^2\,kg^{-1}}$, corresponding to a reduction of about 20%.

A build-up of convective available potential energy (CAPE) is found in ERA-Interim data towards 1200 UTC 25 November (Figure 7(d)) with very high values exceeding 3400 $\mathrm{J\,kg^{-1}}$ just to

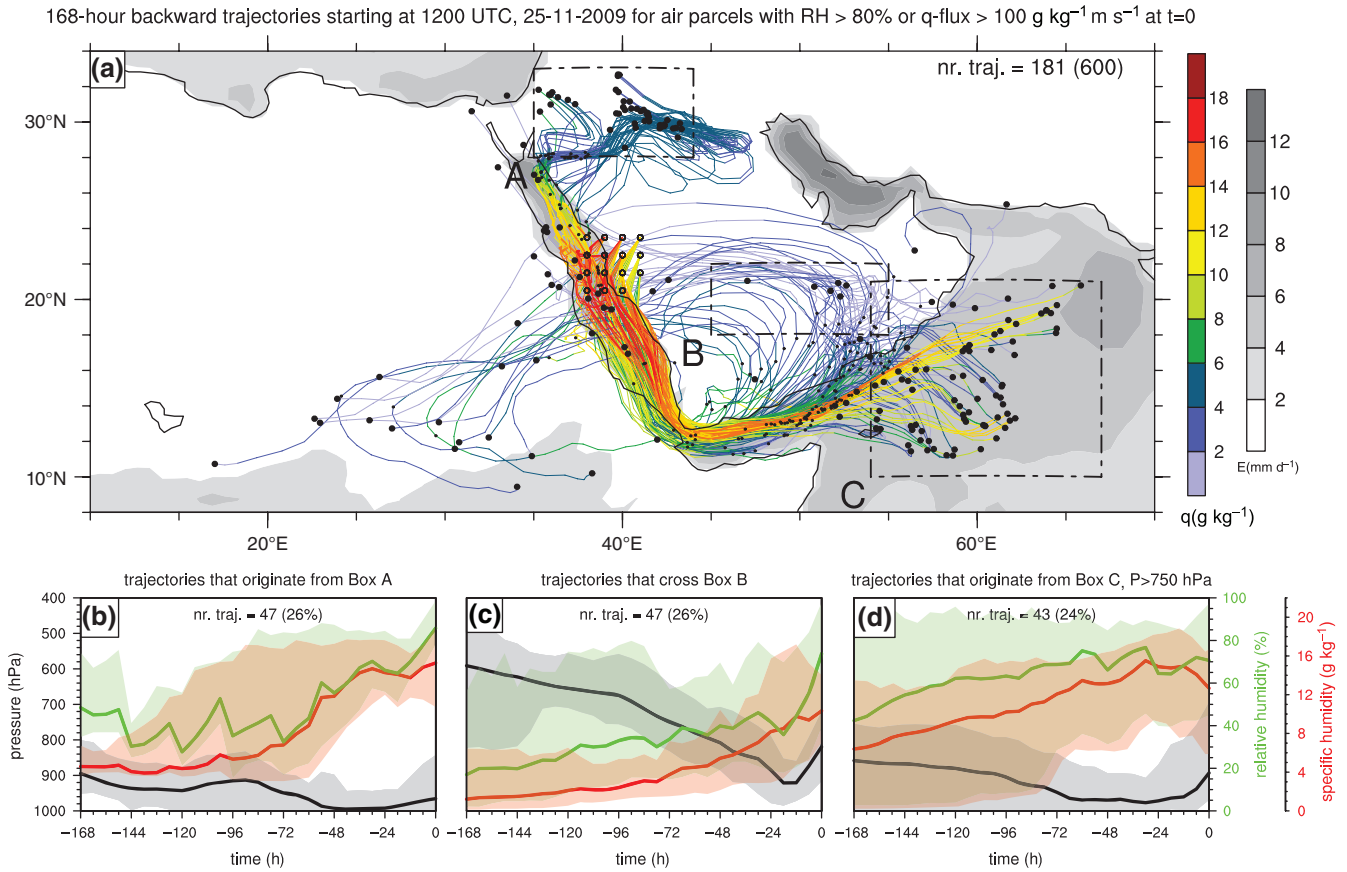

Figure 6. The 168-hour backward trajectories started at 1200 UTC 25 November 2009 from all grid points in the box depicted in Figure 3(a,b) between surface and 200 hPa and with a relative humidity >80% or moisture flux $>100\,\mathrm{g\,kg^{-1}\,m\,s^{-1}}$ at $t=0$. (a) depicts the specific humidity ($\mathrm{g\,kg^{-1}}$) along the trajectories in colours and the surface evaporation ($\mathrm{mm\,day^{-1}}$), averaged over the duration of the trajectories, in grey shading. Open circles denote the start points and filled circles the end points of the trajectories, and small filled circles are plotted at −72 h. Meteorological variables along trajectories from (a) are displayed for subsets of air parcels that (b) are located in box A (35–44°E, 28–33°N) at −168 h, (c) cross box B (45–55°E, 18–22°N) at any time, and (d) are located in box C (54–67°E, 10–21°N) with pressure >750 hPa at −168 h. (b)–(d) demonstrate the mean (thick lines) and spread (shaded intervals), determined by the minimum and maximum values at each time step, of the pressure (hPa) in black and grey, relative humidity (%) in green and light green, and specific humidity ($\mathrm{g\,kg^{-1}}$) in red and light red along the subsets of trajectories. The numbers of trajectories are stated in each panel, in (b)–(d) followed by their percentage of the selected trajectories as in (a) in brackets, and in (a) followed by the number of total calculated trajectories in brackets.

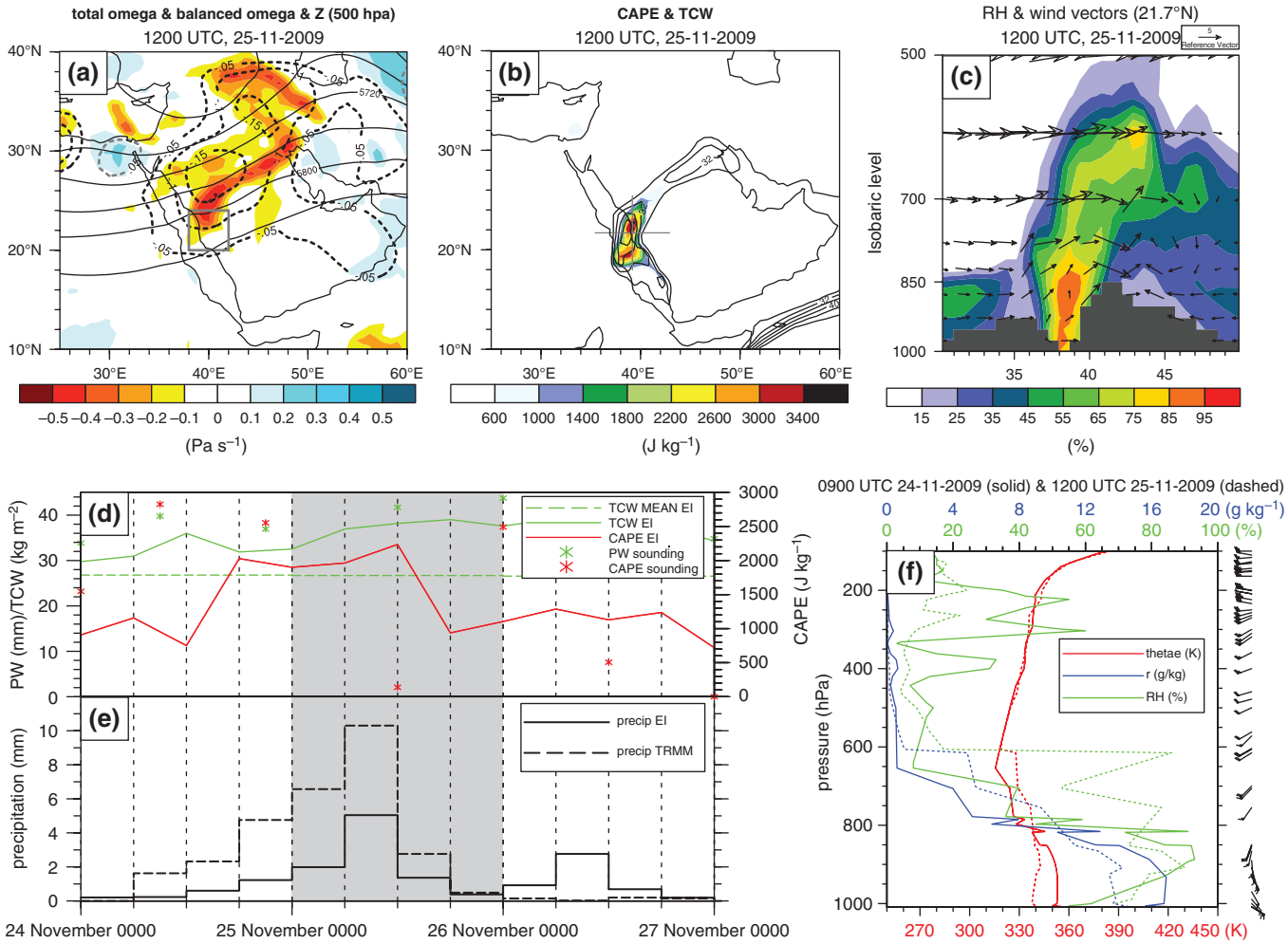

Figure 7. At 1200 UTC 25 November 2009: (a) total omega (Pa s^{-1}; red colours denote ascent), balanced omega, detailed in the text, in thick dashed black (negative values) and grey (positive values) contours at 0.05 Pa s^{-1} intervals, and geopotential height contours (thin lines at 40 gpm intervals) at 500 hPa, (b) CAPE (J kg^{-1}) +12 h forecast at 0000 UTC 25 November 2009 and TCW (contours at intervals of 4 kg m^{-2}, starting at 28 kg m^{-2}), and (c) vertical cross-section (21.7°N) of relative humidity (%) and wind vectors (m s^{-1}) with the vertical component scaled by a factor ×100. The temporal evolution of (d) CAPE (J kg^{-1}) and precipitable water (mm) in sounding data from the Jeddah station (39.18°E, 21.7°N, 17 m; see the grey marker in (b)), and in ERA-Interim, at the corresponding location, CAPE (J kg^{-1}) +6 and +12 h forecasts at 0000 and 1200 UTC, and the instantaneous and long-term (1979–2013) 21-day running mean of TCW (mm), and (e) the domain averaged precipitation (mm) derived from +6 to +12 h forecasts in ERA-Interim and 3-hourly data in TRMM. In (f), the vertical profile of equivalent potential temperature (K), relative humidity (%) and mixing ratio (g kg^{-1}) in the sounding data of the Jeddah station at 0900 UTC 24 November (solid lines) and 1200 UTC 25 November 2009 (dashed lines and wind barbs). The domain averages in (e) are calculated over the grid points in the box as in Figure 3(a,b) which is for clarity also depicted in grey in (a). The grey shading in (d)–(e) emphasises the day of interest.

the north of Jeddah (Figure 7(b)). Interestingly, in the sounding data of the Jeddah station, high CAPE values (>2500 J kg^{-1}) at 0900 UTC and 2100 UTC 24 November were followed by a very low CAPE value at 1200 UTC 25 November, demonstrating the release of CAPE during the period with the most heavy rainfall in ERA-Interim and TRMM data (Figure 7(d,e)). Thus, the reduced static stability and enhanced tropospheric moisture content over Jeddah, locally reaching up to 40 kg m^{-2} (Figure 7(b,d)), promoted favourable thermodynamic conditions for deep moist convection.

The sounding profile at 0900 UTC 24 November reveals that the lower troposphere was characterized by high water vapour mixing ratio (16 g kg^{-1}) and relative humidity (>90%). Large potential instability is evident as the equivalent potential temperature decreased from 353 K near the surface to a minimum of 316 K at 654 hPa (Figure 7(f)). By 1200 UTC 25 November, the profile was roughly moist adiabatic, indicating that the potential instability was largely released (Figure 7(f)). Most likely, orographic lifting of the westerly flow over the mountainous Red Sea coast (Figure 7(c)) led to parcel saturation and the release of potential instability, supporting the formation of the mesoscale convective system over Jeddah as observed in satellite imagery (section 3.1). This formation was likely favoured by strong vertical wind shear (26.5 m s^{-1} between 17 m ASL and 4179 m ASL) found in sounding data (Figure 7(f)), which is associated with development of supercell storms (Holton, 2004). Furthermore, the strong low-level moisture convergence (see section 3.3) may have sustained the deep moist convection.

In summary, the interaction between the midlatitude and tropical circulations resulted in enhanced moisture transport towards the Jeddah region. Locally, low-level moisture convergence, reduction of static stability, and orographic lifting favoured the build-up and release of potential instability, supporting the deep moist convection and the heavy rainfall.

4. Heavy rainfall in northwestern Saudi Arabia in January 2005

4.1. *Precipitation characteristics*

On 22 January 2005, widespread and heavy precipitation affected the northern parts of the Arabian Peninsula (Figure 8). TRMM daily estimates in Figure 8(b) exceeded 60 mm day^{-1} over a substantial part of Saudi Arabia, and were locally greater than 120 mm day^{-1} in the Al Madinah region where floods occurred (Table 1). The amounts, spatial distribution and timing of ERA-Interim precipitation correspond fairly well to the TRMM rainfall estimates (Figure 8(a,b,d), see also Figure 13(e)), except for the local maxima in the Al Madinah region.

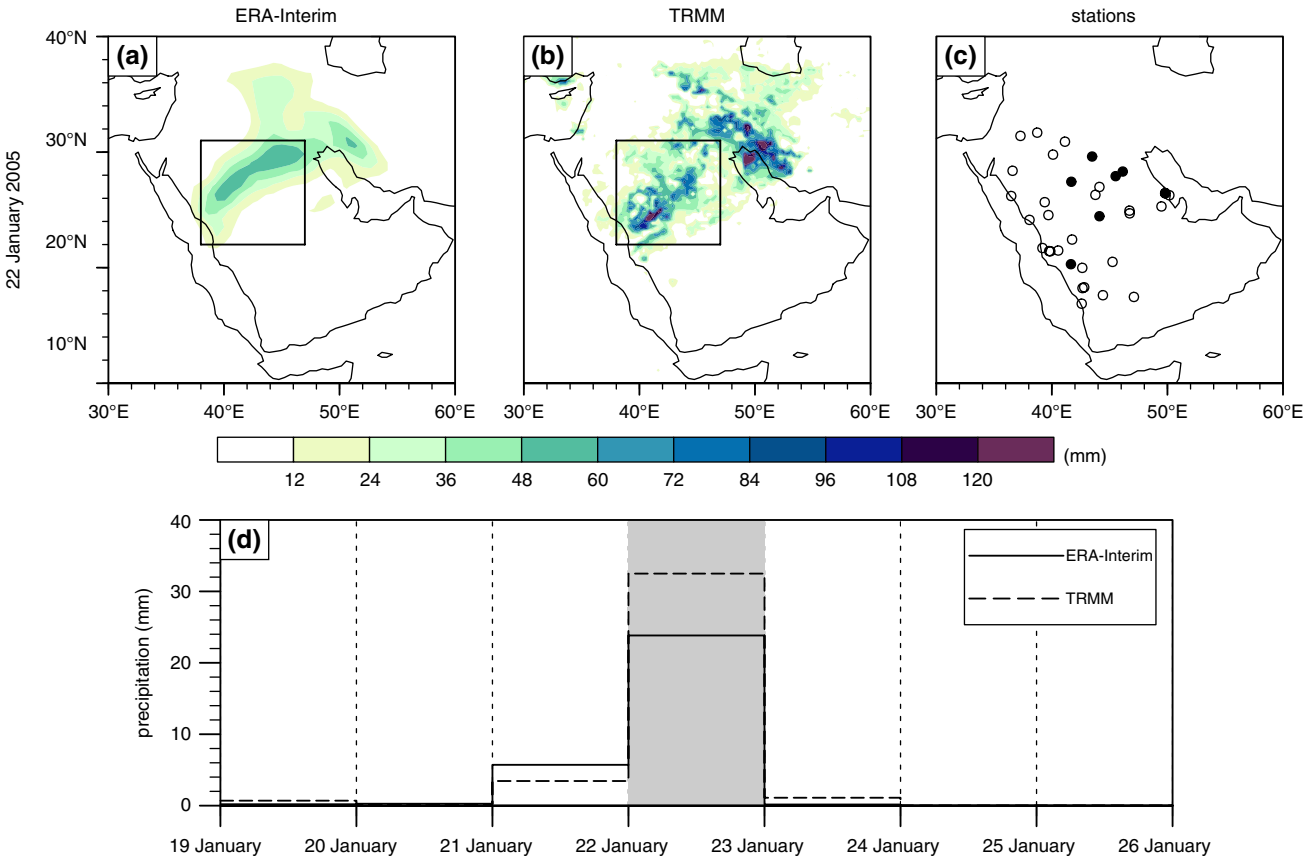

Figure 8. As Figure 3, but for the January case: (a)–(c) on 22 January 2005 and (d) the time evolution of domain averages over the grid points in the box (38–47°E, 22–31°N) depicted in (a) and (b).

GSOD data have strong limitations for this case as stations reported only zero and missing values on 22 January (Figure 8(c)). For example, the Al Madinah station indicated zero rainfall, while the Emergency Events Database reported 29 fatalities and 67 affected persons in the region, attributed to floods (Table 1). It should be noted though, that flags in GSOD data, not presented in Figure 8(c), indicate missing 6-hourly reports and rain and/or thunder for several stations in northern Saudi Arabia, including the Al Madinah station, suggesting incomplete data records.

Satellite imagery demonstrates extensive clouds over the Arabian Peninsula with scattered tail structures reaching from equatorial Africa (Figure 2(b)), resembling characteristics of tropical plumes affecting the Middle East (Ziv, 2001; Rubin *et al.*, 2007; Tubi and Dayan, 2014). In the next section, we will show that not only the cloud characteristics, but also the dynamics are similar to those of tropical plumes.

4.2. *Synoptic circulation*

Prior to the January case, strong midlatitude wave amplification in the far upstream region resulted in the formation of a pronounced block over the eastern Atlantic. Along its downstream flank, a short-wave trough rapidly developed and intruded far into the subtropics over North Africa (20 January), thinned substantially (21 January), and swept over northern Saudi Arabia (22 January), see Figure 9(a–c). Normalized anomalies in the 500 hPa geopotential height on 21 January exceeded 4 STD below normal and reached as far as 10°N, highlighting the extreme nature of the equatorward upper-level trough intrusion (Figure 9(b)). The midlatitude trough was part of a wave train that travelled from the midlatitudes towards the Tropics. The 500 hPa geopotential height normalized anomalies in Figure 9(a–c) illustrate this wave train with three centres, reaching their respective maxima over the eastern Atlantic on 20 January (>1.5 STD above normal), over North Africa on 21 January (>4 STD below normal) and the Arabian Peninsula on 22 January (>2 STD above normal). Beneath the latter anomaly, the Arabian anticyclone intensified on 21 January (>1 STD; Figure 10(a)) and promoted the poleward transport of tropical moisture (section 4.3).

Unlike the November case, a surface cyclone formed over the Mediterranean Sea. The cyclone approached the North African coast and then connected with the low-pressure belt over equatorial Africa as the pressure within the intervening region decreased (20 January; Figure 9(d)). As a result, a low-pressure zone formed over northeastern Africa and the Red Sea region (21 January; Figure 9(e)), followed by cyclogenesis over the Levant on the following day (Figure 9(f)). In contrast to the Jeddah flooding case, the normalized anomalies (Figure 9(a–c)) in the upper-level circulation were very large (>4 STD), emphasizing that the midlatitude forcing was very pronounced. Consistent with these large STDs, the pressure pattern in the lower troposphere did not exhibit the Red Sea Trough feature, but was dominated by the coupling of the midlatitude upper-level trough and the equatorial low-pressure zone.

Synoptic charts in a PV framework exhibit a meridionally elongating PV streamer over northeastern Africa extending southward to 20°N, illustrating anticyclonic wave breaking, and a northward amplifying low-level potential temperature maximum farther downstream (Figure 10(b)). This phase relationship suggests strong and rapid baroclinic wave growth throughout the troposphere (Hoskins *et al.*, 1985).

The dynamics of the January case show similarities to those of tropical plumes associated with extreme precipitation over subtropical regions: Rossby wave train propagation towards the Tropics, anticyclonic wave breaking and the intrusion of the upper-level trough into low latitudes (Ziv, 2001; Knippertz, 2005, 2007; Knippertz and Martin, 2005; Rubin *et al.*, 2007; Hart *et al.*, 2010; Tubi and Dayan, 2014). Also consistent with tropical plumes, the upper-tropospheric circulation exhibited poleward outflow from the Tropics and a subtropical jet with anticyclonic curvature, accompanied by a jet streak on the eastern flank of the

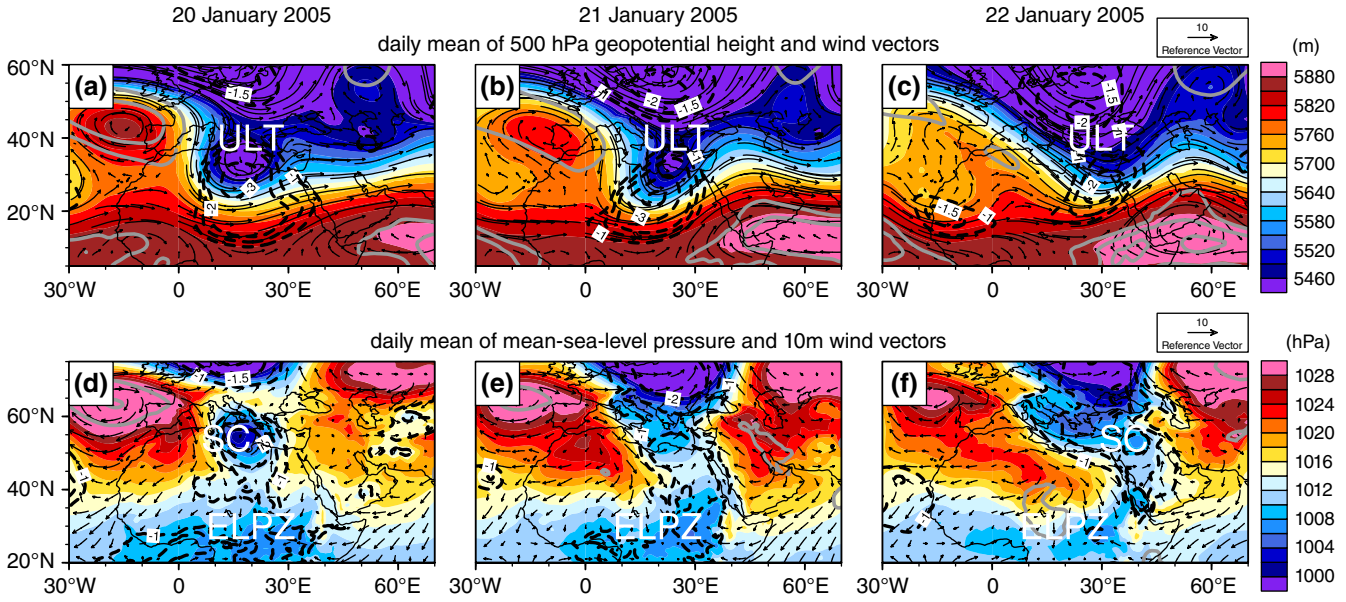

Figure 9. As Figure 4(a)–(f), but for the January case at (a,d) 20, (b,e) 21, and (c,f) 22 January 2005. The positions of the upper-level trough (ULT), surface cyclone (SC) and equatorial low-pressure zone (ELPZ) are indicated.

midlatitude trough with southwest–northeast tilt and velocities reaching over 72 m s^{-1} (Figure 10(c)).

4.3. *Moisture transport pathways*

The coupling between the midlatitude and tropical circulations facilitated the export of tropical moisture towards the Arabian Peninsula. During 20–22 January, enhanced IVFs are observed over the Arabian and Red Seas, equatorial and northeastern Africa, and the Arabian Peninsula, leading to above-normal TCW (>3 STD) over the larger part of northern Saudi Arabia on 22 January (Figure 11(a)). Moisture fluxes in the lower troposphere (1000–700 hPa) occurred predominantly over the Arabian and Red Seas (not shown) and were driven by the intensified Arabian anticyclone (Figure 10(a)). In the middle and upper troposphere (700–300 hPa), IVFs exhibited a clear maximum on the eastern flank of the midlatitude trough which transported the tropical moisture over the dry planetary boundary layer across equatorial and northeastern Africa towards the Middle East (Figure 11(b)), being typical of tropical plumes over the region (Ziv, 2001; Rubin *et al.*, 2007; Tubi and Dayan, 2014).

We calculated backward trajectories from grid points in the box (38–47°E, 22–31°N), as shown in Figure 8(a,b), starting at 1200 UTC 22 January. The calculations differ in some aspects from the November and April–May cases: trajectories are calculated from grid points at 200 km intervals since the target area is large and only 120 h back in time as the synoptic circulation was strong and air parcels travelled over large distances in a relatively short time period. We retained only the trajectories with a relative humidity >80% at the initial time as precipitation was reasonably well represented in ERA-Interim data.

The trajectories depict a complex situation with air parcels originating from various source regions (Figure 12(a)). We focus on three regions that together provide the majority of the air parcels: the eastern Mediterranean Basin, equatorial Africa, and the Arabian and Red Seas. Air masses from the eastern Mediterranean Basin and vicinity (Box A in Figure 12(a)) contained very low moisture amounts that only gradually increased along their pathways over the Red Sea and Arabian Gulf, indicating a negligible moisture contribution from the Mediterranean Sea (Figure 12(b)). A large number of trajectories stemmed from equatorial Africa (Box B in Figure 12(a)). The 'mean' air parcel from the sub-region resided at 650–700 hPa and advected moderate moisture amounts (4–5 g kg^{-1}) towards Saudi Arabia (Figure 12(c)). Air masses over the Arabian Sea (Box C in Figure 12(a)) contained large mean specific humidity amounts (7 g kg^{-1}) at −120 h and provided the major contribution to precipitation as these air parcels demonstrate the largest drop in specific humidity upon arrival over the target area (Figure 12(d)). The majority of these trajectories reached the target area via the Gulf of Aden and the Red Sea, where their mean moisture content further increased up to 12 g kg^{-1} (Figure 12(d)). Only a few trajectories originated in the Atlantic and West Africa and carried little moisture at middle levels towards Saudi Arabia, while other air parcels that held large moisture amounts remained over the Red Sea until intruding into Saudi Arabia, not detailed in Figure 12. As for the November case, negligible precipitation along the trajectory bundles indicates minimal loss of moisture along their pathways (not shown).

4.4. *Upward motion*

The January case was, in contrast to the November case, characterized by very strong mid-tropospheric ascent over the region of interest (Figure 13(a)). The domain-averaged 500 hPa total omega reached up to −0.8 Pa s^{-1} and locally exceeded −2.0 Pa s^{-1} over the Al Madinah region (Figure 13(a,d)) where the heaviest rainfall was observed in TRMM data. We find a clear dipole of ascending and descending motion on the eastern and western flank of the upper-level trough, respectively. The balanced omega demonstrates a centre of descending motion over Egypt that corresponds very well in spatial distribution and magnitude to the total omega, supporting the confidence in the alternative-balance omega diagnostics. Regarding the ascending motion, we observe a substantial deviation between the location of the maxima in the total omega (−2 Pa s^{-1} over the Al Madinah region) and the balanced omega (−0.8 Pa s^{-1} over the Negev desert). Time series of domain-averaged vertical motion in Figure 13(d) indicate that dynamical lifting explains roughly 30–38% of the total omega over the region of interest between 0000 and 1200 UTC 22 January, coinciding with the heaviest rainfall in ERA-Interim data. These findings demonstrate that dynamical lifting was important for ascent, but suggest that other forcing factors were at work also, such as diabatic heating and orographic lifting, as discussed below.

The advection of tropical moisture discussed above led to an extremely high tropospheric moisture content over northern Saudi Arabia (Figure 13(b)), locally reaching up to 40 kg m^{-2} over Al Madinah and thus exceeding the climatological TCW by multiple times (Figure 13(d)). Importantly, the strong

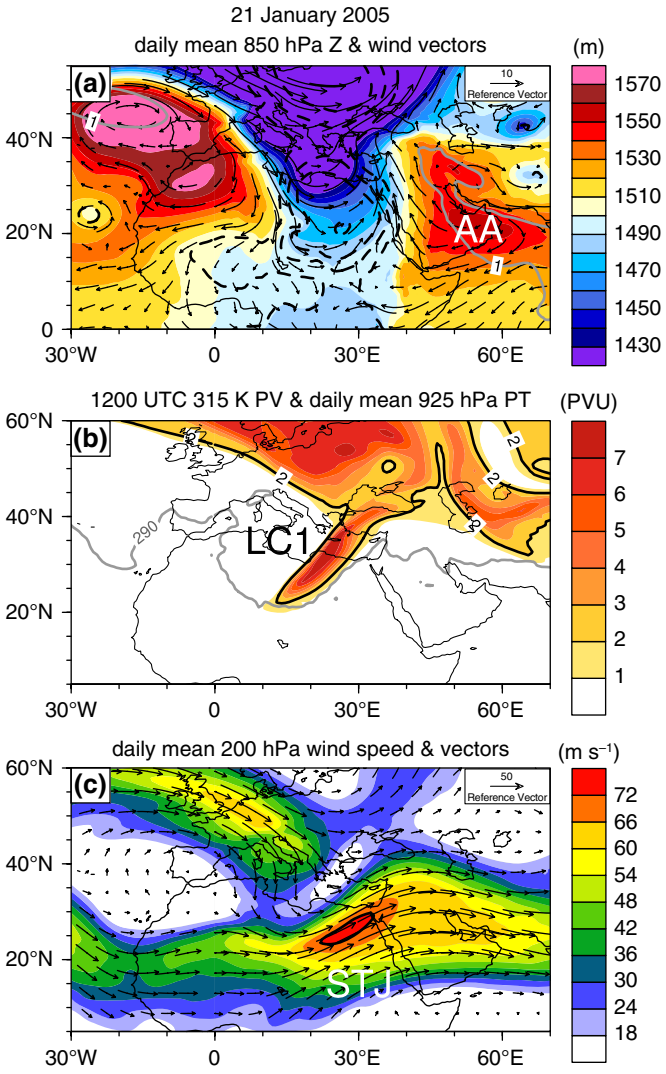

Figure 10. (a) Geopotential height (shaded, gpm) and wind vectors (m s^{-1}) at 850 hPa, (b) PV (shaded, PVU) with the 2 PVU contour (thick black line) at 315 K and the 290 K potential temperature contour (thick grey line) at 925 hPa, and (c) wind speeds (shaded, m s^{-1}) with the 72 m s^{-1} contour (thick line) and wind vectors (m s^{-1}) at 200 hPa on 21 January 2005. The panels show 6-hourly data (1200 UTC) for PV and daily means for all other variables. Normalized anomalies of geopotential height in (a) are displayed in thick contours at 1, 1.5, 2, 3 and 4 STD in grey solid lines (positive values) and black dashed lines (negative values); see the text for details. The positions of the Arabian anticyclone (AA), anticyclonic Rossby wave breaking (LC1) and the subtropical jet (STJ) are indicated.

southwesterly flow (Figure 9(c,f)) encountered the mountain range along the Red Sea and forced the uplifting and saturation of the very moist air mass over the coastal zone (Figure 13(c)), leading to strong diabatic heating that further enhanced the ascending motion. Near-saturation conditions are also found in sounding data of the Al Madinah station, showing high relative humidity (>80%) in the lower and middle troposphere at 0000 UTC and 1200 UTC 22 January (Figure 13(f)). Furthermore, the equivalent potential temperature profile in the sounding data reveals potential instability between 850 and 700 hPa at 0000 UTC 22 January, which was largely released during the next 12 h. CAPE values in ERA-Interim data are relatively low (<1400 J kg^{-1}; Figure 13(b)) and remain remarkably close to zero in sounding data (not shown), due to the low-level inversion (Figure 13(f)) at 850 hPa (0000 UTC) and 700 hPa (1200 UTC).

Thus, strong orographic and dynamical lifting, further reinforced by diabatic heating, led to heavy rainfall downstream of the upper-level trough. The intrusion of the 4-STD midlatitude trough and the associated PV streamer into low latitudes was essential for (i) exporting tropical moisture, (ii) steering the moist air flow towards the topographic barrier along the Red Sea coast, and (iii) inducing dynamical lifting on its eastern flank.

5. Extreme precipitation in Saudi Arabia in April–May 2013

5.1. *Precipitation characteristics*

In spring 2013, a large part of the Arabian Peninsula was affected by an outbreak of severe weather during an episode lasting from 25 April to 7 May (Figure 14(a,b,c,g)). The heaviest rainfall occurred on 1 May over southwestern Saudi Arabia (Figure 14(d,e,f,g)) and caused floods with 20 fatalities in the Bishah province on 2 May (Table 1). Locally, the TRMM-derived precipitation reached over 80 mm day^{-1} (Figure 14(e)). Two stations in the region, Bishah and Wadi al-Dawasir, reported 135 and 50 mm rainfall (Figure 14(f)), substantially exceeding the annual means of 88.7 and 25.5 mm (Almazroui *et al.*, 2012), respectively. ERA-Interim strongly underestimates precipitation amounts compared to the TRMM data (by a factor of almost 2.5, see Figure 14(d,e,g)). Localised spots of high precipitation in TRMM (Figure 14(e)) and clouds in satellite images (Figure 2(c)) indicate that the extreme rainfall resulted from multiple convective storms.

5.2. *Synoptic circulation*

As for the November and January cases, the April–May case was associated with wave amplification of the midlatitude circulation over the Atlantic, involving two consecutive anticyclonic Rossby wave breaking events and cut-off low formation over northwestern Africa on 23–26 April and 27 April–3 May (Figure 15(a–c)). Downstream development towards the Middle East resulted in an amplifying ridge over the Mediterranean (25–27 April; Figure 15(a)), succeeded by anticyclonic wave breaking and cut-off low formation over the northern Arabian Peninsula on 28 April (Figure 15(b)). The cut-off low remained centred over northern Saudi Arabia, and reached its most pronounced state on 1 May (>3 STD below normal in the 500 hPa geopotential height; Figure 15(c)), when the most severe rainfall occurred.

The formation of the quasi-stationary upper-level trough was accompanied by the northward expansion of the Red Sea Trough from 26 April onwards (Figure 15(d–f)), followed by cyclogenesis over northeastern Saudi Arabia on 2 May (not shown). Normalized anomalies in the mean-sea-level pressure exceeded 1–1.5 STD over the Red Sea region from 26 April to 3 May (Figure 15(d–f)). Interestingly, the Arabian anticyclone was, in contrast to the November case, positioned more southeastward, over the Arabian Sea (Figure 15(g–i)), allowing the low-level moist air to reach over most of Saudi Arabia, as further detailed in section 5.3. The Arabian anticyclone persisted from 23 April until 1 May and dissipated afterwards. Positive STDs in the 850 hPa geopotential height (>1–2 STD above normal) demonstrate the pronounced state of the Arabian anticyclone over a range of days (23–27 and 29–30 April), only shown in Figure 15(g) for 26 April.

In terms of PV dynamics, an upper-tropospheric high-PV intrusion expanded gradually southwestwards across the Red Sea region, coinciding with a northward amplifying potential temperature maximum in the lower troposphere (Figure 15(j–l)). Surprisingly, the centre of the PV maximum was positioned to the *east* of the potential temperature maximum, suggesting an unfavourable phase relationship for baroclinic growth. The zonal flow in this region, however, exhibits easterly vertical shear (Figure 15(b,c)), not the commonly expected westerly shear. The phase relationship between the PV and potential temperature fields is therefore consistent with baroclinic growth. In addition, the meridional profile of the zonal wind exhibits an inflection point over the same region, which is a necessary condition for barotropic instability. This suggests that wave amplification over the Arabian Peninsula occurred through a combination of baroclinic and barotropic instability. Thus, as for the November and January cases, we observe interaction between the midlatitude upper-level and tropical lower-level circulations.

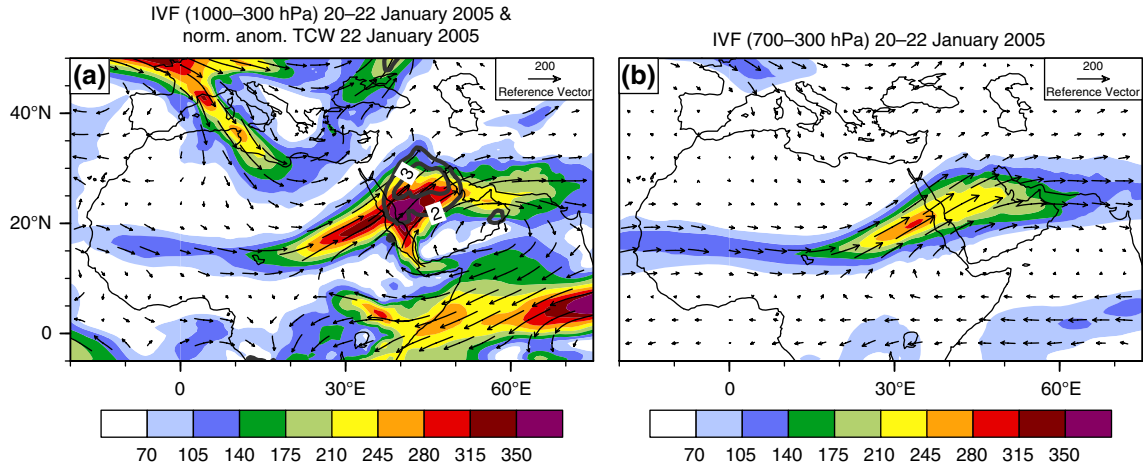

Figure 11. Magnitude (shaded) and direction (vectors) of IVFs (kg m^{-1} s^{-1}) averaged over 20–22 January 2005 over pressure levels from (a) 1000 to 300 hPa, and (b) 700 to 300 hPa. The thick grey contour lines in (a) depict the normalized anomalies of TCW at 2 and 3 STD above normal at 22 January 2005.

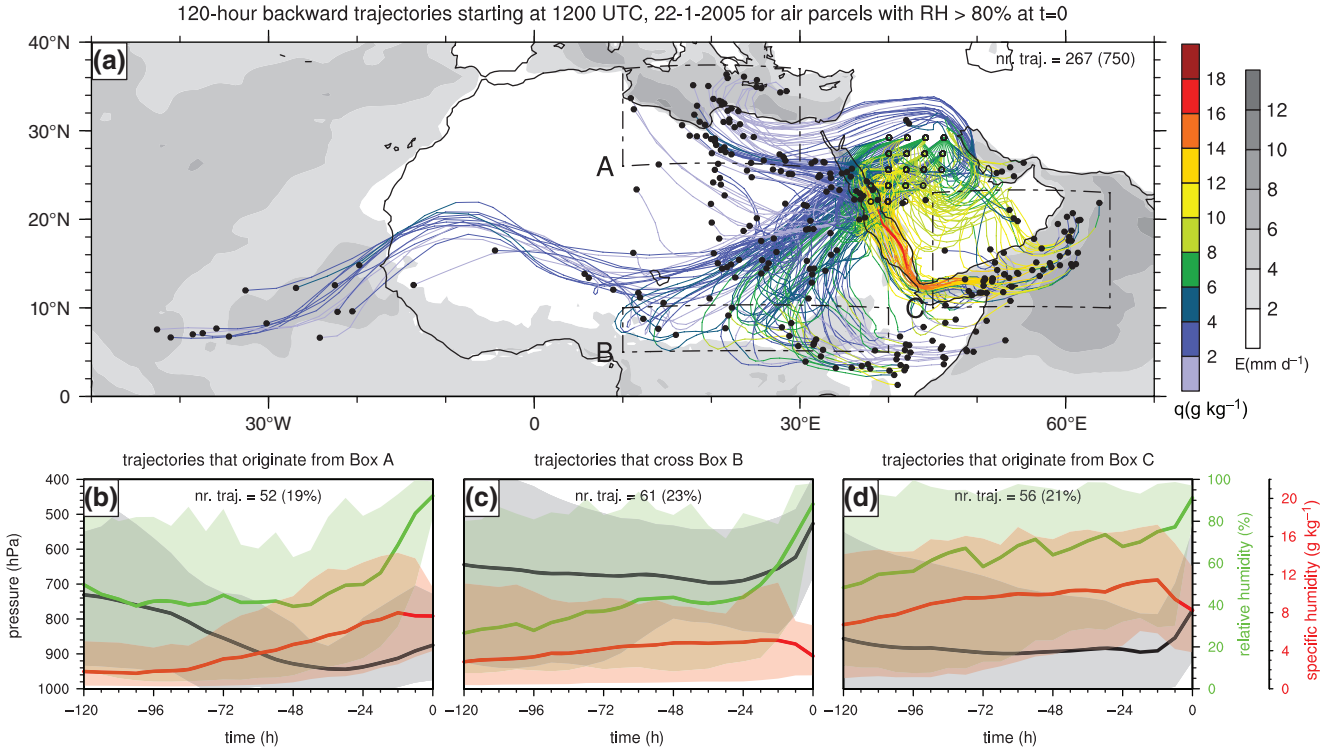

Figure 12. As Figure 6, but for the January case. The 120-hour backward trajectories started at 1200 UTC 22 January 2005 from grid points at 200 km intervals in the box depicted in Figure 8(a,b) between surface and 200 hPa and with a relative humidity >80% at $t = 0$. The mean and spread of meteorological variables along trajectories from (a) are displayed for subsets of air parcels that (b) are located in box A (10–30°E, 26–37°N) at −120 h, (c) cross box B (10–40°E, 5–10°N) at any time, and (d) are located in box C (45–65°E, 10–23°N) at −120 h.

5.3. *Moisture transport pathways*

The coupling of the midlatitude and tropical circulations and the positioning of the Arabian anticyclone over the Arabian Sea favoured the intrusion of tropical moist air masses over the Arabian Peninsula. IVFs during 25 April–1 May reveal moisture transport pathways with two distinct origins (Figure 16). Moist air masses over the warm waters of the Arabian Sea were transported towards Saudi Arabia by the persistent anticyclonic low-level flow. Interestingly, another moisture transport pathway with roots over the south Indian Ocean followed along the East African coast and entered Saudi Arabia via the Red Sea basin. In other words, we find cross-equatorial flow, suggestive of moisture from the Southern Hemisphere, contributing to the heavy precipitation over Saudi Arabia in the April–May case. The cross-equatorial moisture transport was accompanied by a persistent upper-level trough along the eastern coast of South Africa (Figure 16). We hypothesize that the southern hemispheric midlatitude forcing initiated the cross-equatorial surge as also found by Fukutomi and Yasunari (2005, 2009) for cross-equatorial flow and moisture transport over the eastern Indian Ocean. The persistent advection of moist air mass over the tropical seas was mostly confined to the lower troposphere (not shown), and led to above-normal TCW amounts (>2 STD) over a large part of Saudi Arabia during the April–May case, as shown for 1 May in Figure 16.

The rather surprising moisture transport pathways during the April–May case require a more thorough investigation, here provided by a detailed Lagrangian analysis with focus on the extreme rainfall over southwestern Saudi Arabia on 1 May. As for the November case, we calculated 168-hour backward trajectories from all grid points in the region of interest (40–46°E, 17–21°N), started at 1200 UTC 1 May 2013, and retain the trajectories of air parcels with a relative humidity >80% or a moisture flux >100 g kg^{-1} m s^{-1} at the initial time.

These backward trajectories, displayed in Figure 17(a), confirm the two distinct moisture transport pathways from the south Indian Ocean and the southern Arabian Sea/northern Indian Ocean, which merged over the Red Sea basin and entered Saudi

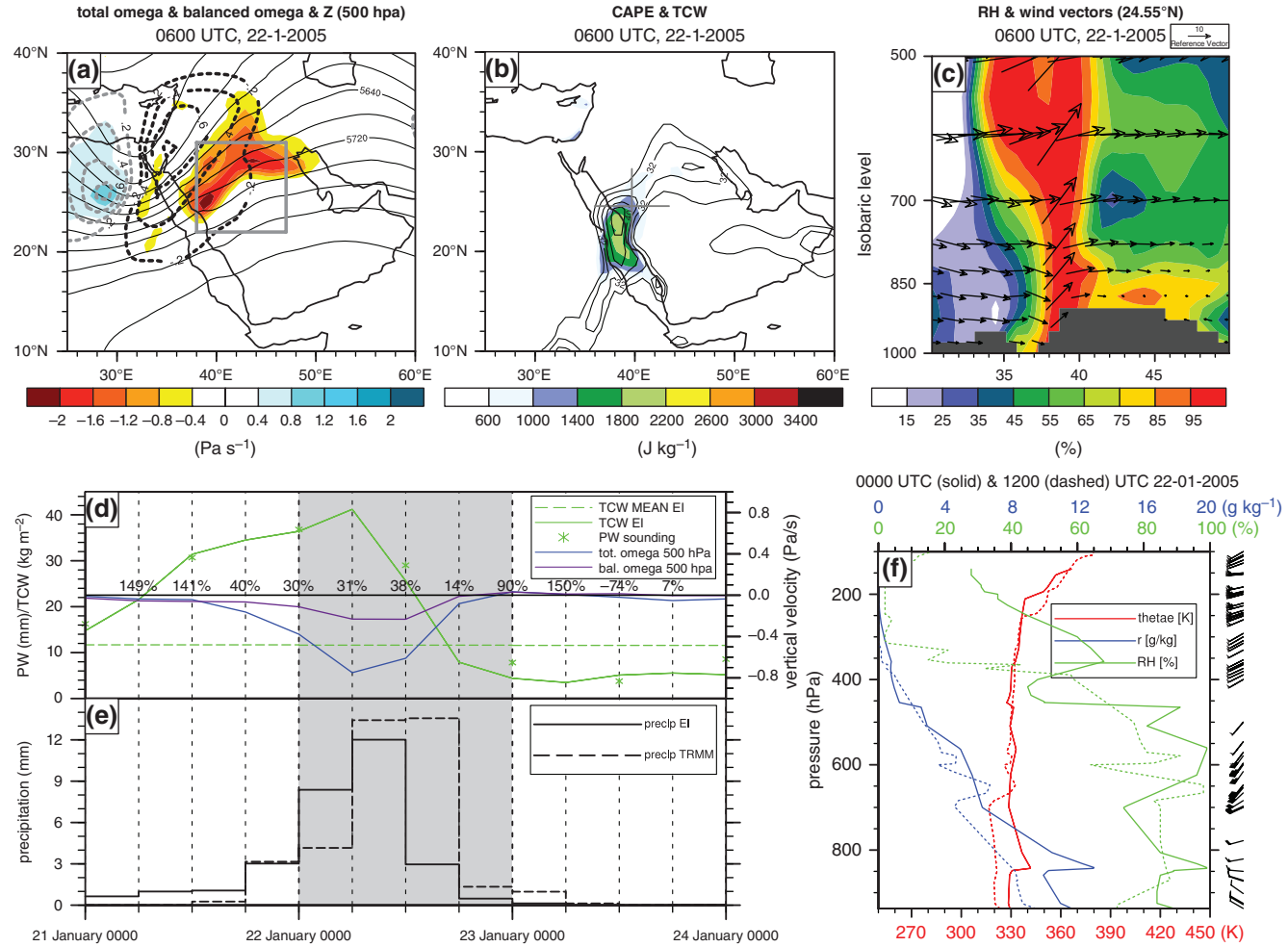

Figure 13. As Figure 7, but for the January case at (a)–(c) 0600 UTC 22 January 2005 with (a) omega in different colour scales and the balanced omega in contour lines at 0.2 Pa s^{-1} intervals, (b) CAPE + 6 h forecast at 0000 UTC 22 January 2005, and (c) the vertical cross-section at 24.55°N. In (d), the temporal evolution of domain-averaged total and balanced omega (Pa s^{-1}) at 500 hPa and precipitable water (mm) in sounding data from the Al Madinah station (39.7°E, 24.55°N, 636 m; see the grey marker in (b)), and in ERA-Interim, at the corresponding location the instantaneous and long-term (1979–2013) 21-day running mean of TCW (mm). In (f), the sounding data of the Jeddah station at 0000 UTC (solid lines) and 1200 UTC (dashed lines and wind barbs) 22 January 2005. The percentages in (d) reflect the proportion of balanced omega to the total omega at 500 hPa. The averaging domain for variables in (d) and (e) corresponds to the box in Figure 8(a,b) which is for clarity also depicted in grey in (a).

Arabia over the steep western flanks of the Asir Mountains. Interestingly, a large number of air parcels from the Southern Hemisphere (Box A in Figure 17(a)) travelled over an evaporation 'hot spot' (>10 mm day^{-1}) along the East African coast and to the west of Madagascar (Figure 17(a,b)). Substantial amounts of moisture may have precipitated out along their pathways over the Tropics and the eastern flank of the Ethiopian Highlands between 132 h and 72 h (Figure 17(b)) before reaching southwestern Saudi Arabia. In other words, the trajectories originating over the south Indian Ocean passed through a tropical region where convective precipitation may have depleted southern hemispheric moisture from the air masses. Interestingly, however, most of the moisture in the air parcels was preserved during the last 72 h prior to arrival over the target area, while the evaporation over the underlying surface and moisture increases were relatively low, pointing to the relevance of remote moisture sources. Thus, the Lagrangian analysis demonstrates that moist air masses from over the south Indian Ocean reached southwestern Saudi Arabia. However, it is uncertain whether the moisture contributing to the extreme rainfall was primarily sourced over the remote south Indian Ocean, or was predominantly collected over nearer regions along their pathways towards the Arabian Peninsula. Further study may address this open question, for example through quantification of moisture sources (e.g. Sodemann *et al.*, 2008) utilizing model data that adequately represent the precipitation over the region of interest.

Another cluster of trajectories originated over the southern Arabian Sea/northern Indian Ocean (Box B in Figure 17(a)). Air parcels already contained large mean moisture amounts (10 g kg^{-1}) 168 h before reaching southwestern Saudi Arabia that gradually increased (up to 14 g kg^{-1}) along their pathways over the Gulf of Aden and the Red Sea (Figure 17(a,c)). Loss of moisture along these pathways due to precipitation was negligible, and thus, most of the moisture provided by this trajectory branch stemmed from the remote southern Arabian Sea/northern Indian Ocean.

5.4. *Upward motion*

Upward motion occurred on the eastern flank of the quasi-stationary upper-level trough and extended partly over southwestern Saudi Arabia at 1200 UTC 1 May (Figure 18(a)). The spatial distribution of the balanced omega at 500 hPa agrees to a large extent with the total omega. In the specific region of our interest, however, the balanced ascent was very weak. Thus, dynamical lifting cannot directly explain the upward motion. Arguably, more localized forcing plays the dominant role in this case, as detailed below.

High CAPE values in ERA-Interim data over the Bishah region, exceeding 3000 J kg^{-1}, indicate a high probability of deep moist convection (Figure 18(b)). Note that high CAPE values over the warm Red Sea are common, and do not necessarily imply a high probability of convective storms, as confirmed by the absence of cloud evolution in the satellite images. Unfortunately, sounding data are not available from the Bishah station where the most severe rainfall was observed (Figure 14(f)). The sounding profile

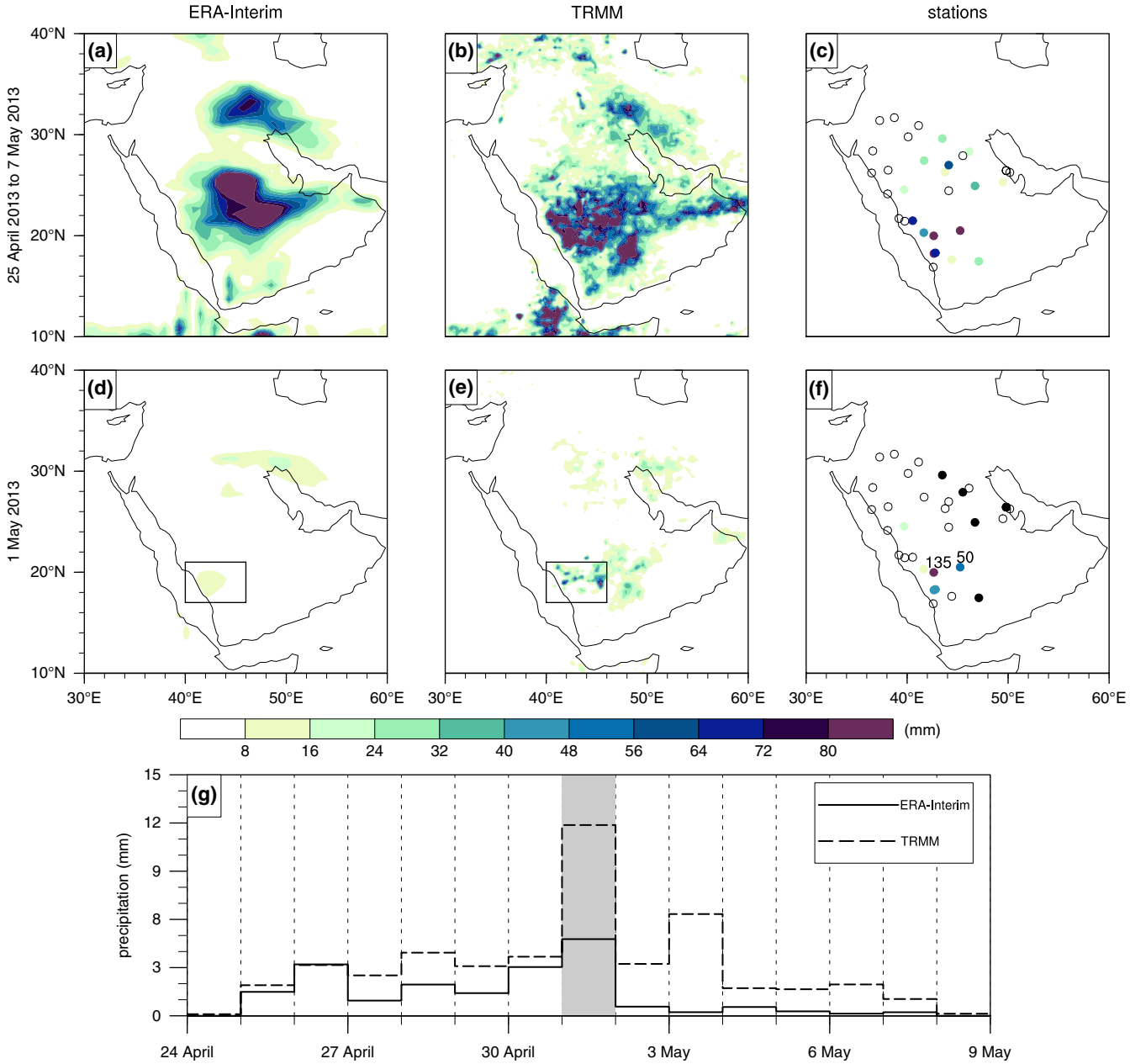

Figure 14. As Figure 3, but for the April–May case, the (a)–(c) accumulated precipitation from 25 April to 7 May 2013, and (d)–(f) on 1 May 2013. The time evolution in (g) is the domain-averaged daily precipitation in ERA-Interim and TRMM over the grid points in the box (40–46°E, 17–21°N) depicted in (d) and (e). The Bishah (410840) and Wadi al-Dawasir (410610) stations, indicated in (f), measured 135 mm and 50 mm rainfall, respectively.

from the nearest station, Abha, exhibits potential instability between the surface and 640 hPa at 0000 UTC 1 May, which was likely to be released as near-saturation conditions were observed from the surface up to 500 hPa (Figure 18(f)). The sounding profile at 1200 UTC 1 May confirms the release of potential instability, aided by orographic uplift of the westerly low-level moist air flow over the Red Sea coast (Figure 18(c)).

Importantly, time series of surface sensible heat flux and TRMM precipitation data in Figure 18(d,e) demonstrate daily maxima in surface heating between 0600 and 1200 UTC (0900–1500 local time), followed by daily peaks in precipitation between 1200 and 1800 UTC (1500–2100 local time). Satellite imagery reveals a striking diurnal cycle of the convective storms throughout the April–May case. The storms developed in the afternoon over the mountainous Red Sea coast under the influence of strong thermal heating (1200 UTC; 1500 local time; see e.g. Figure 2(c)), grew to mature stages during the evening while moving eastward over Saudi Arabia (1800 UTC; 2100 local time), and decayed at night and in the early morning over its eastern part (0000 and 0600 UTC; 0300 and 0900 local time).

Thus, the scattered convective storms over Saudi Arabia developed in a synoptically destabilized environment under the local influence of strong surface heating and of the orographic uplift of the moist westerly flow over the mountainous Red Sea coast. The coupling of the midlatitude and tropical circulations was essential for guiding the intrusion of tropical moist air masses over the Arabian Peninsula and for orienting the westerly flow towards the topographic barrier along the Red Sea coast. The moderate vertical wind shear in the sounding data (15.9 m s^{-1} between the surface (2093 m ASL) and 6005 m ASL, see also Figure 18(f)) likely favoured the organisation of multicell storms (Holton, 2004) over southwestern Saudi Arabia (Figure 2(c)).

6. A seasonal perspective

All three cases were associated with tropospheric circulation and/or moisture content anomalies that were unusual or extreme (> 3 STD for the November and April–May cases and >4 STD for the January case) with respect to the background circulation during the respective seasons. In this section we argue that the differences in the configuration of the synoptic circulations between the three cases can be linked to the seasonal variability of the large-scale circulation.

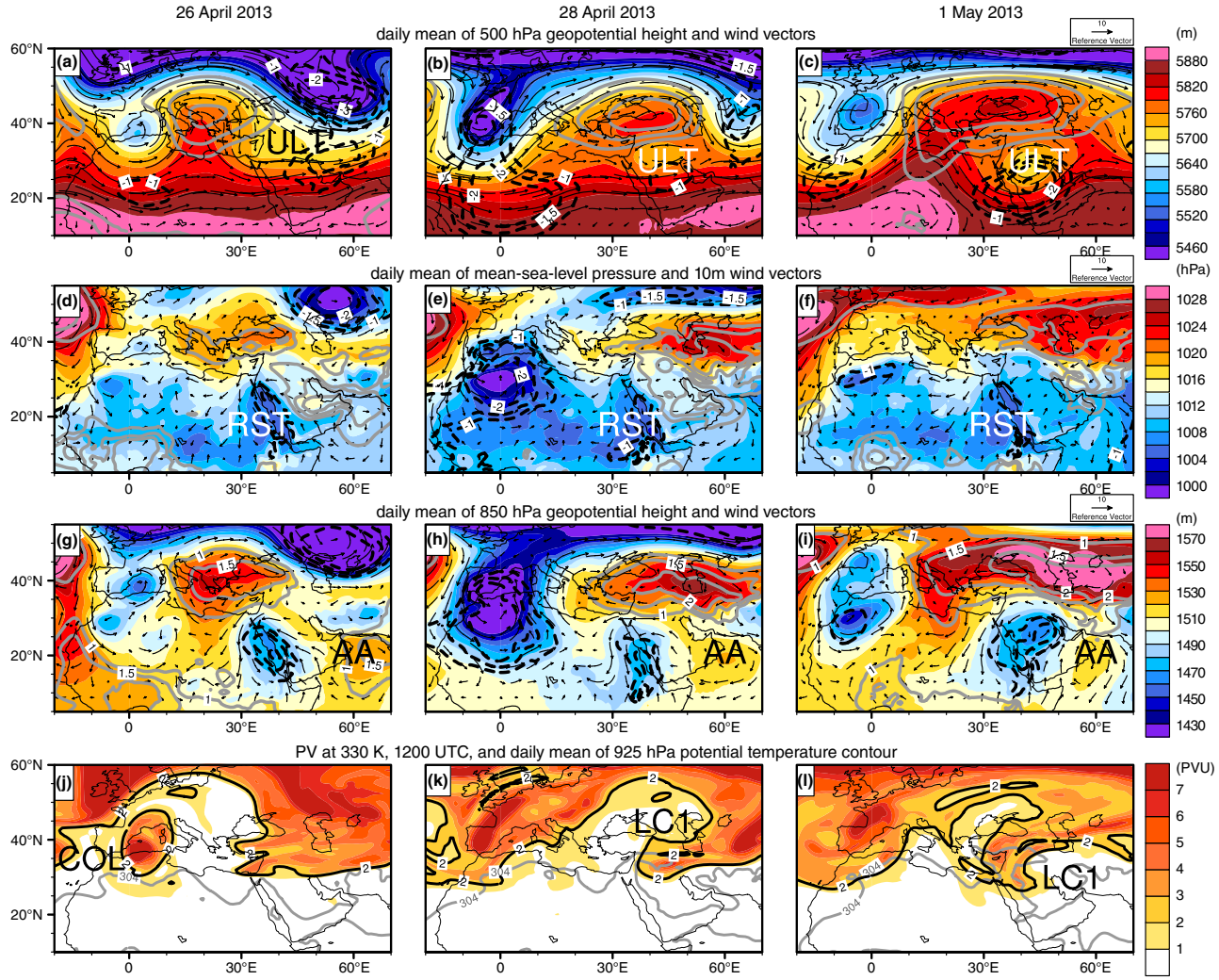

Figure 15. As Figure 4, but for the April–May case at (a,d,g,j) 26 April, (b,e,h,k) 28 April, and (c,f,i,l) 1 May 2013, and the 304 K potential temperature contour line at 925 hPa.

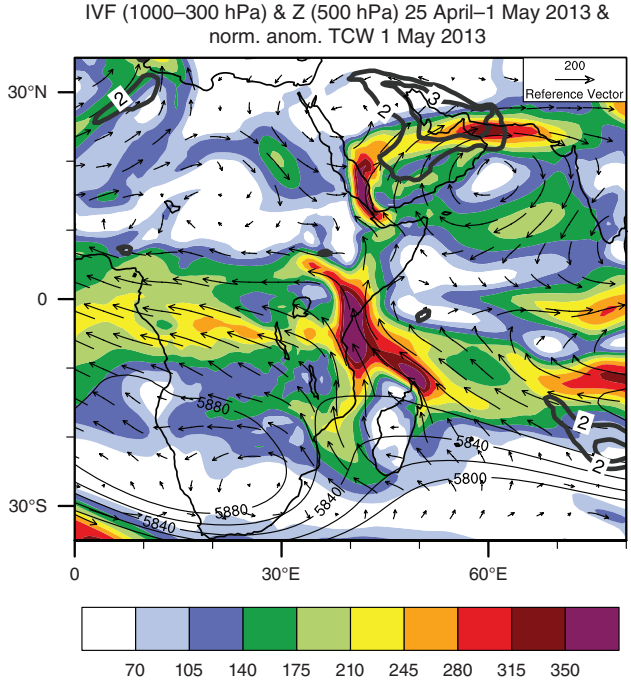

Figure 16. Magnitude (shaded) and direction (vectors) of IVFs (kg m^{-1} s^{-1}) over pressure levels from 1000 to 300 hPa and 500 hPa geopotential height contours (thin lines) at intervals of 20 gpm, between 5800 and 5880 gpm in the Southern Hemisphere, averaged over 25 April–1 May 2013. The thick grey contour lines depict the normalized anomalies of TCW at 2 and 3 STD above normal on 1 May 2013.

The November case revealed the interaction between a midlatitude upper-tropospheric trough and the climatological Red Sea Trough near the surface farther downstream, being dynamically characteristic of the Active Red Sea Trough (De Vries *et al.*, 2013). This phenomenon typically occurs in autumn (Kahana *et al.*, 2002; Krichak *et al.*, 2012; Shentsis *et al.*, 2012; De Vries *et al.*, 2013) since the Red Sea Trough is most prominent in this season (Alpert *et al.*, 2004b; Tsvieli and Zangvil, 2005). The January case was characterised by cloud bands from the Tropics, an intensified subtropical jet, a midlatitude trough as a part of a Rossby wave train moving into the Tropics, and large moisture fluxes at middle and upper levels on the eastern flank of the trough. These features are typical of tropical plumes (Knippertz, 2007, and references therein) which are most likely to occur over the Middle East during the winter season (Ziv, 2001; Rubin *et al.*, 2007; Tubi and Dayan, 2014), when the baroclinic zone is closest to the region and midlatitude disturbances are most likely to reach deep into the subtropics. The April–May case involved a long-lasting rainfall episode, resulting from a quasi-stationary upper-level trough and persistent northward advection of tropical moist air masses. The coincidence of cross-equatorial flow and the Arabian anticyclone played a central role in the transport of tropical moisture towards the Arabian Peninsula. Cross-equatorial flow can be explained by the seasonal evolution of the large-scale circulation. In May, a clockwise lower-tropospheric moist air flow develops along the East African coast, referred to as the Somali or Findlater jet (Joseph and Sijikumar, 2004) which is associated with the onset of the Asian summer monsoon. Thus, the moisture incursion over the Arabian Peninsula preceded the onset of the Asian summer monsoon and can be linked to the seasonal evolution of the large-scale circulation in spring.

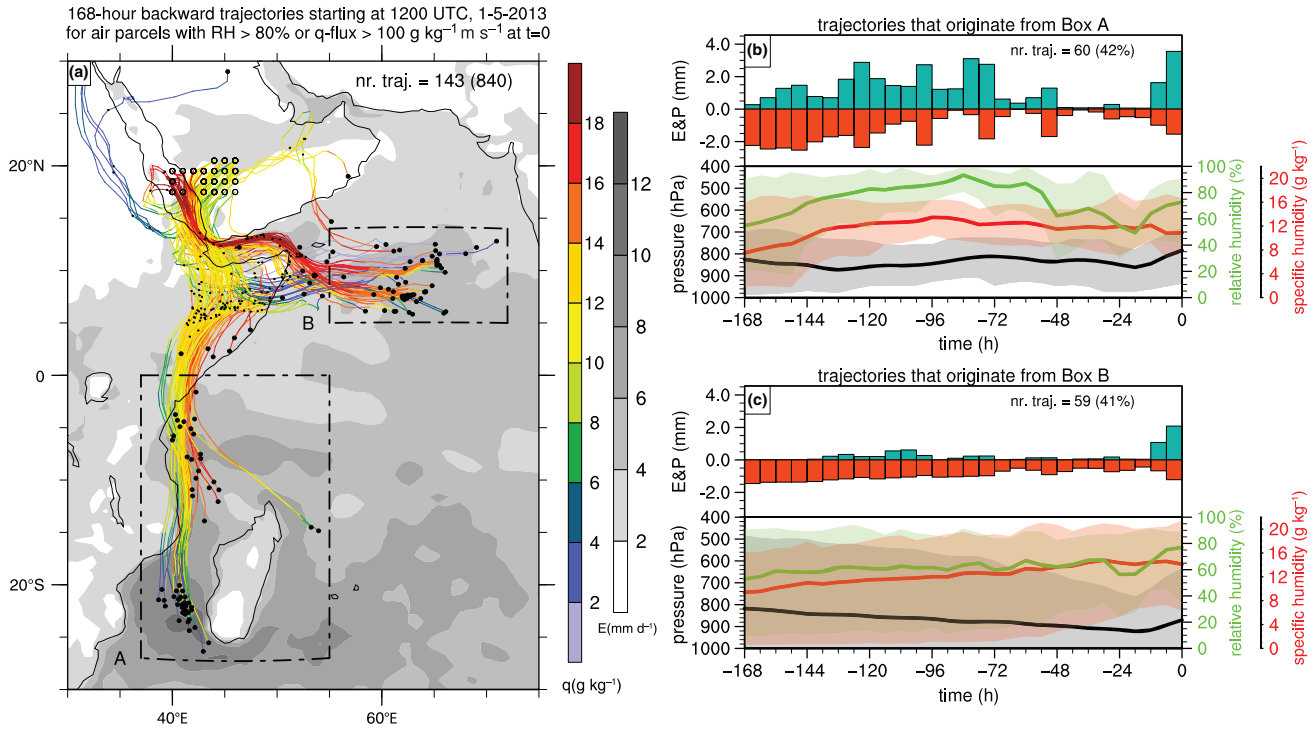

Figure 17. As Figure 6, but for the April–May case. The 168-h backward trajectories started at 1200 UTC 1 May 2013 from all grid points in the box depicted in Figure 14(d,e) between surface and 200 hPa and with a relative humidity >80% or moisture flux >100 g kg^{-1} m s^{-1} at $t = 0$. The mean and spread of meteorological variables along trajectories from (a) are displayed for subsets of air parcels that (b) are located in box A (37–55°E, 27°S–0°N) and (c) box B (55–72°E, 5–14°N) at −168 h. (b)–(d) demonstrate, in addition, the mean 6-hourly accumulated precipitation (mm (6 h)$^{-1}$; green bars) and evaporation (mm (6 h)$^{-1}$; red bars). In (a) small dots are plotted at −72 h.

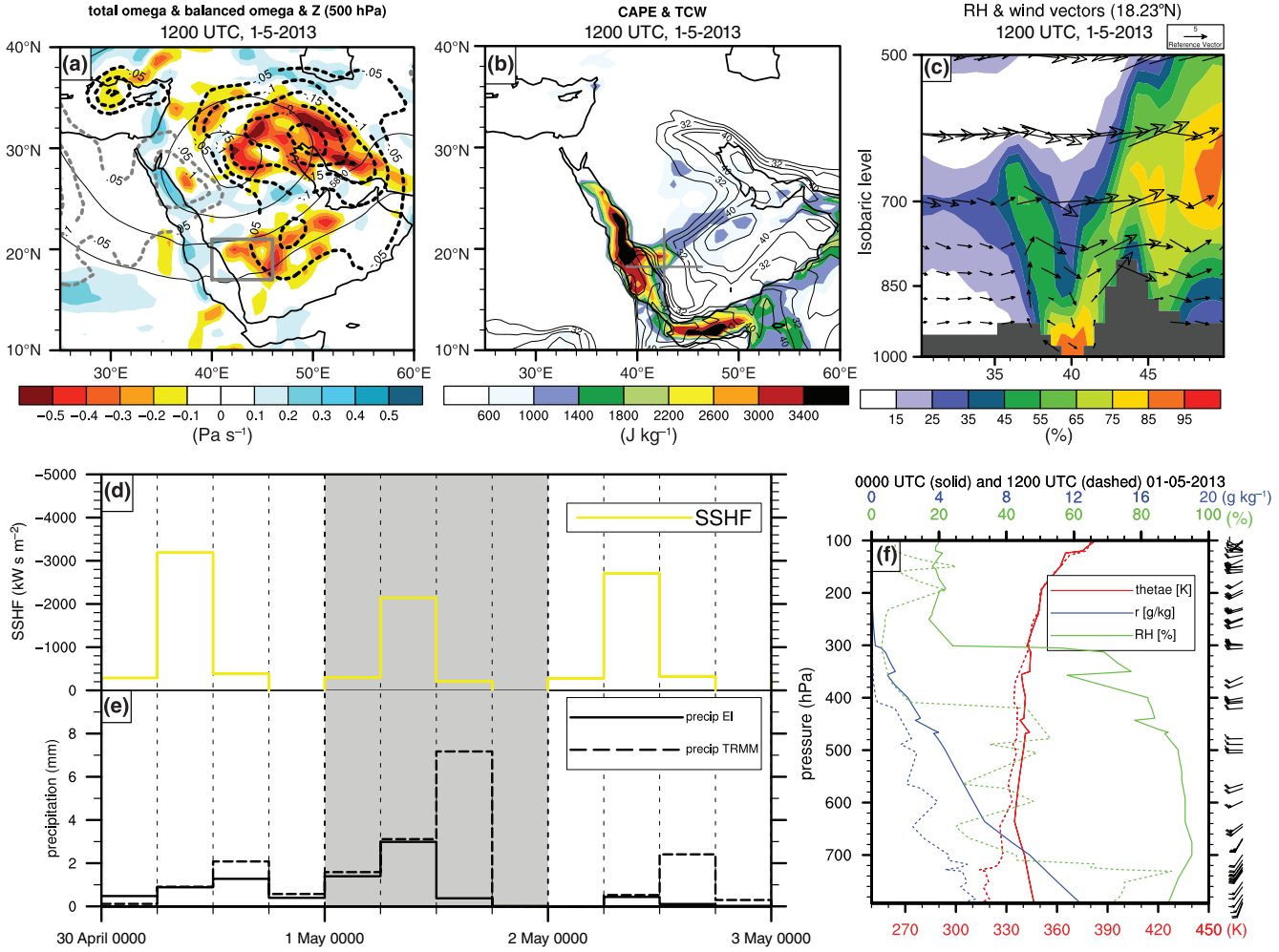

Figure 18. As Figure 7, but for the April–May case at (a)–(c) 1200 UTC 1 May 2013 with (b) CAPE +12 h forecast at 0000 UTC 1 May 2013, and (c) the vertical cross-section at 18.23°N. In (d), the temporal evolution of domain-averaged 6-hourly accumulated surface sensible heat flux (kW s m^{-2}), and in (f), the sounding data of the Abha station (42.65°E, 18.23°N, 2093 m) at 0000 UTC (solid lines) and 1200 UTC (dashed lines and wind barbs) 1 May 2013. The averaging domain for variables in (d) and (e) corresponds to the box in Figure 14(d,e) which is for clarity also depicted in grey in (a).

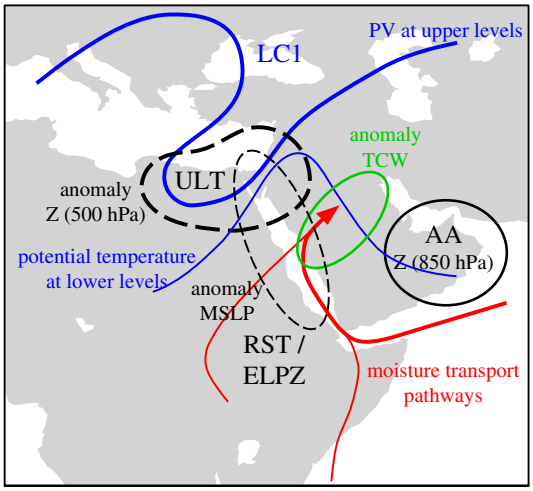

Figure 19. Schematic presentation of the common synoptic-scale key features of the three cases: anticyclonic Rossby wave breaking (LC1), an upper-level trough (ULT), the Arabian anticyclone (AA), the Red Sea Trough (RST; for the November and April–May cases), equatorial low pressure zone (ELPZ; for the January case), moisture transport pathways and anomalous TCW. 'Z' and 'MSLP' denote geopotential height and mean-sea-level pressure, respectively. Note that the thin red lines (arrows) refer to the moisture transport pathways as only observed during the January case (equatorial Africa) and the April–May case (south Indian Ocean).

Also, the moisture transport pathways during the three cases are to some extent tied to the climatological background circulation during the different seasons. In particular, during the November and April–May cases, the varying position of the Arabian anticyclone largely regulated the moisture transport pathways (De Vries *et al.*, 2013) and the spatial distribution of rainfall over the Arabian Peninsula. During autumn, the semi-permanent Arabian anticyclone is located over the Arabian Peninsula and channels the low-level moist air masses over the Arabian Sea into the Red Sea region, which can intrude over the Arabian Peninsula across the western coast under the influence of a transient midlatitude upper-level trough. During spring, the Arabian anticyclone is situated farther to the southeast, over the Arabian Sea, which can allow the low-level moist air masses and precipitation to spread across most of Saudi Arabia. Accordingly, the autumn climatological precipitation is largely confined to the Jeddah region and a narrow belt stretching towards northeastern Saudi Arabia, whereas rainfall in spring reaches relatively high amounts over much of Saudi Arabia with a maximum over the southwestern territories (Almazroui, 2011, his Fig. 3; Mashat and Basset, 2011, their Figs 5B and 4B). Thus, the moisture transport pathways and precipitation distribution during the November and April–May cases are consistent with the climatological patterns during the respective seasons.

During the January case, the relatively low tropospheric moisture amounts over the cooler Arabian and Red Seas were complemented by high moisture fluxes within the strong synoptic flow and moisture transport from remote regions such as equatorial Africa. The moisture transport was particularly large at middle tropospheric levels, which may explain why rainfall during the January case was not only confined to the mountainous coastal zone, but also reached into the interior and northern parts of the Arabian Peninsula. From a climatological perspective, rainfall in the winter season reaches a maximum over the northern territories of Saudi Arabia (Almazroui, 2011, his Fig. 3; Mashat and Basset, 2011, their Fig. 4A). Thus, it is no coincidence that flash floods affected the Jeddah and Makkah (Mecca) regions in November 2003 and 2009, the northwestern parts of Saudi Arabia in December 1985 and January 2005, and the southwestern regions of Saudi Arabia in April 1964, 2004, 2005, 2012 and 2013 (Table 1), considering the climatological precipitation patterns of the different seasons.

In summary, the general patterns of the synoptic circulations, moisture transport pathways and spatial distribution of precipitation of the three cases are consistent with the seasonal variability of the large-scale circulation. The specific events exhibited unusual or extreme synoptic characteristics *within* the varying background large-scale circulation of the different seasons.

7. Conclusions

We presented three case-studies of extreme precipitation over Saudi Arabia that caused flooding with severe societal impacts. All three cases involved strong tropical–extratropical interactions. The extreme precipitation events were initiated by midlatitude forcing through an upper-level trough intrusion into low latitudes, which instigated tropical moisture transport towards the Arabian Peninsula that fuelled the heavy rainfall. The extreme precipitation and storms were in all three cases embedded in an environment controlled by the synoptic-scale circulation. Our focus on the large-scale, rather than the mesoscale, is based on the perspective that the formation of convective storms is strongly tied to the larger-scale tropospheric environment. This section summarises the key synoptic-scale features, schematically depicted in Figure 19, and outlines avenues for future research that may build on our findings.

The three events were preceded by amplification and breaking of midlatitude Rossby waves in the far upstream region over the Atlantic, followed by downstream development towards the Middle East. Subsequent anticyclonic Rossby wave breaking over the Middle East resulted in an upper-level trough that intruded into the subtropics (the LC1 baroclinic life cycle of Thorncroft *et al.* (1993)) and interacted with the tropical lower-level circulation. The accompanying upper-tropospheric high-PV intrusion and lower-tropospheric potential temperature maximum downstream demonstrate a phase relationship that is consistent with wave amplification through baroclinic growth (Hoskins *et al.*, 1985). PV streamers and anticyclonic wave breaking have also been associated with extreme precipitation events in regions elsewhere (Massacand *et al.*, 1998; Martius *et al.*, 2006, 2013; Knippertz and Martin, 2007a, 2007b). Future work may investigate the large-scale processes upstream that initiate wave amplification such as diabatic PV destruction and negative PV advection (Knippertz and Martin, 2005, 2007b; Martius *et al.*, 2008; Hart *et al.*, 2010).

The coupling of the midlatitude and tropical circulations facilitated the transport of tropical moisture towards the Arabian Peninsula, leading to above-normal moisture content over the region of interest (>2 or >3 STD). The moisture pathways varied between the cases; however, in each case they involved enhanced moisture transport over the Arabian and Red Seas through the intensified Arabian anticyclone. Interestingly, this feature was also found to be important for precipitation and extreme precipitation over the Levant (Ziv *et al.*, 2005; De Vries *et al.*, 2013) and Iran (Raziei *et al.*, 2012). Our Lagrangian trajectory analysis indicated not only an important moisture contribution from the nearby Red Sea, but also substantial moisture transport from remote tropical regions. As an extension to our findings, it would be interesting to quantify the moisture sources, for example through algorithms (e.g. Sodemann *et al.*, 2008) or the tagging of evaporated water in high-resolution numerical model simulations.

The forcing mechanisms for upward motion were in all three cases associated with orographic lifting of moist air masses over the mountainous Red Sea coast and the release of potential instability. Furthermore, the January case was characterised by widespread heavy precipitation, favoured by strong dynamical lifting and diabatic heating. The November and April–May cases showed concentrated extreme rainfall, and were associated with local low-level moisture convergence and reduced static stability (November case), and strong surface sensible heating (April–May case).

The findings in this study may contribute to a deeper understanding of the underlying synoptic-scale dynamics of

extreme precipitation events over Saudi Arabia, which can support future work on their predictability and early warning systems to help mitigate the potential impacts of flooding. Furthermore, this study may provide context for future studies elaborating on mesoscale processes through modelling approaches. Finally, our analysis of the synoptic-scale processes may benefit climatological studies on current and future rainfall trends and variability, which are of crucial importance for anticipating changes in water availability and extreme weather events in the context of climate change.

Acknowledgements

The research leading to these results has received funding from the European Research Council under the European Union's Seventh Framework Programme (FP7/2007–2014)/ERC grant agreement no. 226144 and the National Science Foundation grants AGS-1036858 and AGS-1401220 from the United States. Marlene Baumgart acknowledges support from the DFG Collaborative Research Center TRR 165/1, project A01: Upscale impact of diabatic processes from convective to near-hemispheric scale, and Internal University Research Funding (phase I) from the JGU, Mainz. This work was supported by the Cy-Tera Project, which is co-funded by the European Regional Development Fund and the Republic of Cyprus through the Research Promotion Foundation. The authors wish to thank CRED, Dundee Satellite Receiving Station/EUMETSAT, ECMWF, NASA, JAXA, NCDC and the University of Wyoming for providing their datasets. We also thank H. Merx for obtaining part of the data. The data are visualized with the National Center for Atmospheric Research (NCAR) Command Language (NCL) package (version 6.2.1). Finally, we thank Neil Hart and an anonymous reviewer whose comments helped to improve the manuscript.

References

Abdullah MA, Almazroui MA. 1998. Climatological study of the southwestern region of Saudi Arabia. I. Rainfall analysis. *Clim. Res.* **9**: 213–223.

Al-Khalaf AK, Basset HA. 2013. Diagnostic study of a severe thunderstorm over Jeddah. *Atmos. Clim. Sci.* **3**: 150–164.

Almazroui M. 2011. Calibration of TRMM rainfall climatology over Saudi Arabia during 1998–2009. *Atmos. Res.* **99**: 400–414.

Almazroui M, Islam MN, Athar H, Jones PD, Rahman MA. 2012. Recent climate change in the Arabian Peninsula: Annual rainfall and temperature analysis of Saudi Arabia for 1978–2009. *Int. J. Climatol.* **32**: 953–966.

Alpert P, Osetinsky I, Ziv B, Shafir H. 2004a. Semi-objective classification for daily synoptic systems: Application to the eastern Mediterranean climate change. *Int. J. Climatol.* **24**: 1001–1011.

Alpert P, Osetinsky I, Ziv B, Shafir H. 2004b. A new seasons definition based on classified daily synoptic systems: An example for the eastern Mediterranean. *Int. J. Climatol.* **24**: 1013–1021.

Barth HJ, Steinkohl F. 2004. Origin of winter precipitation in the central coastal lowlands of Saudi Arabia. *J. Arid Environ.* **57**: 101–115.

Chakraborty A, Behera SK, Mujumdar M, Ohba R, Yamagata T. 2006. Diagnosis of tropospheric moisture over Saudi Arabia and influences of IOD and ENSO. *Mon. Weather Rev.* **134**: 598–617.

Davies-Jones R. 1991. The frontogenetical forcing of secondary circulations. Part I: The duality and generalization of the Q vector. *J. Atmos. Sci.* **48**: 497–509.

Dayan U, Ziv B, Margalit A, Morin E, Sharon D. 2001. A severe autumn storm over the Middle-East: Synoptic and mesoscale convection analysis. *Theor. Appl. Climatol.* **69**: 103–122.

Dayan U, Nissen K, Ulbrich U. 2015. Review article: Atmospheric conditions inducing extreme precipitation over the eastern and western Mediterranean. *Nat. Hazards Earth Syst. Sci.* **15**: 2525–2544.

Dee DP, Uppala SM, Simmons AJ, Berrisford P, Poli P, Kobayashi S, Andrae U, Balmaseda MA, Balsamo G, Bauer P, Bechtold P, Beljaars ACM, van de Berg L, Bidlot J, Bormann N, Delsol C, Dragani R, Fuentes M, Geer AJ, Haimberger L, Healy SB, Hersbach H, Hólm EV, Isaksen L, Kållberg P, Kohler M, Matricardi M, McNally AP, Monge-Sanz BM, Morcrette JJ, Park BK, Peubey C, de Rosnay P, Tavolato C, Thépaut JN, Vitart J. 2011. The ERA-Interim reanalysis: Configuration and performance of the data assimilation system. *Q. J. R. Meteorol. Soc.* **137**: 553–597.

Deng LP, McCabe MF, Stenchikov G, Evans JP, Kucera PA. 2015. Simulation of flash-flood-producing storm events in Saudi Arabia using the Weather Research and Forecasting model. *J. Hydrometeorol.* **16**: 615–630.

De Vries AJ, Tyrlis E, Edry D, Krichak SO, Steil B, Lelieveld J. 2013. Extreme precipitation events in the Middle East: Dynamics of the Active Red Sea Trough. *J. Geophys. Res. Atmos.* **118**: 7087–7108.

Doswell CA III. 1987. The distinction between large-scale and mesoscale contribution to severe convection: A case study example. *Weather and Forecasting* **2**: 3–16.

Evans JP, Smith RB. 2006. Water vapor transport and the production of precipitation in the eastern Fertile Crescent. *J. Hydrometeorol.* **7**: 1295–1307.

Evans JP, Smith RB, Oglesby RJ. 2004. Middle East climate simulation and dominant precipitation processes. *Int. J. Climatol.* **24**: 1671–1694.

Fukutomi Y, Yasunari T. 2005. Southerly surges on submonthly time scales over the eastern Indian Ocean during the Southern Hemisphere winter. *Mon. Weather Rev.* **133**: 1637–1654.

Fukutomi Y, Yasunari T. 2009. Cross-equatorial influences of submonthly scale southerly surges over the eastern Indian Ocean during Southern Hemisphere winter. *J. Geophys. Res.* **114**: D20119, doi: 10.1029/2008JD011441.

Galarneau TJ Jr, Dole RM, Hamill TM, Perlwitz J. 2012. A multiscale analysis of the extreme weather events over western Russia and northern Pakistan during July 2010. *Mon. Weather Rev.* **140**: 1639–1664.

Haggag M, El-Badry H. 2013. Mesoscale numerical study of quasi-stationary convective system over Jeddah in November 2009. *Atmos. Clim. Sci.* **3**: 73–86.

Hart RE, Grumm RH. 2001. Using normalized climatological anomalies to rank synoptic-scale events objectively. *Mon. Weather Rev.* **129**: 2426–2442.

Hart NCG, Reason CJC, Fauchereau N. 2010. Tropical–extratropical interactions over southern Africa: Three cases of heavy summer season rainfall. *Mon. Weather Rev.* **138**: 2608–2623.

Holton JR. 2004. *An Introduction to Dynamic Meteorology*. Elsevier Academic Press: Cambridge, MA.

Hoskins BJ, McIntyre ME, Robertson AW. 1985. On the use and significance of isentropic potential vorticity maps. *Q. J. R. Meteorol. Soc.* **111**: 877–946.

Huffman GJ, Adler RF, Bolvin DT, Gu G, Nelkin EJ, Bowman KP, Hong Y, Stocker EF, Wolff DB. 2007. The TRMM multisatellite precipitation analysis (TMPA): Quasi-global, multiyear, combined-sensor precipitation estimates at fine scales. *J. Hydrometeorol.* **8**: 38–55.

Joseph PV, Sijikumar S. 2004. Intraseasonal variability of the low-level jet stream of the Asian summer monsoon. *J. Clim.* **17**: 1449–1458.

Kahana R, Ziv B, Enzel Y, Dayan U. 2002. Synoptic climatology of major floods in the Negev desert, Israel. *Int. J. Climatol.* **22**: 867–882.

Knippertz P. 2005. Tropical–extratropical interactions associated with an Atlantic tropical plume and subtropical jet streak. *Mon. Weather Rev.* **133**: 2759–2776.

Knippertz P. 2007. Tropical–extratropical interactions related to upper-troughs at low latitudes. *Dyn. Atmos. Oceans* **43**: 36–62.

Knippertz P, Martin JE. 2005. Tropical plumes and extreme precipitation in subtropical and tropical West Africa. *Q. J. R. Meteorol. Soc.* **131**: 2337–2365.

Knippertz P, Martin JE. 2007a. A Pacific moisture conveyor belt and its relationship to a significant precipitation event in the semiarid southwestern United States. *Weather and Forecasting* **22**: 125–144.

Knippertz P, Martin JE. 2007b. The role of dynamic and diabatic processes in the generation of cut-off lows over northwest Africa. *Meteorol. Atmos. Phys.* **96**: 3–19.

Knippertz P, Fink AH, Reiner A, Speth P. 2003. Three late summer/early autumn cases of tropical–extratropical interactions causing precipitation in northwest Africa. *Mon. Weather Rev.* **131**: 116–135.

Knippertz P, Wernli H, Glaser G. 2013. A global climatology of tropical moisture exports. *J. Clim.* **17**: 1449–1458.

Kottek K, Grieser J, Beck C, Rudolf B, Rubel F. 2006. World map of the Köppen–Geiger climate classification updated. *Meteorol. Z.* **15**: 259–263.

Krichak SO, Breitgand JS, Feldstein SB. 2012. A conceptual model for the identification of the Active Red Sea Trough synoptic events over the southeastern Mediterranean. *J. Appl. Meteorol. Clim.* **51**: 962–971.

Kumar KN, Entekhabi D, Molini A. 2015. Hydrological extremes in hyperarid regions: A diagnostic characterization of intense precipitation over the central Arabian Peninsula. *J. Geophys. Res. Atmos.* **120**: 1637–1650, doi: 10.1002/2014JD022341.

Lelieveld J, Hadjinicolaou P, Kostopoulou E, Chenoweth J, El Maayar M, Giannakopoulos C, Hannidis C, Lange MA, Tanarhte M, Tyrlis E, Xoplaki E. 2012. Climate change and impacts in the eastern Mediterranean and the Middle East. *Clim. Change* **114**: 667–687.

Lelieveld J, Hadjinicolaou P, Kostopoulou E, Giannakopoulos C, Pozzer A, Tanarhte M, Tyrlis E. 2013. Model projected heat extremes and air pollution in the eastern Mediterranean and Middle East in the 21st century. *Reg. Environ. Change* **14**: 1937–1949.

Martius O, Zenklusen E, Schwierz C, Davies HC. 2006. Episodes of Alpine heavy precipitation with an overlying elongated stratospheric intrusion: A climatology. *Int. J. Climatol.* **26**: 1149–1164.

Martius O, Schwierz C, Davies HC. 2008. Far-upstream precursors of heavy precipitation events on the Alpine south-side. *Q. J. R. Meteorol. Soc.* **134**: 417–428.

Martius O, Sodemann H, Joos H, Pfahl S, Winschall A, Croci-Maspoli M, Graf M, Madonna E, Mueller B, Schemm S, Sedlacek J, Sprenger M, Wernli H. 2013. The role of upper-level dynamics and surface processes for the Pakistan flood of July 2010. *Q. J. R. Meteorol. Soc.* **139**: 1780–1797.

Mashat A, Basset HA. 2011. Analysis of rainfall over Saudi Arabia. *Env. Arid Land Agric. Sci.* **22**: 59–78.

Massacand AC, Wernli H, Davies HC. 1998. Heavy precipitation on the Alpine southside: An upper-level precursor. *Geophys. Res. Lett.* **25**: 1435–1438, doi: 10.1029/98GL50869.

Moore BJ, Neiman BJ, Ralph FM, Barthold FE. 2012. Physical processes associated with heavy flooding rainfall in Nashville, Tennessee, and vicinity during 1–2 May 2010: The role of an atmospheric river and mesoscale convective systems. *Mon. Weather Rev.* **140**: 358–378.

Nazemosadat MJ, Ghaedamini H. 2010. On the relationships between the Madden–Julian Oscillation and precipitation variability in southern Iran and the Arabian Peninsula: Atmospheric circulation analysis. *J. Clim.* **23**: 887–904.

Piaget N, Froidevaux P, Giannakaki P, Gierth F, Martius O, Riemer M, Wolf G, Grams CM. 2015. Dynamics of a local Alpine flooding event in October 2011: Moisture source and large-scale circulation. *Q. J. R. Meteorol. Soc.* **141**: 1922–1937.

Raziei T, Mofidi A, Santos AJ, Bordi I. 2012. Spatial patterns and regimes of daily precipitation in Iran in relation to large-scale atmospheric circulation. *Int. J. Climatol.* **32**: 1226–1237.

Riemer M, Baumgart M, Eiermann S. 2014. Cyclogenesis downstream of extratropical transition analyzed by Q-vector partitioning based on flow geometry. *J. Atmos. Sci.* **71**: 4204–4220.

Rodwell MJ, Hoskins BJ. 1996. Monsoons and the dynamics of deserts. *Q. J. R. Meteorol. Soc.* **122**: 1385–1404.

Rubin S, Ziv B, Paldor N. 2007. Tropical plumes over eastern North Africa as a source of rain in the Middle East. *Mon. Weather Rev.* **135**: 4135–4148.

Shentsis I, Laronne JB, Alpert P. 2012. Red Sea Trough floods in the Negev, Israel (1964–2007). *Hydrol. Sci. J.* **57**: 42–51.

Sodemann H, Schwierz C, Wernli H. 2008. Interannual variability of Greenland winter precipitation sources: Lagrangian moisture diagnostic and North Atlantic Oscillation influence. *J. Geophys. Res.* **113**: D03107, doi: 10.1029/2007JD008503.

Sprenger M, Wernli H. 2015. The LAGRANTO Lagrangian analysis tool – version 2.0. *Geosci. Model Dev.* **8**: 2569–2586.

Thorncroft CD, Hoskins BJ, McIntyre ME. 1993. Two paradigms of baroclinic-wave life-cycle behaviour. *Q. J. R. Meteorol. Soc.* **119**: 17–55.

Tsvieli Y, Zangvil A. 2005. Synoptic climatological analysis of 'wet' and 'dry' Red Sea Troughs over Israel. *Int. J. Climatol.* **25**: 1997–2015.

Tubi A, Dayan U. 2014. Tropical plumes over the Middle East: Climatology and synoptic conditions. *Atmos. Res.* **145–146**: 168–181.

Tyrlis E, Lelieveld E, Steil B. 2013. The summer circulation over the eastern Mediterranean and the Middle East: Influence of the South Asian monsoon. *Clim. Dyn.* **40**: 1103–1123.

Wernli H, Davies DC. 1997. A Lagrangian-based analysis of extratropical cyclones. I: The method and some applications. *Q. J. R. Meteorol. Soc.* **123**: 467–489.

Ziv B. 2001. A subtropical rainstorm associated with a tropical plume over Africa and the Middle-East. *Theor. Appl. Climatol.* **68**: 91–102.

Ziv B, Dayan U, Sharon D. 2005. A mid-winter, tropical extreme flood-producing storm in southern Israel: Synoptic scale analysis. *Meteorol. Atmos. Phys.* **88**: 53–63.

Appendix C3. *De Vries et al.* (2018)

Published in the Journal of Geophysical Research - Atmospheres in 2018

Identification of Tropical-Extratropical Interactions and Extreme Precipitation Events in the Middle East based on Potential Vorticity and Moisture Transport

Authors: A.J. de Vries[1], H.G. Ouwersloot[1], S.B. Feldstein[2], M. Riemer[3], A.M. El Kenawy[4], M.F. McCabe[5], J. Lelieveld[1,6]

[1]) Atmospheric Chemistry Department, Max Planck Institute for Chemistry, Mainz, Germany
[2]) Department of Meteorology, The Pennsylvania State University, University Park, USA
[3]) Institut für Physik der Atmosphäre, University of Mainz, Germany
[4]) Department of Geography, Mansoura University, Egypt
[5]) Water Desalination and Reuse Center, Division of Biological and Environmental Sciences and Engineering, King Abdullah University of Science and Technology, Jeddah, Saudi Arabia
[6]) Energy, Environment and Water Research Center, The Cyprus Institute, Nicosia, Cyprus

AGU PUBLICATIONS

JGR

Journal of Geophysical Research: Atmospheres

RESEARCH ARTICLE
10.1002/2017JD027587

Key Points:
- We combine stratospheric PV intrusions and poleward IVT structures for identification of extreme precipitation in the Middle East
- IVT is a potentially more pertinent predictor for extreme precipitation than PV
- Tropical-extratropical interactions contribute to a large fraction of the climatological rainfall amounts and extreme precipitation days

Correspondence to:
A. J. de Vries,
a.devries@mpic.de

Citation:
de Vries, A. J., Ouwersloot, H. G., Feldstein, S. B., Riemer, M., El Kenawy, A. M., McCabe, M. F., & Lelieveld, J. (2018). Identification of tropical-extratropical interactions and extreme precipitation events in the Middle East based on potential vorticity and moisture transport. *Journal of Geophysical Research: Atmospheres*, *123*, 861–881. https://doi.org/10.1002/2017JD027587

Received 12 AUG 2017
Accepted 19 DEC 2017
Accepted article online 26 DEC 2017
Published online 24 JAN 2018

Identification of Tropical-Extratropical Interactions and Extreme Precipitation Events in the Middle East Based On Potential Vorticity and Moisture Transport

A. J. de Vries[1], H. G. Ouwersloot[1], S. B. Feldstein[2], M. Riemer[3], A. M. El Kenawy[4], M. F. McCabe[5], and J. Lelieveld[1,6]

[1]Atmospheric Chemistry Department, Max Planck Institute for Chemistry, Mainz, Germany, [2]Department of Meteorology, Pennsylvania State University, University Park, PA, USA, [3]Institut für Physik der Atmosphäre, University of Mainz, Mainz, Germany, [4]Department of Geography, Mansoura University, Mansoura, Egypt, [5]Water Desalination and Reuse Center, Division of Biological and Environmental Sciences and Engineering, King Abdullah University of Science and Technology, Jeddah, Saudi Arabia, [6]Energy, Environment and Water Research Center, Cyprus Institute, Nicosia, Cyprus

Abstract Extreme precipitation events in the otherwise arid Middle East can cause flooding with dramatic socioeconomic impacts. Most of these events are associated with tropical-extratropical interactions, whereby a stratospheric potential vorticity (PV) intrusion reaches deep into the subtropics and forces an incursion of high poleward vertically integrated water vapor transport (IVT) into the Middle East. This study presents an object-based identification method for extreme precipitation events based on the combination of these two larger-scale meteorological features. The general motivation for this approach is that precipitation is often poorly simulated in relatively coarse weather and climate models, whereas the synoptic-scale circulation is much better represented. The algorithm is applied to ERA-Interim reanalysis data (1979–2015) and detects 90% (83%) of the 99th (97.5th) percentile of extreme precipitation days in the region of interest. Our results show that stratospheric PV intrusions and IVT structures are intimately connected to extreme precipitation intensity and seasonality. The farther south a stratospheric PV intrusion reaches, the larger the IVT magnitude, and the longer the duration of their combined occurrence, the more extreme the precipitation. Our algorithm detects a large fraction of the climatological rainfall amounts (40–70%), heavy precipitation days (50–80%), and the top 10 extreme precipitation days (60–90%) at many sites in southern Israel and the northern and western parts of Saudi Arabia. This identification method provides a new tool for future work to disentangle teleconnections, assess medium-range predictability, and improve understanding of climatic changes of extreme precipitation in the Middle East and elsewhere.

Plain Language Summary Torrential rains lead almost every year to flooding and fatalities in the arid Middle East. At the same time, such heavy rainfall events can recharge scarce freshwater resources in the subtropical desert region. These events often occur when the atmospheric circulations of the midlatitudes and the tropics interact with another. More specifically, a disturbance from the midlatitudes intrudes into the subtropics and initiates an incursion of tropical moisture across the Middle East. In our study we developed an identification method for heavy rainfall events based on the combination of these two meteorological processes. This unique approach avoids dependency on rainfall data which is often poorly simulated in numerical weather and climate models, whereas the atmospheric circulation is much better represented. Our method successfully detects events that contribute to a large fraction of annual rainfall amounts (40–70%) and heavy rainfall days (50–90%) in the arid parts of the Levant and the Arabian Peninsula. Moreover, the characteristics and duration of the midlatitude disturbances and tropical moisture incursions strongly influence the rainfall severity. This knowledge and identification method can support weather prediction and early warnings for heavy rainfall events as well as future studies on their climatic changes due to global warming.

1. Introduction

Extreme precipitation events in the otherwise arid Middle East can have dramatic socioeconomic impacts. In Egypt, Israel, Jordan, and Saudi Arabia, 39 flood events over the period of 1900–2016 caused 1,508 fatalities, affected 291,387 people, and resulted in damages exceeding 1.8 billion US dollars (Emergency Events Database, unpublished data, provided on 19 April 2017 by the Centre for Research on the Epidemiology of

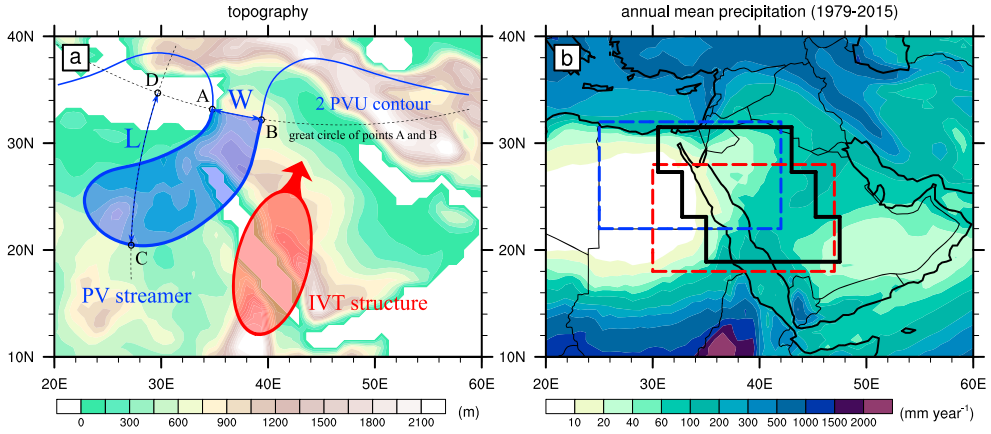

Figure 1. The Middle East region with (a) the topography from ERA-Interim data and a schematic representation of tropical-extratropical interactions, involving the intrusion of a midlatitude upper-level trough and an incursion of tropical moisture into the region, and (b) the annual mean precipitation (mm yr^{-1}) in ERA-Interim data (1979–2015). In Figure 1a, the potential vorticity streamer geometrical criteria are depicted, being the width (*W*) and length (*L*) for the pair of contour points A and B on a 2 PVU contour at an isentropic surface; see the text in section 2.3 for details. In Figure 1b the box for defining the extreme precipitation days is illustrated by black lines encompassing three imaginary boxes from north to south: box 1 (27.3–31.5°N, 30.5–43.0°E), box 2 (23.1–27.3°N, 32.75–45.25°E), and box 3 (18.9–23.1°N and 35.0–47.5°E); see section 2.2. Figure 1b also depicts the target areas for defining PV (blue box; 22–32°N, 25–42°E) and IVT (red box; 18–28°N, 30–47°E) incursions; see section 3.3.

Disasters; CRED). At the same time, these recurrent rainfall events replenish scarce freshwater resources that are crucial for agriculture (Amin et al., 2016; Schulz et al., 2016). Therefore, the understanding of extreme precipitation events in the Middle East, their predictability, and changes due to global warming are of high interest.

Extreme precipitation events in the Middle East often result from tropical-extratropical interaction, whereby midlatitude forcing and poleward transport of tropical moisture are of central importance (Figure 1a). Case studies of such events revealed the intrusion of a midlatitude upper-level trough into the subtropics, which interacts with the tropical low-level circulation and initiates an incursion of tropical moisture into the region (De Vries et al., 2013, 2016). Also, from a climatological perspective, heavy rainfall over the Middle East is typically associated with an upper-level cyclonic circulation and enhanced southerly moisture fluxes (Almazroui et al., 2016; Evans & Smith, 2006; Kahana et al., 2004; Krichak et al., 2012; Kumar et al., 2015). Apart from the Middle East, tropical-extratropical interactions and extreme precipitation events also affect arid subtropical regions elsewhere, including northwestern Africa, southwestern North America, southern Africa, Pakistan, the Himalayas, and Australia (Favors & Abatzoglou, 2013; Hart et al., 2010; Knippertz et al., 2003; Martius et al., 2013; Vellore et al., 2016; Wright, 1997).

Previous studies have presented various identification methods for atmospheric features that have direct relevance to tropical-extratropical interactions and/or extreme precipitation. These include cloud bands or tropical plumes based on satellite imagery (Fröhlich et al., 2013; Hart et al., 2012, 2013), tropical moisture exports (Knippertz, 2003; Knippertz et al., 2013; Knipperz & Wernli, 2010), and warm conveyor belts (Madonna, Wernli et al., 2014; Pfahl et al., 2014) using trajectories, moisture surges or monsoon bursts through applying statistically based thresholds on moisture flux and wind fields (Cavazos et al., 2002; Favors & Abatzoglou, 2013; Pascale & Bordoni, 2016), and atmospheric rivers. Atmospheric rivers have received increased attention over the last decade as they are a key feature in heavy rainfall and flooding across North America and Europe (e.g., Lavers & Villarini, 2013a, 2013b; Ralph et al., 2006; Waliser & Guan, 2017). They are characterized by narrow and elongated plume-like structures of strong moisture transport, and their features are often detected using vertically integrated water vapor fluxes (IVT) (e.g., Guan & Waliser, 2015; Mahoney et al., 2016; Mundhenk, Barnes, & Maloney, 2016; Rutz et al., 2014). Besides application for identification of atmospheric rivers, IVT is also widely recognized as a large-scale precursor, environmental characteristic, and medium-range predictor of extreme precipitation occurrence (e.g., Froidevaux & Martius, 2016; Lavers et al., 2014; Moore et al., 2015). Furthermore, several case studies and climatological

investigations adopted IVT to identify moisture pathways associated with extreme precipitation events (e.g., Knippertz et al., 2003; Swales et al., 2016).

Another atmospheric feature that has our specific interest are stratospheric potential vorticity (PV) intrusions, which have been identified as precursors of extreme precipitation in the Alpine region, southern Africa, and northwestern Africa (Hart et al., 2010; Knippertz & Martin, 2005; Massacand et al., 1998). Martius et al. (2006) presented climatological evidence for the relationship between objectively identified stratospheric PV intrusions and extreme precipitation in the southern Alps. Also, heavy rainfall in the Middle East has been associated with upper-tropospheric PV anomalies (De Vries et al., 2016; Evans & Smith, 2006; Kumar et al., 2015). Stratospheric PV intrusions can drive convection and extreme precipitation through (i) reducing the static stability in the lower troposphere and building up convective potential available energy, (ii) inducing dynamical lifting ahead of the PV anomaly, (iii) transporting moisture on its downstream flank, and (iv) orographic lifting through orienting the low-level winds toward a topographic barrier (Funatsu & Waugh, 2008; Martius et al., 2013; Schlemmer et al., 2010). In addition, stratospheric PV intrusions can also indirectly contribute to the formation of extreme precipitation in subtropical regions when they extend far into low latitudes, interact with the tropical low-level circulation, and thus pave the way for a tropical moisture excursion (Knippertz, 2007). Although the importance of both stratospheric PV intrusions and high moisture fluxes for heavy rainfall has been recognized in several studies (Barton et al., 2016; Evans & Smith, 2006; Froidevaux & Martius, 2016; Martius et al., 2006), they have thus far not been combined in an algorithm for the identification of extreme precipitation events.

In this study, we present for the first time an object-based identification method for extreme precipitation events based on the combination of stratospheric PV intrusions and structures of high IVT. The motivations for this approach are threefold: (1) Stratospheric PV intrusions and IVT structures represent the midlatitude forcing and tropical moisture contributions, respectively, of tropical-extratropical interactions, (2) PV and IVT are both larger-scale meteorological precursors of extreme precipitation, and (3) their application introduces the novelty of combining these features in an algorithm for the detection of extreme precipitation. The aim of this approach is to identify extreme precipitation events without using precipitation data themselves, which are often subject to limitations of relatively coarse resolution model simulations or the observational data products (e.g., Donat et al., 2014; Zhang et al., 2011). In contrast, the synoptic-scale circulation in meteorological data sets is much better represented, which introduces the perspective to apply the algorithm on long-term reanalysis data sets and climate model output in future studies.

The organization of the paper is as follows. Section 2 describes the employed data sets, the definition of extreme precipitation days, and the algorithm for identifying stratospheric PV intrusions and IVT structures. Next, we apply the algorithm to the Middle East region using reanalysis data (section 3) and we investigate the importance of PV and IVT for extreme precipitation events in a climatological context (section 4). Furthermore, section 5 addresses the relation between the PV and IVT characteristics and the severity of the precipitation. Finally, we quantify the contribution of the tropical-extratropical interactions to climatological rainfall amounts and extreme precipitation days in the Middle East using observational precipitation data (section 6). Section 7 presents the conclusions and some implications of the study.

2. Data and Methods

2.1. Reanalysis and Observational Precipitation Data

We employed 6-hourly ERA-Interim reanalysis data on a N128 Gaussian grid (~0.7° × 0.7°) for the period 1979–2015 (Dee et al., 2011) to identify stratospheric PV intrusions and IVT structures. Zonal and meridional IVT fields are available, and PV was computed from data on model levels and then linearly interpolated onto isentropic levels between 295 and 370 K, with 5 K intervals. Figure 2a presents an example of PV on an isentropic surface and the full IVT field.

Furthermore, we used precipitation from reanalysis, gridded observational, satellite-based and individual station data to examine the contribution of the stratospheric PV intrusions and IVT structures to the climatological precipitation amounts and extreme precipitation days. Each precipitation data set has its strengths and limitations, motivating us to use a variety of different data sources. Daily precipitation from ERA-Interim data was constructed from 12-hourly accumulated forecasts from 00 and 12 UTC. Aphrodite (V1101) contains

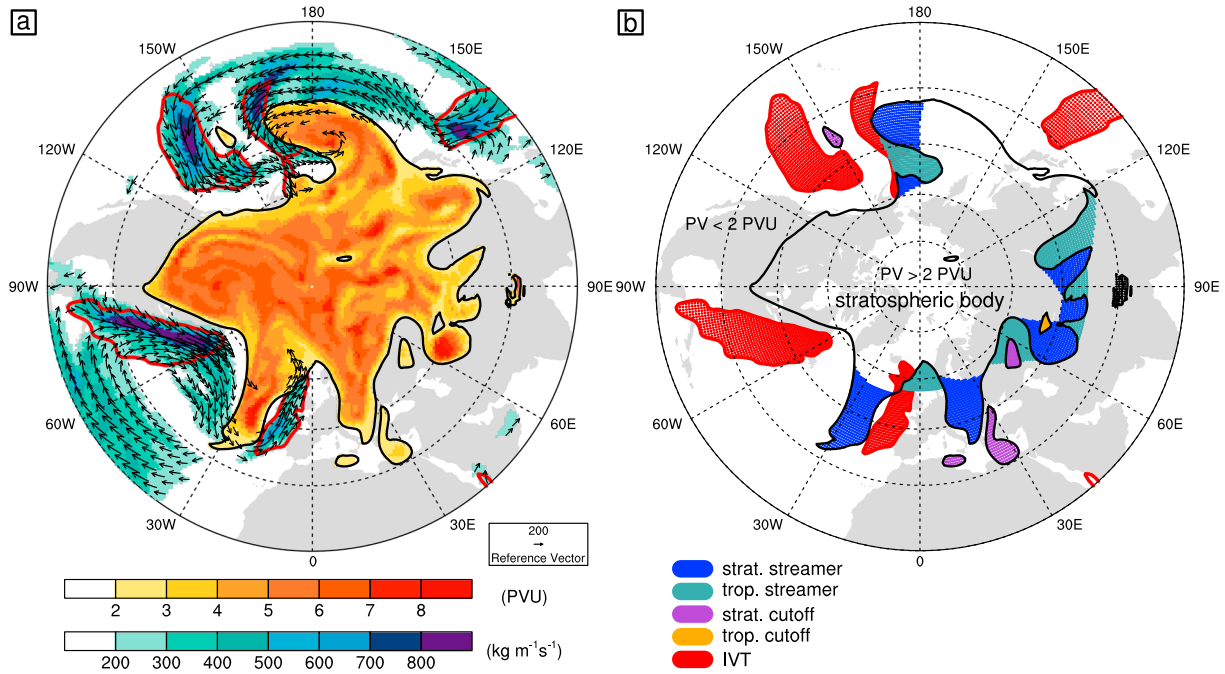

Figure 2. An example of the algorithm results on 14 January 2005, 12 UTC, showing (a) the PV (PVU) at 315 K, the magnitude and vectors of the full IVT (kg m^{-1} s^{-1}), the 2 PVU contours (black lines) and the 200 kg m^{-1} s^{-1} meridional IVT contours (red lines); and (b) the identified stratospheric and tropospheric PV streamers and cutoffs, and IVT structures, as indicated in the legend.

gridded daily precipitation, based on station data, with a spatial resolution of 0.25° × 0.25°, spanning the years 1951–2007 (Yatagai et al., 2012). Also, we used daily rainfall data of the 3B42 version 7 product of the Tropical Rainfall Measuring Mission Multisatellite Precipitation Analysis (hereafter TRMM), with a 0.25° × 0.25° spatial resolution, available from 1998 to the present (Huffman et al., 2007). Note that we limit the analysis for this particular data set until 2013 as the TRMM satellite was decommissioned in 2014. Furthermore, we used daily rainfall records from stations in Saudi Arabia and Israel. For Saudi Arabia, the data set presented by El Kenawy and McCabe (2016) provides ground-based observations, comprising 240 individual daily rainfall records spanning 1979 to 2012. We only used time series with less than 50% missing values, resulting in 192 daily rainfall records. Station data from Israel were provided by the Israel Meteorological Service (IMS). We used 158 rainfall records that covered at least 20 years of the 37 year period of 1979–2015. Daily observations with flags indicating that the rainfall amount may be interpolated or accumulated over multiple days were treated as missing values.

2.2. Definitions of Extreme Precipitation Days

The region of interest encompasses eastern Egypt, southern Israel, Jordan, and the northern and western parts of Saudi Arabia (depicted by the black box in Figure 1b), where extreme precipitation events with devastating impacts have been recurrent. This area covers the arid subtropical desert region with very low annual rainfall amounts between the wetter eastern Mediterranean to the northwest and the tropical rain belt to the south. Previous studies adopted varying definitions of extreme precipitation ranging from straightforward percentile-based thresholds on individual grid points or area-averaged precipitation (Favors & Abatzoglou, 2013; Martius et al., 2006; Pfahl & Wernli, 2012; Škerlak et al., 2015) to more sophisticated methods such as object-based approaches (Mahoney et al., 2016; Moore et al., 2015). Since the available reanalysis and observational data are subject to several limitations, we opted for a relatively simple and straightforward approach. We define extreme precipitation days (EPDs) by the 99th and 97.5th percentiles of daily precipitation in ERA-Interim data, averaged over the grid points in the black box in Figure 1b. This definition of EPDs is rather crude and can include both localized heavy rainfall and less intense, widespread rainfall. Both types of events are of interest here as precipitation in the dry desert region has by nature an extreme character. Throughout this study we will mostly use the 97.5th percentile EPDs, as these include

all relevant extreme precipitation events as identified by visual inspection of daily precipitation in ERA-Interim, Aphrodite, and TRMM data.

The use of precipitation data from ERA-Interim for EPDs introduces a potential constraint in that it is the same data set as for which we apply the algorithm and that localized heavy rainfall may not be adequately resolved, but it has the advantage of suitable spatial and temporal coverage. Available observational data sets do not cover the extended period of 1979–2015 under consideration (Aphrodite and TRMM), underestimate rainfall amounts (Aphrodite, see Tanarhte et al., 2012), and suffer from a relatively poor-density station network (Aphrodite and stations) and limited availability in the region of interest (stations). To evaluate the fidelity of using ERA-Interim data for defining EPDs, we compare these to EPDs derived from Aphrodite and TRMM, after interpolating the data from the regular $0.25° \times 0.25°$ grid to a N128 Gaussian grid, for the time period that is covered by all three data sets (1998–2007). Of the 99th (97.5th) percentile EPDs in ERA-Interim data, 79% (71%) matches with EPDs in Aphrodite or TRMM data, indicating a reasonable representativeness of the EPDs using ERA-Interim data. Also, Pfahl and Wernli (2012) demonstrated in their Figure 3 a reasonable agreement between 6-hourly 99th percentile precipitation in ERA-Interim and the Climate Prediction Center morphing method (CMORPH), ranging from $>$50% over eastern Egypt up to $>$90% over the northwestern portions of Saudi Arabia.

2.3. Algorithm for PV Intrusions and IVT Structures

We identify PV intrusions following Wernli and Sprenger (2007) and Sprenger et al. (2013). This approach has been adopted by many studies addressing the climatological characteristics of PV intrusions (Isotta et al., 2008; Martius, Schwierz, & Davies, 2008), their representation in global circulation models (Béguin et al., 2013), and their relation to extreme weather events, warm conveyor belts, and the exchange of tropical-extratropical and stratospheric-tropospheric air masses (Kunz et al., 2015; Madonna, Limbach, et al., 2014; Martius et al., 2006; Martius, Schwierz, Sprenger, 2008; Sprenger et al., 2013, 2007). Following the approach of Wernli and Sprenger (2007) and Sprenger et al. (2013), we consider the 2 potential vorticity unit (PVU; 1 PVU = 10^{-6} K kg^{-1} m^2 s^{-1}) surface as the dynamical tropopause, separating the stratospheric (PV $>$ 2 PVU) and tropospheric (PV $<$ 2 PVU) air masses (Figure 2). The 2 PVU contours on isentropic surfaces serve to identify PV intrusions, which are indicators of Rossby wave breaking. These PV contours can form narrow and elongated filaments (PV streamers) and can split off from the main stratospheric or tropospheric reservoirs (PV cutoffs). This specific method has advantages over other approaches that consider stratospheric PV intrusions from a vertical perspective or by overturning of PV contours in the meridional direction on the quasi-horizontal plane. The former approach refers to multiple crossings of the dynamical tropopause in vertical profiles, so-called tropopause folds, which have been associated with the occurrence of extreme precipitation (Škerlak et al., 2015). However, as these authors remarked, the precipitation is related to the larger-scale trough in which the fold is embedded, rather than the mesoscale fold itself, motivating our choice to identify stratospheric PV intrusions on a quasi-horizontal plane. In the latter approach, meridionally overturning PV contours serve as an indicator of Rossby wave breaking (e.g., Liu et al., 2014; McIntyre & Palmer, 1983; Strong & Magnusdottir, 2008). This implies that meridionally elongated PV streamers without meridional overturning of PV contours would be ignored, although such stratospheric PV intrusions can be important for extreme precipitation, further supporting our choice to identify PV intrusions using the method of Wernli and Sprenger (2007) and Sprenger et al. (2013). For the sake of clarity, we describe our reproduced algorithm with special emphasis on a few modifications.

The algorithm is applied on isentropic surfaces between 300 and 350 K with 5 K intervals and consists of the following four steps. First, at each 6-hourly time instance and on each isentropic surface, we retrieve the +2 PVU contour and the contour point coordinates (Figures 1a and 2). Accordingly, only PV intrusions relevant to the Northern Hemisphere are considered. The coordinates of the 2 PVU contour points are determined by a visualization routine of the National Center for Atmospheric Research (NCAR) Command Language (NCL) package version 6.3.0 that is designed to draw contour lines. Second, the stratospheric body is determined, which corresponds to the extensive reservoir of stratospheric air mass that covers higher latitudes (Figure 2b). To this end, we select the 2 PVU contour with the lowest latitude that encircles the Northern Hemisphere. If such a contour is not available, we appoint the longest 2 PVU contour that has a zonal extent $>$180° and at least one contour point $>$80°N as the stratospheric body. In case such a contour is also not available, the PV streamer identification is not applied. All remaining 2 PVU contours are considered as PV cutoffs. Third, for the

Table 1
Sensitivity of PV Streamer Geometry and Thresholds (1979–2015)

	All days	EPD hits ≥99th percentile	EPD hits ≥97.5th percentile	False alarm ratio <95th percentile precipitation
PV streamer geometry previous studies				
$W < 800$, $LC > 1{,}500$ km (Wernli & Sprenger, 2007)	37.9%	88.3%	83.5%	89.4%
$W < 1{,}500$, $LC > 2{,}000$ km, $r > 2$ (Sprenger et al., 2013)	42.4%	93.4%	90.0%	89.8%
$W < 1{,}500$, $LC > 3{,}000$ km, $r > 3$	34.3%	87.6%	79.4%	89.0%
New PV streamer geometry				
$W < 1{,}500$, $L > 650$ km, $r > 0.65$	**41.4%**	**92.0%**	**90.3%**	**89.6%**
$W < 1{,}500$, $L > 800$ km, $r > 0.8$	37.8%	91.2%	86.1%	89.2%
$W < 1{,}500$, $L > 1{,}000$ km, $r > 1$	34.1%	86.1%	80.5%	88.8%

Note. In bold are the streamer criteria used in this study unless mentioned otherwise.

identification of PV streamers, we evaluate for each pair of contour points of the stratospheric body the geometrical criteria of the potential streamer: the width (W), length (L), and ratio (r) of L over W (Figure 1a). The width of the potential streamer is defined as the great-circle distance (shortest distance between two points on a sphere, measured over the surface of the sphere) between the contour points A and B. To determine the length of the potential streamer, we evaluate the shortest great-circle distances of all contour points between points A and B (for example, point C in Figure 1a) to the great circle defined by points A and B (point D in Figure 1a). The largest of these great-circle distances is defined as the length of the potential streamer. Fourth, all grid points within the polygons of the PV streamers and cutoffs are classified as being stratospheric (PV $>$ 2 PVU) or tropospheric (PV $<$ 2 PVU) intrusions. Figure 2b illustrates the successful identification of complex PV intrusion structures such as double, triple, or multiple neighboring streamers (over Europe, the Pacific Ocean, and Asia, respectively), a streamer being encapsulated within another streamer (to the east of the Caspian Sea), and cutoffs being located within streamers (to the north and east of the Caspian Sea).

Our streamer length definition deviates from Wernli and Sprenger (2007) and Sprenger et al. (2013), who used the contour length (LC) between points A and B. We define the length of the PV streamer perpendicular to the great circle of points A and B to introduce a more appropriate geometrical length measure of the PV streamers and to avoid features with wriggles and twisted contour lines. To evaluate the skill of the previous and new geometrical streamer definitions to detect EPDs, we perform sensitivity tests with both streamer definitions and various thresholds and quantify the coincidences between EPDs and days with stratospheric PV intrusions (i.e., PV incursions; for their definition, see section 3.3). More specifically, we use measures of the contingency matrix and calculate the EPD hits (EPDs coinciding with PV incursions divided by all EPDs) and false alarm ratios (PV incursions coinciding with <95th percentile precipitation days, divided by all PV incursions; Table 1). Our new streamer definition outperforms that applied in Wernli and Sprenger (2007) and reaches about equal scores as that applied in Sprenger et al. (2013) for extreme precipitation events in the Middle East. For example, the streamer criteria of the latter study ($W < 1{,}500$ km, $LC > 2{,}000$ km, and $r > 2$) coincides with 93.4% of the 99th percentile EPDs and 90.0% of the 97.5th percentile EPDs and had a false alarm ratio of 89.8% (Table 1). These scores are close to our new PV streamer geometry with thresholds of $W < 1{,}500$ km, $L > 650$ km, and $r > 0.65$ and show a slight deterioration for the 99th percentile EPDs (92.0%) and a slight improvement with regard to the 97.5th percentile EPDs (90.3%) as well as the false alarm ratio (89.6%). Throughout the remainder of this article we use the PV streamer thresholds $W < 1{,}500$ km, $L > 650$ km, and $r > 0.65$ unless mentioned otherwise.

IVT structures are defined as all grid points with a positive meridional (northward directed) IVT > 200 kg m^{-1} s^{-1} (Figure 2b). Here we use the meridional component of the IVT instead of the full IVT field as we are particularly interested in the poleward moisture transport. Most studies on the identification of atmospheric rivers adopted static thresholds on IVT or anomalous IVT that typically range between 250 and 500 kg m^{-1} s^{-1} (Mahoney et al., 2016; Mundhenk, Barnes, & Maloney, 2016; Payne & Magnusdottir, 2014; Rutz et al., 2014). We apply a somewhat lower threshold of 200 kg m^{-1} s^{-1} since we adopt only the meridional IVT component and to adjust to the lower background moisture transport in the Middle East region.

In the final stage, we retrieve unique characteristics of all individual PV and IVT features. These include, for example, the southward extent of stratospheric PV intrusions and the magnitude of the IVT structures, defined by the minimum latitude of the stratospheric PV intrusions and the maximum IVT value of the IVT structures, respectively. Furthermore, we reject (1) relatively small PV intrusions and IVT structures with a surface area $< 100{,}000\ km^2$ (for example, the tropospheric PV cutoff over the North Pole and the IVT structure over the southern Red Sea in Figure 2), (2) all PV streamers if >50% of the stratospheric body consists of stratospheric PV streamers, and (3) cutoffs if any grid point within the structure on the isentropic surface is below the surface topography (for example, the stratospheric cutoff over the Himalayas in Figure 2). The first criterion aims to retain only larger-scale features. The second criterion prevents the larger part of the stratospheric body from being a PV streamer when the 2 PVU contour is very distorted, similar to the 80% threshold of the contour length of the stratospheric body used by Sprenger et al. (2013). The third criterion removes a part of the "stratospheric" PV cutoffs that are associated with frictional processes near topography rather than with intrusions of stratospheric air masses.

3. Application in the Middle East

3.1. Examples of Extreme Precipitation Cases

Figure 3 demonstrates the functionality of the algorithm in four cases of extreme precipitation in the Middle East that resulted in flooding and severe societal impacts. In each case we find a stratospheric PV intrusion over northeast Africa accompanied by an IVT structure on its eastern flank. This meteorological configuration reflects Rossby wave breaking along with a midlatitude upper-level trough that intrudes into the subtropics and induces southerly moisture fluxes on its downstream flank. These stratospheric PV intrusions and IVT structures are clearly present during the events on 2 November 1994 and 22 January 2005 (Figures 3b and 3c) when extreme precipitation affected larger parts of Egypt and Saudi Arabia and resulted in 600 and 29 fatalities, respectively (De Vries et al., 2013, 2016). Interestingly, a very similar larger-scale meteorological constellation is observed during the localized heavy rainfall event that affected Jeddah on 25 November 2009 (Figure 3d) and caused 161 deaths, 10,000 people being affected, and an estimated damage of about US$ 900 million (De Vries et al., 2016; Deng et al., 2015; Yesubabu et al., 2016). In October 1979, flooding occurred in the eastern parts of Egypt with 50 fatalities and 66,000 people affected (De Vries et al., 2013; Moawad, 2012). Surprisingly, ERA-Interim did not generate precipitation over Egypt; nevertheless, a vigorous stratospheric PV intrusion and IVT structure are clearly apparent over the region (Figure 3a). The absence of simulated precipitation in ERA-Interim is likely related to poorer information of upper-air observations and satellite data during the early reanalysis period (Dee et al., 2011). Aphrodite data indicate a local precipitation spot over northwest Saudi Arabia and very low rainfall amounts that extend over eastern Egypt (Figure 3a), which suggests a large underestimation due to the sparse station network in this region. Thus, the algorithm can detect extreme precipitation events based on the larger-scale meteorological features, even when precipitation is underestimated or not represented in the reanalysis and/or observational data sets.

3.2. Spatial Distribution of PV and IVT Occurrences

In the next step, we identify the important regions where stratospheric PV intrusions and IVT structures occur during EPDs. Figure 4 presents the spatial distribution of 6-hourly occurrence frequencies of stratospheric PV intrusions and IVT structures during the period of 1979–2015. The calculation of stratospheric PV intrusion occurrences is based on stratospheric PV streamers and cutoffs vertically aggregated over the isentropic surfaces between 310 and 340 K, with 5 K intervals. For example, a frequency of 10% at a particular grid point means that a stratospheric PV streamer or cutoff is present at 10% of all considered 6-hourly time instances at any of the isentropic surfaces at that specific grid point. A detailed analysis of stratospheric PV intrusions during EPDs on all individual isentropic surfaces demonstrated their importance between 310 and 340 K (not shown), which is consistent with the selection of isentropic surfaces for year-round extreme precipitation events in the Alpine region by Martius et al. (2006). This range of isentropic surfaces warrants a seasonally independent detection of extreme precipitation events as the isentropic levels where stratospheric PV intrusions typically occur vary with the seasons.

The spatial distribution of stratospheric PV intrusion occurrences for all 6-hourly time instances reflect the midlatitude baroclinic zone to the north of the Middle East (Figure 4a), where Rossby wave breaking is frequent. Likewise, occurrences of IVT structures reveal the prevalent signature of the Somali jet along the

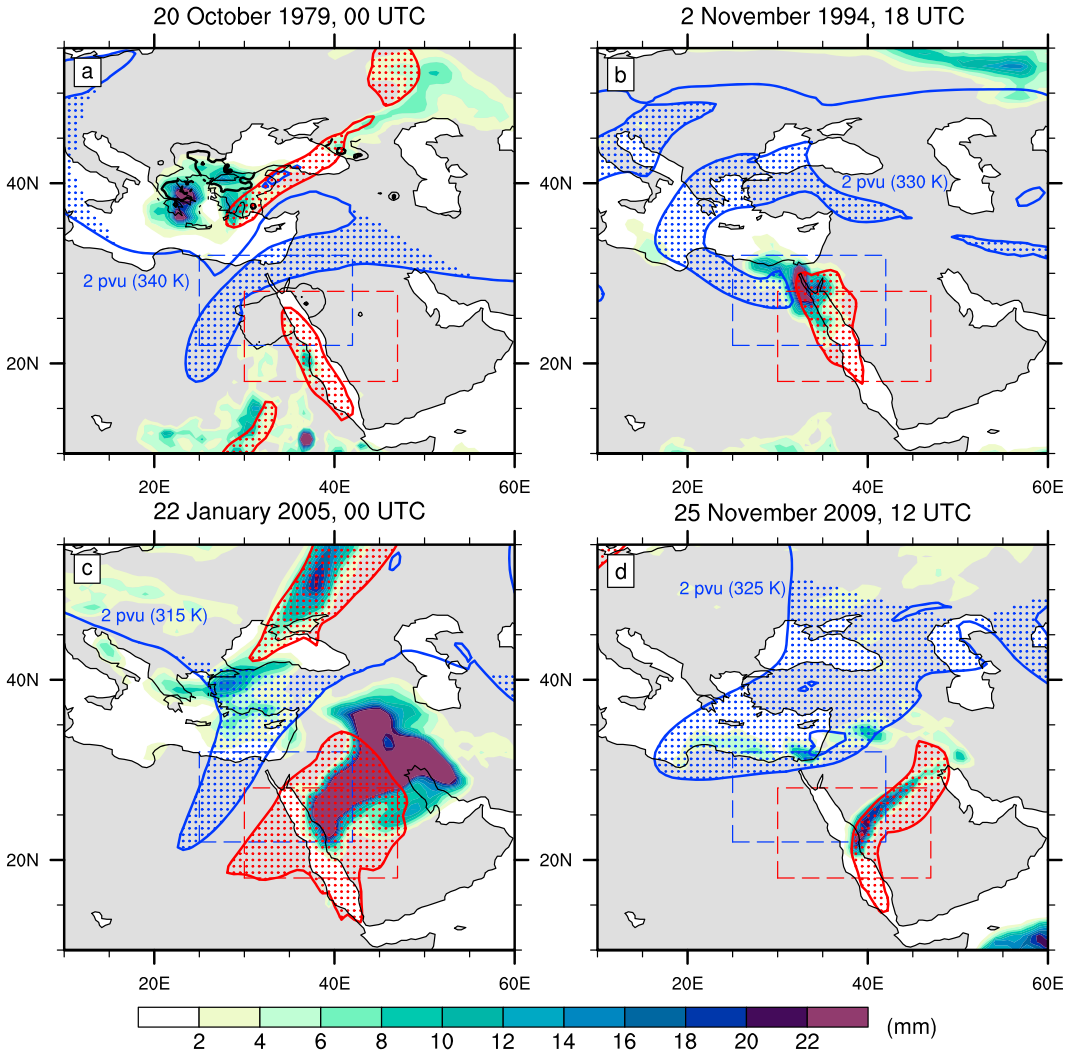

Figure 3. Daily precipitation (mm) from ERA-Interim data (colors), 2 PVU contours at indicated isentropic surfaces (blue lines), 200 kg m^{-1} s^{-1} meridional IVT contours (red lines), the grid points of stratospheric PV streamers and cutoffs (blue dots), and IVT structures (red dots) for four example cases; (a) 20 October 1979, 00 UTC, (b) 2 November 1994, 18 UTC, (c) 22 January 2005, 00 UTC, and (d) 25 November 2009, 12 UTC. In Figure 3a also the daily precipitation from Aphrodite data in black contours at 2 mm d^{-1} (thin lines) and 10 mm d^{-1} (thick lines). The dashed blue and red boxes in Figures 3a–3d bound the target areas for defining PV and IVT incursions, as in Figure 1b; see the text in section 3.3.

east African coast that transports moisture toward southwest Asia during summer (Figure 4d). For 6-hourly time instances during the 97.5th percentile EPDs, stratospheric PV intrusion and IVT structure frequencies reach their maxima over the eastern Mediterranean (>54%) and the southern Red Sea basin (>60%), respectively (Figures 4b and 4e), confirming the importance of midlatitude forcing and poleward moisture transport for extreme precipitation in the Middle East. Figures 4c and 4f display the percentage of occurrences of stratospheric PV intrusions and IVT structures during the EPDs relative to all their occurrences. Here the important areas emerge where stratospheric PV intrusions and IVT structures occur during extreme precipitation events over the region of interest, marked by the blue (25–42°E, 22–32°N) and red (30–47°E, 18–28°N) boxes in Figures 4c and 4f, respectively, also depicted in Figures 1b and 3. The relatively higher frequencies of IVT structure occurrences as compared to stratospheric PV intrusion occurrences hold some clues of IVT being more important for extreme precipitation than PV.

3.3. Definitions of PV and IVT Incursions

To facilitate comparison with EPDs and daily rainfall observations, we formulate the following spatial and temporal criteria for days with stratospheric PV intrusions and IVT structures, hereafter, PV and IVT

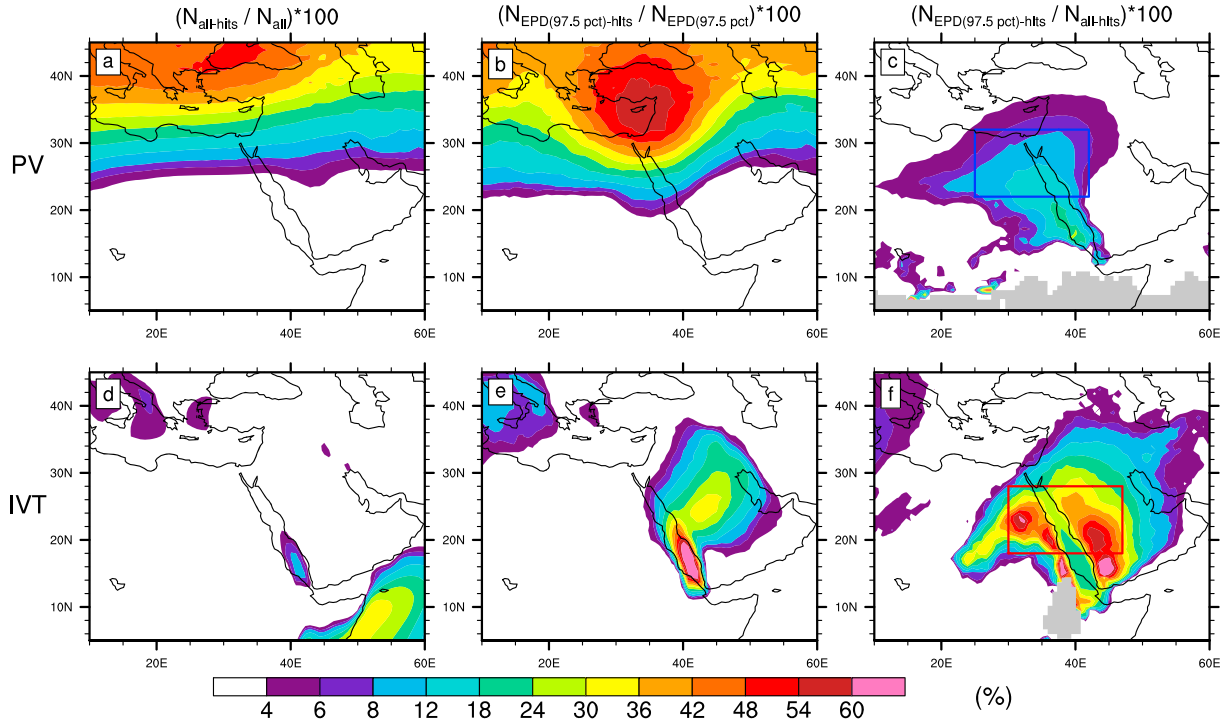

Figure 4. The climatology of 6-hourly occurrence frequencies (%) of (a–c) aggregated stratospheric PV streamers and cutoffs, and (d–f) IVT structures during the period 1979–2015. The panels show their frequencies for all time instances (Figures 4a and 4d), their frequencies for the time instances during the 97.5th percentile EPDs (Figures 4b and 4e), and the frequencies of their occurrences during the 97.5th percentile EPDs relative to their occurrences during all time instances (Figures 4c and 4f). The vertically aggregated fields in Figures 4a and 4b are obtained through translating for each 6-hourly time instance the three-dimensional binary field to two-dimensional binary field with a "1" if any isentropic surface between 310 and 340 K with 5 K intervals has a stratospheric PV streamer or cutoff and a "0" otherwise. Gray shading in Figures 4c and 4f indicate areas where the PV and IVT have zero occurrences during all time instances. The blue and red boxes in Figures 4c and 4f mark the target areas for defining PV and IVT incursions, respectively, as in Figures 1b and 3.

incursions. Days with PV incursions should have a stratospheric PV streamer or cutoff that overlaps the target area (blue box in Figures 1b, 3, and 4c) for at least three of the four time instances per day (00, 06, 12, and 18 UTC) at *one* specific level of any isentropic surface between 310 and 340 K. The rationale behind the requirement of having the stratospheric PV intrusion at one level instead of allowing various levels for different time instances is that isentropic PV is conserved under adiabatic and frictionless conditions and the intention to detect a persistent PV feature. Similarly, days with IVT incursions should have an IVT structure overlapping the target area (red box in Figures 1b, 3, and 4f) for at least three of the four time instances per day. Note that the northwest-southeast shift between the target areas for the PV and IVT incursions is not a coincidence but reflects the nature of stratospheric PV intrusions that initiate southerly moisture transport at their downstream flanks, which is consistent with the example cases in Figure 3. Also, we define days with *combined PV and IVT incursions* when both concur at a particular day. These combined PV and IVT incursions signify tropical-extratropical interactions and enable us to evaluate their climatological importance for precipitation and extreme precipitation in the Middle East.

4. Importance of PV and IVT Incursions for EPDs

4.1. Detection EPDs, Precipitation Intensity, and Seasonality

The combined PV and IVT incursions occur on 8.5% of all days during 1979–2015 and coincide with 89.8% (83.2%) of the 99th (97.5th) percentile EPDs (Table 2). PV incursions are relatively common and occur on 41.4% of all days. In contrast, IVT incursions occur on 11.8% of all days. Nevertheless, IVT incursions correspond to higher EPD hits (97.8% and 92.0% for the 99th and 97.5th percentile EPDs, respectively) as compared to the EPD hits of PV incursions (92.0% and 90.3% for the 99th and 97.5th percentile EPDs, respectively). This finding indicates that IVT is a potentially more pertinent predictor for extreme precipitation than

Table 2
Performance Algorithm (1979–2015)

	All days	EPD hits ≥99th percentile	EPD hits ≥97.5th percentile	False alarm ratio <95th percentile precipitation
Generous criteria PV (W < 1,500 km, $\mathbf{L > 650}$ **km,** $\mathbf{r > 0.65}$) and meridional IVT (**200 kg m^{-1} s^{-1}**)				
PV	41.4%	92.0%	90.3%	89.6%
IVT	11.8%	97.8%	92.0%	65.6%
PV and IVT	8.5%	89.8%	83.2%	58.3%
Restrictive criteria PV (W < 1,500 km, $\mathbf{L > 1{,}000}$ **km,** $\mathbf{r > 1}$) and meridional IVT (**250 kg m^{-1} s^{-1}**)				
PV	34.1%	86.1%	80.5%	88.8%
IVT	5.3%	81.8%	70.2%	49.0%
PV and IVT	3.8%	70.8%	59.6%	41.6%

Note. In bold are the different settings of the generous and restrictive criteria.

PV. A possible explanation is linked to the underlying causality of the atmospheric processes that drive extreme precipitation occurrence; stratospheric PV intrusions reach into the subtropics and extract moisture from the tropics that in turn support the heavy rainfall (De Vries et al., 2016), suggesting that IVT is more directly connected to (extreme) precipitation than PV. Indeed, PV and IVT incursions do not occur independently; 72.3% of IVT incursions are accompanied by PV incursions.

The greater importance of IVT over PV for extreme precipitation also emerges in Figure 5a, which shows the percentage of PV and IVT incursion frequencies for the precipitation intensity distribution ranging from the 13th to the ≥99th percentiles, with 1 percentile increments. Here the precipitation distribution is derived from daily ERA-Interim precipitation averaged over the region of interest. IVT incursions occur at 97.8% of the ≥99th precipitation percentile (representing 23.7% of the total precipitation amounts) and rapidly diminish toward lower percentiles, whereas PV incursion frequencies attain a maximum of 92.6% at the 98th–99th precipitation percentile and gradually reduce for lower precipitation intensities. Despite the greater importance of IVT for extreme precipitation than PV, we use the combination of PV and IVT incursions throughout the remainder of the study to reduce the false alarm ratio (Table 2) and to focus on (extreme) precipitation

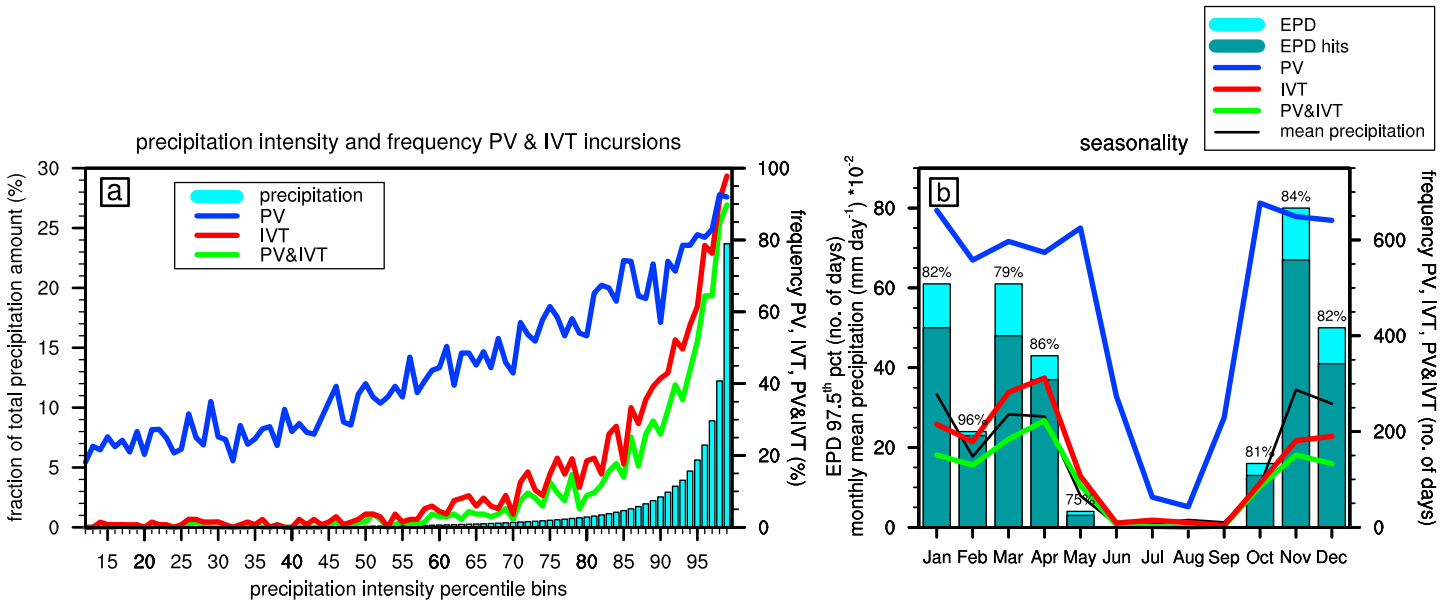

Figure 5. (a) Precipitation intensity bins from the 13th to the 99th percentiles with 1 percentile increments, the corresponding fractions of the total precipitation amount over the region of interest (blue bars), and the corresponding frequencies (%) of coinciding PV incursions (blue lines), IVT incursions (red lines), and combined PV and IVT incursions (green lines). (b) The monthly distribution of all 97.5th percentile EPDs (light blue color bars), the EPDs detected by the combined PV and IVT incursions (green color bars), the number of PV incursions (blue lines), number of IVT incursions (red lines), number of combined PV and IVT incursions (green lines), and the mean precipitation amounts (black thin lines). The fractions of EPDs that coincide with combined PV and IVT incursions relative to all EPDs (%) are indicated by the numbers above the color bars.

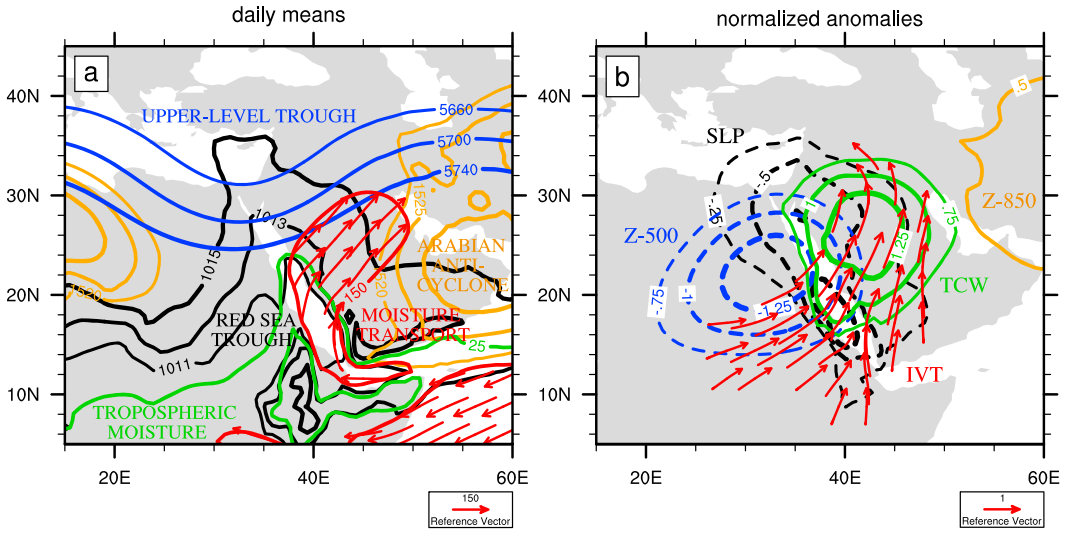

Figure 6. Composites of (a) daily means and (b) normalized anomalies for 97.5th percentile EPD hits (282 days); see the text for details. Figure 6a displays the sea level pressure (hPa; black contours), geopotential height (gpm) at 500 hPa (blue contours) and at 850 hPa (orange contours), total column water (green contour at 25 kg m^{-2}), and the IVT magnitude (red contour at 150 kg m^{-1} s^{-1}) and IVT direction where their magnitude exceeds 150 kg m^{-1} s^{-1} (red vectors). Figure 6b shows the normalized anomalies (SD), as in Figure 6a, but without the IVT magnitude and with the IVT vectors constructed from their zonal and meridional components and are only displayed where their vector length exceeds 1 SD.

resulting from tropical-extratropical interactions. The combined PV and IVT incursions have somewhat lower frequencies over the entire precipitation intensity distribution than IVT alone and show a maximum of 89.8% for the ≥99th fraction and then rapidly decrease following the distribution of the precipitation intensity. Importantly, Figure 5a provides clear evidence that both PV and IVT incursions are strongly connected to the precipitation intensity.

Figure 5b demonstrates the seasonal distribution of 97.5th percentile EPDs and the frequencies of PV and IVT incursions. EPDs are most frequent in late autumn/early winter (November–January) and early spring (March–April). During the summer months (June–September) the region of interest remains dry, as precipitation generation is suppressed by midtropospheric subtropical anticyclones (Zarrin et al., 2010) and middle- and upper-tropospheric large-scale subsidence imposed by the Asian summer monsoon-driven circulation (Rodwell & Hoskins, 1996; Tyrlis et al., 2013; Ziv et al., 2004), further strengthened by the regional heat-driven circulation over the Zagros Plateau (Zaitchik et al., 2007). PV incursions occur frequently from October to May (±50% of the days) and decline substantially from June to September, reflecting the northward retreat of the midlatitude baroclinic zone during summer. Likewise, IVT incursions are observed from October to May and diminish from June to September, when northerly winds dominate the low-level circulation over the Red Sea basin (Tyrlis et al., 2013). Overall, the combined PV and IVT incursions follow the seasonal distribution of the EPDs, supporting the confidence in the algorithm.

4.2. Tropospheric Circulation of EPD Hits

Figure 6 shows composites of daily means and normalized anomalies of the tropospheric circulation for EPD hits (i.e., the 282 days of the 97.5th percentile EPDs that coincide with combined PV and IVT incursions). Normalized anomalies were calculated using the 21 day running mean and standard deviation values of daily means over the period of 1979–2015, following De Vries et al. (2016). These composites provide clear insight into the larger-scale tropospheric circulation associated with the tropical-extratropical interactions that lead to the formation of extreme precipitation. Daily means and normalized anomalies of the 500 hPa geopotential height and sea level pressure demonstrate the intrusion of a midlatitude upper-level trough into the subtropics (<−1.25 SD, standard deviation) and the deepening and northward amplification of the climatological surface trough over the Red Sea region (i.e., the Red Sea Trough) farther downstream (<−0.75 SD), respectively. This picture is consistent both with phase locking of the tropical and

midlatitude troughs and with baroclinic wave growth as was observed for extreme precipitation events in the region (De Vries et al., 2013, 2016; Rubin et al., 2007). To the east we notice the features of the climatological subtropical anticyclone over the eastern margins of the Arabian Peninsula (i.e., the Arabian anticyclone). This meteorological configuration induces strong poleward moisture transport over the Red Sea basin (Figures 6a and 6b), leading to enhanced tropospheric moisture content over the region of interest (Figure 6b). Note that absolute total column water (TCW) amounts are high over the Red Sea basin akin to the features of the semipermanent Red Sea Trough (Figure 6a), whereas anomalous TCW amounts are particularly large over the interior of the Arabian Peninsula (>1.25 SD; Figure 6b). This larger-scale meteorological environment favors subsynoptic forcing for ascent and the development of (convective) rainstorms and extreme precipitation over the dry desert regions of the Middle East (De Vries et al., 2016). The tropospheric circulation in Figure 6 corroborates those as observed in case studies and climatological analyses of extreme precipitation events in the region (De Vries et al., 2016; Evans & Smith, 2006; Kumar et al., 2015) as well as those that have direct relevance to the Active Red Sea Trough phenomenon (De Vries et al., 2013; Kahana et al., 2004; Krichak et al., 2012; Ziv et al., 2005) and tropical plumes (Rubin et al., 2007; Ziv, 2001).

4.3. Missed EPDs and False Alarms

Since the aim of the algorithm is to detect EPDs, it is of interest to understand why particular EPDs are missed by the algorithm and why, on other days, combined PV and IVT incursions occurred without any resulting extreme precipitation. First of all, it is noteworthy that missed EPDs are not confined to particular months or seasons but are roughly equally distributed throughout the year (Figure 5b). The 97.5th percentile EPDs that were missed by the algorithm lacked PV incursions on 33 days and IVT incursions on 27 days. Case-by-case exploration revealed that many EPDs without PV incursions had a broad PV trough over northeast Africa or a stratospheric PV intrusion over the eastern Mediterranean that did not reach into the Middle East. Relaxing the streamer geometrical criteria or expanding the northern boundary of the target area for PV incursions may include some of these missed EPDs, but it would also lead to an excessive increase of false alarms. It is worth noting that broad PV trough structures were also observed by Martius et al. (2006) for extreme precipitation events over the Alpine region that did not coincide with elongated PV streamers. Missed EPDs that lacked IVT incursions exhibited in many cases IVT incursions during one or several days preceding the EPDs, suggesting that sufficient tropospheric moisture amounts were already available over the region of interest. Other missed EPDs that lacked IVT incursions had a relatively large zonal IVT; 10 of the 27 missed EPDs without IVT incursions would be detected when applying a 250 kg m^{-1} s^{-1} threshold on the full IVT field. Nevertheless, sensitivity tests demonstrated a substantial deterioration of EPD hits and false alarm ratios when using the full IVT field as compared to the meridional IVT component (not shown), supporting our choice for the latter.

These findings are confirmed by composites of normalized anomalies of TCW, PV at 330 K, and IVT vectors constructed from their zonal and meridional components for missed EPDs and false alarms (Figure 7). As a reference, we show composites for EPD hits in Figure 7a, which demonstrate a center of above-normal PV over northeast Africa (>1.25 SD), anomalous northward directed IVT to its east (>2 SD in the meridional IVT), and above-normal TCW over the Arabian Peninsula (>1.25 SD). In the composite for missed EPDs that lacked PV incursions (Figure 7c), we find above-normal PV anomalies over northeast Africa and the eastern Mediterranean with magnitudes of 0.75 SD and 0.5 SD over the respective regions. These PV normalized anomaly patterns thus reflect the signatures of the broad PV trough structures without an elongated form and more northward positioned stratospheric PV intrusions. Regarding missed EPDs that lacked IVT incursions, the composites reveal above-normal TCW anomalies of the same magnitude as for EPD hits (>1.25 SD), though for a more confined region (Figure 7d), which corroborates that sufficient tropospheric moisture content was already present over the region of interest at the day of extreme precipitation. This finding is in line with Kumar et al. (2015), who found a buildup of tropospheric moisture content up to 8 days prior to extreme rainfall occurrence over the central part of the Arabian Peninsula. Furthermore, Figure 7d exhibits weak above-normal eastward directed IVT anomalies, reflecting missed EPDs that lacked IVT incursions but had a large zonal IVT.

Days with combined PV and IVT incursions that remained dry (<95th precipitation percentile) are considered as false alarms, which corresponds to a false alarm ratio of 58.3% (Table 2). False alarm days have at least two different reasons. In reality, these days were not dry, or a physical process or quantity, which is required for

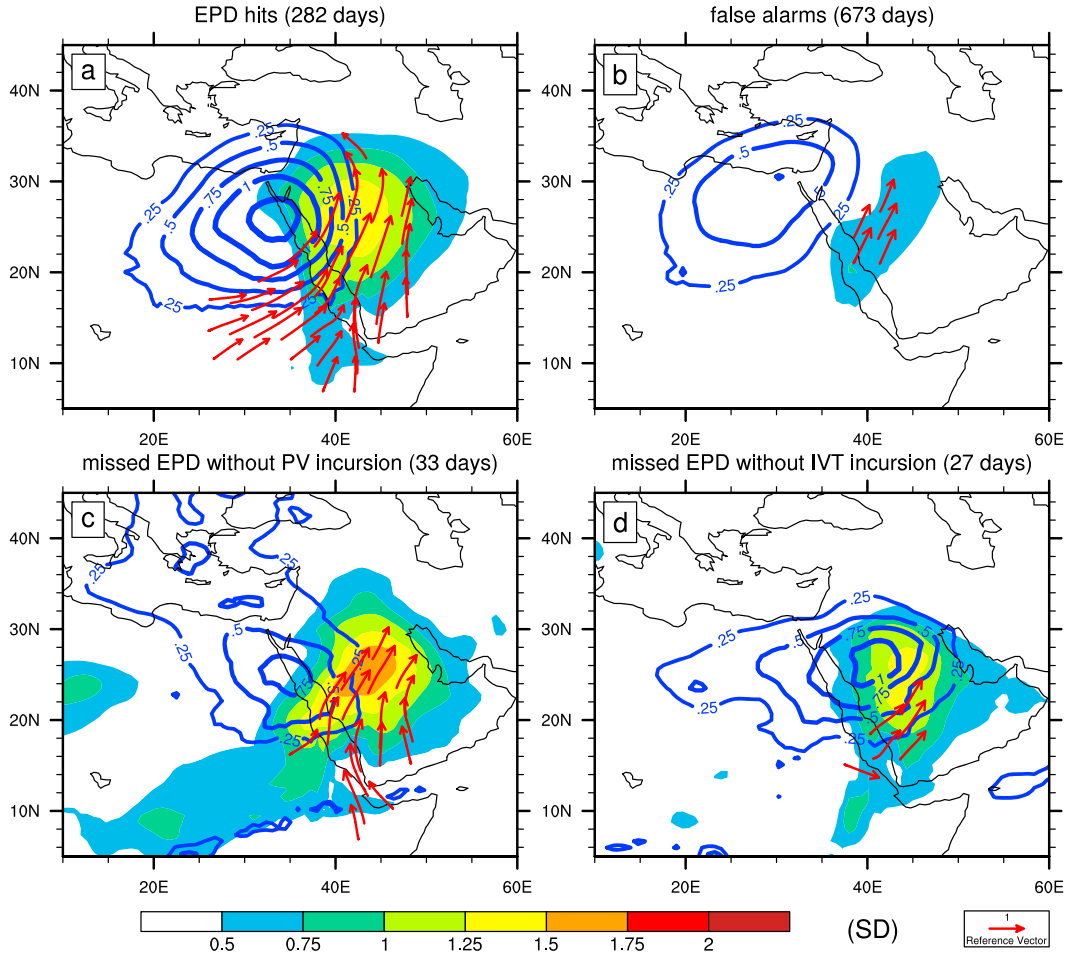

Figure 7. Composites of normalized anomalies (SD) of TCW (colors), PV at 330 K (blue contour lines), and the IVT vectors (red) constructed from their zonal and meridional components and only displayed where their vector length exceeds 1 SD for (a) EPD hits, (b) false alarms, (c) missed EPDs without PV incursion, and (d) missed EPDs without IVT incursion. The EPDs correspond to the ≥97.5th percentile, while the false alarms are defined as days with combined PV and IVT incursions and <95th percentile of daily precipitation in ERA-Interim averaged over the grid points in the region of interest.

precipitation generation, was not considered in the algorithm. Heavy rainfall, especially when occurring locally, may not be adequately represented in ERA-Interim. For example, extreme precipitation and flooding occurred over Egypt and southern Israel in the October months of 1979 (Figure 3a), 1988, 1991, and 1994 (Cools et al., 2012; De Vries et al., 2013; Moawad, 2012). Daily ERA-Interim precipitation over the region of interest remained below the 95th percentile during these episodes, although combined PV and IVT incursions were detected (not shown). This highlights the capability of the algorithm to recognize the potential for (local) extreme precipitation based on the larger-scale meteorological environment while the precipitation simulation can be of limited quality. Other false alarm days remained indeed dry. Only 9% (26%) of the false alarms days exceeded the 97.5th (95th) precipitation percentile in either Aphrodite or TRMM data (over the period of 1998–2007). Composites reveal a key ingredient for extreme precipitation that was missing: high tropospheric moisture content (Figure 7b). TCW normalized anomalies remain relatively low for false alarm days (~0.5 SD) as compared to EPDs that were either detected or missed by the algorithm (~1.25 SD). This finding is in line with Giannakaki and Martius (2016), who found that tropospheric moisture content can be a main factor to distinguish between moderate and extreme precipitation over northern Switzerland. In addition, upper-tropospheric PV anomalies for false alarm days are weaker and centered farther to the northwest (Figure 7b) as compared to EPD hits and missed EPDs (Figures 7a, 7c, and 7d), suggesting that the PV forcing was insufficient for the formation of (convective) rainstorms and extreme precipitation.

4.4. Sensitivity of the Algorithm

Obviously, the performance of the algorithm is sensitive to a number of criteria as specified in sections 2 and 3, including the PV streamer geometry, IVT threshold, the minimum area of the PV and IVT features, and the boundaries of their target areas. We applied the criteria in a manner to maximize the EPD hits and to minimize the false alarms. The most sensitive criteria were found to be the PV streamer length, the IVT threshold, the northern boundary of the target area for PV incursions, and the southern boundary of the target area for IVT incursions. Obviously, these two boundaries are strongly related to the extratropical and tropical origin of the stratospheric PV intrusions and IVT structures, respectively, which is also clearly visible in their occurrence frequencies in Figure 4. To illustrate the sensitivity of those parameters, we include EPD hits and false alarm ratios for more restrictive criteria (Table 2), being PV streamer criteria with a length $L > 1{,}000$ km, a ratio of length over width > 1, and a 250 kg m^{-1} s^{-1} threshold on the meridional IVT. The combined PV and IVT incursions occurred on 3.8% of all days during 1979–2015 and detected 70.8% (59.6%) of the 99th (97.5th) percentile EPDs. The false alarm ratio decreased from 58.3% to 41.6%, corresponding to a substantial reduction of 673 to 211 false alarm days. Thus, false alarm ratios reduce substantially when applying more restrictive criteria; however, the EPD hits also deteriorate.

5. PV and IVT Characteristics and the Precipitation Severity

Figure 8a shows the temporal evolution composite of the mean precipitation amounts over the region of interest for the 97.5th percentile EPDs and the corresponding frequencies of 6-hourly stratospheric PV intrusions and IVT structures overlapping their target areas, hereafter 6-hourly PV and IVT incursions. The 6-hourly PV and IVT incursions occur most frequently from −12 UTC to 00 UTC/+06 UTC, confirming their relation to the EPDs. The larger peak in 6-hourly IVT incursion frequencies as compared to 6-hourly PV incursion frequencies confirms again that IVT is a better indicator of extreme precipitation occurrence than PV. Note that the noisy signal in the 6-hourly PV and IVT incursion frequencies stems from diurnal variability, which is also observed for nonextreme precipitation days (not shown). Figure 8a also depicts the characteristics of the 6-hourly PV and IVT incursions, being the averages of the southward extent of the stratospheric PV intrusions and the IVT magnitudes. Interestingly, the average southward extent of 6-hourly PV incursions reaches a minimum in latitude of about 24.5°N between −42 UTC and 00 UTC and the average IVT magnitude of 6-hourly IVT incursions attains a maximum of about 420 kg m^{-1} s^{-1} between −12 UTC and +24 UTC. This time shift between the minimum of southward reaching PV incursions and peak in IVT magnitude is suggestive of a causal relationship between PV incursions that reach far into the subtropics and initiate the tropical moisture transport into the Middle East, eventually supporting the extreme precipitation events.

We further investigate the relation between the PV and IVT characteristics and the level of extreme precipitation using three categories of precipitation intensities; the ≥99th, 97.5th–99th, and 95th–97.5th percentiles of daily precipitation in ERA-Interim averaged over the region of interest. Figure 8b depicts for each of the three precipitation categories the statistical dispersion and averages of the minimum latitude of stratospheric PV intrusions and IVT magnitudes for time instances having both a 6-hourly PV and IVT incursion. The ≥99th precipitation percentile is associated with 6-hourly PV incursions reaching to an average latitude of about 24°N and an average IVT magnitude of 439 kg m^{-1} s^{-1}. We find that for the two less severe precipitation categories, on average, the PV incursions reach less far south and the IVT magnitudes reduce, following an almost linear relationship (Figure 8b). In conclusion, the farther south a stratospheric PV intrusion reaches and the higher the IVT magnitude, the more extreme the precipitation.

Another aspect likely to influence the severity of the precipitation is the duration of the PV and IVT incursions. Previous studies have suggested that extreme precipitation events in arid subtropical regions require a persistent disturbance or two successive disturbances (Knippertz, 2007), or a "period of incubation" (Kahana et al., 2004; Rubin et al., 2007), to export the moisture from the remote tropics into the subtropics. Likewise, Martius et al. (2006) found that stationarity of PV streamers is linked to the intensity of precipitation over the Alps. We investigate this possible relation through quantifying the average duration of combined PV and IVT incursions preceding the (extreme) precipitation days of the three precipitation categories as specified above and used for this calculation only the precipitation days that coincide with combined PV and IVT incursions. The combined PV and IVT incursions lasted 1.36 days, 1.03 days, and 0.93 days prior to the

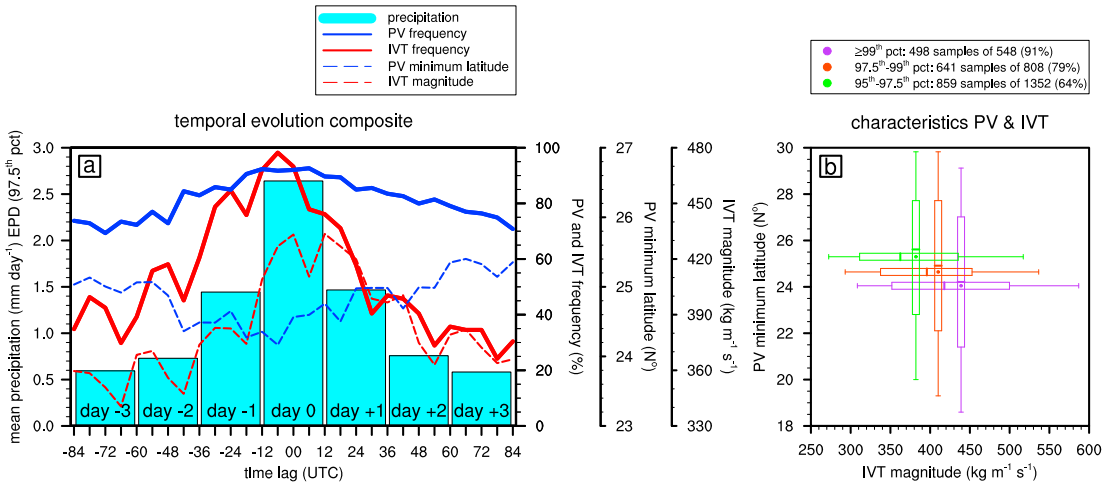

Figure 8. (a) Composites of the temporal evolution of the daily mean precipitation amounts, averaged over the grid points in the region of interest, indicated by the black box in Figure 1b, for the 97.5th percentile EPDs (blue color bars), and the corresponding 6-hourly frequencies of PV (blue lines) and IVT (red lines) incursions. Average minimum latitudes (°N) and IVT magnitudes (kg m^{-1} s^{-1}) of these 6-hourly PV and IVT incursions are denoted by the dashed blue and red lines, respectively. (b) The statistical dispersion (boxes and whiskers) and averages (dots) of the characteristics of 6-hourly PV and IVT incursions for three precipitation intensity categories with the ≥99th (purple), 97.5th–99th (orange), and 95th–97.5th (green) precipitation percentiles. The vertically (horizontally) oriented boxes and whiskers display the spread of the PV minimum latitude (IVT magnitude) and are positioned on the average IVT magnitude (PV minimum latitude) of the corresponding precipitation intensity category. The boxes denote the lower and upper quartiles, the whiskers the lower and upper deciles, and the thick lines within the boxes the medians. For the calculation of the spread and averages, we only used the 6-hourly time instances that have both a PV and IVT incursion. The numbers of these time instances (samples) and their percentage relative to all available time instances of the precipitation intensity categories are indicated in the legend. When 6-hourly time instances have multiple stratospheric PV intrusions in the target area and/or at multiple isentropic surfaces, we use the stratospheric PV intrusion with the lowest latitude. Likewise, when 6-hourly time instances have multiple IVT structures in the target area, we use the IVT structure with the largest IVT magnitude.

(extreme) precipitation day for the ≥99th, 97.5th–99th, and 95th–97.5th precipitation percentile categories, respectively. Accordingly, the precipitation extreme is subject to a weak influence of the persistence of the combined PV and IVT incursions; that is, the longer their duration, the more extreme the precipitation.

6. Contribution of Tropical-Extratropical Interactions to (Extreme) Precipitation

6.1. Gridded Precipitation Data

In this section, we quantify the contribution of tropical-extratropical interactions to the climatological precipitation amounts and the extreme precipitation days through calculating their fractions that coincide with combined PV and IVT incursions. To this end we use gridded precipitation data from ERA-Interim, Aphrodite, and TRMM. In general, their annual mean precipitation amounts and spatial distribution are in agreement (Figures 9a–9c). Note that the periods covered by these data sets differ; however, the focus is primarily on the evaluation of the algorithm rather than intercomparison of the data sets, which has been the subject of other studies (e.g., El Kenawy & McCabe, 2016; Tanarhte et al., 2012).

The combined PV and IVT incursions coincide with more than 50% of the climatological precipitation amounts over the larger part of the region of interest in all three data sets (Figures 9d–9f). Locally, the fractions of climatological precipitation amounts that are detected by the algorithm exceed 70% in ERA-Interim and TRMM data and 60% in Aphrodite data. Furthermore, we evaluate the fraction of the 99.5th percentile of extreme precipitation days that are detected by the algorithm, which correspond to 69 days, 54 days, and 31 days for the various periods covered by the ERA-Interim, Aphrodite, and TRMM data sets, respectively. In ERA-Interim, the algorithm captures more than 80% of the extreme precipitation days over the northwestern parts of Saudi Arabia and over 60% in a region that extends from eastern Egypt into the southern margins of Syria and across the larger parts of Iraq (Figure 9g). In Aphrodite and TRMM data, the algorithm detects more than 60% of the extreme precipitation days over large portions in the region of interest and locally in excess of 70% up to 80% (Figures 9h and 9i).

Relatively low detection rates of the 99.5th percentile of extreme precipitation days over eastern Egypt in Aphrodite data (<60%), and in particular in TRMM data (<40%), can be explained by the lack of

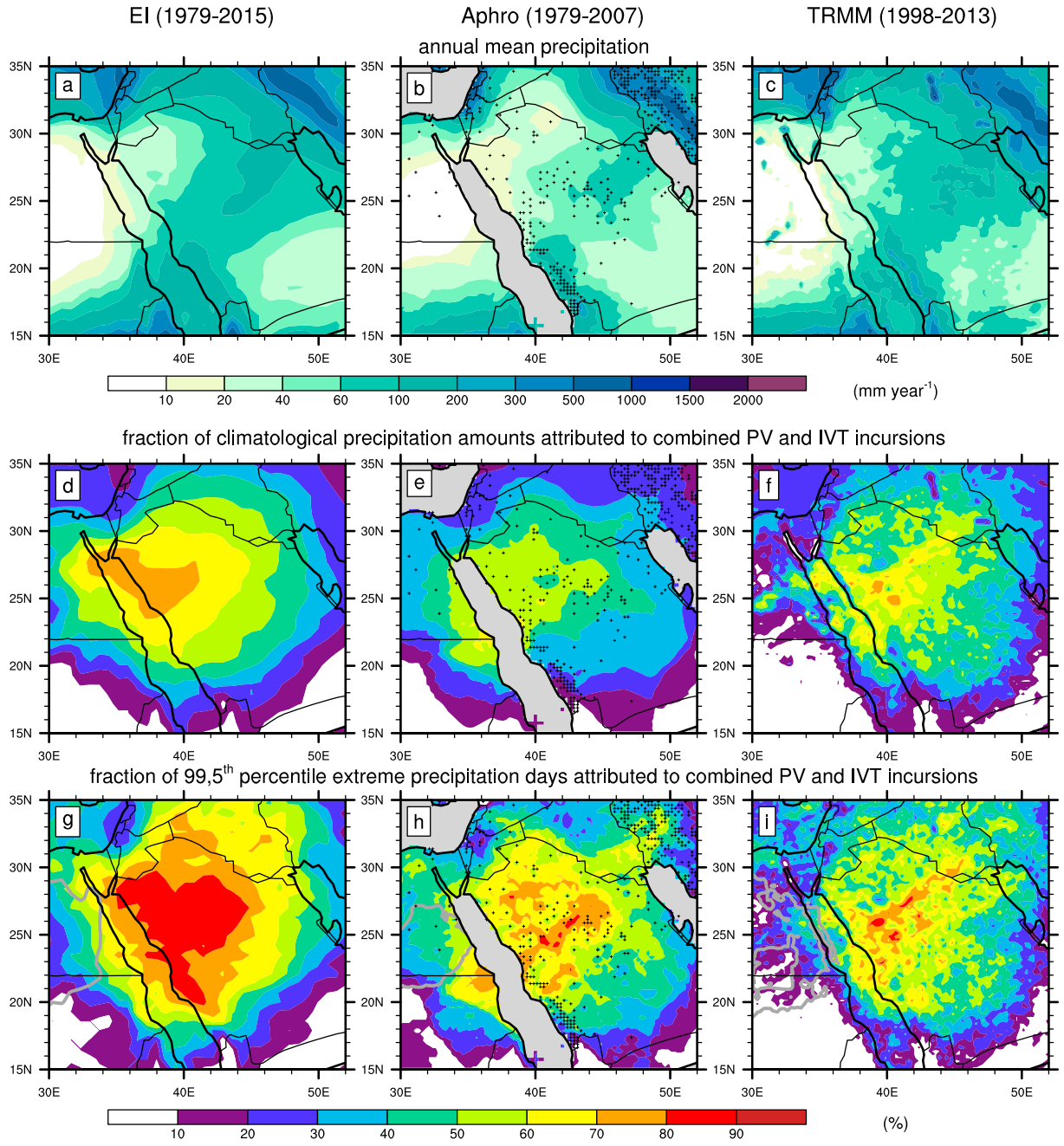

Figure 9. The spatial distribution of the (a–c) annual mean precipitation amounts (mm yr^{-1}) and the fractions of (d–f) the climatological precipitation amounts and (g–i) the 99.5th percentile extreme precipitation days that coincide with combined PV and IVT incursions in (Figures 9a, 9d, and 9g) ERA-Interim (1979–2015), (Figures 9b, 9e, and 9h) Aphrodite (1979–2007), and (Figures 9c, 9f, and 9i) TRMM (1998–2013). The markers in Figures 9b, 9e, and 9h display the grid boxes that are represented by at least one station in Aphrodite data for >50% of the days, and the gray shading masks areas with missing values for >50% of the days. The gray contour lines in Figures 9g–9i denote a precipitation threshold of 1 mm d^{-1} that corresponds to the 99.5th precipitation percentile.

meaningful extreme precipitation days over this region. The corresponding precipitation amounts are less than 1 mm d^{-1}, as depicted by the gray contour lines in Figures 9h and 9i. Overall, the fractions of detected climatological precipitation amounts and extreme precipitation days are slightly higher in ERA-Interim data than in Aphrodite and TRMM data. Most likely, this stems from the underestimation of localized heavy precipitation in ERA-Interim data, along with heavy rainfall resulting from smaller-scale convective storms being less likely detected by the algorithm than events in which the larger-scale meteorological processes play a more dominant role.

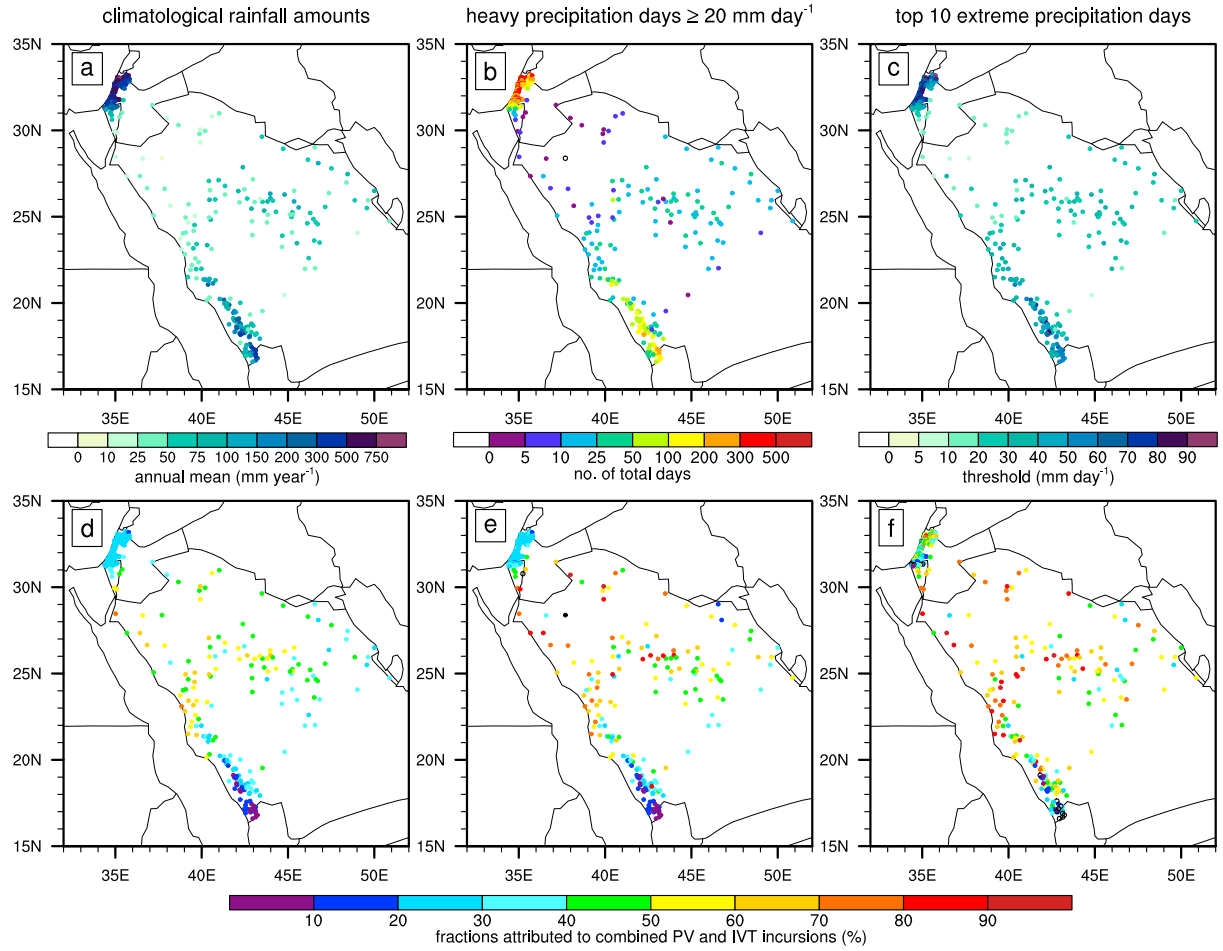

Figure 10. For rainfall observations of stations in Saudi Arabia (1979–2012) and Israel (1979–2015), the (a) annual mean precipitation amounts (mm yr^{-1}), (b) total number of heavy precipitation days with ≥20 mm d^{-1}, and (c) the threshold of precipitation (mm d^{-1}) that corresponds to the top 10 extreme precipitation days, and (d–f) their fractions (%) that coincide with combined PV and IVT incursions. Black open circles in Figures 10b, 10e, and 10f denote zero values, and black filled circles in Figure 10e represent stations without any heavy precipitation day.

6.2. Rainfall Records of Stations in Israel and Saudi Arabia

Finally, we evaluate the performance of the algorithm using daily rainfall records of stations in Israel (1979–2015) and Saudi Arabia (1979–2012). Their spatial distribution over the region of interest is somewhat inhomogeneous and has a relatively low density, but this data source provides highly valuable ground-based rainfall measurements. In general, the annual mean precipitation amounts (Figure 10a) corroborate the rainfall characteristics of the region with a relatively wet climate over northern Israel and southwestern Saudi Arabia and very dry conditions over the Negev desert and the northwestern and southeastern parts of Saudi Arabia.

Combined PV and IVT incursions contribute to 40–70% of climatological precipitation amounts at many stations in southern Israel and the northern and western parts of Saudi Arabia (Figure 10d). Similarly, the algorithm captures 50–80% of the heavy precipitation days (≥ 20 mm d^{-1}), a commonly adopted climatic index (Zhang et al., 2011), at many stations in this region, with 12 stations exceeding 80% and 2 stations reaching a score of 100% (Figure 10e). These detection rates should be interpreted with some caution as several records, in particular for stations in northwestern Saudi Arabia and southeastern Israel, contain only one up to five heavy precipitation days over the entire period under consideration (Figure 10b). To obtain a more coherent sample size of the most severe extreme precipitation days, we consider the top 10 extreme precipitation days of each station. The corresponding precipitation thresholds to extract these 10 days range between 8 and 93 mm d^{-1} and are depicted in Figure 10c. Importantly, the algorithm detects 60–90% of the top 10 extreme precipitation days at many stations in southern Israel and the northern and western parts of Saudi Arabia.

This analysis underscores the importance of tropical-extratropical interactions for precipitation and extreme precipitation in the arid parts of the Arabian Peninsula and Levant. Beyond this region, the detection rates deteriorate quickly (Figures 10d–10f) due to the restriction of the defined target areas for the PV and IVT incursions as well as the different weather regimes that control the precipitation generation in the extratropics to the north and the tropics to the south. Rainfall along the eastern Mediterranean coast, including northern Israel, stems mostly from Mediterranean cyclones, which are characterized by baroclinic systems that do not necessarily reach far into the subtropics along with westerly moisture transport over the Mediterranean Sea (Saaroni et al., 2010; Ziv et al., 2010). Precipitation over the elevated topography in southwestern Saudi Arabia is associated with the African monsoon during summer (Almazroui et al., 2012), which explains the anticorrelation between rainfall of several stations in this area and the combined PV and IVT incursions.

7. Conclusions

Recurrent extreme precipitation events in the arid Middle East can have destructive societal impacts as well as provide essential supplies for freshwater resources. These extreme precipitation events often result from tropical-extratropical interactions, whereby midlatitude forcing and tropical moisture play a key role. In this study, we developed an object-based identification method for extreme precipitation events using stratospheric PV intrusions and structures of high meridional IVT. These two physical processes have previously been postulated as important large-scale precursors for extreme precipitation events but had thus far not been combined in an algorithm for their identification. PV and IVT features were extracted from ERA-Interim reanalysis data (1979–2015), and the performance of the algorithm was evaluated using various observational precipitation data sets. This approach facilitates an assessment of the importance of tropical-extratropical interactions for precipitation and extreme precipitation in the region that comprises eastern Egypt, southern Israel, Jordan, and the northern and western parts of Saudi Arabia.

Both PV and IVT incursions are intimately linked to extreme precipitation events in the Middle East. Combined PV and IVT incursions (i) detect 90% of the 99th percentile EPDs and 83% of the 97.5th percentile EPDs, (ii) are highly associated with the precipitation intensity distribution, and (iii) follow the seasonality of EPDs with dry summer months and peaks in late autumn/early winter and early spring. The severity of the precipitation depends on the PV and IVT characteristics and the persistence of the combined PV and IVT incursions. The farther south a stratospheric PV intrusion reaches, the larger the IVT magnitude, and the longer their combined duration, the more extreme the precipitation. Another important finding is that IVT incursions alone perform nearly as good as the combination of PV and IVT incursions to identify EPDs, indicating a higher potential of IVT as a predictor of extreme precipitation than PV. Application of IVT structures for identification of extreme precipitation in regions elsewhere may require application of the full IVT field instead of only the meridional component and adjustment of the IVT threshold due to spatial variability in background IVT, for example, through adopting percentile-based IVT thresholds as in Guan and Waliser (2015) or anomalous IVT as in Mundhenk, Barnes, and Maloney (2016).

The tropospheric circulation during EPD hits (EPDs that coincided with combined PV and IVT incursions) highlights the interaction between the tropical and midlatitude circulations. As a result, tropical moist air masses intrude into the Middle East and support the formation of localized convective storms and widespread rainstorms, which are typical of Active Red Sea Trough events and tropical plumes, respectively. These tropical-extratropical interactions contribute to a substantial fraction of climatological precipitation amounts (40–70%), a large number of heavy precipitation days exceeding 20 mm d^{-1} (50–80%), and the top 10 extreme precipitation days (60–90%) in the arid parts of the Levant and the Arabian Peninsula. Thus, tropical-extratropical interactions are not only important for extreme precipitation events that give rise to flood hazards but also for rainfall that can replenish freshwater resources. The combination of PV and IVT may serve as a concept of synoptic-scale precursors and ingredients for precipitation and extreme precipitation events. Accordingly, the algorithm may find application for detection of precipitation and extreme precipitation in other dry subtropical regions as well as higher latitudes where stratospheric PV intrusions and southerly moisture fluxes have been associated with extreme precipitation (e.g., Froidevaux & Martius, 2016; Martius et al., 2006). Other relevant applications of the algorithm may facilitate an evaluation of the role of PV intrusions in (1) the formation and landfall of atmospheric rivers (Mundhenk, Barnes, Maloney, et al.,

2016; Payne & Magnusdottir, 2014), and (2) moist air incursions into the Arctic (Baggett et al., 2016; Liu & Barnes, 2015), which both have been associated with Rossby wave breaking.

Limitations of the algorithm are exemplified through analyzing missed EPDs and false alarms. Missed EPDs are associated with (i) broad PV troughs, (ii) stratospheric PV intrusions that did not reach far into the subtropics, (iii) the prior presence of large tropospheric moisture amounts, and (iv) a large zonal IVT. False alarm days may in reality have experienced localized heavy rainfall that is not represented in the ERA-Interim data or have remained dry due to insufficient tropospheric moisture amounts. Thus, tropospheric moisture content can explain missed EPDs that lacked IVT incursions (high above-normal TCW anomalies) as well as days with combined PV and IVT incursions that remained dry (low above-normal TCW anomalies). Here the question arises as to whether the algorithm should be complemented by TCW as a third component or as an alternative to IVT. We refrained from including TCW in the algorithm, as absolute TCW amounts are usually large over the Red Sea region and subject to a strong seasonal cycle, associated with the Red Sea Trough (De Vries et al., 2013). The use of normalized anomalies of TCW may circumvent these issues; however, this would require statistically based climatological information of the data set, which is not needed for the current algorithm.

The strength of the algorithm is the identification of local-scale extreme precipitation based on larger-scale meteorological features without depending on precipitation data and their inherent limitations. Thus, the algorithm has the potential to serve medium-range weather prediction and early warning systems and future studies on climatological aspects of extreme precipitation such as their associated teleconnection patterns, interannual variability and trends, and changes due to global warming.

Acknowledgments

The authors wish to thank CRED, ECMWF, NASA, JAXA, and APHRODITE for providing their data sets, which are available under the following links: EM-DAT (http://www.emdat.be/), ERA-Interim (https://www.ecmwf.int/en/research/climate-reanalysis/era-interim), TRMM (https://pmm.nasa.gov/data-access/downloads/trmm), and Aphrodite (http://www.chikyu.ac.jp/precip/english/). We acknowledge the Israeli Atmospheric and Climatic Data Centre (IACDC), supported by the Israeli Ministry of Science, Technology and Space, for providing the Israel Meteorological Service (IMS) daily rainfall records as well as the Ministry of Environment, Water and Agriculture (MEWA) in the Kingdom of Saudi Arabia for providing daily rainfall data. The algorithm is written in the National Center for Atmospheric Research (NCAR) Command Language (NCL) package version 6.3.0, which was also used for the visualization of the data. The algorithm output, as described in section 2.3, are available from the corresponding author upon request. S. B. F. was supported by National Science Foundation grants AGS-1401220 and AGS-1723832. The authors wish to thank Michael Sprenger and Heini Wernli for their helpful suggestions for writing the algorithm for PV intrusions. We greatly appreciate the constructive comments of three anonymous reviewers that helped to improve the quality of the manuscript.

References

Almazroui, M., Islam, M. N., Jones, P. D., Athar, H., & Rahman, M. A. (2012). Recent climate change in the Arabian Peninsula: Seasonal rainfall and temperature climatology of Saudi Arabia for 1979–2009. *Atmospheric Research*, *111*, 29–45. https://doi.org/10.1016/j.atmosres.2012.02.013

Almazroui, M., Kamil, S., Ammar, K., Keay, K., & Alamoudi, A. O. (2016). Climatology of the 500-hPa Mediterranean storms associated with Saudi Arabia wet season precipitation. *Climate Dynamics*, *48*, 3309–3324.

Amin, M. T., Mahmoud, S. H., & Alazba, A. A. (2016). Observations, projections and impacts of climate change on water resources in Arabian Peninsula: Current and future scenarios. *Environment and Earth Science*, *75*(10). https://doi.org/10.1007/s12665-016-5684-4

Baggett, C., Lee, S., & Feldstein, S. B. (2016). An investigation of the presence of atmospheric rivers over the North Pacific during planetary-scale wave life cycles and their role in Arctic warming. *Journal of the Atmospheric Sciences*, *73*(11), 4329–4347. https://doi.org/10.1175/JAS-D-16-0033.1

Barton, Y., Giannakaki, P., von Waldow, H., Chevalier, C., Pfahl, S., & Martius, O. (2016). Clustering of regional-scale extreme precipitation events in Southern Switzerland. *Monthly Weather Review*, *144*(1), 347–369. https://doi.org/10.1175/MWR-D-15-0205.1

Béguin, A., Martius, O., Sprenger, M., Spichtinger, P., Folini, D., & Wernli, H. (2013). Tropopause level Rossby wave breaking in the Northern Hemisphere: A feature-based validation of the ECHAM5-HAM climate model. *International Journal of Climatology*, *3*, 3073–3082.

Cavazos, T., Comrie, A. C., & Liverman, D. M. (2002). Intraseasonal variability associated with wet monsoons in southeast Arizona. *Journal of Climate*, *15*(17), 2477–2490. https://doi.org/10.1175/1520-0442(2002)015,2477:IVAWWM.2.0.CO;2

Cools, J., Vanderkrimpen, P., El Afandi, G., Abdelkhalek, A., Fockedey, S., El Sammany, M., … Huygens, M. (2012). An early warning system for fl an floods in hyper-arid Egypt. *Natural Hazards and Earth System Sciences*, *12*, 443–457. https://doi.org/10.5194/nhess-12-443-2012

De Vries, A. J., Tyrlis, E., Edry, D., Krichak, S. O., Steil, B., & Lelieveld, J. (2013). Extreme precipitation events in the Middle East: Dynamics of the Active Red Sea Trough. *Journal of Geophysical Research: Atmospheres*, *118*, 7087–7108. https://doi.org/10.1002/jgrd.50569

De Vries, A. J., Feldstein, S. B., Riemer, M., Tyrlis, E., Sprenger, M., Baumgart, M., … Lelieveld, J. (2016). Dynamics of tropical-extratropical interactions and extreme precipitation events in Saudi Arabia in autumn, winter and spring. *Quarterly Journal of the Royal Meteorological Society*, *142*(697), 1862–1880. https://doi.org/10.1002/qj.2781

Dee, D. P., Uppala, S. M., Simmons, A. J., Berrisford, P., Poli, P., Kobayashi, S., … Vitart, F. (2011). The ERA-Interim reanalysis: Configuration and performance of the data assimilation system. *Quarterly Journal of the Royal Meteorological Society*, *137*, 553–597. https://doi.org/10.1002/qj.828

Deng, L. P., McCabe, M. F., Stenchikov, G., Evans, J. P., & Kucera, P. A. (2015). Simulation of flash-flood-producing storm events in Saudi Arabia using the Weather Research and Forecasting Model. *Journal of Hydrometeorology*, *16*(2), 615–630. https://doi.org/10.1175/JHM-D-14-0126.1

Donat, M. G., Sillmann, J., Wild, S., Alexander, L. V., Lippmann, T., & Zwiers, F. W. (2014). Consistency of temperature and precipitation extremes across various global gridded in situ and reanalysis datasets. *Journal of Climate*, *27*(13), 5019–5035. https://doi.org/10.1175/JCLI-D-13-00405.1

El Kenawy, A. M., & McCabe, M. F. (2016). A multi-decadal assessment of the performance of gauge- and model-based rainfall products over Saudi Arabia: Climatology, anomalies and trends. *International Journal of Climatology*, *36*(2), 656–674. https://doi.org/10.1002/joc.4374

Evans, J. P., & Smith, R. B. (2006). Water vapor transport and the production of precipitation in the eastern fertile crescent. *Journal of Hydrometeorology*, *7*(6), 1295–1307. https://doi.org/10.1175/JHM550.1

Favors, J. E., & Abatzoglou, J. T. (2013). Regional surges of monsoonal moisture into the southwestern United States. *Monthly Weather Review*, *141*(1), 182–191. https://doi.org/10.1175/MWR-D-12-00037.1

Fröhlich, L., Knippertz, P., Fink, A. H., & Hohberger, E. (2013). An objective climatology of tropical plumes. *Journal of Climate*, *26*(14), 5044–5060. https://doi.org/10.1175/JCLI-D-12-00351.1

Froidevaux, P., & Martius, O. (2016). Exceptional integrated vapor transport toward orography: An important precursor to severe floods in Switzerland. *Quarterly Journal of the Royal Meteorological Society*, *142*(698), 1997–2012. https://doi.org/10.1002/qj.2793

Funatsu, B. M., & Waugh, D. W. (2008). Connections between potential vorticity intrusions and convection in the Eastern Tropical Pacific. *Journal of the Atmospheric Sciences*, *65*(3), 987–1002. https://doi.org/10.1175/2007JAS2248.1

Giannakaki, P., & Martius, O. (2016). Synoptic-scale flow structures associated with extreme precipitation events in northern Switzerland. *International Journal of Climatology*, *36*(6), 2497–2515. https://doi.org/10.1002/joc.4508

Guan, B., & Waliser, D. E. (2015). Detection of atmospheric rivers: Evaluation and application of an algorithm for global studies. *Journal of Geophysical Research: Atmospheres*, *120*(24), 12,514–12,535. https://doi.org/10.1002/2015JD024257

Hart, N. C. G., Reason, C. J. C., & Fauchereau, N. (2010). Tropical-extratropical interactions over southern Africa: Three cases of heavy summer season rainfall. *Monthly Weather Review*, *138*, 2608–2623. https://doi.org/10.1175/2010MWR3070.1

Hart, N. C. G., Reason, C. J. C., & Fauchereau, N. (2012). Building a tropical extratropical cloud band metbot. *Monthly Weather Review*, *140*, 4005–4016. https://doi.org/10.1175/MWR-D-12-00127.1

Hart, N. C. G., Reason, C. J. C., & Fauchereau, N. (2013). Cloud bands over southern Africa: Seasonality, contribution to rainfall variability and modulation by the MJO. *Climate Dynamics*, *41*(5-6), 1199–1212. https://doi.org/10.1007/s00382-012-1589-4

Huffman, G. J., Adler, R. F., Bolvin, D. T., Gu, G., Nelkin, E. J., Bowman, K. P., … Wolff, D. B. (2007). The TRMM multisatellite precipitation analysis (TMPA): Quasi-global, multiyear, combined-sensor precipitation estimates at fine scales. *Journal of Hydrometeorology*, *8*, 38–55. https://doi.org/10.1175/JHM560.1

Isotta, F., Martius, O., Sprenger, M., & Schwierz, C. (2008). Long-term trends of synoptic-scale breaking. Rossby waves in the Northern Hemisphere between 1958 and 2001. *International Journal of Climatology*, *28*, 1551–1562. https://doi.org/10.1002/joc.1647

Kahana, R., Ziv, B., Dayan, U., & Enzel, Y. (2004). Atmospheric predictors for major floods in the Negev desert, Israel. *International Journal of Climatology*, *24*, 1137–1147. https://doi.org/10.1002/joc.1056

Knippertz, P. (2003). Tropical-extratropical interactions causing precipitation in northwest Africa: Statistical analysis and seasonal variations. *Monthly Weather Review*, *131*(12), 3069–3076. https://doi.org/10.1175/1520-0493

Knippertz, P. (2007). Tropical-extratropical interactions related to upper-troughs at low latitudes. *Dynamics of Atmospheres and Oceans*, *43*, 36–62. https://doi.org/10.1016/j.dynatmoce.2006.06.003

Knippertz, P., & Martin, J. E. (2005). Tropical plumes and extreme precipitation in subtropical and tropical West Africa. *Quarterly Journal of the Royal Meteorological Society*, *131*, 2337–2365. https://doi.org/10.1256/qj.04.148

Knippertz, P., Fink, A. H., Reiner, A., & Speth, P. (2003). Three late summer/early autumn cases of tropical-extratropical interactions causing precipitation in northwest Africa. *Monthly Weather Review*, *131*(1), 116–135. https://doi.org/10.1175/1520-0493(2003)131%3C0116:TLSEAC%3E2.0.CO;2

Knippertz, P., Wernli, H., & Glaser, G. (2013). A global climatology of tropical moisture exports. *Journal of Climate*, *17*, 1449–1458.

Knipperz, P., & Wernli, H. (2010). A Lagrangian climatology of tropical moisture exports to the Northern Hemisphere extratropics. *Journal of Climate*, *23*(4), 987–1003. https://doi.org/10.1175/2009JCLI3333.1

Krichak, S. O., Breitgand, J. S., & Feldstein, S. B. (2012). A conceptual model for the identification of the Active Red Sea Trough Synoptic events over the southeastern Mediterranean. *Journal of Applied Meteorology and Climatology*, *51*(5), 962–971. https://doi.org/10.1175/JAMC-D-11-0223.1

Kumar, K. N., Entekhabi, D., & Molini, A. (2015). Hydrological extremes in hyperarid regions: A diagnostic characterization of intense precipitation over the Central Arabian Peninsula. *Journal of Geophysical Research: Atmospheres*, *120*, 1637–1650. https://doi.org/10.1002/2014JD022341

Kunz, A., Sprenger, M., & Wernli, H. (2015). Climatology of potential vorticity streamers and associated isentropic transport pathways across PV gradient barriers. *Journal of Geophysical Research: Atmospheres*, *120*, 3802–3821. https://doi.org/10.1002/2014JD022615

Lavers, A., & Villarini, G. (2013a). The nexus between atmospheric rivers and extreme precipitation across Europe. *Geophysical Research Letters*, *40*, 3259–3264. https://doi.org/10.1002/grl.50636

Lavers, D. A., & Villarini, G. (2013b). Atmospheric rivers and flooding over the central United States. *Journal of Climate*, *26*(20), 7829–7836. https://doi.org/10.1175/JCLI-D-13-00212.1

Lavers, D. A., Pappenberger, F., & Zsoter, E. (2014). Extending medium-range predictability of extreme hydrological events in Europe. *Nature Communications*, *5*, 5382. https://doi.org/10.1038/ncomms6382

Liu, C., & Barnes, E. A. (2015). Extreme moisture transport into the Arctic linked to Rossby wave breaking. *Journal of Geophysical Research: Atmospheres*, *120*(9), 3774–3788. https://doi.org/10.1002/2014JD022796

Liu, C., Ren, X., & Yang, X. (2014). Mean flow-storm track relationship and Rossby wave breaking in two types of El-Niño. *Advances in Atmospheric Sciences*, *31*(1), 197–210. https://doi.org/10.1007/s00376-013-2297-7

Madonna, E., Limbach, S., Aebi, C., Joos, H., Wernli, H., & Martius, O. (2014). On the co-occurrence of warm conveyor belt outflows and PV streamers. *Journal of the Atmospheric Sciences*, *71*(10), 3668–3673. https://doi.org/10.1175/JAS-D-14-0119.1

Madonna, E., Wernli, H., Joos, H., & Martius, O. (2014). Warm conveyor belts in the ERA-Interim Dataset (1979–2010). Part I: Climatology and potential vorticity evolution. *Journal of Climate*, *27*(1), 3–26. https://doi.org/10.1175/JCLI-D-12-00720.1

Mahoney, K., Jackson, D. L., Neiman, P., Hughes, M., Darby, L., Wick, G., … Cifelli, C. (2016). Understanding the role of atmospheric rivers in heavy precipitation in the southeast United States. *Monthly Weather Review*, *144*(4), 1617–1632. https://doi.org/10.1175/MWR-D-15-0279.1

Martius, O., Zenklusen, E., Schwierz, C., & Davies, H. C. (2006). Episodes of Apline heavy precipitation with an overlying elongated stratospheric intrusion: A climatology. *International Journal of Climatology*, *26*, 1149–1164. https://doi.org/10.1002/joc.1295

Martius, O., Schwierz, C., & Davies, H. C. (2008). Far-upstream precursors of heavy precipitation events on the Alpine south-side. *Quarterly Journal of the Royal Meteorological Society*, *134*, 417–428. https://doi.org/10.1002/qj.229

Martius, O., Schwierz, C., & Sprenger, M. (2008). Dynamical tropopause variability and potential vorticity streamers in the Northern Hemisphere—A climatological analysis. *Advances in Atmospheric Sciences*, *25*, 367–380. https://doi.org/10.1007/s00376-008-0367-z

Martius, O., Sodemann, H., Joos, H., Pfahl, S., Winschall, A., Croci-Maspoli, M., … Wernli, H. (2013). The role of upper-level dynamics and surface processes for the Pakistan flood of July 2010. *Quarterly Journal of the Royal Meteorological Society*, *139*(676), 1780–1797. https://doi.org/10.1002/qj.2082

Massacand, A. C., Wernli, H., & Davies, H. C. (1998). Heavy precipitation on the Alpine southside: An upper-level precursor. *Geophysical Research Letters*, *25*(9), 1435–1438. https://doi.org/10.1029/98GL50869

McIntyre, M. E., & Palmer, T. N. (1983). Breaking planetary waves in the stratosphere. *Nature*, *305*(5935), 593–600. https://doi.org/10.1038/305593a0

Moawad, M. B. (2012). Predicting and analyzing flash floods of ungauged small-scale drainage basins in the eastern desert of Egypt. *Journal of Geomatics*, *6*(1), 23–30.

Moore, B. J., Mahoney, K. M., Sukovich, E. M., Cifelli, R., & Hamill, T. M. (2015). Climatology and environmental characteristics of extreme precipitation events in the southeastern United States. *Monthly Weather Review*, *143*(3), 718–741. https://doi.org/10.1175/MWR-D-14-00065.1

Mundhenk, B. D., Barnes, E. A., & Maloney, E. D. (2016). All-season climatology and variability of atmospheric river frequencies over the North Pacific. *Journal of Climate*, *29*(13), 4885–4903. https://doi.org/10.1175/JCLI-D-15-0655.1

Mundhenk, B. D., Barnes, E. A., Maloney, E. D., & Nardi, K. M. (2016). Modulation of atmospheric rivers near Alaska and the US West Coast by northeast Pacific height anomalies. *Journal of Geophysical Research: Atmospheres*, *121*, 12,751–12,765. https://doi.org/10.1002/2016JD025350

Pascale, S., & Bordoni, S. (2016). Tropical and extratropical controls of Gulf of California surges and summertime precipitation over the southwestern United States. *Monthly Weather Review*, *144*(7), 2695–2718. https://doi.org/10.1175/MWR-D-15-0429.1

Payne, A. E., & Magnusdottir, G. (2014). Dynamics of landfalling atmospheric rivers over the North Pacific in 30 years of MERRA reanalysis. *Journal of Climate*, *27*(18), 7133–7150. https://doi.org/10.1175/JCLI-D-14-00034.1

Pfahl, S., & Wernli, H. (2012). Quantifying the relevance of cyclones for precipitation extremes. *Journal of Climate*, *25*, 6770–6780. https://doi.org/10.1175/JCLI-D-11-00705.1

Pfahl, S., Madonna, E., Boettcher, M., Joos, H., & Wernli, H. (2014). Warm conveyor belts in the ERA-Interim data set (1979) (1979) set (19791) Moisture origin and relevance for precipitation. *Journal of Climate*, *27*, 27.im. origin and relevance for preci(1), 27–40. https://doi.org/10.1175/JCLI-D-13-00223.1

Ralph, F. M., Nieman, P. J., Wick, G. A., Gutman, S. I., Dettinger, M. D., Cayan, D. R., & White, A. B. (2006). Flooding on California's Russian River: Role of atmospheric rivers. *Geophysical Research Letters*, *33*, L13801. https://doi.org/10.1029/2006GL026689

Rodwell, M. J., & Hoskins, B. J. (1996). Monsoon and the dynamics of deserts. *Quarterly Journal of the Royal Meteorological Society*, *122*(534), 1385–1404. https://doi.org/10.1002/qj.49712253408

Rubin, S., Ziv, B., & Paldor, N. (2007). Tropical plumes over eastern North Africa as a source of rain in the Middle East. *Monthly Weather Review*, *135*, 4135–4148. https://doi.org/10.1175/2007MWR1919.1

Rutz, J. J., Steenburgh, W. J., & Ralph, F. M. (2014). Climatological characteristics of atmospheric rivers and their inland penetration over the western United States. *Monthly Weather Review*, *142*(2), 905–921. https://doi.org/10.1175/MWR-D-13-00168.1

Saaroni, H., Halfon, N., Ziv, B., Alpert, P., & Kutiel, H. (2010). Links between the rainfall regime in Israel and location and intensity of Cyprus Lows. *International Journal of Climatology*, *30*, 1014–1025. https://doi.org/10.1002/joc.1912

Schlemmer, L., Martius, O., Sprenger, M., Schwierz, C., & Twitchett, A. (2010). Disentangling the forcing mechanisms of a heavy precipitation event along the alpine south side using potential vorticity inversion. *Monthly Weather Review*, *138*(6), 2336–2353. https://doi.org/10.1175/2009MWR3202.1

Schulz, S., de Rooij, G. H., Michelsen, N., Rausch, R., Siebert, C., Schüth, C., … Merz, R. (2016). Estimating groundwater recharge for an arid karst system using a combined approach of time-lapse camera monitoring and water balance modelling. *Hydrological Processes*, *30*(5), 771–782. https://doi.org/10.1002/hyp.10647

Škerlak, B., Sprenger, M., Pfahl, S., Tyrlis, E., & Wernli, H. (2015). Tropopause folds in ERA-Interim: Global climatology and relation to extreme weather events. *Journal of Geophysical Research: Atmospheres*, *120*, 4860–4877. https://doi.org/10.1002/2014JD022787

Sprenger, M., Wernli, H., & Bourqui, M. (2007). Stratosphere-troposphere exchange and its relation to potential vorticity streamers and cutoffs near the extratropical tropopause. *Journal of the Atmospheric Sciences*, *64*, 1587–1602. https://doi.org/10.1175/JAS3911.1

Sprenger, M., Martius, O., & Arnold, J. (2013). Cold surge episodes over southeastern Brazil—A potential vorticity perspective. *International Journal of Climatology*, *33*, 2758–2767.

Strong, C., & Magnusdottir, G. (2008). Tropospheric Rossby wave breaking and the NAO/NAM. *Journal of the Atmospheric Sciences*, *65*, 2861–2876. https://doi.org/10.1175/2008JAS2632.1

Swales, D., Alexander, M., & Hughes, M. (2016). Examining moisture pathways and extreme precipitation in the U.S. Intermountain West using self-organizing maps. *Geophysical Research Letters*, *43*, 1727–1735. https://doi.org/10.1002/2015GL067478

Tanarhte, M., Hadjinicolaou, P., & Lelieveld, J. (2012). Intercomparison of temperature and precipitation data sets based on observations in the Mediterranean and the Middle East. *Journal of Geophysical Research*, *117*, D12102. https://doi.org/10.1029/2011JD017293

Tyrlis, E., Lelieveld, J., & Steil, B. (2013). The summer circulation over the eastern Mediterranean and the Middle East: Influence of the South Asian monsoon. *Climate Dynamics*, *40*(5-6), 1103–1123. https://doi.org/10.1007/s00382-012-1528-4

Vellore, R., Kaplan, M., Krishnan, R., Lewis, J., Sabade, S., Deshpande, N., … Rama Rao, M. V. S. (2016). Monsoon–extratropical circulation interactions in Himalayan extreme rainfall. *Climate Dynamics*, *46*(11-12), 3517–3546. https://doi.org/10.1007/s00382-015-2784-x

Waliser, D., & Guan, B. (2017). Extreme winds and precipitation during landfall of atmospheric rivers. *Nature*, *10*(3), 179–183.

Wernli, H., & Sprenger, M. (2007). Identification and ERA-15 climatology of potential vorticity streamers and cutoffs near the extratropical tropopause. *Journal of the Atmospheric Sciences*, *64*, 1569–1586. https://doi.org/10.1175/JAS3912.1

Wright, W. J. (1997). Tropical-extratropical cloudbands and Australian rainfall: 1. Climatology. *International Journal of Climatology*, *17*(8), 807–829. https://doi.org/10.1002/(SICI)1097-0088(19970630)17:8%3C807::AID-JOC162%3E3.0.CO;2-J

Yatagai, A., Kamiguchi, K., Arakawa, O., Hamada, A., Yasutomi, N., & Kitoh, A. (2012). Aphrodite constructing a long-term daily gridded precipitation dataset for Asia based on a dense network of rain gauges. *Bulletin of the American Meteorological Society*, *93*, 1401–1415. https://doi.org/10.1175/BAMS-D-11-00122.1

Yesubabu, V., Srinivas, C. V., Langodan, S., & Hoteit, I. (2016). Predicting extreme rainfall events over Jeddah, Saudi Arabia: Impact of data assimilation with conventional and satellite observations. *Quarterly Journal of the Royal Meteorological Society*, *142*(694), 327–348. https://doi.org/10.1002/qj.2654

Zaitchik, B. J., Evans, J. P., & Smith, R. B. (2007). Regional impact of an elevated heat source: The Zagros Plateau of Iran. *Journal of Climate*, *20*, 4133–4146. https://doi.org/10.1175/JCLI4248.1

Zarrin, A., Ghaemi, H., Azadi, M., & Farajzadeh, M. (2010). The spatial pattern of summertime subtropical anticyclones over Asia and Africa: A climatological review. *International Journal of Climatology*, *30*, 159–173. https://doi.org/10.1002/joc.1879

Zhang, X., Alexander, L., Hegerl, G. C., Jones, P., Klein Tank, A., Peterson, T. C., … Zwiers, F. W. (2011). Indices for monitoring changes in extremes based on daily temperature and precipitation data. *Climatic Change*, *2*, 851–870. https://doi.org/10.1002/xcc.147

Ziv, B. (2001). A subtropical rainstorm associated with a tropical plume over Africa and the Middle-East. *Theoretical and Applied Climatology*, *68*(1–2), 91–102.

Ziv, B., Saaroni, H., & Alpert, P. (2004). The factors governing the summer regime of the eastern Mediterranean. *International Journal of Climatology*, *24*, 1859–1871. https://doi.org/10.1002/joc.1113

Ziv, B., Dayan, U., & Sharon, D. (2005). A mid-winter, tropical extreme flood-producing storm in southern Israel: Synoptic scale analysis. *Meteorology and Atmospheric Physics*, *88*, 53–63. https://doi.org/10.1007/s00703-003-0054-7

Ziv, B., Saaroni, H., Romem, M., Heifetz, E., Harnik, N., & Baharad, A. (2010). Analysis of conveyor belts in winter Mediterranean cyclones. *Theoretical and Applied Climatology*, *99*, 441–455. https://doi.org/10.1007/s00704-009-0150-9